University of Baghdad
College of Engineering
JE
JOURNAL OF ENGINEERING

Journal of Engineering

journal homepage: www.jcoeng.edu.iq
Number 3 Volume 24 Month 3

Chemical, Petroleum and Environmental Engineering

Synthesis and Characterization of Nanocrystalline Aluminophosphate $AlPO_4$-5 Molecular Sieve

Asir Alnaama
Instructor Dr. , Consultant in Student Affairs Dept., lecturer in Chem.Eng. Dept.,
Engineering college-Baghdad University
Email:dr.asir.alnaama@gmail.com

ABSTRACT

Nanocrystalline aluminophosphate $AlPO_4$-5 molecular sieves were synthesized by hydrothermal method (HTS). Synthesis parameters like time and temperature of crystallization were investigated. Type of template (R) and ratio of R/P_2O_5 were studied also. Characterization of the synthesized $AlPO_4$-5 were done by powder X-ray diffraction (XRD), scanning electron microscopy (SEM/EDX), Fourier transform infrared (FTIR), differential scanning calorimetry-thermogravimetry analysis (DSC-TGA), and N_2 adsorption-desorption BET analysis. XRD patterns results showed excellent crystallinity for two types of templates, di-n-propylamine (DPA) and tetrapropyl ammonium hydroxide (TPAOH) for alumminophosphate five (AFI) structure. Nano-level for particle size of 66 nm was revealed by AFM test. Good thermal stability was obtained in DSC-TGA results. Best time and temperature of crystallization of 24h and 190 ^{O} C were got. Optimum R/P_2O_5 for two kind of template was established.

Keywords: Aluminophosphate, AFI, $AlPO_4$-5, Molecular sieves, Nanocrystalline.

1. INTRODUCTION

Aluminophosphate ($AlPO_4$) molecular sieves have drawn the attention of the researchers and extensively investigated due to thier excellent properties. Similar to, zeolite $AlPO_4$ molecular sieves are constructed by phosphorous and aluminum tetrahedral. Their metal substituted (isomorphously) molecular sieves have many applications in catalysis and catalytic reactions like isomerization and others, **Rajesh, et al., 2001, Hartmann** and **Elangovan, 2003, Choi, et al., 2006, Wekhysen, et al., 1991, Wang, et al., 2009,** and **Li, et al., 2004**.

The novel structure of aluminophosphate ($AlPO_4$) based molecular sieves showed a variety in pore size and can be classified to large pore (0.7-0.8nm) like $AlPO_4$-5 (AFI-aluminophosphate five structure), intermediate pore (0.6nm) like $AlPO_4$-11 (AEL-aluminophosphate eleven structure), small pore (0.4nm) like $AlPO_4$-14 (AFN-Aluminophosphate fourteen structure), **Rajesh, et al., 2001**.

The framework of $AlPO_4$-5 (AFI) is hexagonal with a=1.373 nm, c=0.848 nm and consists of columns of twisted 4- and 6- rings parallel to c-axis giving a unidimensional 12-rings and free diameter of pore 0.73 nm. The framework of $AlPO_4$-11(AEL) is generated by elimination of one-third of the rings from $AlPO_4$-5 framework and conversion of each 12-ring rounded channel into an elliptical 10-ring channel with diameter of 0.67nm by 0.40nm, by The templates used in incorporation into channel during synthesis are di-n-propylamine (DPA) for $AlPO_4$-5 and tetrapropyl ammonium forming $AlPO_4$-11, **Flanigen, et al., 1986.**

$AlPO_4$ molecular sieves exhibit excellent thermal and hydrothermal stability comparable to zeolites. The frameworks of $AlPO_4$‘s are neutral and exhibit weakly acidic catalytic properties, so isomorphous incorporation of metals is essential for improving the catalytic performance of $AlPO_4$‘s.

Synthesis of $AlPO_4$ were investigated using different techniques mostly by hydrothermal (Solvothermal) synthesis (HTS)**, Gielgens, et al., 1995, Hassanvan** and **Ashgari, 2012, Wan, et al., 2000, Klap, et al., 1999, Zhang, 2013,** and **Naydenov, 2003,** and recently by ionothermal synthesis using ionic liquid solution (ILS), **Wei, et al., 2010, Fayad, et al., 2010, Han, et al., 2007, Xu, et al., 2006,** and **Sun, 2012s**.

Li, et al., **2012**, investigated the effect of precursor gel preparation on the microstructure of aluminophosphate $AlPO_4$-5 in the hydrothermal synthesis. They studied synthesis of $AlPO_4$-5 via two different route, one-off addition (acid and template) without stirring and no stirring in the overnight aging process (Route 1), and dropwise addition of reagents with stirring and continuous stirring in the overnight aging process (Route 2).They concluded that the gel preparation by route 2 is likely affects early crystallization more than prolonged crystallization.

Khoo, et al., 2012, investigated the synthesis of $AlPO_4$ by ionothermal synthesis using 1-ethyl-2,3 dimethylimidazolium bromide ([edmim]Br) ionic liquid (IL) as both solvent and structure directing agent (SDA), they found that crystallinity, size of the $AlPO_4$-5 to be strongly affected by chemical composition of the gel solution and heating time of the gel mixture.

Wan, et al., **2004,** investigated the role of water content in the hydrothermal synthesis and characteristics of $AlPO_4$-5 samples, they concluded that when $AlPO_4$-5 samples are synthesized from molar gel compositions with 10 or $20H_2O$ there is preference for the formation of thin hexagonal platelets, and when the gel composition with 30 or $40H_2O$, the preferred morphology are spheres.

In this research work $AlPO_4$-5 (AFI) investigated using tetrapropyl ammonium hydroxide (TPAOH) and di-n-propylamine (DPA) as template, aluminum isopropoxide (API) and phosphoric acid as structural element sources, with hydrothermal synthesis using autoclave as described previously in, **Alnaama, 2015.**

2. EXPERIMENTAL

2.1 Materials

Phosphoric acid (85 wt.%, Merck) and aluminum isopropoxide (AIP, sigma Aldrich) were used as phosphor and alumina sources respectively, tetrapropyl ammonium hydroxide (TPAOH-Wuhan kemi chemical-chinese) and di-n-propylamine (Merck) as template (R), and deionized water.

2.2 Synthesis methods

Aluminum isopropoxide (AIP) 5 g was mixed with 45 ml deionized water and stirred for 30 min. Phosphoric acid (85%) 5.65 g was added to the solution of AIP by dropwise method in 30 min period of time. Different amounts of template (R) tetrapropyl ammonium hydroxide (TPAOH) or di-n-propylamine (DPA) were added to the solution and stirred for 2h. the gel solution was transferred into the autoclave and operated at 190^{o}C temperature for 24h. Then the autoclave was cooled and the sample product washed, filtered, and dried overnight at 100^{o}C in oven. The dried samples then calcined for 5h at 550^{o}C.

2.3 Characterization Techniques

The crystalline phase of the samples was determined by X-ray diffraction (XRD) (PHASER/Bruker, **Germany, 2010**), with Ni-filtered CuKα radiation with $\lambda = 1.54$ Å (30 Kv, 10 mA) with a 0.02^{o} 2θ step and 0.5 s per step. XRD includes also the analysis of Scherer for crystallite size for each peak.
Fourier transform infrared (FTIR) spectrum was carried using sample diluted in KBr (1% in 99% KBr) and analyzed by IR-Prestige-21 (Shimazdu).
Scanning electron microscopy (SEM/EDX) for the morphology were conducted by Inspect S50 including energy dispersive XRD (EDX) , FEI (USA). DSC-TGA was analyzed by Linseis Model STA PT-1000 (Germany) with sample weight 20 mg and temperature ramp 10 ^{o} C.

3. RESULTS AND DISCUSSION

3.1 Characterization

3.1.1 XRD

Analysis of XRD pattern showed that peaks positions for the AFI structure was obtained, with 95% crystallinity for $AlPO_4$-5 (M9) and as shown in **Table 2** and **Fig. 1**, when comparing the peak positions (2θ), space distance (d_s) with theoretical value stated in, **Meier, et al**., **1996,** showed excellent agreement.

3.1.2 SEM/EDX

Energy dispersive X-ray was tested and as shown in **Fig. 5** for elemental analysis. Morphology of AlPO4-5 (AFI) was investigated by SEM as shown in **Fig. 6**. The electronic images revealed a highly crystalline aggregates of crystals and formation of microparticles caused by agglomeration of nanoparticles, which in turn can lead to mesoporosity created by interparticles voids, the creation of these voids are as consequence of agglomeration besides some defects may appear in crystals formation.

3.1.3 Atomic Force Microscopy (AFM)

Fig. 7 and **8** showed the AFM images for samples 9M and 11M respectively, the images revealed the detailed observation of nano-scale events at crystal surface, showing also the height of terraces and layer of growth. These observations are well agreed with the work of **Aghabozog, et al., 2012**.

Average particle size of 66.5 nm obtained for sample M11 and 84.9 nm for M9. This result is confirmed, by comparing the crystallite size calculated by Scherer analysis through the measurement of FWHM (the broadening of the peaks) in XRD pattern, which gave an average of 23.5, 39.8 and 46.2 nm for samples M9, M10, and M11 respectively for crystallite size analyzed by scherer analysis through XRD pattern and as shown in **Table 3** below.

3.1.4 BET Analysis

The results of BET surface area is as shown in **Fig. 9** for isotherm plot for $AlPO_4$-5 (sample M9), where quantity adsorbed is plotted versus relative pressure p/p_o, in which the adsorption-desorption curve reveals a hystresis loop that means it has little porosity. BET surface is 185 m^2/g and pore volume is 0.153 cm^3/g, these results are in agreements with reported results in **MacIntosh, 2012**.

3.1.5 Fourier transform Infrared (FTIR)

FTIR spectrum for produced sample is shown in **Fig. 16**, the results are well agree with reported data in, **Rajesh, et al., 2001, Khoo, et al., 2013, Zhu, et al., 2001**.

The details of bands located in the spectrum are summarized in **Table 3** below, and T-O-T represent Al-O-P. The location of asymmetric and symmetric stretching bands and bending band were mentioned.

3.1.6 DSC-TGA

DSC-TGA result of sample $AlPO_4$-5 (M9), revealed that the synthesized and calcined product is thermally stable and showed that there is no occluded water and/or template in product as shown in **Fig. 11**.

3.2 Effect of Synthesis parameters

3.2.1 Temperature of Crystallization

Crystallization temperature of 180^{o}C and 190^{o}C were experienced and revealed that good crystallization can be obtained at 180^{o}C, meantime at 190^{o}C besides good crystallization, it gave best results towards decreasing particle size (66.5 nm). The effect of increasing temperature of crystallization were also concluded by **Alnaama**, **2012** in synthesis of aluminosilicate (zeolites), and **Zhu, et al., 2001,** in synthesis of aluminophosphates indicating a behavior similarity in effect of crystallization temperature for both types of molecular sieves in obtaining nanocrystalline molecular sieves. **MacIntosh**, **2012,** investigated crystallization of aluminophosphate molecular sieves family and concluded that they have few subtle differences in crystallization from zeolites, and the reaction of aluminum oxide with phosphoric acid to form amorphous aluminophosphate and the solid phase rearranges as the crystallization proceeds more rapidly as temperature increases.

3.2.2 Template

Type of template and ratio of template to phosphoric pentoxide (R/P_2O_5) found to have vital role in getting good crystallinity and nanocrystalline powder. The choice for the value of this ratio were carfully studied through the literature survey besides considering the technical procedures used in samples preparations and syntheses. TPAOH used with molar ratio of 1.0 ($TPAOH/P_2O_5$) gave, in AFM test, average particle size of 66 nm. While DPA gave 84 nm in molar ratio (DPA/P_2O_5) of 1.8. This difference in molar ratio can be explained by the difference in size of template molecule, for larger molecule as in TPAOH needs less molar ratio, but for smaller one DPA needs more molar ratio to occupy the inside viod in the structure, in other words, the size of template molecule play a major role in occupying the necessary volume inside the pore volume of structure, so as TPAOH molecule is bigger than DPA molecule so it needs less no. of moles to give the same results in structuring the molecular sieve.

4. CONCLUSIONS

The concluded notes of this research can be summarized as following:

-Nanocrystalline aluminophosphate $AlPO_4$-5 (AFI) molecular sieves can be synthesized by hydrothermal (solvothermal) reaction method with optimum ratio of R/P_2O_5 at specified time and temperature of crystallization.

-Both templates TPAOH and DPA gave nano-scale particle size results at optimum ratio of R/P_2O_5 where it was 1.8 for DPA and 1.0 for TPAOH.

-Temperaure of crystallization has vital role on getting nano-scale for particle size.

ACKNOWLEDGMENT

The Author express his thanks for college of pure science-ibnalhaytham for DSC-TGA. College of Science, Univ. of Baghdad for conducting XRD and AFM. College of science-Univ. of Alnahrain for SEM and EDX. Ibn Sina laboratory for FTIR.

5. REFERENCES

- B.Rajesh, M.Palanichamy, V.Murugesan, 2001, *Mesoporous Aluminophosphate and silicoaluminophosphate Molecular Sieves:Room Temperature Synthesis, Characterization, and Catalytic Performance*, Indian journal of Chemistry, Vol.40A, pp1262-1268.
- M.Hartmann, S.P.Elangovan,2003, *Isomerization and Hydrocracking of n-decane over Magnesium-containing Molecular Sieves with AEL, AFI, and AFO Topology*, Wiley on line, Vol.26, issue 12, pp.1232-1235.
- M.Choi, R.Srivastra, R.Ryoo,2006, *Organosilane Surfactant-Directed Synthesis of Mesoporous Aluminophosphate Constructed with Crystalline Microporous Frameworks*, J. Chem. Comm., issue 42, pp.4380-4388.
- B.M. Weckhuysen, R.R.Rao, J.A.Martens, R.A.Schoonheydet,1999, *Transition Metal Ions in Microporous Crystalline Aluminophosphate:Isomorphous Substitution*, Eur.J. of Inorg.Chem.,pp.565-577.
- Q.Wang, G.Chen, S.Xu, 2009, *Hierachical Architecture Observed in Microspheres Comprising AlPO4-11 Nanocrystals*, J.Micropor.Mesopor.Mater., Vol.119, pp.315-321.
- J.J.Li, G.D.Li, C.Y.Xi, Y.Guo, J.S.Chen, 2004, *Synthesis and Characterization of AlPO4 and MAPO-11 Single Crystal*, Chem.Res.Chinese, Vol.20, No.2, pp. 131-133.

- E.M.Flanigen, B.M.Lok, R.L.Patton, S.T.Wilson, 1986, *Aluminophosphate Molecular Sieves and the Periodic Table*, J. Pure & appl.Chem., Vol.58, No.10, pp 1351-1358.
- L.H.Gielgens, I.H.E.Veenstra, V.Ponee, M.J. Haanepen, J.H.C. Van Hoof, 1995, *Selective Isomerization of n-butene by Crystalline Aluminophosphates*, J. Catalysis Letters, Vol.32, pp 195-203.
- -A.Hassanvan, M.Asghari, 2012, *Fabrication and Characterization of $AlPO_4$-5 Nanozeolite: Effect of Hydrothermal Temperature and Duration*, J.of Ceramic processing Research, Vol.13, No.1, pp 56-68.
- Y.Wan, C.D.Williams, C.V.A.Duke, J.J.Cox, 2000, *Systematic Studies on the Effect of Water Content on the Synthesis, Crystallization, Conversion, and Morphology of $AlPO_4$-5 Molecular Sieve*, J.of Materials Chemistry, Vol.10, pp2857-2862.
- G.L.Klap, M.Wubbenhorst, J.C.Jansen, H.Van Koningsveld, H.Van Bekkum, J.Van Turnhhout, 1999, *polar Growth and Directional Adsorption of large $AlPO_4$-5 Crystals Determined by Scanning Pyroelectric Microscopy*, J.of Chemistry Letters, Vol.11, pp 3497-3503.
- L.Zhang, 2013, *Investigation of the Crystallization Process of Molecular Sieves*, Ph.D. Thesis, School of Graduate and Postdoctoral Studies, University of Western Ontario, Canada
- V.Naydenov, 2003, *Structured Molecular Sieves: Synthesis, Modification and Characterization*, Ph.D. Thesis, Department of Chemical and Metallurgical Engineering, division of Chemical Technology, Lulea university of technology.
- Y.Wei, Z.Tian, H.Gies, R.Xu, H.Ma, R.Pie, W.Zhang, Y.Xu, L.Wang, K.Li, B.Wang, G.Wen, L.Lin, 2010, *Ionothermal Synthesis of an aluminophosphate Molecular Sieve with 20-ring Pore Opening*, Angew.Chem.,Vol.122, pp 5495-5498.
- E.J.Fayad, N.Bats, C.E.A.Kirschhock, B.Rebours, A.A.Quineaud, J.A.Martens, 2010, *A Rational Approach to the Ionothermal Synthesis of an $AlPO_4$ Molecular Sieve with an LTA-Type Framework*, Angew.chem., pp 4689-4692.
- L.Han, Y.Wang, C.Li, S.Zhang, X.Lu, M.Cao, 2007, *Simple and Safe Synthesis of Microporous Aluminophosphate Molecular Sieves by Ionothermal Approach*, J.AICHE, Vol.54, No.1, pp 280-287.
- Y.P.Xu, Z.J.Tian, S.J.Wang, Y.Mu, L.Wang, B.C.Wang, Y.C.Ma, L.Hou, J.Y.Yu, L.W.Lin, 2006, *microwave-Enhanced Ionothermal Synthesis of Aluminophosphate Molecular Sieves*, Angewchem.Int.Ed., Vol.45, pp 3965-3970.
- X.Sun, 2012, *Fundemental Research of the Solvent Role in the Ionothermal Synthesis of Microporous Materials*, Ph.D. Dissertation, Dept. of Chem. Eng., Kansas State Univ., USA.
- D.Li, J.F.Yao, H.Wang, 2012, *Hydrothermal Synthesis of $AlPO_4$-5: Effect of Precursor Gel Preparation on the Morphology of Crystals*, J. Progress in Natural Science: Materials International, Vol.22, Issue 6, pp.684-692.
- D.Y.Khoo, W.M.Kok, R.R.Mukti, S.Mintova, E.P.Ng, 2013, *Ionothermal Approach for Synthesizing $AlPO_4$-5 with Hexagonal Thin-Plate Morphology influenced by Various parameters at Ambient Pressure*, J. of Solid State Science, Vol.25, pp 63-69.

- Y.Wan, D.Craig, C.V.A.Duke, J.C.Jeff, 2004, *Systematic Studies on the Effect of Water Content on the Synthesis, Crystallization, Conversion and Morphology of* $AlPO_4$ *Molecular Sieves*, J. of Materials Chemistry, Vol.10, pp 2857-2862.
- A.A.Alnaama, 2015, *Synthesis and Characterization of Nanocrystalline ZSM-5 and ZSM-5/MCM-41 Composite Zeolite for Biodiesel Production*, Ph.D. Thesis, Chem. Eng. Dept., College of Eng., Univ. of Baghdad.
- W.M.Meier, D.H.Olson, C.H. Baerlocher, 1996, *Atlas of Zeolite Structure Types*, 4^{th} ed., Elsevier, Amestrdam.
- H.Aghabozog, S.Hassani, F.Salehirad, 2012, *Crystal growth Study of Nano-zeolite by Atomic Force Microscopy In: N.Kolesnikov, ed. Modern Aspects of Bulk Crystal and Thin Film Preparation*, S.1.:S.n, pp 357-372.
- G.Zhu, S.Qui, F.Gao, G.Wu, R.Wang, B.Li, Q.Fang, Y.Li, B.Gao, Y.Li, X.Xu, O.Terasaki, 2001, *Synthesis of Aluminophosphate Molecular Sieve* $AlPO_4$*-11 Nanocrystals*, Micropor. Mesopor. Mater., Vol.50, pp.129-135.
- A.R.MacIntosh, 2012, *Studies on Molecular Sieve Crystallzation and Heteroatomic Substitution*, M.Sc. Thesis, Univ. of Western Ontario, Canada.

Table 1. Molar Composition of Samples.

Sample	Molar composition
M9	$1.8R_1.Al_2O_3.P_2O_5.102H_2O$
M10	$1.2R_1.Al_2O_3.P_2O_5.102H_2O$
M11	$1.0R_2.Al_2O_3.P_2O_5.102H_2O$

Where R_1*=DPA (di-n-propylamine)*

R_2*=TPAOH (tetrapropyl ammonium hydroxide)*

Table 2. XRD Data for sample M9 compared with theoretical values**.**

hkl	2θ	ds,Å	I_{re1s}
100	7.401(7.43)	11.9346(11.899)	100(100)
110	12.82(12.89)	6.8958(6.870)	20.2(6.3)
200	14.84(14.89)	5.9632(5.950)	9.1(20.6)
210	19.679(19.74)	4.5075(4.497)	28.1(42.4)
002	20.37(20.97)	4.3561(4.237)	13.4(45.3)
102	22.37(22.27)	3.9708(3.992)	37.2(12.5)
220	25.833(25.94)	3.4459(3.435)	13.4(19.6)

The values between parenthesis represents the theoretical values abstracted from, **Meier, et al., 1996.**

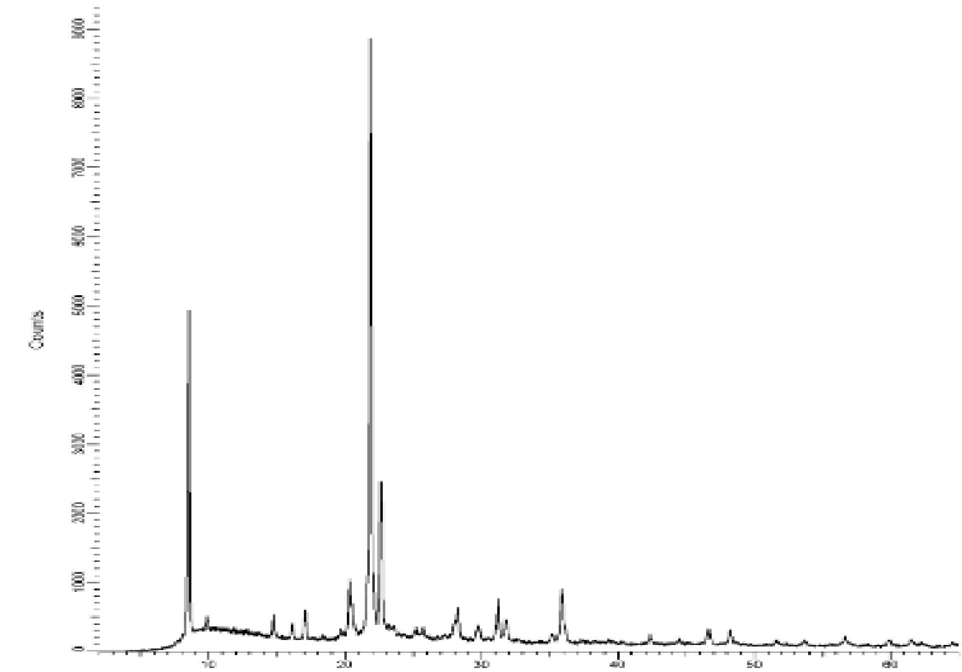

Figure 1. XRD for M9.

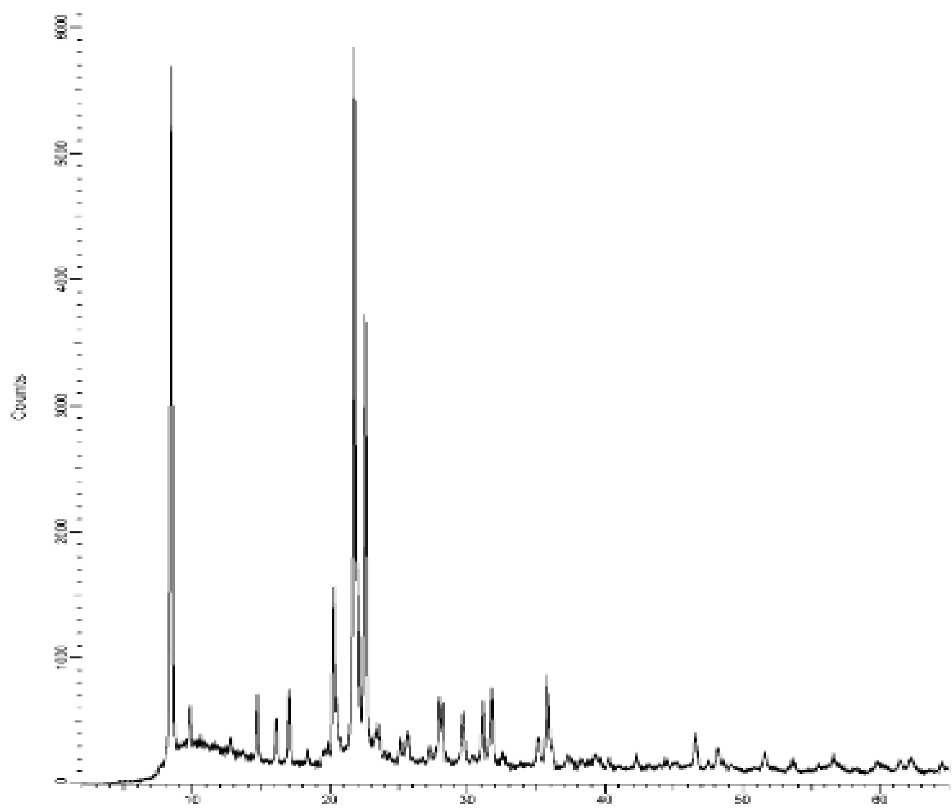

Figure 2. XRD for M10.

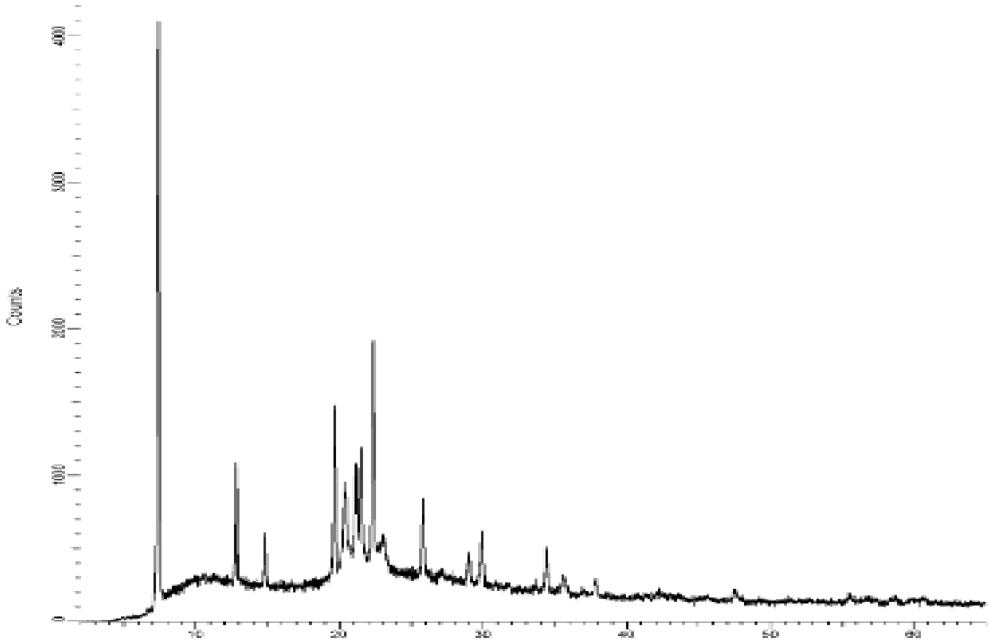

Figure 3. XRD for M11.

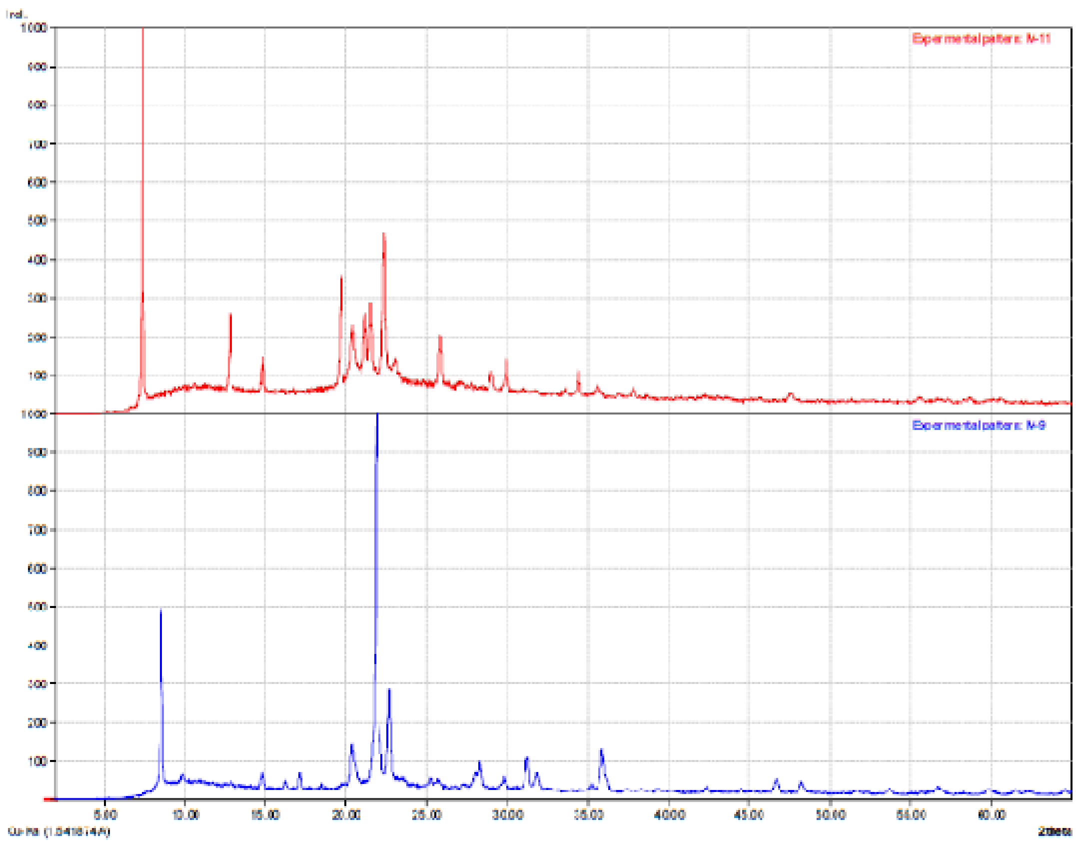

Figure 4. XRD for M9 and M11.

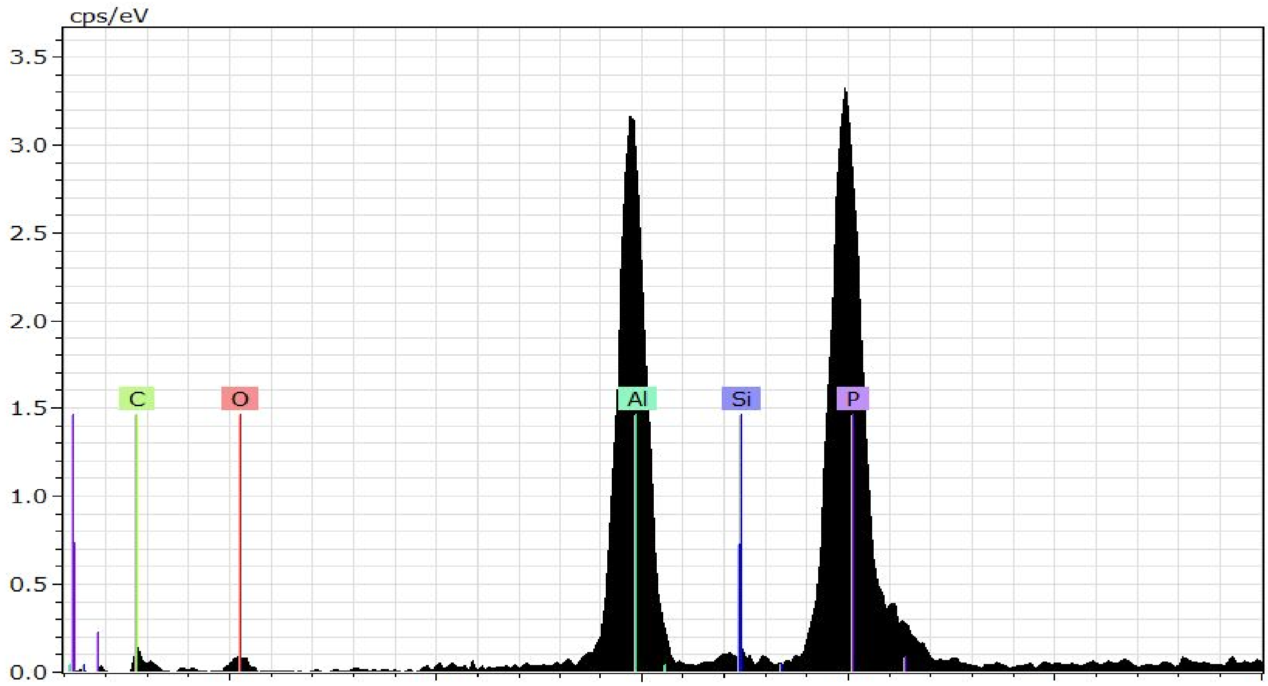

Figure 5. EDX for M9.

Table 3. Particle size and Crystallite size**.**

	Sherer Crystallite size range,nm	**Scherer Ave. Crystallite size, nm**	**AFM particle size,nm**
M9	10.8-60.4	23.5	84.9
M10	9.5-100	39.8	32.1
M11	13.2-100	46.2	66.5

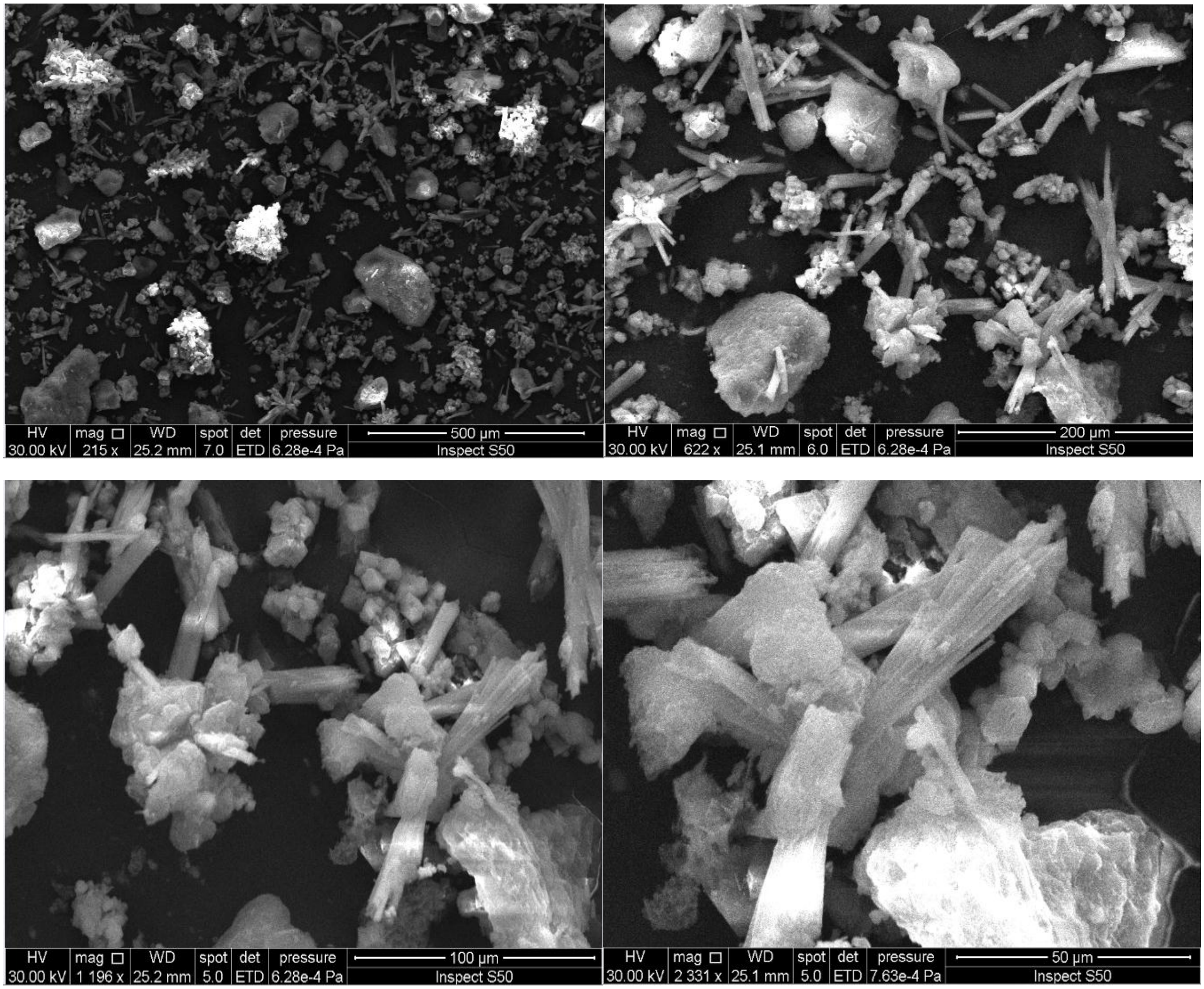

Figure 6. SEM Images for $AlPO_4$-5 (sample M9)**.**

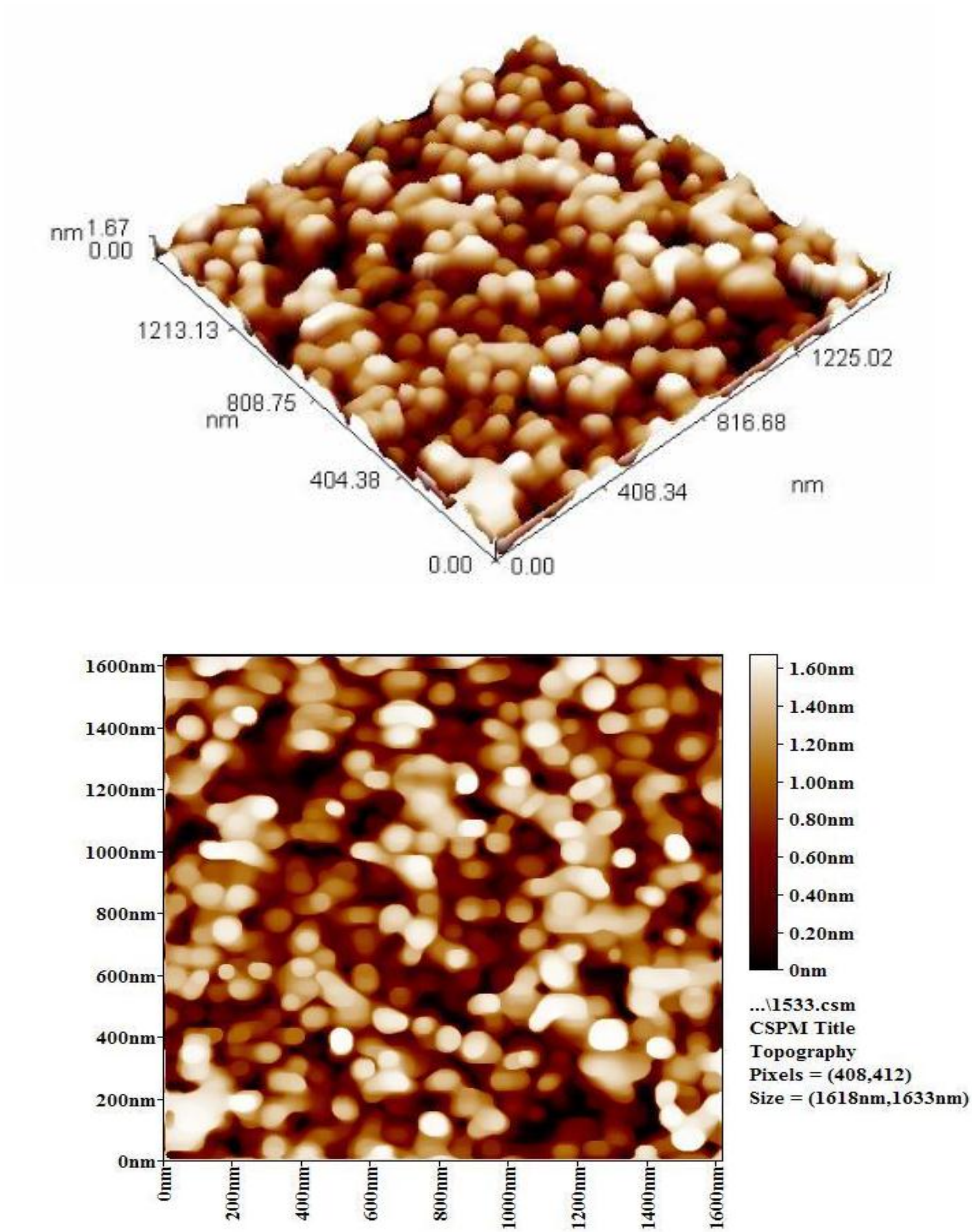

Figure 7. Two and Three dimension AFM Image for $AlPO_4$-5 (sample 9).

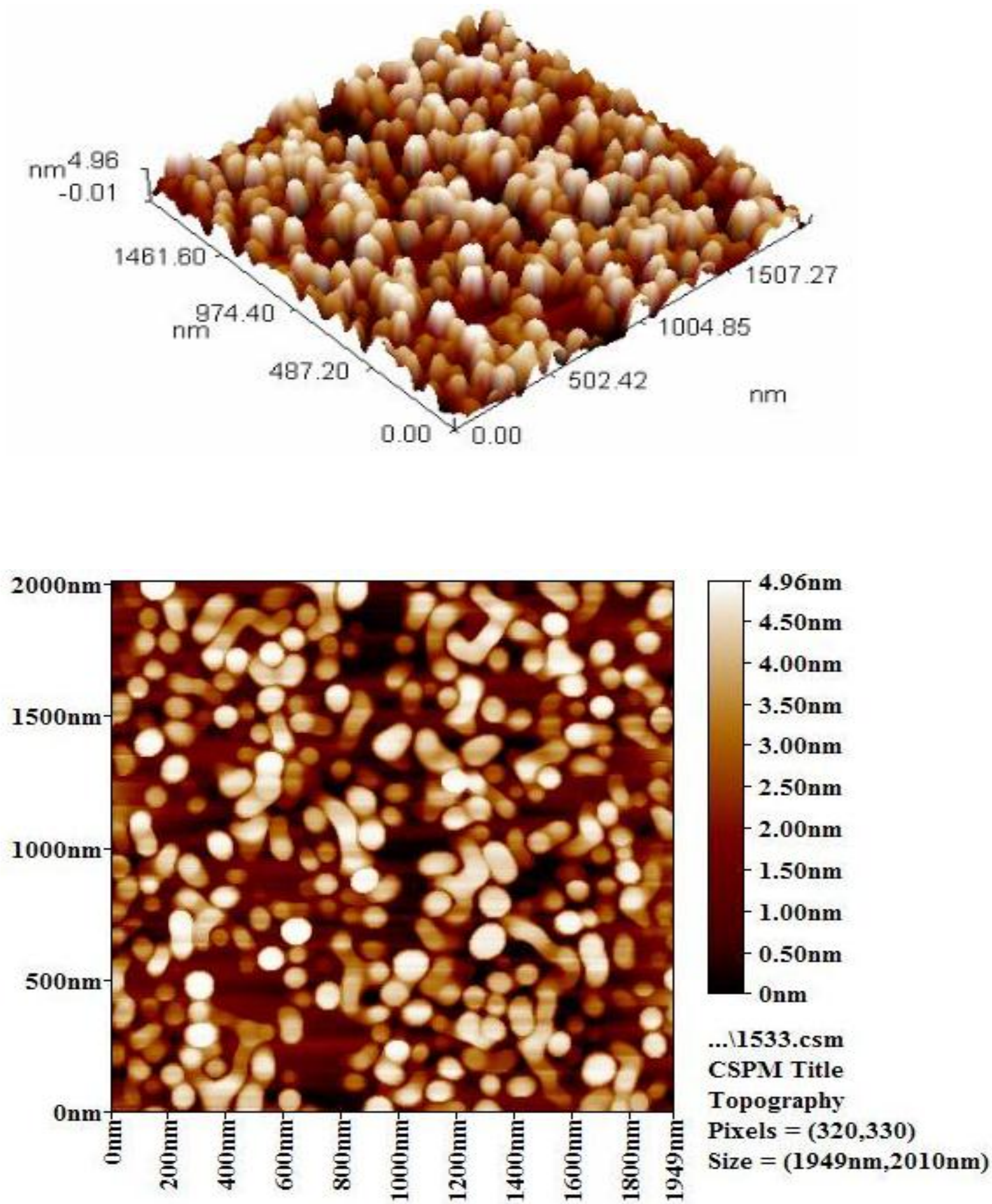

Figure 8. Two and Three dimension AFM Image for $AlPO_4$-5 (sample 11).

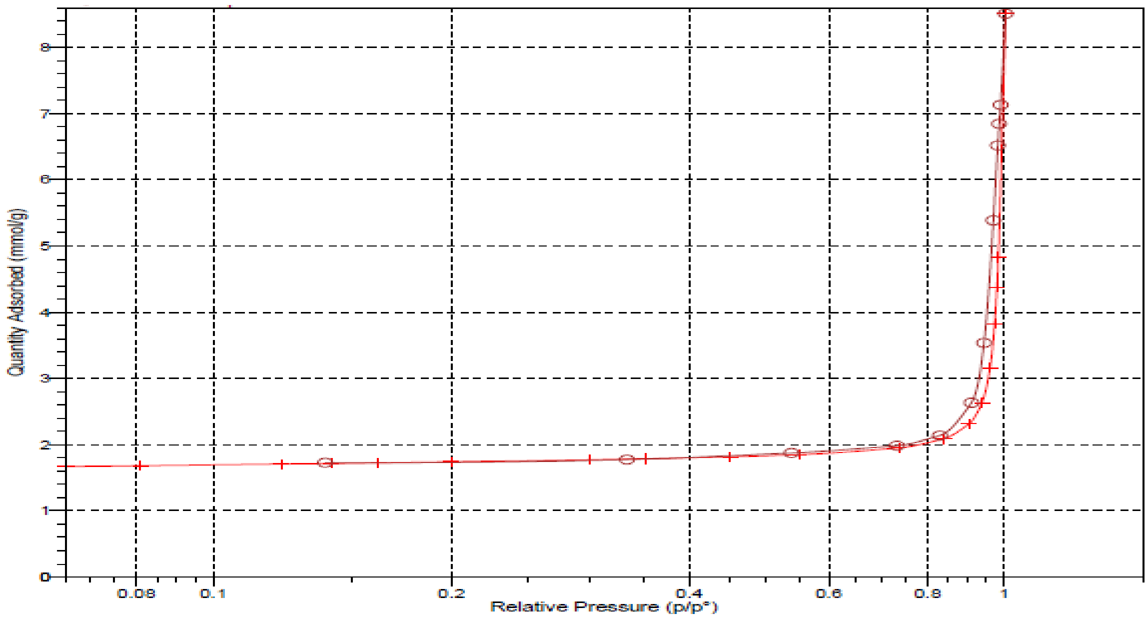

Figure 9. Isotherm Plot for $AlPO_4$-5 (M9).

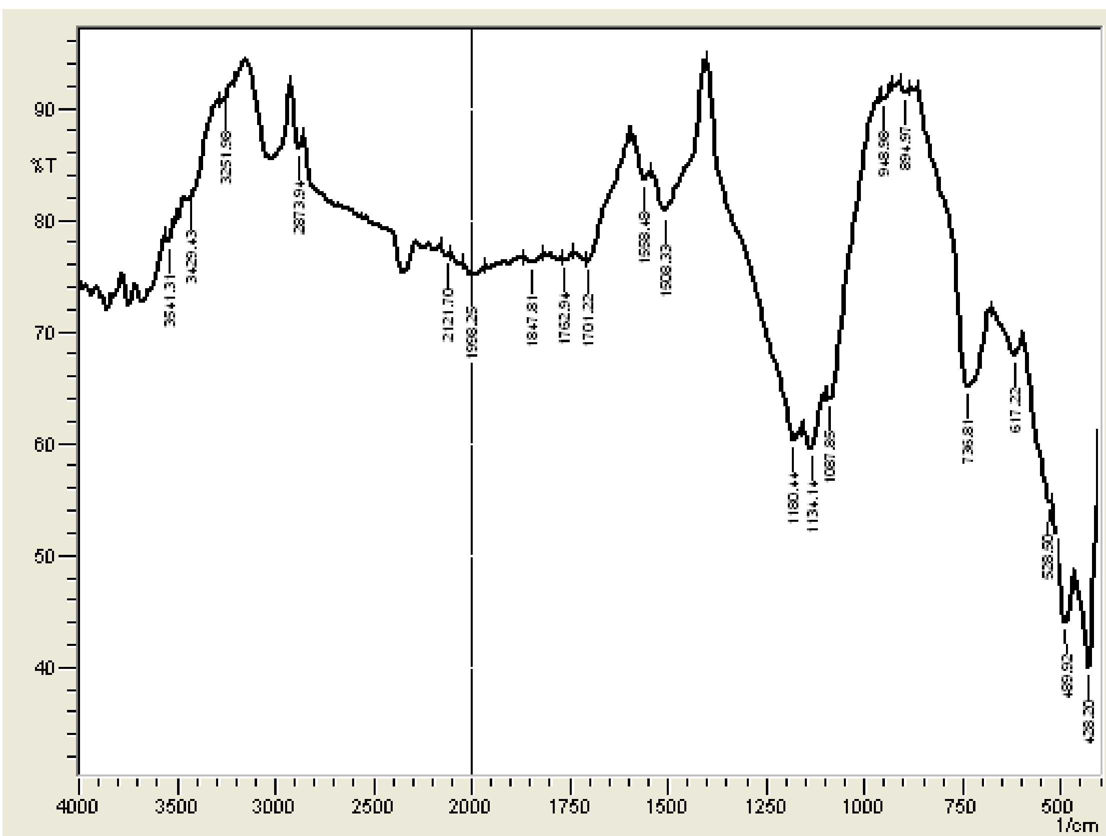

Figure 10. FTIR spectrum for $AlPO_4$-5.

Table 4. Types of bands in FTIR spectrum**.**

Type of Band	Wave length, cm^{-1}
T-O-T Asymmetric stretching	1160, 1130, 1087
T-O-T Symmetric stretching	736.8
T-O-T Bending	439 with shoulder at 489

T is either Al or P

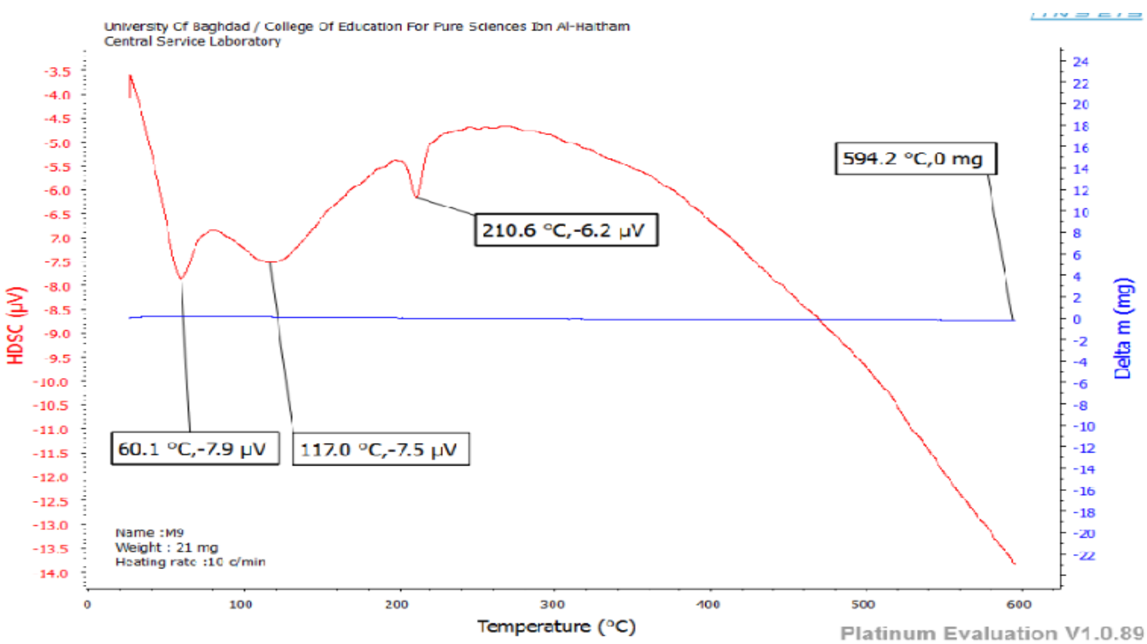

Figure 11. DSC-TGA for $AlPO_4$ (M9)**.**

University of Baghdad
College of Engineering
JOURNAL OF ENGINEERING

Journal of Engineering

journal homepage: www.jcoeng.edu.iq
Number 3 Volume 24 Month 3

Mechanical and Energy Engineering

Tribological Characteristics Evaluation of Mustard Oil Blends

Mohammed Hassan Jabal
Lecturer
Dept, Electromechanical Eng. University of Technology
mhjutm@gmail.com

Muhannad Zaidan Khalefa
Assistant Professor
Dept, Electromechanical Eng. University of Technology
bearing2018design@gmail.com

ABSTRACT

A progressive increase in the desire for environmentally friendly lubricants by users and strict government regulations for the use of these lubricants has provided an opportunity to use plant oils as biodegradable lubricants, therefore vegetable oils have been investigated to replace oil lubricants because of their maintaining the conditions of nature (environment) properties. In this paper, the influences of the blending ratio of mustard seeds oil with commercial mineral oil (SAE40) on the tribological characteristics were investigated and compared with mineral oil using the four-ball tribotester. Mustard seeds oil was blended with mineral oil at a volumetric ratio ranging from 22.5 to 90%. All experimental works were confirmed to ASTM D4172-B standard. The results exhibit that some blends of mustard seeds oil with mineral oil have lower wear scar diameter, friction torque, Friction coefficient and a higher parameter of flash temperature value compared to mineral oil and neat mustard seed oil. In conclusion, the mustard seed oil blend (MU22.5) shows a better anti-wear and anti-friction performance compared to oil samples. Therefore, mustard seeds oil has the potential to be used as a lubricant of mating surfaces.

Keywords: Mustard oil; bio-lubricant, four-ball tribotester; wear scar diameter; parameter of flash or glow temperature.

تقييم خصائص المداهنة لخلائط زيت الخردل

مهند زيدان خليفة
استاذ مساعد
قسم الهندسة الكهروميكانيكية،الجامعة التكنولوجية

محمد حسان جبل
مدرس
قسم الهندسة الكهروميكانيكية،الجامعة التكنولوجية

الخلاصة

ان الزيادة في الطلب على مواد التزييت الصديقة للبيئة من قبل المستهلكين نتيجة للوائح الحكومية الصارمة بضرورة أستخدام زيوت ومواد تشحيم صديقة للبيئة وقابلة للتحلل قد فتحت الأفاق في محاولات استخدام الزيوت النباتية كبدائل عن الزيوت والشحوم البترولية كونها قابلة للتحلل وبالتالي هي صديقة للبيئة، في هذه الدراسة، تم التحقيق في تأثير نسبة المزج لزيت بذور الخردل مع زيت معدني تجاري(SAE40) في خصائص المداهنة ومقارنتها بخصائص المداهنة للزيت المعدني وذلك بأستخدام جهاز الاربع كرات. وكانت نسب الخلط الحجمية المعتمدة لزيت بذور الخردل مع الزيت المعدني تتراوح (22.5-90%). كما تم اعتماد المواصفة الامريكية (ASTM D4172-B) في اجراء جميع الاختبارات. واظهرت النتائج اداءاً متفوقا لبعض نسب

المزج لزيت بذور الخردل مع الزيت المعدني من خلال اعطاء اصغر قطر ندبة، عزم دوران احتكاك ومعامل احتكاك كما اعطت هذه النسب اعلى قيمة لمعامل درجة الحرارة الوميض بالمقارنة مع الزيت المعدني والزيت النقي لبذور الخردل.كما اظهرت النتائج ان مزيج زيت بذور الخردل (MU22.5) حقق أفضل أداء في مكافحة التآكل ومقاومة الاحتكاك بالمقارنة مع نماذج خلائط الزيوت الاخرى. بذلك يكون لزيت بذور الخردل القدرة على استخدامة كزيت تشحيم في السطوح المتلاصقة.

1. INTRODUCTION

The environmental pollution and toxicity issues attributed to the use of mineral oils mainly as lubricants including their various additives and the rising costs linked to a global shortage have resulted in fresh interests in the utilization of the following vegetable oils **Lathi** and **Mattiasson, 2007** such as canola, soybean, coconut, sunflower, castor, and sesame as lubricants that are eco-friendly **Rudnick, 2009.**

Normally, vegetable oils have efficient lubrication properties, for instance, they have low volatility, they have a natural lubricity quality, they are highly viscosity index, non-toxic and they can easily mix with other fluids **Wilson, 1998.** The increased demand for materials that are biodegradable in nature has led to fresh avenues for using vegetable oils as a substitute to mineral oil lubricants **Li, et al., 2001,** mainly in running machines. The public awareness regarding issues related to environmental destruction has been constantly growing, **Eichenberger, 1991.**

Better intrinsic lubrication features are observed in the long chain fatty acids and the large amount of unsaturated and polar ester groups present in vegetable oils, **Petlyuk and Adams, 2004.** These lubricants can work to provide great lubrication as they help in minimizing friction coefficients. However, many researchers have also reported that most agricultural oils have little friction coefficient and higher non-chemical corrosion rate **Golshokouh, et al., 2014a.**

Many studies have been performed on engineering applications of vegetable oils under headings like the potential of vegetable oils as lubricants, hydraulic fluid, biodiesel and used as an additive **Golshokouh, et al., 2014b, Jabal, et al.,2014** and **Golshokouh, et al., 2013a,** most of these studies indicate low non-chemical resistance to corrosion and thermal stability. **Anbumani** and **Singh, 2006,** conducted experiments with different ratios of mixing mustard and neat bio-neutral in C.I. Engine found mustard oil in a mixture of 20% better leads among them. Mainly has been used mustard oil in butyl esters extract, and blend of 20% diesel satisfies the ASTM standard biodiesel properties. Down your fuel consumption slightly (0.135 kJ/kW-h to 0.045 kJ/kW-h) due to better fuel combustion. **Zannatul, et al., 2011** experimented with 20%, 30% and 50% mustard oil blended with diesel and found BSFC is inversely proportional to load. **Bannikov, 2011** investigated the direct injection diesel engine using mustard oil methyl ester as fuel and found a 15% increase of BSFC and 3% decrease the efficiency of fuel conversion performance brake compared to diesel fuel while the performance of mechanical efficiency was not changed.

By using the four-ball tribo-tester compliance with the ASTM D4172-B standard, this paper presents the tribological behaviour characteristics for the mustard oil with mineral oil blends as a bio-lubricant.

2. EXPERIMENTAL WORK

2.1 Experimental apparatus

In the investigation of the characteristics of lubrication, friction and wear (non-chemical corrosion) of the lubricant samples, a four-ball wears tester machine was used which was in compliant with the ASTM D4172-B standards shown in **Fig.1(a,b)**. The tribotester had total 4 balls; three balls in the bottom part, while placing the remaining ball on the upper part. The balls were held firmly down inside the ball container containing the lubricants to be confirmed, and the pressure was placed on the overall system against the ball in the upper. The upper ball is rotated as quickly as possible and three of the balls were placed in the bottom part are pressed. Some measures must precede the adoption of the tests, use acetone for cleaning the surfaces of all components. The thermal inside the ball base was embedded to know the temperature property of oil, also a block to heat down the ball bowl that helps control the temperature adjustment experiment. A study of wear was performed at 1200 rpm for one hour, with 40 kg of pregnancy at 75 ° C.

2.2 Balls

The balls were standardized in this paper, they have been developed from chrome-alloy steel EIS-52100. Characteristics of balls 12.7 $X10^{-3}$ m in diameter, 25 grade Eb and 64-66 Hardness (R.WC hardness test). Includes all tests, four new balls were used with all the above characteristics.

2.3 Lubricants

This study adopted lubricants neat mustard oil (MU) and SAE40 mineral engine oil (MO). Moreover, four blend lubricant samples of mustard oil with mineral engine oil under several percentages (i.e., 22.5-90% v/v of vegetable oil as shows **Table 1** were prepared by using the measuring tube and electric mixer under rotation speed 500 rpm and for 30 min.

2.4 Kinematic viscosity

Fluids used have a very important property in determining resistance to the internal impulse provided by the fluid against spills. It affects the high fluid surface directly along with wear the surface rate at which the fluid slips.
To find the viscosity value limits for lubricants, a rotary viscosity device was used. There is a spindle within the viscosity meter that rotates at a certain velocity. The spindle was introduced inside emollients, thus providing resistant to the impulse resistance oils.

2.5 Wear surface characteristics

Optically add high-resolution electron detection microscope was used to study the properties of non-chemical corrosion from the worn surface and to wear scars on the three balls for bearings after complete experiments. Micrograph pictures captured through microscopes were used to find radius scars wear, the median value was determined.

2.6 Torque and coefficient for the friction

To determinate the resistance of contact between the surfaces, torque must be calculated. There is also a need to calculate the value of the friction coefficient and this data can be fed directly into the Windocom program of a four-balls tribe machine. The proportion of force that maintains contact with the body and strength of friction coefficient that resists the velocity of a body it shows through friction coefficient. Using this equation to determine the value***:***

$$\mu = \frac{F}{N}$$

$$F = \frac{T}{r}$$

$$N = \frac{3.W.r}{\sqrt{6}}$$

$$\mu = \frac{T\sqrt{6}}{3.W.r} \quad (1)$$

2.7 Flash temperature parameter

Flash temperature parameter(FTP), it is a non-dimensional value, stating the critical this parameter when emollients will fail to operating conditions. The expected of degeneration of the lubricant films can be observed for this parameter, **Masjuki,** and **Maleque, 1997.** Increase the value of FTP demonstrates good performance.
FTP value is found from the following equation:

$$FTP = \frac{W}{(WSD)^{1.4}} \quad (2)$$

3. RESULTS AND DISCUSSION

3.1 Kinematic viscosity

A comparison of this parameter quantities for neat mustard oil, mineral oil and blends of mustard with mineral oil under different temperatures of (25-100^{o}C) and freeload, were illustrated in **Fig. 2**. Adoption of this figure previously mentioned kinematic viscosity of all tested samples was reduced when temperatures increased. Consequential results on reducing the viscosity value were obtained through high temperatures by **Golshokouh, et al., 2013b** and **Haseeb** and **Masjuki, 2010.** The viscosity of all oils was similar to each other.
At a high temperature of 75°C, the viscosity of all oils performed was comparable to each other. The blending process resulted in increasing the values of kinematic viscosity compared to the neat mustard oil. Also, this type of viscosity values was obtained for the oil samples ISO VG32 requested level. Depending on the results of the kinematic viscosity in **Fig.2**, it can be concluded that the blend MU22.5 had shown higher kinematic viscosity, then the blend MU45 compared to other oil samples. The neat mustard oil MU100 and blend MU90 were comparable to each other in the terms of the kinematic viscosity.

3.2 Wear surface characteristics

Fig.3 representing blends of mustard and mineral oil ball specimens shows variable abrasive wear values forms with parallel grooves on the worn surface. The grooves in the dark region are deep, whereas those in light-colored areas are shallow with different scars; these have been the surfaces of the ball identified as shown in **Fig.3 (d and f).**
Wear scars for all blending ratios of mustard and mineral oil had the circular view is evident in **Fig.3**. As clear in **Fig.3** and **Fig.4**, the blending process of mustard and mineral oil blends reduce

the value of WSD compared to neat mustard oil and mineral oil, such as in the cases of MU22.2 and MU45, **Shahabuddin, et al., 2013,** and **Liaquat, et al., 2012.** The lowest value of diameter wear scar value was 420.56 µm for the MU22.5 blend, compared with neat mustard oil 647.73µm as well as for mineral oil 578.8µm.

3.3 Friction torque

The data for friction torque were tabulated from four-ball tribo-tester with the help of a computer and presented statistically as clear by **Fig.5**, It compares the moment torque friction value for blends of mustard and mineral oils. The final figure illustrates friction torque values were reduced compared to clean mustard and mineral oils during the blending procedure **Masjuki, et al., 2011.** The lowest FT are calculated 0.09715 Nm for MU90 blend, for comparison pure mustard oil at 0.13182 Nm and that of mineral oil at 0.14424 Nm.

Fig.6 shows the friction torque plotted against the sliding time for various mustard oil based bio-lubricants. The results of **Fig.6** show that the friction torque is highest at the beginning and then it came down rapidly. Throughout the operation time, the bio-lubricant percentage 90% (MU90) showed the lowest values of friction torque compared to another oil samples. The fatty acid components of the bio-lubricants formed a multi and monolayer on the surface of the rubbing zone and made a stable film to prevent the contact between the surfaces.

3.4 Coefficient of friction

Fig.7 shows the comparison of this coefficient values for mustard and mineral oil mixtures. From the figure, this coefficient values will decrease by comparison with pure mustard and mineral oils due to mixing procedure **Shahabuddin, et al., 2013, Liaquat, et al., 2012** and **Masjuki, et al., 2011.** The value was the smallest value of the friction coefficient 0.05508, which was identified in the sample of the MU90 blend, compared to that of neat mustard oil at 0.07474 and that of mineral oil at 0.08179.

Relationship of this coefficient value of various blending ratio percentages of bio-lubricants with the sliding time given in the **Fig.8**, show the results that the MU90 has the highest potential to reduce the friction coefficient compared with another oil samples and show that this coefficient is highest at the beginning and then it came down rapidly.

3.5 Flash temperature parameter (FTP)

Fig.9 shows the outcomes of this parameter *FTP* for mix mustard and mineral oil, pure mustard oil, and mineral oil. Based on this figure, blending process escalated the *FTP* values as shown in the case of MU22.5 and MU45, compared to neat mustard and mineral oils **Shahabuddin, et al., 2013**, and **Liaquat, et al., 2012.**

The highest value for the flash temperature was 134.49 for the MU22.5 blend, compared to that of neat mustard oil at 73.47 and that of mineral oil at 86.01.

4. CONCLUSIONS

The conclusions drawn from this paper will be presented.

i. The mixing process leads to reduce the value of the wear scar diameter compared to the value of the neat mustard oil and mineral oil.

ii. The blending process results in an improvement in the tribological characteristics, which led to reduce the friction coefficient. In addition, the blending process led to the value goes up *FTP*.

iii. From the study, it can be recommended that the blends of mustard oil with mineral engine oil (MU22.5 and MU45) could be an effective alternative bio-lubricant, as it shows better impact on wear and offered a good lubricant characteristic.

REFERENCES

- Lathi, P. S. and Mattiasson, B.,2007, Green Approach for the Preparation of Biodegradable Lubricant Base Stock from Epoxidized Vegetable Oil, Applied Catalysis B: Environmental.Vol.69, No.3, PP. 207-212.

- Rudnick, L. R., 2009, Lubricant Additives: Chemistry and Applications, USA: CRC Press.

- Wilson, B.,1998, Lubricants and Functional Fluids from Renewable Sources, Industrial Lubrication, and Tribology, Vol. 50, No. 1, PP. 6-15.

- Li, F., Hanson, M. V.and Larock, R. C.,2001, Soybean Oil–Divinylbenzene Thermosetting Polymers: Synthesis, Structure, Properties and Their Relationships, Polymer, Vol.42, No.4, PP.1567-1579.

- Eichenberger, H. F., 1991, Biodegradable Hydraulic Lubricant an Overview of Current Developments in Central Europe. Society of Automotive Engineers (SAE) Technical Paper, SAE 910962.

- Petlyuk, A. M. and Adams, R. J.,2004, Oxidation Stability and Tribological Behavior of Vegetable Oil Hydraulic Fluids, Tribology Transactions, Vol.47, No. 2, PP. 182-187.

- Golshokouh, I., Syahrullail, S., Shariatmadari, S. and Ani, F. N ., 2014a, InvestigateJatropha Oil as New Source of Lubricant Oil, Applied Mechanics and Materials, Vol. 465, PP.201-205.

- Golshokouh, I., Syahrullail, S. and Ani, F. N .,2014b, Influence of Normal Load and Temperature on Tribological Properties of Jatropha Oil, Journal Teknologi, Vol.7, No. 2, PP.145-150.

- Jabal, M.H., Ani, F.N. and Syahrullail, S.,2014, The Tribological Characteristic of the Blends of RBD Palm Olein with Mineral Oil using Four-ball Tribotester, Jurnal Teknologi, Vol.69, No. 6, PP.11-14.
- Golshokouh, I., Syahrullail, S., Ani, F. N. and Golshokouh, M., 2013a, Jatropha Oil as Alternative Source of Lubricant Oil, Life Science Journal, Vol.10, No. 8, PP.268-276.

- Anbumani, K. and Singh, A.P., 2006, Performance of Mustard and Neem Oil Blends with Diesel Fuel in CI Engine, Carbon Vol.86, No. 78, PP.14-20.
-
- Zannatul M. H., Jomir H., Saikat B. and Asif I.,2011, Bio-Diesel from Mustard Oil: A Renewable Alternative Fuel for Small Diesel Engines, Modern Mechanical Engineering, Vol.1, PP.77-83.

- Bannikov, M., 2011, Combustion and Emission Characteristics of Mustard, Biodiesel, PP.1-5.
- Masjuki, H.H., and Maleque, M.A., 1997, Investigation of The Anti-Wear Characteristics of Palm Oil Methyl Ester (POME) Contaminated with Lube Oil Using a Four-Ball Machine of IP239 Standard, Wear, Vol. 206, PP.179-186.
- Golshokouh, I., Wira, J. Y., Ani, F. N. and S.Syahrullail, 2013b, Palm fatty acid distillate as an alternative source for hydraulic oil, Applied Mechanics, and Materials, Vol.315, PP. 941-945.
- Haseeb, M. A., and Masjuki, H. H., 2010, Effect of Temperature on Tribological Properties of Palm Biodiesel, Energy, Vol. 35, PP.1460-1464.
- Shahabuddin, M., Masjuki, H. H., Kalam, M.A., Bhuiya, M.M.K. and Mehta,H., 2013, Comparative Tribological Investigation of Bio-Lubricant Formulated from a Non-Edible Oil Source (Jatropha oil), Industrial Crops and Products, Vol.47, PP.323-330.
- Liaquat, A. M., Masjuki, H. H., Kalam, M. A., and Rasyidi, A., 2012, Experimental Analysis of Wear and Friction Characteristics of Jatropha Oil Added Lubricants, Applied Mechanics, and Materials, Vol.110, PP. 914-919.
- Masjuki, H. H., Kalam, M. A., Nurul, M. F. and Varman, M., 2011, Environmentally Friendly Bio-Lubricant Lubricity Testing, Proceedings in Clean Energy and Technology (CET)",27-29 June 2011. Kuala Lumpur, Malaysia, IEEE, PP.140-144.

NOMENCLATURE

F=frictional force ,N .
FT= friction torque,N.m
FTP=flash temperature parameter
MO =mineral engine oil
N=normal load ,N
r = the length between the hub and contact center on the balls is placed at lower surface, 3.67mm
W= application value of loads, kg.
WSD=wear scar diameter, μm
μ =friction coefficient.

Table 1. Percentages of the mustard oil and mineral oil in each sample**.**

Sample		**Mustard oil (%)**		**Mineral oil(%)**
MU22.5		22.5		77.5
MU45		45		55
MU67.5		67.5		32.5
MU90		90		10
MU100		100		0
MO100		0		100

Figure 1a. Photograph of the four-ball tester machine.

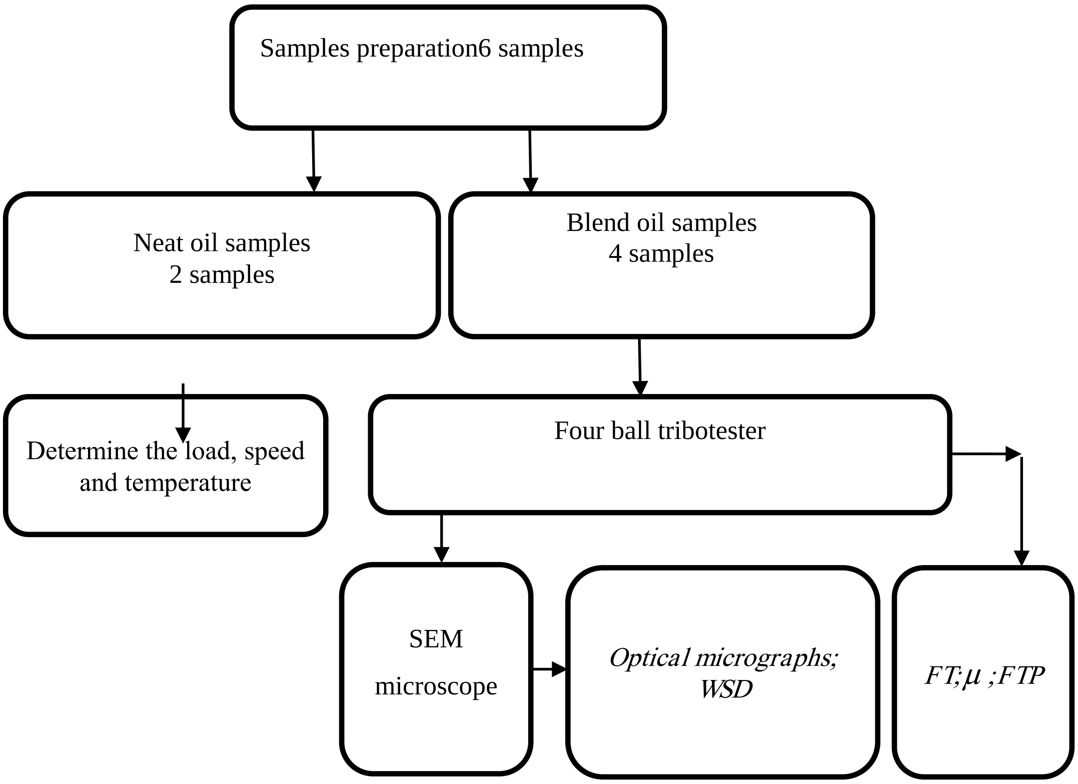

Figure 1b. Block diagrams of friction and wear testing of the four-ball tester machine.

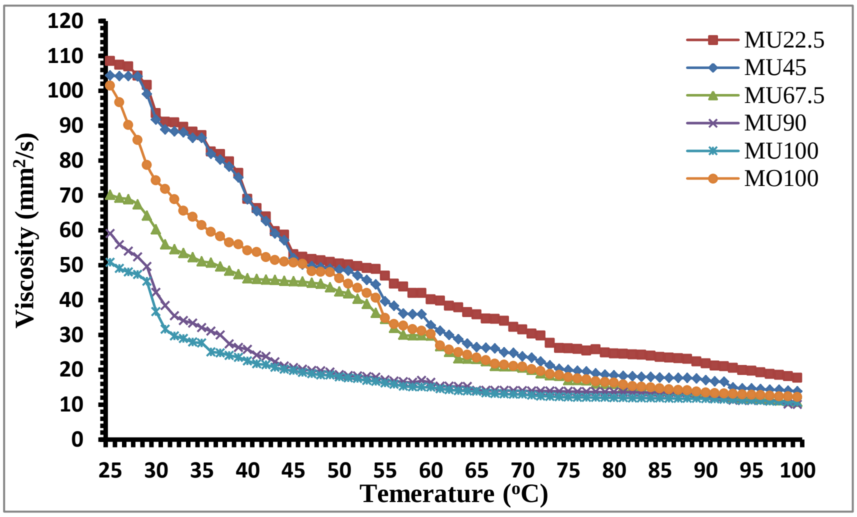

Figure 2. Kinematic viscosity values for the oil samples under different temperatures.

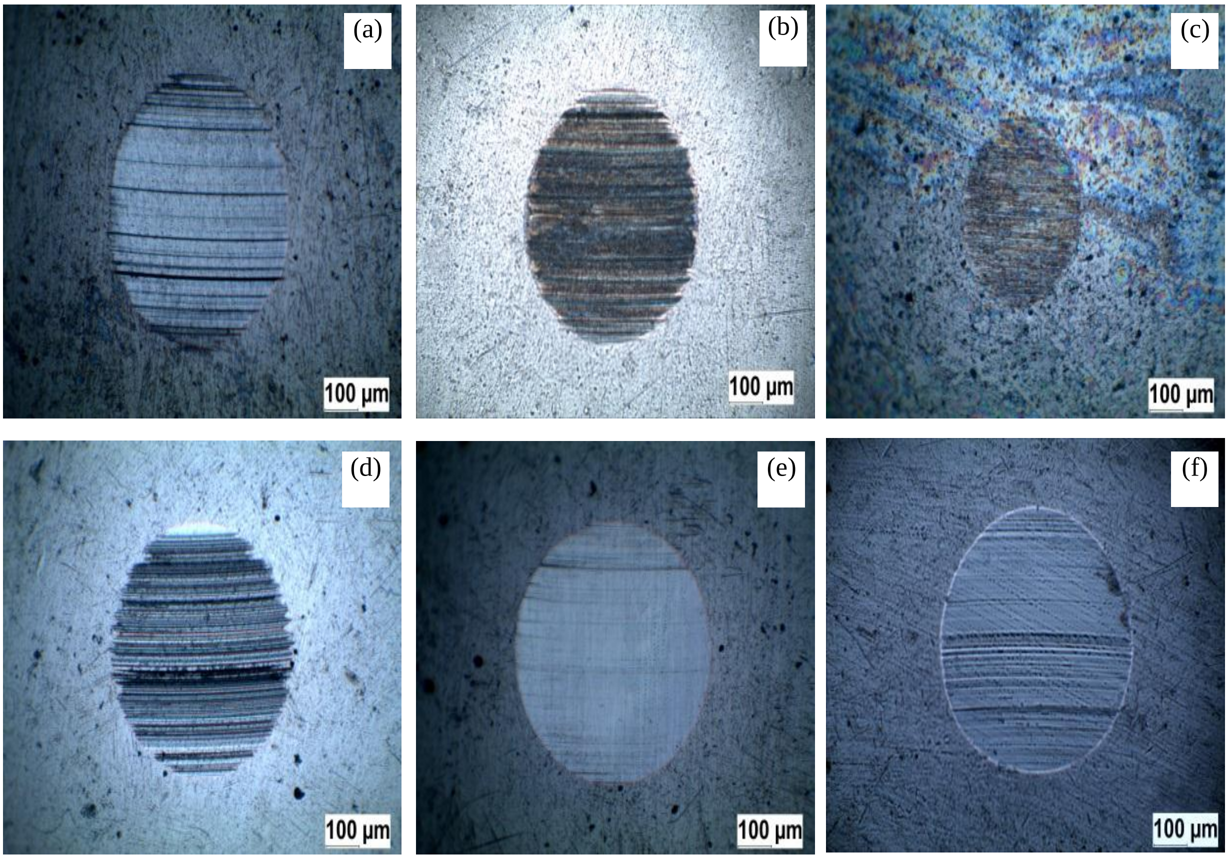

Figure 3. Optical micrographs of mustard oil samples in different volumetric blending ratio: (a) MU100; (b) MO100; (c) MU22.5 ; (d) MU45; (e) MU67.5 ;(f) MU90.

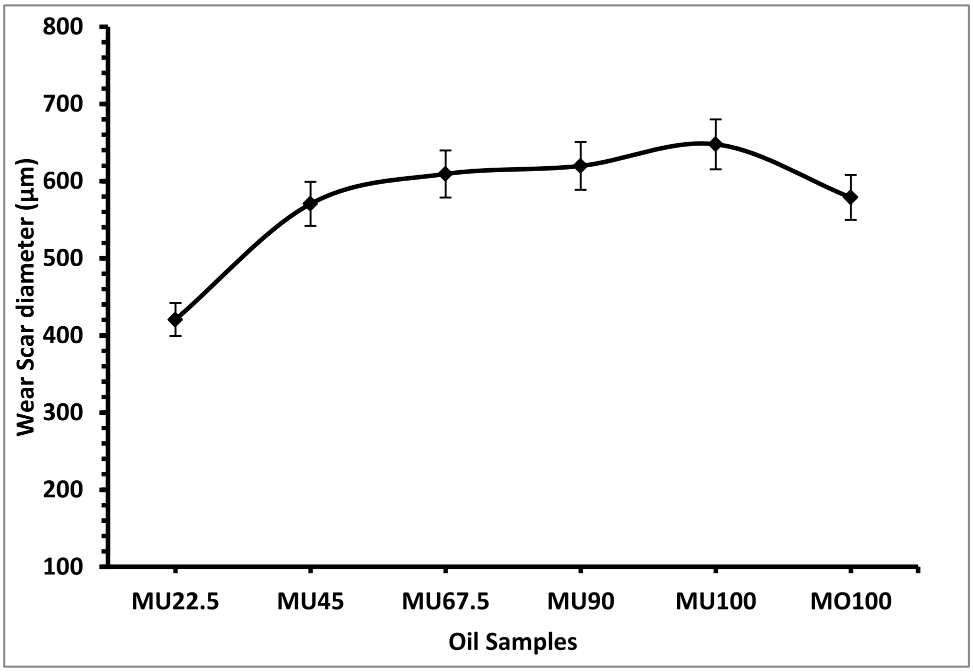

Figure 4. Wear scar diameter for the oil samples.

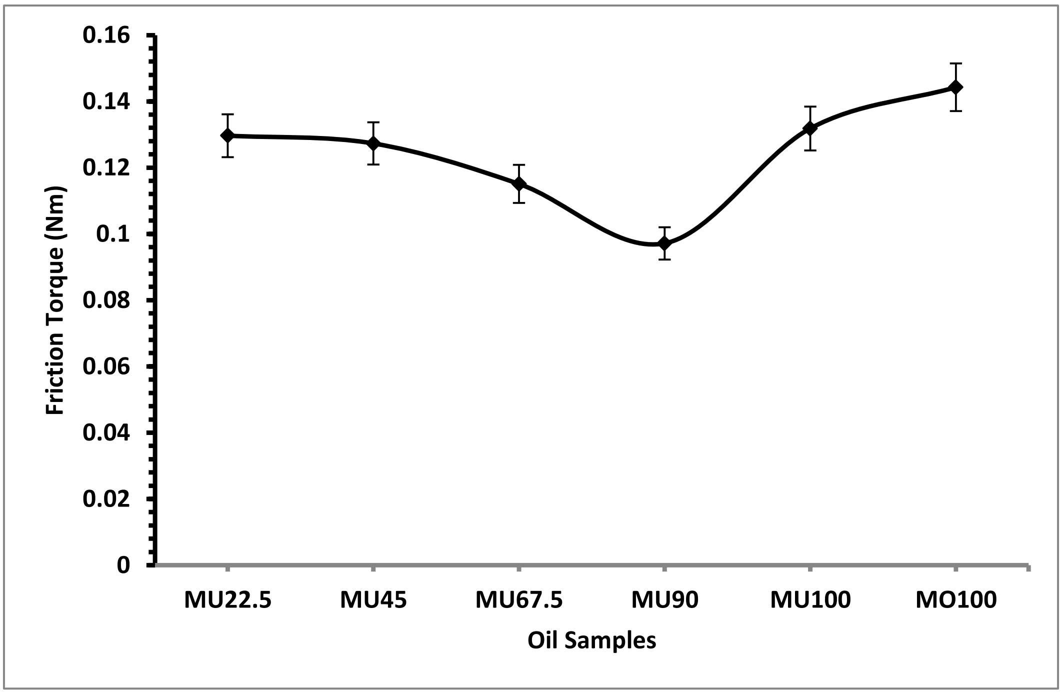

Figure 5. Friction torque values for oil samples.

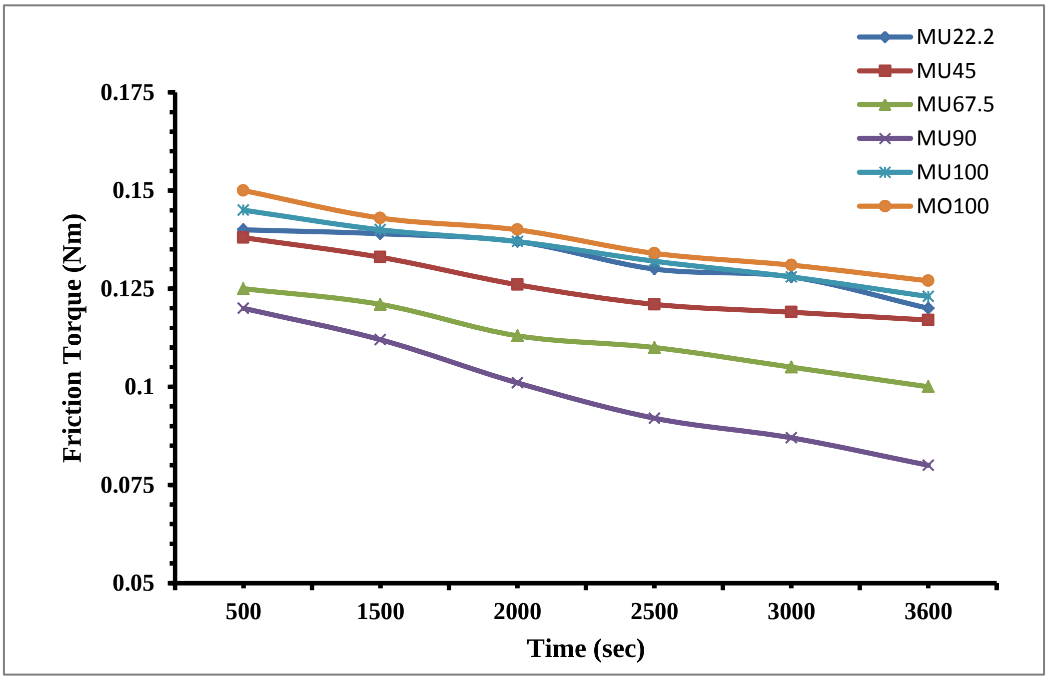

Figure 6. Friction torque as a function of sliding time for oil samples.

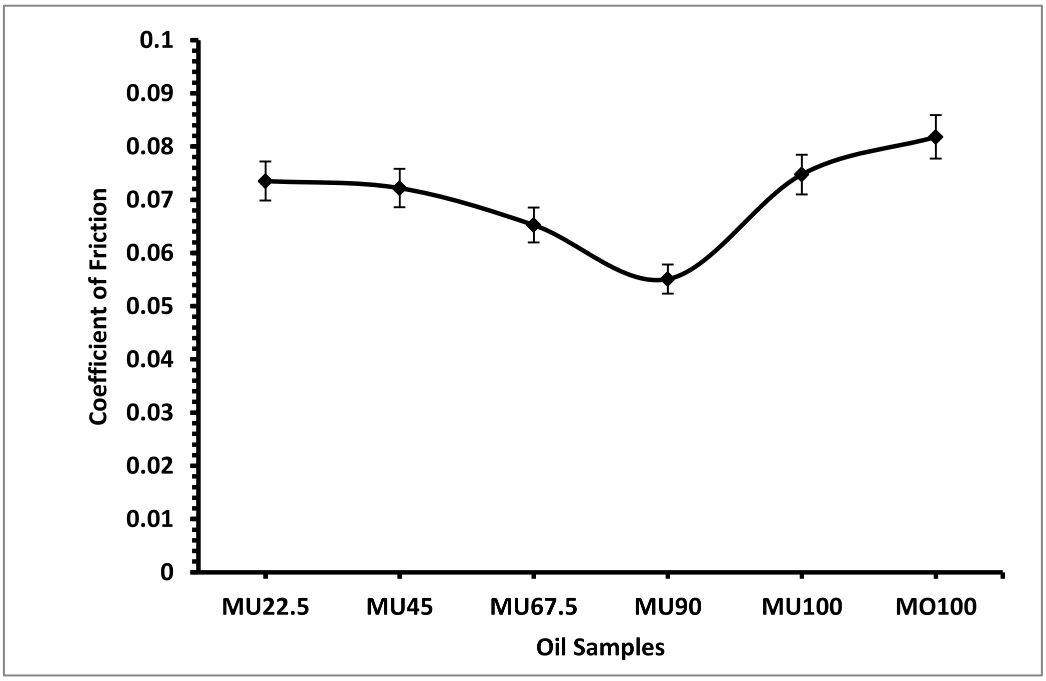

Figure 7. Coefficient of friction values for oil samples.

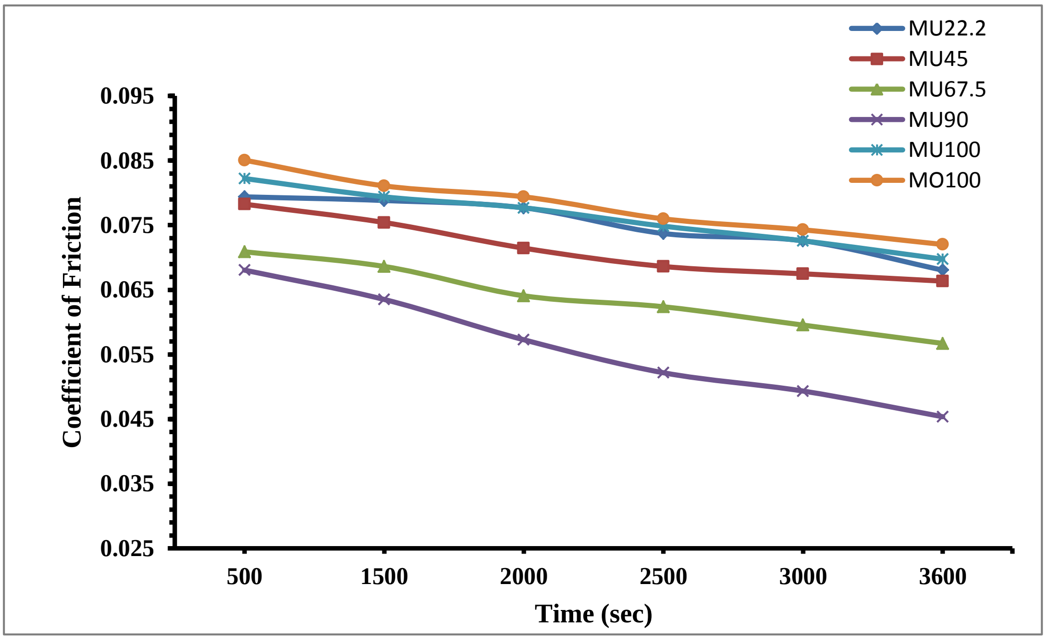

Figure 8. Coefficient of friction as a function of sliding time for oil samples**.**

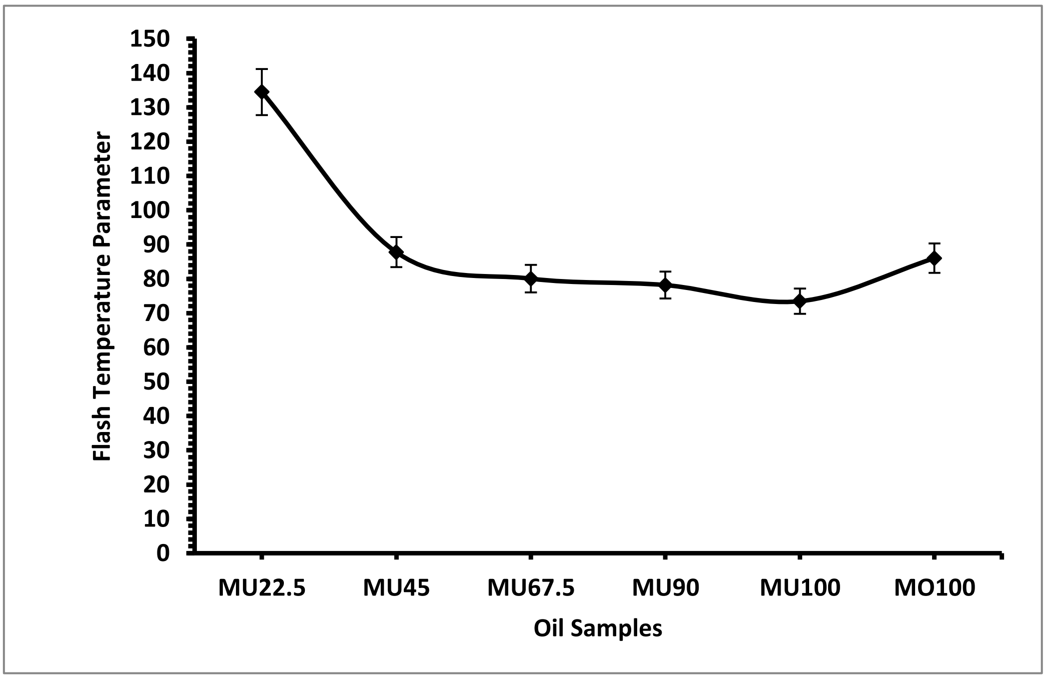

Figure 9. Flash temperature parameter values for oil samples.

University of Baghdad
College of Engineering
JE
JOURNAL OF ENGINEERING

Journal of Engineering

journal homepage: www.jcoeng.edu.iq
Number 3 Volume 24 Month 3

Mechanical and Energy Engineering

Impact Response for Two Designs of Athletic Prosthetic Feet

Dr. Mohsin N. Hamzah
Assistant Professor
Mechanical Engineering Department
University of Technology
20066@uotechnology.edu.iq

Dr. Ammar S. Merza
Lecturer
Mechanical Engineering Department
University of Technology
20086@uotechnology.edu.iq

Lamees Hussein Ali
BSc. In Mechanical Eng.
Mechanical Engineering Department
University of Technology
lamees.mail@gmail.com

ABSTRACT

The present work evaluated the differences in mechanical properties of two athletic prosthetic feet samples when subjected to impact while running. Two feet samples designated as design A and B were manufactured using layers of different orientations of woven glass fiber reinforced with unsaturated polyester resin as bonding epoxy. The samples' layers were fabricated with hand lay-up method. A theoretical study was carried out to calculate the mechanical properties of the composite material used in feet manufacturing, then experimental load-deflection test was applied at 0 degree position and 25 degree dorsiflexion feet position and impact test were applied for both feet designs to observe the behavior of the feet under static and impact loading and compare properties like stiffness, efficiency, rigidity, and shock absorption at different drop angles range from 25 degrees to 60 degrees which perform the foot positions while running. The load-deflection test result shows that the maximum deflection of the proposed design B was 32.2 mm at 0° and 38.45mm at 25°. While it was 41mm at 0˚ and 39mm at 25˚ for design A. Impact test result shows that design B foot gives peak load of 128 .7 kg with a peak time of 0.06 sec, while design Afoot gives 125.32 kg peak load with a time of 0.069 sec.

Keywords: Athletic prosthetic feet; composite materials, impact test.

استجابه الصدمه لتصميمين من الاقدام الاصطناعية الرياضيه

د. محسن نوري حمزه
أستاذ مساعد
قسم الهندسة الميكانيكية
الجامعة التكنولوجية

د. عمار سليم حميد
مدرس
قسم الهندسة الميكانيكية
الجامعة التكنولوجية

لميس حسين علي
بكالوريوس هندسة ميكانيكية
قسم الهندسة الميكانيكية
الجامعة التكنولوجية

الخلاصه

يقيم البحث الحالي الاختلافات في الخواص الميكانيكية لعينتين من الاقدام الاصطناعية عند التعرض للصدمه أثناء العدو.حيث في هذا العمل، تم تصنيع عينتين اشير اليها ب Aو B باستخدام طبقات من الألياف الزجاجية المنسوجه بأتجاهات مختلفه والتي تم ربطها مع بعضها باستخدام راتنجات البوليستر غير المشبعة باستخدام طريقه الترتيب اليدوي لطبقات الالياف.ثم أجريت دراسة نظرية لحساب الخواص الميكانيكية للمواد المركبة المستخدمة في تصنيع الأقدام، و تم تطبيق عده اختبارات تجريبيه منها اختبارالحمل-الانحراف عند وضع القدم بزاويه 0 و 25 درجة واختبار صدمه على كلا العينتين لمراقبة سلوك القدمين تحت تأثير الحمل الثابت وحمل الصدمه ومقارنه خصائص كالصلابه والكفاءه والصلاده وقابليه امتصاص الصدمة عند زوايا سقوط مختلفه

تتراوح من 25 درجه الى 60 درجه والتي تمثل مواقع القدم اثناء دوره العدو.من نتائج اختبار الحمل-الانحراف تبين ان اقصى انحراف لعينه القدم B كان 32.2 ملم عند زاويه 0 و 38.45 ملم عند زاويه 25 في حين كان 41 ملم عند زاويه 0 و39 ملم عند زاويه 25 لعينه القدم A. نتائج اختبار الصدمه اظهرت ان عينه القدم B تعطي حمل ذروه يعادل128.7 كغم خلال 0.06 ثانيه في حين عينه القدم A تعطي 125.32كغم حمل ذروه خلال 0.069 ثانيه.

الكلمات الرئيسه: قدم اصطناعيه رياضيه; مواد مركبه ،اختبار صدمه.

1. INTRODUCTION

The energy storage prosthetic foot is a new generation of prosthetic feet that appears and becomes common, especially among athletes, **Michael, 1987**. In 1977 Terry Fox, **Scrivener, 2010,** an athlete runner was diagnosed with bone cancer and that force his leg to be amputated. In 1979 he started training on marathon using a heavy prosthetic leg that is not designed for running, that prosthetic was not designed to absorb the shock created by running, so the foot was adjusted by adding a spring but it broke while Terry Fox was running to Sault Ste. After that incident, he died but inspired a lot of peoples to develop a prosthetic leg suited for running. Bruin and Iler (cited in reference **Marshall, 2008**, designed an improved prosthetic leg with a spring shaft that reduces shock and shortens the leg to lower the center of gravity while compression, then all the energy will be released while toe-off pushing the runner forward. Lower limb prosthetics have enhanced broadly since 1980, numerous sorts and states of these feet were created, for example, SACH foot, CHEETAH flex foot, and FLEX RUN foot. In 1988 the FLEX foot prosthetic was being set up to be wear in the sport. The FLEX foot can deal with change in load while running the foot store energy when compressed by the body weight. The foot then discharges the energy giving a forward movement to the runner, **Niehhar, et al., 2014**. A composite material fiber fortified polymer is the primary materials for building these feet. The composite fiber generally distraught by staking fiber layers in different directions and numbers to give the wanted properties and shape the reinforcement is a polymer, ceramic, or metal. Polymers have a low strength, and rigidity than with metals. Metal has a high ability to deform under tensile load and ceramic is weak. Matrix is used to maintain the directions of the fibers and save them from the surrounding conditions. The best properties of these components are their low density, high strength and stiffness, and lightweight, **Campbell, 2010**. The moment of inertia of both Cheetah and Flex Foot is much lower than the other jointed leg types, due to better mass distribution. That's gives smoother control when moving. Cheetah flex foot can straightforwardly convert the vertical force into a linear movement, **Ossur, 2014**. The size of the elastic area also helps to execute the response of the natural leg during running gait cycle.

Based on popular feet models available in markets, two athletic prosthetic feet were designed and designated as design A and design B, the measurements for both feet designs are calculated using KINOVEA software, by applying a side-view picture of the foot to the program and specifies the known dimension as in our case only the length of the foot as shown in **Fig.1**.The software then will give all the rest of the desired profile dimensions. The width and thickness of both feet were concluded by suggesting different values and applying then on the foot model then analyzing the stresses and deflections of each suggested one to obtain the best width and thickness for the foot. Afterwards, the final feet dimensions resulted then draw using SOLID WORK 2014 software as shown in **Fig. 2** and **Fig. 3**. The current research objective is, firstly, manufacturing of two proposed designs of flexible leaf spring prosthetic feet by using woven fiberglass. Secondly, to evaluate the differences in mechanical properties of two athletic prosthetic feet samples when subjected to impact while running.

2. MANUFACTURING OF ATHLETIC PROSTHETIC FEET SAMPLES

Design A and B athletic prosthetic feet were manufactured in order to study their behavior while running by subjecting them to experimental static and impact tests and compare the obtained results.

2.1 Preparing Mold

Two steel plates are cut in dimensions of 71cm × 15cm, and curved to resemble the profile of the design B foot; one presents the top cover mold and the other plate will be base fixed on a steel column. For Design A prosthetic foot each plate are cut in dimensions of 61cm × 15cm and curved to match the shape of the foot. The steel plates are shielded with a thick sheet of rubber to give a smooth surface to the mold. The second film of a clear plastic sheet is added to protect the foot from adhesion with the mold, as shown in **Fig.4**.

2.2 Preparing Composite

The material used for molding both feet designs is a woven glass fiber reinforced with unsaturated polyester resin. -45˚, 45˚, and 0˚, 90˚ woven fiberglass layers are cut into multiple lengths in order to give the required thickness reduction for the foot **Fig.5**. Several resins to harden mixing ratios were tested in order to obtain a value that gives enough time to finish laying up the fibers before starting to solidify. The resin is mixed with the hardener in a ratio of 1 liter: 1.5 milliliters. This gives an approximate time of 2 hours to start solidifying within outside temperature of 44-degree centigrade.

2.3 Molding

Fibers layers were added in the sequence of 0˚, 90˚ fibers orientation layer followed by -45˚, 45˚ fibers orientation layer. The first layer is added and the resin is laid over it by using a painting brush until the layer is fully saturated, a second layer is then placed and the resin is added over it by means of a brush. After the second layer, a steel teethed roller was used to roll over the added fibers layers before applying any additional resin to remove any trapped air bubbles and ensure equal distribution of the resin along the fibers layers, This process was repeated till all the fabric layers were placed and the required foot thickness was obtained. The assembly afterward transferred into the mold and pressed using special clamps to get rid of excess resin. The mold was then left for 4 days in the outside conditions of 44˚C temperature to dry. **Fig.6** shows the final step of molding including clamps arrangement.

After completely dried, both feet samples are cut to 7 cm width and drilled in order to fix it on test devices.

3. FEET SAMPLES PROPERTIES:

The elastic properties of the composite are calculated using the rule of mixture equations. It is a quick way to estimate the material properties, i.e., the module in 1 and 2 directions of a composite. It assumes that the modulus of the composite is a combination of the modulus of the fiber and the matrix that are related by the volume fraction of the constituent materials. To apply the equation, the properties of the glass fiber and the resin were obtained using the datasheets given by the manufacturing company, and the fiber volume fraction ($\mathcal{V}_f$) was obtained from the densities and weights of fiber used in foot sample as listed in **Table 1** and **2** respectively.

The unidirectional elastic constants of the composite material used in both feet, that includes the elastic modules in x-axis direction (E_1), in y-axis direction (E_2) and in z-axis(E_3), the shear modulus in x-y plane (G_{12}), x-z plane (G_{13}), y-z plane(G_{23}), and the Poisson's ratios in x-y plane (υ_{12}), x-z plain(υ_{13}), y-z plane(υ_{23}), are calculated by applying equations below, **Aly, et al., 2010**.

$$E_1^{udf} = E_f \mathcal{V}_f + E_m\left(1-\mathcal{V}_f\right)$$

$$E_2^{udf} = E_m\left[\frac{E_f + E_m + (E_f - E_m)\mathcal{V}_f}{E_f + E_m - (E_f - E_m)\mathcal{V}_{\mathcal{F}}}\right]$$

$$\upsilon_{12}^{udf} = \upsilon_f \mathcal{V}_f + \upsilon_m(1-\mathcal{V}_f) \qquad (1)$$

$$\upsilon_{23}^{udf} = \upsilon_f \mathcal{V}_f + \upsilon_m\left(1-\mathcal{V}_f\right)\left[\frac{1+\upsilon_m - \frac{\upsilon_{12}E_m}{E_{11}}}{1-\upsilon_m^2 + \frac{\upsilon_m \upsilon_{12} E_m}{E_{11}}}\right]$$

$$G_{12}^{udf} = G_m\left[\frac{G_f + G_m + \left(G_f - G_m\right)\mathcal{V}_f}{G_f + G_m - \left(G_f - G_m\right)\mathcal{V}_f}\right]$$

$$G_{23}^{udf} = \frac{E_{22}}{2(1+\upsilon_{23})}$$

where E_f and E_m are the elastic moduli of the fiber and resin, respectively, υ_f and υ_m are the Poisson's ratio of fiber and resin, G_f and G_m are the shear modules of fiber and resin, respectively, and $\mathcal{V}_f$ is the fiber volume fraction

A composite with a woven of 0, 90 and 45,-45 fibers orientation were used in manufacturing design A and B feet samples. The woven fibers elastic constants can then be calculated by using the following equations:

$$\left(\frac{2}{E_1}\frac{E_1(E_1 + (1-\upsilon_{12}^2)E_2) - \upsilon_{12}^2 E_2^2}{E_1(E_1+2E_2) + (1+2\upsilon_{12}^2)E_2^2}\right)^{udf} = \left(\frac{1}{E_1}\right)^{wf}$$

$$\left(\frac{4}{E_1}\frac{\upsilon_{12}E_2(E_1 - \upsilon_{12}^2 E_2)}{E_1(E_1+2E_2) + (1+2\upsilon_{12}^2)E_2^2}\right)^{udf} = \left(\frac{\upsilon_{12}}{E_1}\right)^{wf}$$

$$\left(\frac{1+\upsilon_{23}}{E_2}+\frac{1}{2G_{12}}\right)^{udf}=\left(\frac{1}{G_{13}}\right)^{Wf} \tag{2}$$

$$\left(\frac{1}{E_1}\frac{E_1(\upsilon_{12}+\upsilon_{23}+\upsilon_{12}\upsilon_{23})+\upsilon_{12}^2E_2}{E_1+(1+2\upsilon_{12})E_2}\right)^{udf}=\left(\frac{\upsilon_{13}}{E_1}\right)^{wf}$$

$$\left(\frac{(1-\upsilon_{23}^2)E_1^2+(1+2\upsilon_{12}+2\upsilon_{12}\upsilon_{23})E_1E_2-\upsilon_{12}^2E_2^2}{E_1E_2(E_1+(1+2\upsilon_{12})E_2)}\right)^{udf}=\left(\frac{1}{E_3}\right)^{wf}$$

$$\left(\frac{1}{G_{12}}\right)^{udf}=\left(\frac{1}{G_{12}}\right)^{wf}$$

Subscripts 1, 2, and 3 present lamina references axes. And *wf* and *udf* denote woven fiber, and unidirectional fiber respectively.

4. EXPERIMENTAL TESTS

A load deflection test was performed to measure the deflection of the foot for 0 degree and 25-degree foot positions by applying a vertical load that equals to three times body weight, increases from zero to 1600 N maximum on both feet. The load was applied on the location of the socket connection to the foot to present the load that the body will force through the period of mid stand (the foot is perpendicular to the ground with maximum weight applied on it) to push off. After mid stance and just before the toe off the period start, the foot developed an angle with the ground. To measure the dorsiflexion angle, the foot was fixed on a triangular shape wood peace fixed on the device frame; a force was applied on the prosthetic foot sample, this force present the ground reaction force while running. By using Dartfish 9 software analyzer, the angle was measured at each desired load value, **Fig. 7** and **8**.

The impact tests were then performed to study the behavior and response of the foot when the first impact the ground while running, the experiments were executed using an impact foot tester device that is set to examine the impact characteristics of athletic prosthetic foot **Merza, 2015**. The device consists of a steel frame, a pendulum arm, a 6 kg mass that is attached to the pendulum end to increase the stance effective mass **Toh, et al., 1990**, and a thick steel plate attached to a load cell, that works as a ground for the foot to hit. Design A foot was fixed to the pendulum mass while raised and dropped each time with a different drop angle range from 25 to 60 degrees that simulate the positions of the foot while running. On each drop, the foot hits the plate with a force that measured by the 1000 kg capacity load cell attached to the plate and transforms it to a DAQ system device, which reads the signals with time and displays it in a chart. The same test procedure was applied to the design B foot sample with some modifications on the way the foot attaches to the pendulum mass, **Figs. 9** and **10.**

5. RESULTS AND DISCUSSION

The elastic properties of the composite materials used in both feet sample were calculated by using the rule of mixture equations (1) and (2) are listed in **Table 3.** It can be noticed that there is a difference in the elastic properties of composite between design A and design B foot in spite of using the same material in manufacturing and that due to the difference in the amount of fiber used (fiber volume fraction)in manufacturing both feet. The elastic modulus of the composite was compared with results from a tensile test performed by **Jweeg, et al.** and it's found to be close at the same woven glass fiber volume fractions with a percentage error of 5%.

The deflection behavior of both feet samples under loading and unloading for both 0 degrees and the 25-degree position was obtained, **Ali, et al., 2017**, in this test and the results demonstrate that the maximum deflection of the design B athletic prosthetic foot was 32.2 mm at 0° and 38.45mm at 25°. While it was 41mm at 0˚ and 39mm at 25˚ for design A athletic prosthetic foot. The difference in stiffness for each foot at 0 and 25-degree position is required to attain a smooth transition from the heel strike to the toe off phases of the running gait as well as the development of an angle that mimics the ankle dorsiflexion angle.

The efficiency to store and release energy for each foot was calculated depending on the loading and the unloading curves of the load-deflection test results, as shown in **Table 4**.

At each drop's angle, the foot load response with time was recorded, the peaks load and the maximum first peek, at each drop angle, for both feet samples were showed graphically in **Figs. 11** through **15.**

Figs. 11 to 13 showed that the behavior of the foot when hits the plat rebound seven times until its settled (which gives seven load peaks) for the design A foot, while six rebound times until settling was recorded for design B foot.

Fig.14 shows that for design A foot sample, at 60-degree drop angle the first peak started from zero at 0.84 sec and increased highly to reach a 125 kg load at 0.867 sec and that means it takes time period equal to 0.027 sec to reach the maximum load. In this period, the foot hit the force plate giving a signal to the load cell to start recording load then deflect giving an extra push toward the plat until reaching the maximum peak load. The foot then started to return to its natural shape leaving the plate and reducing the load until it reaches zero kg at 0.909 sec with a time period equal to 0.042 sec. That gives a total time approximate to 0.069 sec for the peak to start and finish, while for design B foot, at the first peak the load increases from zero to 128kg maximum within 0.032 sec and then the load decreases to zero within 0.028 sec. That gives 0.06 sec time for the peak to finish. The difference in peak shape between design A and B foot is because of the higher peak loading rate for the design B foot while impact due to low cushioning effect which gives a sharper more pointer peak compare to design A foot.

From the data given by the figures, it is possible to determine the peak impact time and peak load value for each foot design, as listed in **Table 5**.

Table 5 indicates that design B foot first peak is higher in value and is taken less time to start and finish than for design A foot.

There are dissimilarities in the overall impact behavior between both feet as shown in **Fig.15**, where the number of peaks produced at the 60-degree impact is 7 peaks for design A and 6 peaks for design B foot, also the peaks values are higher which indicate the variation in stiffness between the two feet.

5. CONCLUSIONS

In the current paper, two athletic prosthetic feet designs have been made using unsaturated polyester resin reinforced with fiberglass by means of hand laying method. Studies of the mechanical behavior of the manufactured feet were performed experimentally using load-deflection test and impact test, and results for both feet were compared as follows:

Under the same load value, the foot sample designated as design B has a higher stiffness than of the corresponding one of design A, taken into account that both feet are within the standard maximum deflection range for athletic prosthetic feet. The dorsiflexion angle of the design B foot is more than that of the corresponding one in design A, which may give a bend up to an acceptable limit gaining a better application for the gait cycle profile according to published work, **Resan, et al., 2011**.

Although the absorbing of the shock when the foot hits the ground while running depends mostly on the existing of a high-density foam or rubber at the foot rear end, the spring characteristic of the fiber forming the foot as well as foot shape has an effect on the shock absorbing **Rihs and Polizzei, 2001**. And that shows on results were the first peak applied time for the design A is longer than the design B, as well as the small difference between the first and second peak load, indicate that design A has a higher ability to observe the shock.

Design B foot has a higher first peak load compare to design A foot which means that design B foot is stiffer since stiffness for a prosthetic athletic foot is defined as the amount of flexibility while impact. The height of the impact peak depends on the stiffness, as the stiffness increase the impact peak load increase, **Fey** and **Neptune, 2011**. The body support will decrease as the foot stiffness decrease, and that will exert an extra work on the leg muscles to support the body. The decrease in foot stiffness led to low body force activity which has generally been known stiffness will provide a big support to the body while decrease stiffness will provide extra forward motion.

REFERENCES

- Ali, L.H., Hamzah, M.N., Merza, A.S., 2017, *Experimental and Numerical Investigations of Athletic Prosthetic Feet Made of Fiber Glass Reinforced Epoxy*, First International Conference on Recent Trends of Engineering Sciences and Sustainability, University of Bagdad.
- Aly, M.F., Goda, I.G.M., Hassan, G.A., 2010, *Experimental Investigation of the Dynamic Characteristics of Laminated Composite Beams*, Int. J. of Mechanical & Mechatronics IJMME-IJENS, Vol. 10 No. 03.
- Campbell, F., 2010, *Structural Composite Materials*, ASM International, Materials Park, Ohio, Ch1 pp.1-31.
- Fey, N.P., Neptune, G.K., 2011, *The Influence of Energy Storage and Return Foot Stiffness on Walking Mechanics and Muscle Activity in Below-Knee Amputees*, Clinical Biomechanics, Vol. 26, No. 10.
- "*JPS Composite Materials Data Book, JPS Composite Materials Corporate Headquarters and US Operations*", JPS Composite Materials Corporation, 2200 South Muray Avenue, Web Source available at http://www.jpscm.com.
- Jweeg, M.J., Hammood, A.S. and Al-Waily, M., 2012, *Experimental and Theoretical Studies of Mechanical Properties for Reinforcement Fiber Types of Composite Materials*, Int. J. of Mechanical & Mechatronics Engineering IJMME-IJENS Vol:12 No:04.
- Marshall, T., 2008, Article name, *Terry Fox*, The Canadian Encyclopedia, Canadian History.
- Merza, A.S., 2015, *Experimental and Theoretical Analysis of an Athletic Prosthetic Foot*, Ph.D. thesis, University of Technology, January.
- Michael, J., 1987, *Energy Storing Feet: A Clinical Comparison*, the American Academy of Orthotics and Prosthetics, Vol. 11, No.3, pp 154-168.
- Neither, T., Park, J., Bollinger F., 2014, *Biomechanics of below Knee Prosthetics*, project for Simon Fraser University.
- Ossur, 2014, *Flex-Foot-Cheetah*, Ossur, Web Source available at http://www.ossur.com/prosthetic-solutions/products/feet/feet/cheetah.
- Resan, K.K., Al-Hilli, A.H., and Ali, M.M., 2011, *Design and Analysis of a New Prosthetic Foot for People of Special Needs*, the Iraqi Journal for Mechanical and Material Engineering, Vol. 11, No. 2.
- Rihs, D., Polizzi, I., 2001, *Prosthetic Foot Design*, Victorian University of Technology, Rehab Tech-Monash rehabilitation technology research unit, Australia.
- Scrivener, L., 2010, Article name, *Terry Fox: His Story*, The (McClelland & Stewart) Canadian Publishing Company.
- Toh, S.L., Goh, J.C., Tan, P.H., Tay, T.E., 1990, *Fatigue Testing of Energy Storing*, Prosthetics and Orthotics International, 17 , pp.180 -188.

- Willer, M.A., 2014, *The Design and Analysis of a Double Transtibial Composite Prosthesis and the Effect of Lateral Movement Load*, Rensselaer Polytechnic Institute Hartford, CT, December.

NOMENCLATURE

E	Modulus of elasticity	N/m^2
G	Shear modulus	N/m^2
$\boldsymbol{\upsilon}$	Poisson's ratio	m/m
$\boldsymbol{\nu_f}$	Fiber volume fraction	
f	Fiber	
m	Matrix	
1	X axis	
2	Y axis	
3	Z axis	
wf	Woven fiber	
udf	Unidirectional fiber	

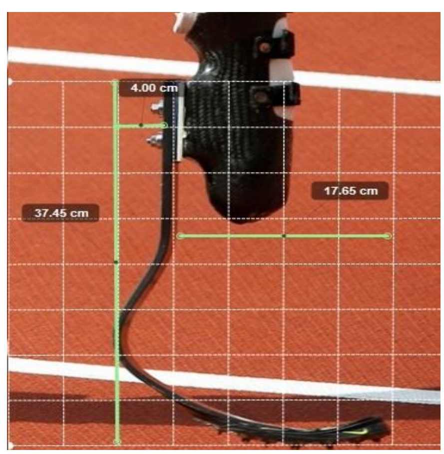

Figure 1. KINOVEA software foot dimensions analyses, **Willer, 2014.**

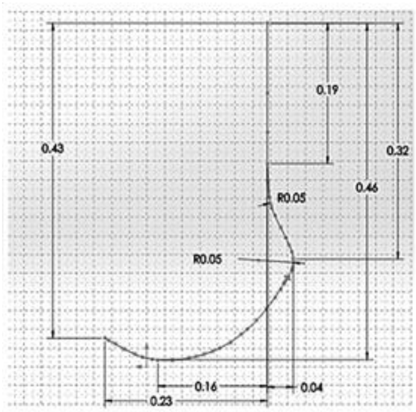

Figure 2. Dimensions of the Design B foot in m.

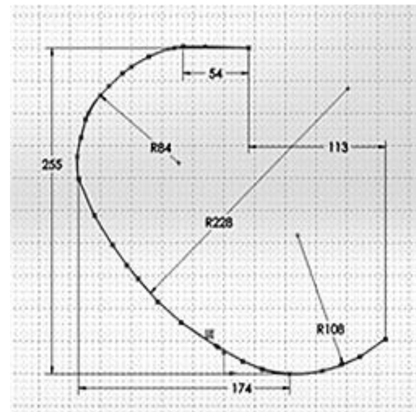

Figure 3. Dimensions of the Design A foot in mm.

Figure 4-A. Design A foot mold.

Figure 4-B. Design B foot mold.

Figure 5. Woven glass fiber layers.

Figure 6. Clamps distribution of the mold.

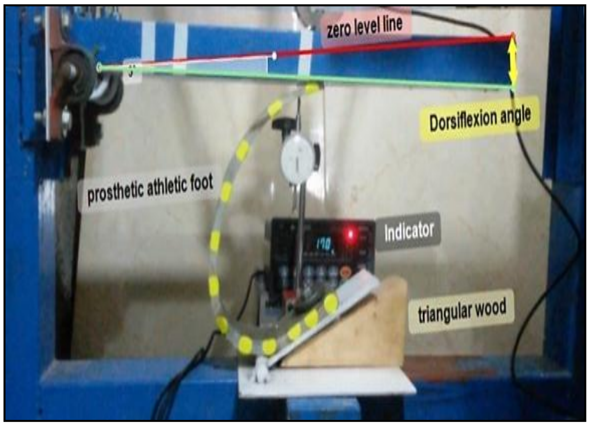

Figure 7. Measuring dorsiflexion angle for design a foot sample.

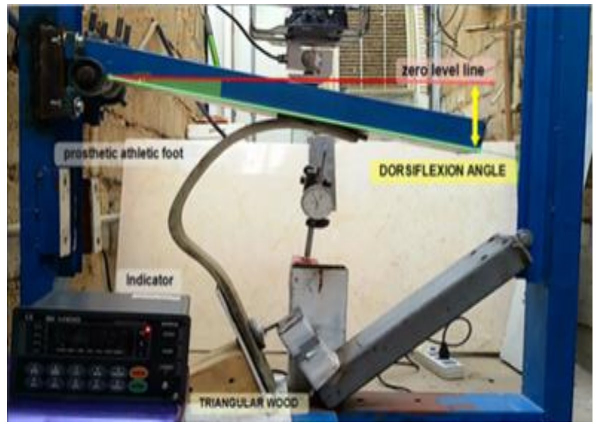

Figure 8. Measuring dorsiflexion angle for design B foot sample.

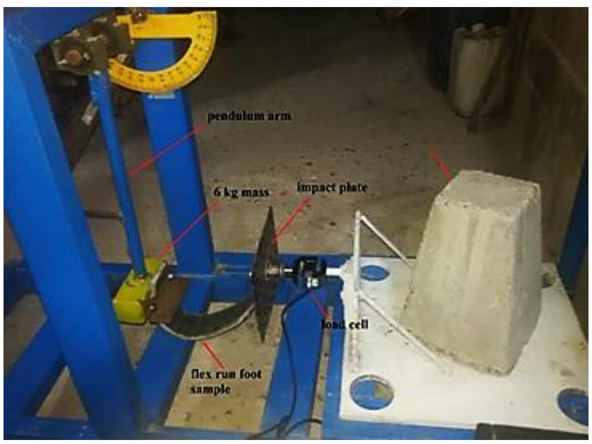

Figure 9. Design a foot impact test.

Figure 10. Design B foot impact test.

Table 1. Material properties giving by manufacturing company, **JPS Composite Materials Corporation.**

Material	Properties	Value
Glass Fibers	Elastic modulus (GPa)	74
	Shear Modulus (GPa)	30
	Density (kg/m^3)	2600
	Poisson’s ratio	0.25

Unsaturated Polyester Resin	Elasticity Modulus (GPa)	4.0
	Shear modulus (GPa)	1.4
	Density (kg/m^3)	1200
	Poisson's Ratio	0.4

Table 2. the weight and volume fractions of fiber and resin used in manufacturing feet samples.

Foot Sample	Fiber Weight (gm.)	Resin Weight (gm.)	Fiber volume Fraction
DESIGN B	954	186	70%
DESIGN A	523	165	68%

Table 3. Elastic properties of woven fiber composite lamina.

Properties	Design B	Design A
Elastic modulusE1=E2 (MPa)	35969.7	35426. 5
Elastic modulus E3 (MPa)	18382.599	17444.59
Shear modulus in plane 1–2 G12 (MPa)	6325.834	5956
Shear modulus in plane 1–3 G13 (MPa)	6360.0	5977
Shear modulus in plane 2–3 G23 (MPa)	6360.0	5977
Poisson's ratio in plane 1–2 υ12	0.1497	0.144577
Poisson's ratio in plane 1–3 υ13	0.364	0.37
Poisson's ratio in plane 2–3 υ23	0.364	0.37

Table 4. Efficiency of design A and design B samples.

Foot	Angle	Efficiency (%)
Design A	0°	78.88
	25°	84.50
Design B	0°	89.77
	25°	71.96

Table 5. Impact foot result at 60 degree drop angle.

	Peak Load (kg)			Firs Peak Time (sec)		
	First	Second	Difference	Start	Finish	Difference
Design A	125.3	103.4	21.85	0.840	0.909	0.069
Design B	128.7	80.31	48.44	0.729	0.789	0.060

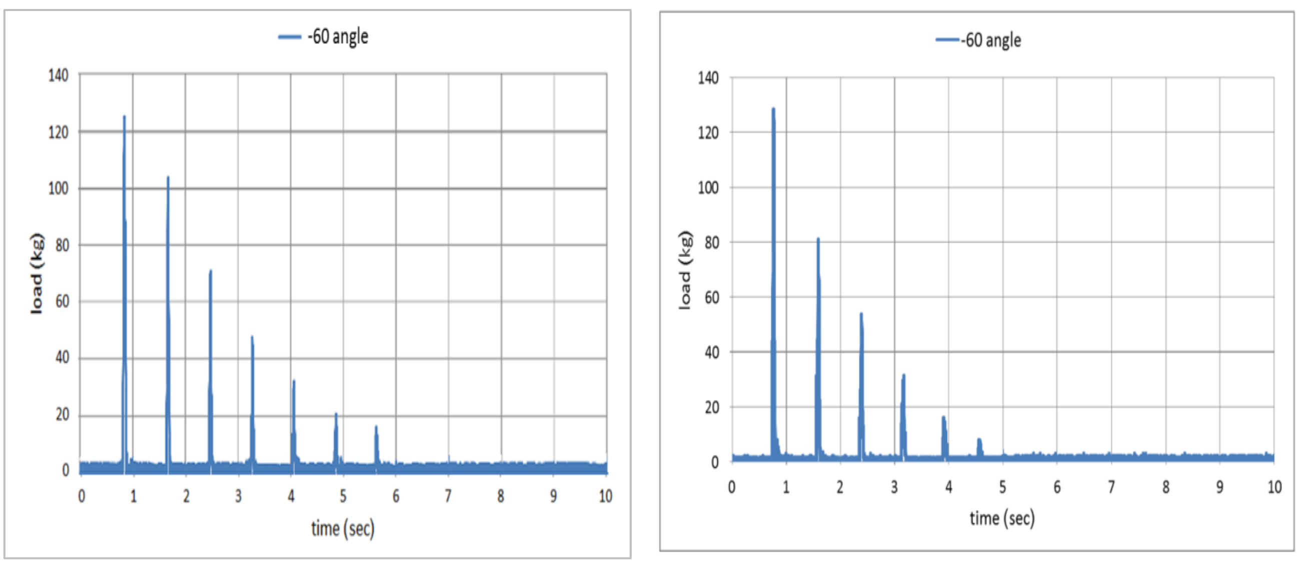

(b)

(a)

Figure 11. Response with time at -60˚angle height for (a) Design A foot (b) Design B foot.

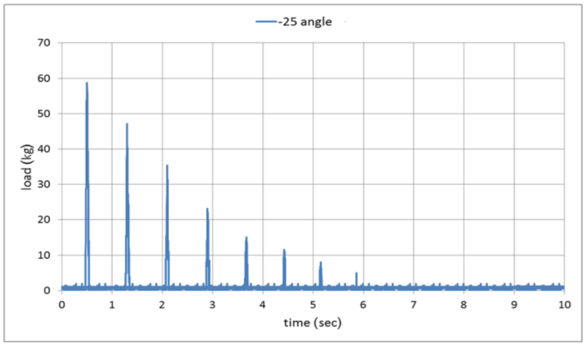

(A)

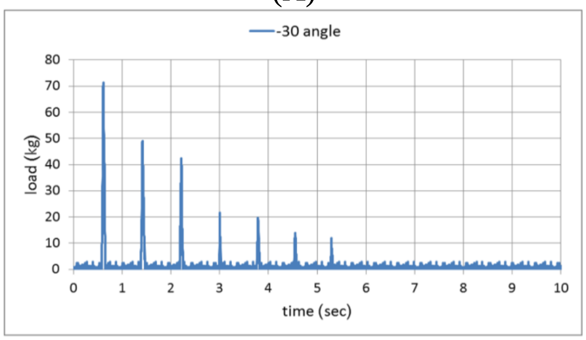

(B)

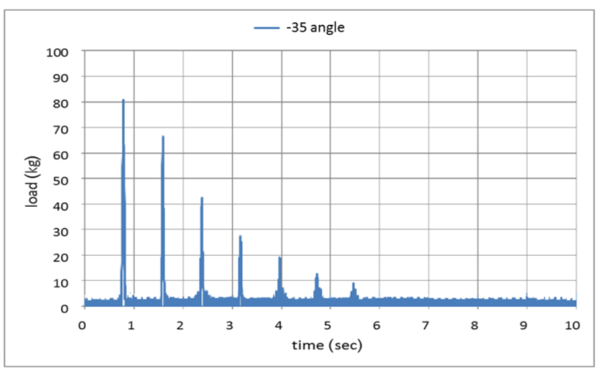

(C)

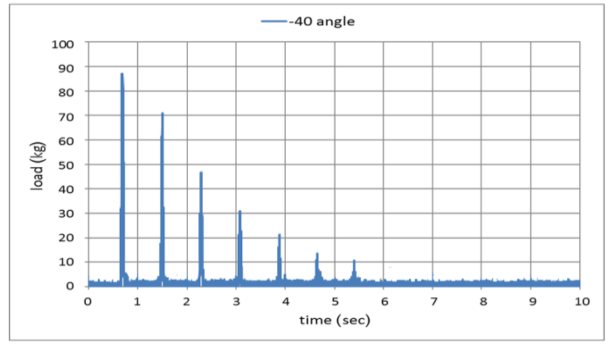

(D)

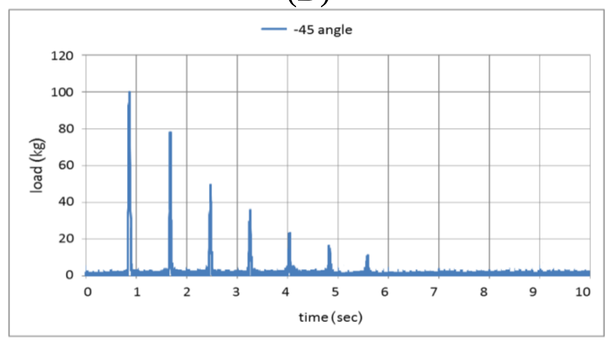

(E)

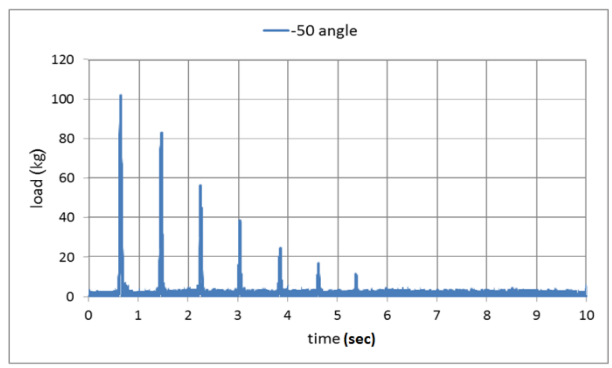

(F)

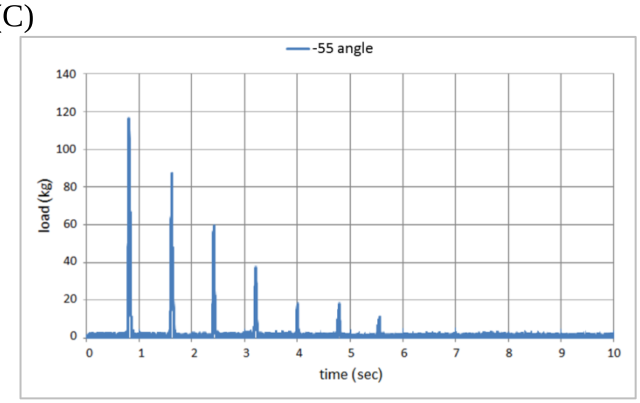

(G)

Figure 12. Impact load response with time for design A foot at: A)25˚, B)30˚, C)35˚, D)40˚, E)45˚, F)50˚, G)55˚.

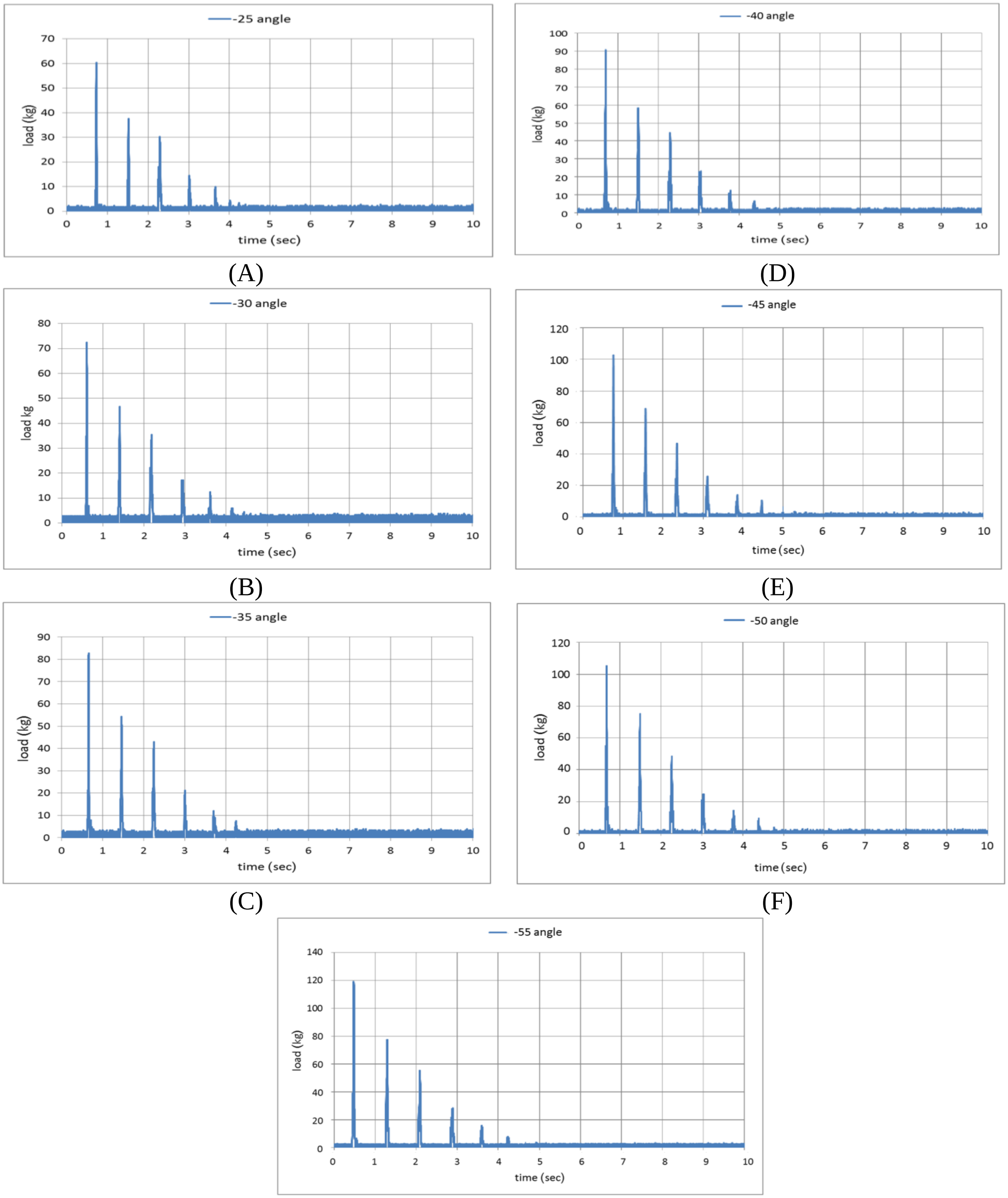

(G)

Figure 13. Impact load response with time for design B foot at: A)25˚, B)30˚, C)35˚, D)40˚, E)45˚, F)50˚, G)55˚.

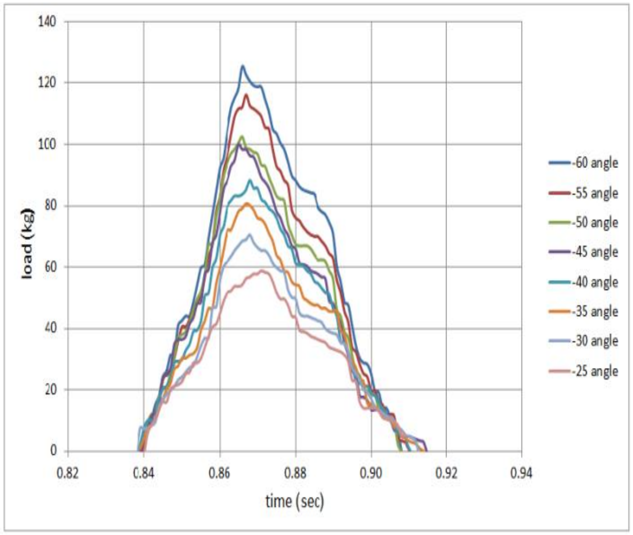

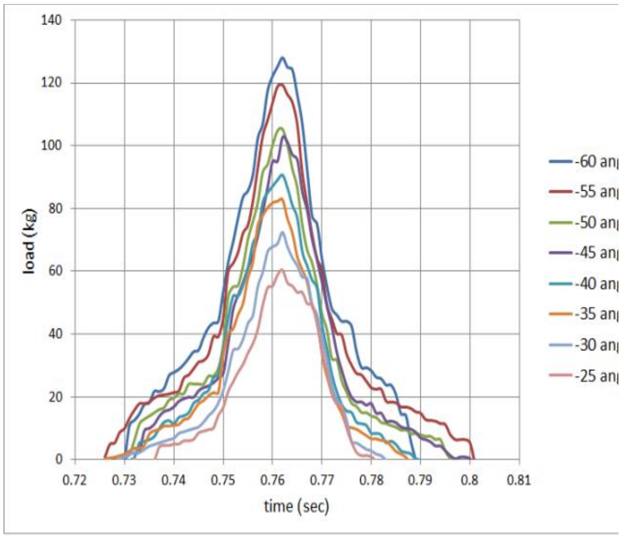

(a) (b)

Figure 14. Maximum first peak load at each drop angle for; (a) Design A foot sample, (b) Design B foot sample.

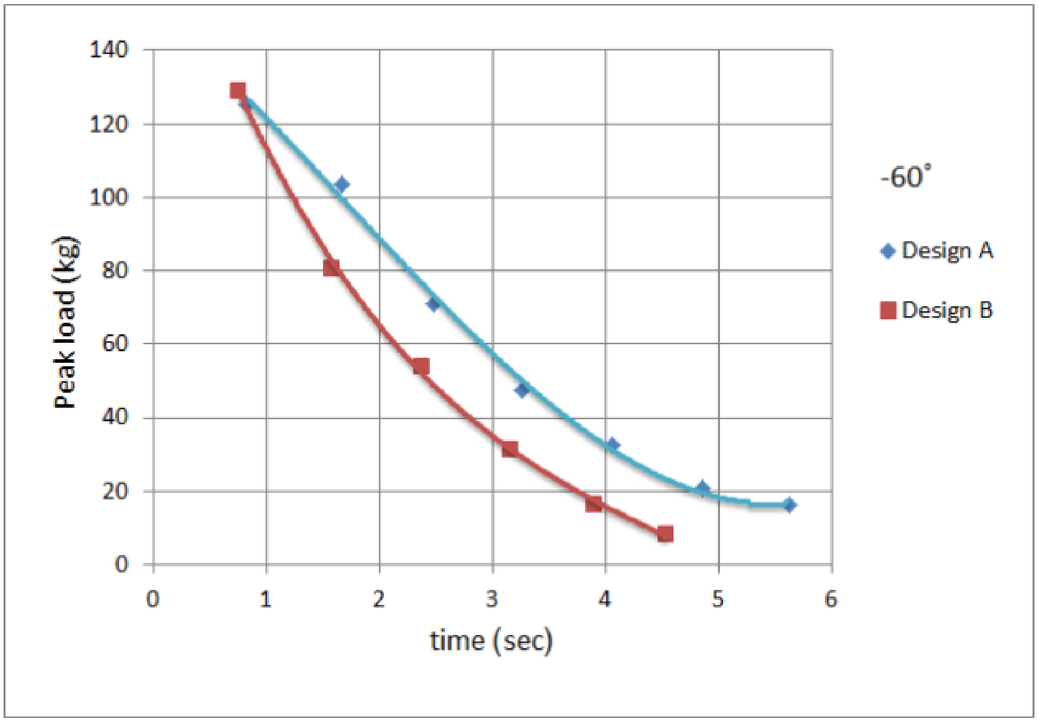

Figure 15. The decreasing of impact load peaks with time at -60˚angle for booth feet.

University of Baghdad
College of Engineering
JE
JOURNAL OF ENGINEERING

Journal of Engineering

journal homepage: www.jcoeng.edu.iq

Number 3 Volume 24 Month 3

Mechanical and Energy Engineering

Numerical Simulation of Thermal-Hydrodynamic Behavior within Solar Air Collector

Mustafa T. Mustafa
Assistant Professor
Technical Engineering College, Middle Technical University
drmustafa6087@yahoo.com

Ayad T. Mustafa
Lecturer
College of Engineering, Al-Nahrain University
ayad_altai@yahoo.com

ABSTRACT

Solar collectors, in general, are utilized to convert the solar energy into heat energy, where it is employed to generate electricity. The non-concentrating solar collector with a circular shape was adopted in the present study. Ambient air is heated under a translucent roof where buoyant air is drawn from outside periphery towards the collector center (tower base). The present study is aimed to predict and visualize the thermal-hydrodynamic behavior for airflow under inclined roof of the solar air collector, SAC. Three-dimensional of the SAC model using the re-normalization group, RNG, $k-\varepsilon$ turbulence viscus model is simulated. The simulation was carried out by using ANSYS-FLUENT 14.5. The simulation results demonstrated that at same insolation; airflow, ground and air temperatures increase when the collector radius decreases towards the collector center. The ground temperature and air velocity increase, while airflow temperature decreases when the inclination angle increases from 0° to 20° due to changing in airflow movement. More decreasing in airflow temperature has been occurred when the inlet height increases from 0.1m to 0.25m. The simulation results were validated by comparing with the experimental data. In conclusions, the obtained results showed the capability of producing warm airflow to generate electricity in Baghdad city.

Key words: numerical simulation; thermal-hydrodynamic analysis; solar collector; solar load model; energy conversion.

المحاكاة العددية للسلوك الحراري الهيدروديناميكي داخل مجمع الهواء الشمسي

م.د. اياد طارق مصطفى
كلية الهندسة/جامعة النهرين

أ.م.د. مصطفى طارق مصطفى
الكلية التقنية الهندسية/الجامعة التقنية الوسطى

الخلاصة

تستخدم المجمعات الشمسية، بشكل عام، لتحويل الطاقة الشمسية إلى طاقة حرارية، حيث ينتفع بها لتوليد الكهرباء. المجمع الشمسي الغير التركيزي ذو الشكل الدائري هو الذي اعتمد في الدراسة الحالية. يتم تسخين الهواء المحيط تحت مظلة شفافة حيث يسحب الهواء الطافي من المحيط الخارجي نحو مركز المجمع (قاعدة البرج). تهدف الدراسة الحالية إلى تنبؤ واظهار السلوك الحراري-الهيدروديناميكي لتدفق الهواء تحت سقف مائل لمجمع هواء شمسي. نموذج مجمع الهواء الشمسي باستخدام نموذج اللزوجة المضطرب RNG $k-\varepsilon$ تم محاكاته. تم تنفيذ المحاكاة باستخدام ANSYS FLUENT 14.5. أظهرت نتائج المحاكاة أنه لنفس الاشعاع الشمسي: تدفق الهواء، درجة حرارة الهواء والارض تزداد عندما يتناقص نصف قطر المجمع تجاه مركزه. درجات

حرارة الارض وسرعة الهواء تزداد، بينما درجات حرارة الهواء تنخفض عندما تزداد زاوية الميل من 0° الى 20° نتيجة لتغير حركة تدفق الهواء. انخفاض اكثر في درجات حرارة الهواء حدث عندما ازداد ارتفاع مدخل المجمع من 0.1 م الى 0.25 م. تم التحقق من صحة نتائج المحاكاة بالمقارنة مع البيانات التجريبية. كشفت الاستنتاجات من النتائج المستخلصة على مقدرة الهواء الساخن المنتج من المجمع الشمسي على توليد الكهرباء في مدينة بغداد.

الكلمات الرئيسية: المحاكاة العددية، التحليل الحراري الهيدروديناميكي، المجمع الشمسي، نموذج الحمل الشمسي، تحويل الطاقة.

1. INTRODUCTION

The solar radiation can be utilized to heating natural airflow within a transparent system. The solar air heating system has advantages of simple construction and maintenance, moreover less corrosion compared with solar water heating system. The solar air heating system is called solar air collector, SAC. Solar air collectors are receivers of solar radiation that is used to convert it to heat energy. Generally speaking, solar collectors are either non-concentrating or concentrating solar radiation. SAC, of non-concentrating type, has a transparent area equivalent to the absorber area. An application for the SAC, a solar updraft tower plant that uses hot air extracted from the SAC to generate electricity by a wind turbine. The SAC utilizes heating technique based on the solar absorbing at the base then airflow heating through heat picks up from the absorber, **Mustafa, et al., 2015**.

Heat transfer and flow field in the solar collector were studied numerically by means of computational fluid dynamics, CFD, and investigated experimentally through a solar collector panel of 12.5 m² in area and 16 parallel horizontal fins. The solar collector panel was investigated in two methods; 1st with an absorber consisting of horizontally inclined strips by **Jianhua, et al., 2007**, and 2nd with an absorber consisting of horizontal fins by **Jianhua, et al., 2005**. Temperature measurements were utilized to validate the flow distribution through the absorber pipes. When high glycol flow rate is used, distribution flow via the fins absorber is uniform. Worst result of the flow distribution in the upper part of the collector panel was obtained when the collector tilt and inlet temperature increased, and the glycol flow rate decreased.

The performance of the unglazed transpired solar collector, UTC, was simulated numerically with computational fluid dynamics CFD tools. **Wang, et al., 2006**, compared numerically UTC with several kinds of traditional solar air collectors. Whilst **Li, et al., 2013**, simulated the convective heat transfer process for both flat and corrugated UTC. The results showed that the UTC have advantages in the ventilation and heating fields, a significant method in corrugated UTC was used by combination the effects of corrugation geometry and incident turbulence intensity. **Fasel**, **et al**., **2012,** and **Hermann**, **et al**., **2013**, employed computational fluid dynamics CFD for investigating the solar chimney power plant, SCPP. The geometric dimensions effect on thermo-fluid dynamics and the power output were investigated. As result to increasing the heat transfer coefficient, the collector efficiency was revealed to improve with increasing SCPP scale, i.e. the solar collector dimensions.

The airflow nature through the duct of a solar air heater with Reynolds number effects ranging from 3000 to 18000 on Nusselt number was investigated. CFD simulation was carried out for the investigation with absorber plate having; triangular rib roughness by **Yadav** and **Bhagoria 2013**, and for rectangular rib roughness by **Rajpoot**, **2013** and **Chaudhari, et al**., **2014** with double glass sheets. Simulation results revealed that the Nusselt number increases with the increase in Reynolds number, and the temperature increases at the duct outlet due to the rectangular shape of the duct. Numerical simulation for drying foods in the solar collector was carried out. **Ingle**, **et al**., **2013,** developed a collector for grape drying. The collector model involving air inlet, wavy structured absorber plate, glass cover plate, and pebble block. **Manilal**, **2016** utilized the solar collector for drying food and increment the efficiency. CFD tool has been used to simulate different types of collector plate having different configurations. The results showed that the temperature of collector outlet depends on the solar radiation, where it's directly proportional with irradiance.

An improvement of the solar collector efficiency was carried out by enhancement techniques. **Islamuddin**, **et al**., **2013**, improved the solar chimney power plants by numerical modeling using ANSYS-FLUENT. The collector enhancement uses thermal hybrid technique of hot exhaust gases combined with the solar radiation. The hybrid technique becomes active all the day, and enhances the power output by 38.8 % at 1000 W/m^2 solar irradiation. Another enhancement to the solar collector was carried out by longitudinal baffles above the absorber to extend the flow and reduce the dead zones to a minimum. **Amraoui**, and **Aliane 2014,** simulated the solar collector and study the heat transfer capability, which leads to increasing the efficiency with baffles technique. These baffles act as fins and improve the heat transfer within the solar collector.

Khilkhal, **et al**., **2014**, simulated the solar collector as a part of solar chimney power plant using finite volume technique by ANSYS-FLUENT. The results show that the velocity increases when the collector diameter increases and when the solar radiation is 300, 450, 600, 750 and 900 W/m^2. **Guo, et al**., **2014** predicted numerically that increasing the ambient temperature has evident effect on air velocity. **Mustafa**, **et al**., **2015,** presented mathematical and experimental study for the SAC. Modeling with conservation equations were carried out and model solution is obtained by utilizing a developed code in MATLAB. Experimental concentric circles was designed and fabricated to perform measurements for thermo-fluid process in the system. The canopy inclination of 8.5^o was performed in modeling. The results showed that at same solar irradiation, the temperatures of airflow are increasing by decreasing the radius toward the center, and airflow temperature decreases when the canopy slope increases. When the solar radiation increases, airflow temperature increases for the same collector radius. The model results agree with the experimental results. **Gholamalizadeh** and **Man-Hoe**, **2016** utilized CFD tools for the solar chimney power plant with an inclined collector roof. The effect of the collector configuration on the plant performance was performed. The results showed that when the collector inclination increases, the mass flow rate increases too.

In summary, the previous studies demonstrated numerical simulation by means of computational fluid dynamics CFD were carried out for the SAC. Moreover, mathematical and experimental modeling was employed. Some studies aim to predict the performance of the solar air duct and unglazed transpired solar collector UTC, or to improve the efficiency by enhancement techniques. Other studies analyzed thermo-fluid properties within the solar chimney power plants SCPP, and the configuration of SCPP with an inclined collector roof effects on the plant performance. The main validation to CFD simulations were made by comparing the obtained results with Manzanares prototype data. It is realized that there are gaps in the methods of investigation for thermo-fluid dynamics processes within 3D inclined collector roof of SCPP.

In this paper, numerical simulation has been utilized to investigate thermal-hydrodynamic behavior within the SAC in Baghdad. The simulation of the SAC was carried out for 3D construction with $k{-}\varepsilon$ viscous model and solar load model by using ANSYS-FLUENT 14.5. The purpose of this study is to predict and visualize heat transfer and flow field within an inclined SAC. The collector roof inclination is modified by increasing the outlet height. A significance of the present study could show through visualization the flow behavior within the SAC under the effect of changing angles of the collector inclination and the collector height. **Fig. 1** shows a sectional view in the SAC. The analysis of the solar chimney is not in the scope of this paper. Simulation model is validated by comparison with previous experimental data.

2. NUMERICAL SIMULATION

Numerical procedures solve the interacting governing equations in a coupled method by finite volume framework. The modeling is carried out in GAMBIT and subsequently the mesh is imported to ANSYS-FLUENT 14.5 for solving and post processing.

2.1 Modeling in GAMBIT

The modeling is carried out in GAMBIT; a quarter circular configuration of the SAC was built, as shown in **Fig. 2**. The SAC model has the collector ground and inclined roof (glass), which produced an outer peripheral collector inlet and a central collector outlet. Ambient air enters at outer peripheral and heated under a transparent roof by the solar radiation where warm air is drawn towards the collector center. The adopted dimensions of the SAC model are; the radius, r, of the collector ground is 5 m, and the radius of the collector outlet is 0.5 m where the rest radius for the roof is 4.5 m. The height, z, of collector roof at inlet, at point 1 shown in **Fig. 1**, is varied via 0.1 m and 0.25 m, as the cases described in **Table 1**.

The simulation cases studied in the present research are shown in **Table 1**. The cases can be described by the angle, ϕ, of the collector roof inclination for two inlet height, 0.1 m and 0.25 m. Angle inclination of the collector roof are 0°, 8.5°, and 20°. Further investigation for the simulation cases were done through different implementation of the solar radiation incident for the same roof inclination, 8.5°, and inlet height, 0.1 m. For this case, the solar radiation, I, utilized is: 500, 750, and 1000 W/m^2, as described in **Table 1**.

The geometry of SAC is meshed using tetrahedral/hybrid elements with T-Grid scheme type, as shown in **Fig. 3**, **Jianhua, et al., 2007**. The geometry meshed by spacing interval size of 0.0275, **Khilkhal, et al., 2014**, and number of generated elements for each case is shown in **Table 1**. Then, the mesh was written out in the format used by FLUENT for solving process. For a successful computational work, the boundary types of the SAC geometry were specified. The boundary types utilize for the SAC model are shown in **Table 2**. The solution is considered convergent if the scaled residual for the continuity and the momentum equations are less than 1.0×10^{-3}, k-epsilon and do-intensity equations are less than1.0×10^{-4}, and the energy equation is less than 1.0×10^{-6}. The iterations of convergent solutions for implemented cases are ranged between 1060 and 2900 during period extended to three hours.

2.2 Simulation with FLUENT

Numerical method employed for the SAC model consist of pressure – velocity coupling scheme used in solving the flow problem in a segregated manner, and advanced viscous RNG $k{-}\varepsilon$ model is considered with standard wall treatment of near wall functions. The RNG based $k{-}\varepsilon$ turbulence model is derived from the instantaneous Navier-Stokes equations, using a mathematical technique called “Re-Normalization Group” (RNG) methods. The RNG $k{-}\varepsilon$ model has a similar form to the standard $k{-}\varepsilon$ model shown in Eqs. (1) and (2) with features. These features make the RNG $k{-}\varepsilon$

model more accurate and reliable for a wider class of flows than the standard $k-\varepsilon$ model, **ANSYS-FLUENT, 2013**.

$$\frac{\partial}{\partial t}(\rho k) + \frac{\partial}{\partial x_i}(\rho k u_i) = \frac{\partial}{\partial x_j}\left(\zeta_k \mu_{eff} \frac{\partial k}{\partial x_j}\right) + G_k + G_b - \rho\varepsilon - Y_M + S_k \quad (1)$$

$$\frac{\partial}{\partial t}(\rho \varepsilon) + \frac{\partial}{\partial x_i}(\rho \varepsilon u_i) = \frac{\partial}{\partial x_j}\left(\zeta_\varepsilon \mu_{eff} \frac{\partial \varepsilon}{\partial x_j}\right) + C_{1\varepsilon}\frac{\varepsilon}{k}(G_k + C_{3\varepsilon}G_b) - C_{2\varepsilon}\rho\frac{\varepsilon^2}{k} - R_\varepsilon + S_\varepsilon \quad (2)$$

where u_i represents velocity component, G_k is the generation of turbulence kinetic energy due to the mean velocity gradients, G_b is the generation of turbulence kinetic energy due to buoyancy, and Y_M represents the contribution of the fluctuating dilatation in compressible turbulence to the overall dissipation rate.

The radiation model was selected with discrete ordinates, DO, for the position of 44.4 in longitude and 33.3 in latitude, which represent Baghdad city. Then the solar load was activated with DO Irradiation for the solar radiation calculations. The collector roof material for transmitted insolation is the glass, which its properties adapted from **Manilal, 2016**. The current study used different direct solar radiation (500, 750, and 1000 W/m^2). Therefore, the numerical simulation under transient state conditions was studied for one geometry volume. The input parameters used in the simulation cases are airflow temperature and velocity, the solar irradiance, inclination angle of the collector roof, and inlet collector height. Meanwhile, numerical simulation of the SAC was carried out successfully by comparing its results with experimental data that obtained by **Mustafa, et al., 2015,** at the same inlet collector height, inclination angle, and collector radius.

3. RESULTS AND DISCUSSIONS

Results of numerical simulation for the SAC were obtained, different simulation cases in Baghdad location were carried out. Thermal and flow field distribution within the SAC model will be presented in contours shape, and then discussed. Numerical results have been compared with previous experimental data.

3.1 Thermal Analysis

Thermal phenomenon occurs in the SAC based on irradiance absorbability of the collector ground, and then emitted to the fluid flow. Therefore, temperature of airflow increases with collector radius decreasing from the collector inlet towards the center. For simulation model with collector radius of 5 m, temperature distribution results of the ground are shown in **Fig. 4** for an inlet height of 0.1 m with different inclination angle. The simulation results show the ground temperature distribution increase with collector radius decreasing towards the center. Furthermore, the ground temperature distribution increases with inclination angle increase from 0° to 20° for the same solar radiation of 1000 W/m^2. Whilst, airflow temperature distribution decreases when inclination angle increases from 0° to 20° for the same solar radiation, as shown in **Fig. 5**. These results dates back to still air under the collector roof when inclination angle is 0°, then when inclination angle increases airflow movement also increases due to free convection. Results of **Fig. 5** are in agreement with obtained results by **Mustafa, et al., 2015**. Further detraction in airflow temperature is shown in **Fig. 6**. The figure shows distribution of airflow temperature decreases when inlet height increases from 0.1 m to 0.25 m with different inclination angle and same solar radiation.

3.2 Flow Analysis

The solar energy is converted to heat energy under a transparent roof of the SAC, where part of the heat energy converts to kinetic energy. Airflow moves towards the collector outlet due to the kinetic energy. Therefore, velocity of airflow increases with collector radius decreasing from the collector inlet towards the center. **Fig. 7** shows velocity distribution of airflow for the SAC model of 5 m in radius, solar radiation of 1000 W/m^2, inclination angle of 0°, and different inlet heights. The simulation results show the velocity distribution increases with collector radius decreasing towards the center, while slightly increases with clear contours arrangement when inlet height increases to 0.25 m. Other results reveal in **Fig. 8** for inclination angle of 8.5° with the same parameters used in simulation results shown in **Fig. 7**. The figure shows increase in airflow velocity towards the collector outlet in comparison with the results of 0° inclination angle. Airflow increment dates back to changing in the heat energy to the kinetic energy. Airflow increases until maximum radiation absorption at a tilt angle that correspond the collector location latitude. Airflow increases when inclination angle increase is in agreement with obtained results by **Gholamalizadeh** and **Man-Hoe, 2016**. Therefore, the power generation increases due to increasing warm airflow rate, as revealed by **Guo, et al**., **2014**.

The solar irradiance is one of the input parameters to the SAC simulation. Hence, when insolation increases through different simulation cases (500, 750, and 1000 W/m^2), temperature of warm air under transparent roof increase too. The temperature of warm air increases due to increasing of ground temperature. Moreover, flow rate of warm air increase when the solar radiation increases due to, slightly, increasing velocity of warm air.

3.3 Validation of Numerical Simulation

Numerical results have been validated by comparing outcomes with experimental data that obtained by **Mustafa, et al., 2015**. The comparison has been carried out at the experimental measurements conditions. Airflow temperatures of the SAC model have been compared numerically and experimentally, as shown in **Fig. 9**. The comparison included air temperature difference between outlet and inlet. The mean percentage of temperature difference in compared results is 5.7%.

4. CONCLUSIONS

Airflow within the SAC is simulated using ANSYS-FLUENT 14.5 with preprocessing using GAMBIT 2.4.6. The simulation was carried out for 3D, $k-\varepsilon$ viscous, and solar load models. Thermo–fluid dynamic analysis of the SAC was visualized through numerical simulation. Simulation results of case study are validated by comparison with the experimental data. The conclusions drawn from simulation results are:

1. The ground and airflow temperatures increase when collector radius decreasing towards the collector center. When inclination angle increases from 0° to 20° for the same solar radiation incidence, the ground temperatures increase while airflow temperatures decrease. Decreasing airflow temperatures dates back to changing in airflow movement. More

detraction in airflow temperatures has been occurred when inlet height increases from 0.1 m to 0.25 m for the same solar radiation incidence.
2. Air velocity increases with collector radius decreasing towards the collector center. Moreover, air velocity increases when inlet height increase from 0.1 m to 0.25 m and when inclination angle increase from 0° to 8.5° for the same solar radiation incidence. Flow increment dates back to changing the heat energy to kinetic energy.
3. Warm air temperatures and flow rate increase when the solar radiation increases for the same collector radius.
4. Increasing production of warm airflow from the SAC capable of spin the wind turbine and generates electricity.
5. The match between the simulation results is acceptable compared with the previous experimental results. The mean percentage of temperature difference in compered results is 5.7%.

REFERENCES

- Amraoui. M. A., Aliane. K., 2014, *Numerical analysis of a three dimensional fluid flow in a flat plate solar collector*, International Journal of Renewable and Sustainable Energy, 3(3): 68-75.

- ANSYS-FLUENT, 2013, *Theory Guide Release R14.5*, ANSYS, Inc.

- Chaudhari, Sohel, Mukesh Makwana, Rajesh Choksi, and Gaurav Patel, 2014, *CFD Analysis of Solar Air Heater*, International Journal of Engineering Research and Applications 4, no. 6: 47-50p.

- Fasel, Hermann F., Ehsan Shams, and Andreas Gross, 2012, *CFD analysis for solar chimney power plants*, 9th International Conference on Heat Transfer, Fluid Mechanics and Thermodynamics.

- Gholamalizadeh, Ehsan, and Man-Hoe Kim, 2016, *CFD (computational fluid dynamics) analysis of a solar-chimney power plant with inclined collector roof*, Energy 107: 661-667.

- Guo, Peng-hua, Jing-yin Li, and Yuan Wang, 2014, *Numerical simulations of solar chimney power plant with radiation model*, Renewable energy, 62: 24-30.

- Hermann F., Fanlong Meng, Ehsan Shams, and Andreas Gross, 2013, *CFD analysis for solar chimney power plants*, Solar Energy, 98: 12-22.

- Ingle, P. W., A. A. Pawar, B. D. Deshmukh, and K. C. Bhosale, 2013, *CFD analysis of solar flat plate collector*, International Journal of Emerging Technology and Advanced Engineering, 3, no. 4: 337-342.

- Islamuddin, Azeemuddin, Hussain H. Al-Kayiem, and Syed I. Gilani, 2013, *Simulation of solar chimney power plant with an external heat source*, IOP Conference Series: Earth and Environmental Science, Vol. 16. No. 1, IOP Publishing.

- Jianhua Fan, Louise Jivan Shah, and Simon Furbo, 2005, *Flow distribution in a solar collector panel with horizontal fins*, Proceedings of the 2005 Solar World Congress.
- Jianhua Fan, Louise Jivan Shah, and Simon Furbo, 2007, *Flow distribution in a solar collector panel with horizontally inclined absorber strips*, Solar Energy 81.12: 1501-1511.
- Khilkhal A. Husain, Shate W. M., and Jassim A. J., 2014, *Numerical Simulation of The Influence of Geometric Parameter on The Flow Behavior in a Solar Chimney Power Plant system*, Journal of Engineering, No. 8, Vol. 20.
- Li S., Karava P., Savory E. and Lin W. E., 2013, *CFD Simulations for Thermal and Airflow Analysis of Unglazed Transpired Solar Collectors*, 6th European and African Conference on Wind Engineering.
- Manilal, Kumavat Mukesh, 2016, *Design, CFD Analysis and Fabrication of Solar Flat Plate Collector*, International Research Journal of Engineering and Technology.
- Mustafa A. T., Al-Kayiem H. H. and Gilani I. U., 2015, *Investigation and Evaluation of the Solar Air Collector Model to Support the Solar Vortex Engine*, ARPN Journal of Engineering and Applied Sciences, Vol. 10, No. 12.
- Rajpoot, Surjeet Singh, and Dinesh Kumar Koli, 2013, *CFD analysis of solar air heater duct with rectangular rib surface*, International Journal of Engineering Trends and Technology, 1.4: 3006-3011.
- Wang, C., Guan, Z., Zhao, X. and Wang, D., 2006, *Numerical simulation study on transpired solar air collector*, Renewable Energy Resources and a Greener Future Vol.VIII-3-4, ICEBO.

- Yadav, Anil Singh, and J. L. Bhagoria, 2013, *A CFD analysis of a solar air heater having triangular rib roughness on the absorber plate*, International Journal of ChemTech Research, 5.2: 964-971.

NOMENCLATURE AND ABBREVIATIONS

Symbol	Description	Unit
I	solar radiation	W/m^2
r	radial coordinate directed	
u_i	velocity component	m/s
z	axial coordinate direction	
ρ	density	kg/m^3
θ	circumferential coordinate direction	
ϕ	inclination angle	degree
CFD	computational fluid dynamics	
DO	discrete ordinates	
RNG	renormalization group	
SAC	solar air collector	
SCPP	solar chimney power plant	
UTC	unglazed transpired solar collector	

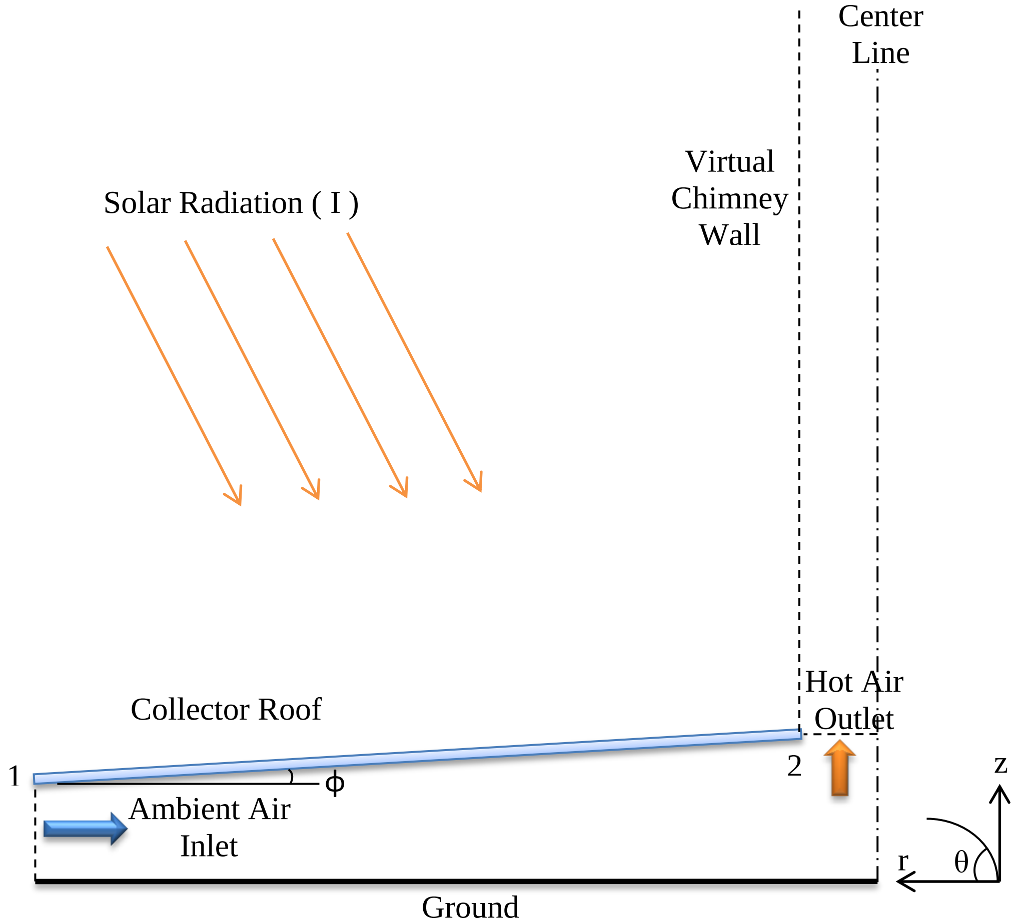

Figure 1. Sectional view in the SAC.

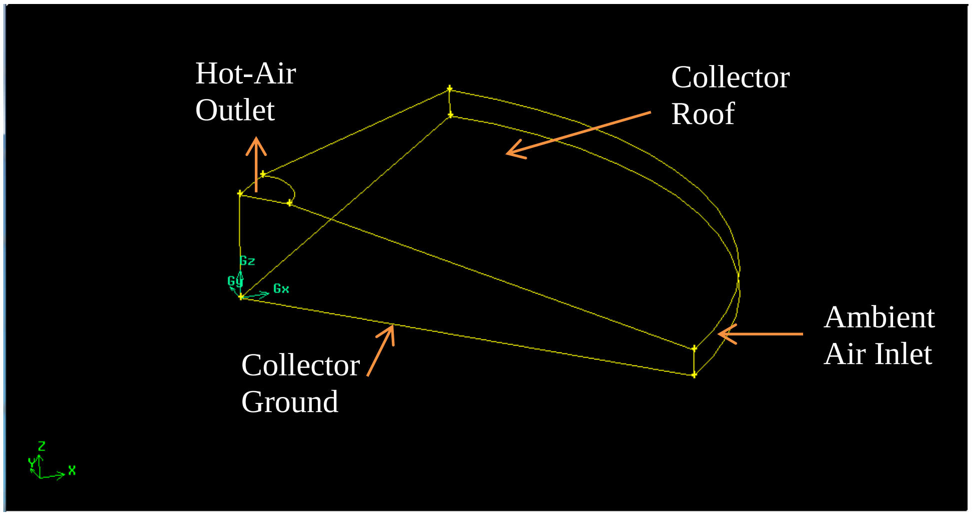

Figure 2. Configuration of the SAC model in GAMBIT.

Table 1. Case-Meshing properties of the SAC model.

Case No.	Collector Roof Angle, ϕ (degree)	No. of Mesh Elements	Solar Radiation Incidence (W/m^2)	Collector Inlet Height, z (m)
1	0°	611564	1000	0.1
2	8.5°	1465661	1000	
			750	
			500	
3	20°	2931385	1000	
1	0°	1528910	1000	0.25
2	8.5°	2383007		

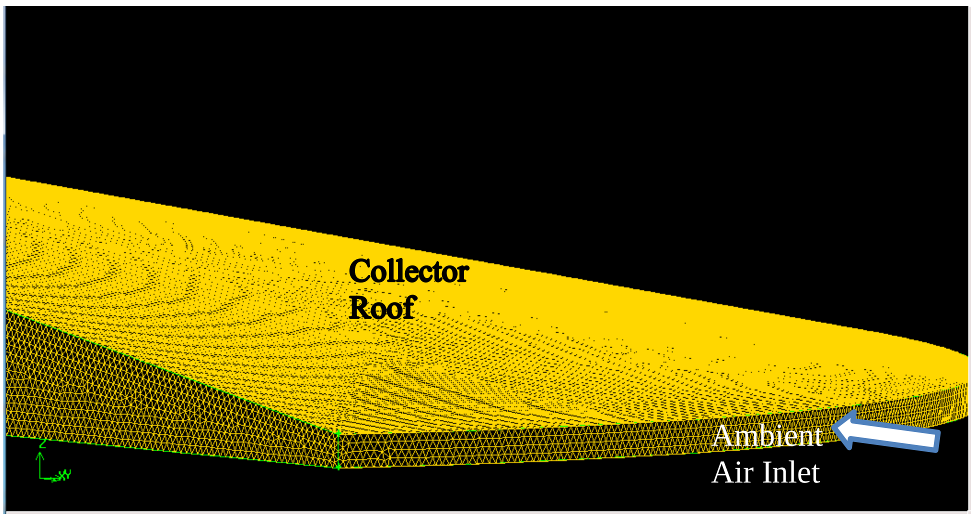

Figure 3. Tetrahedral mesh quality of the SAC model.

Table 2. Boundary types for the SAC model.

Boundary	Type	Boundary Properties
Ground (soil)	Stationary wall	Opaque
Roof (glass)	Stationary wall	Semi-transparent: Radiation-Discrete Ordinates (DO)
Collector inlet	Velocity-inlet	Constant air temperature and velocity
Collector outlet	Outflow	External black body temperature method: Boundary temperature
The collector sides	Stationary wall	Symmetry

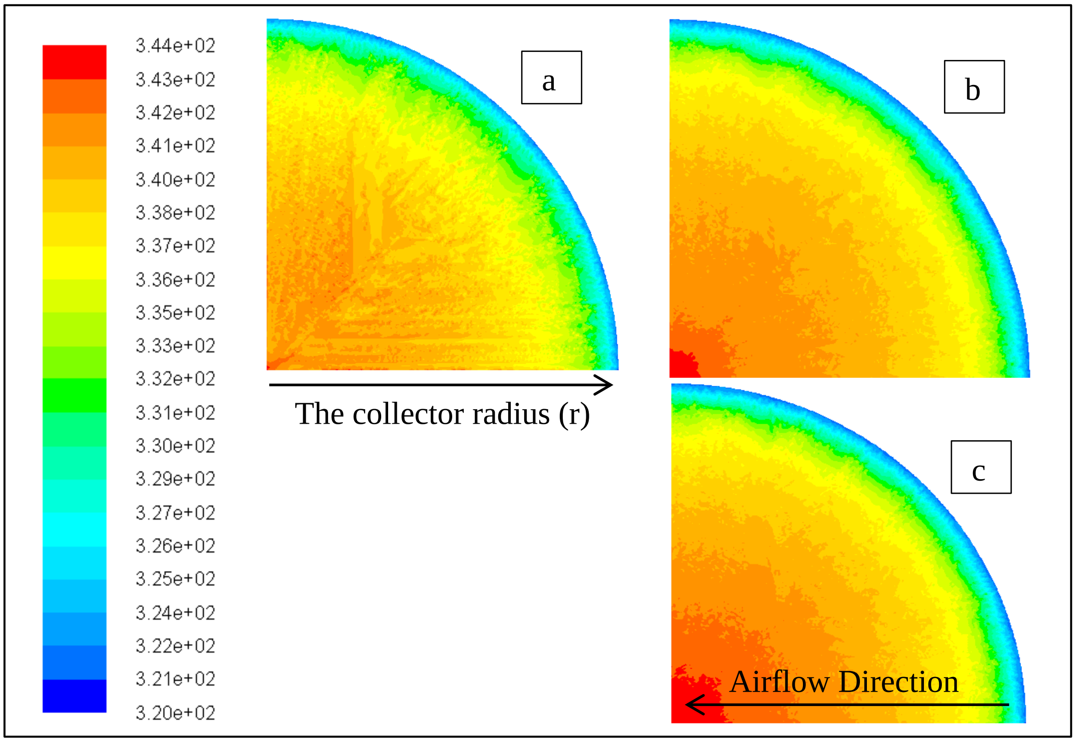

Figure 4. Temperature gradient of the SAC ground in (K) with inlet height of 0.1 m and inclination angle of (a) 0°, (b) 8.5°, and (c) 20°.

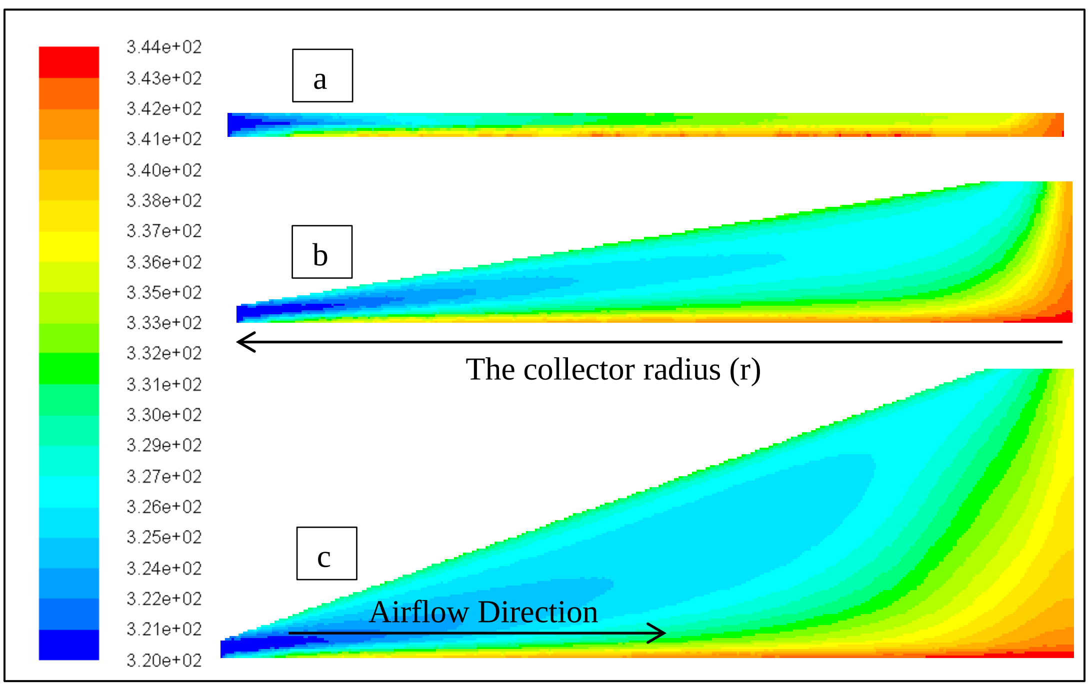

Figure 5. Sectional airflow temperature gradient in the SAC in (K) with inlet height of 0.1 m and inclination angle of (a) 0°, (b) 8.5°, and (c) 20°.

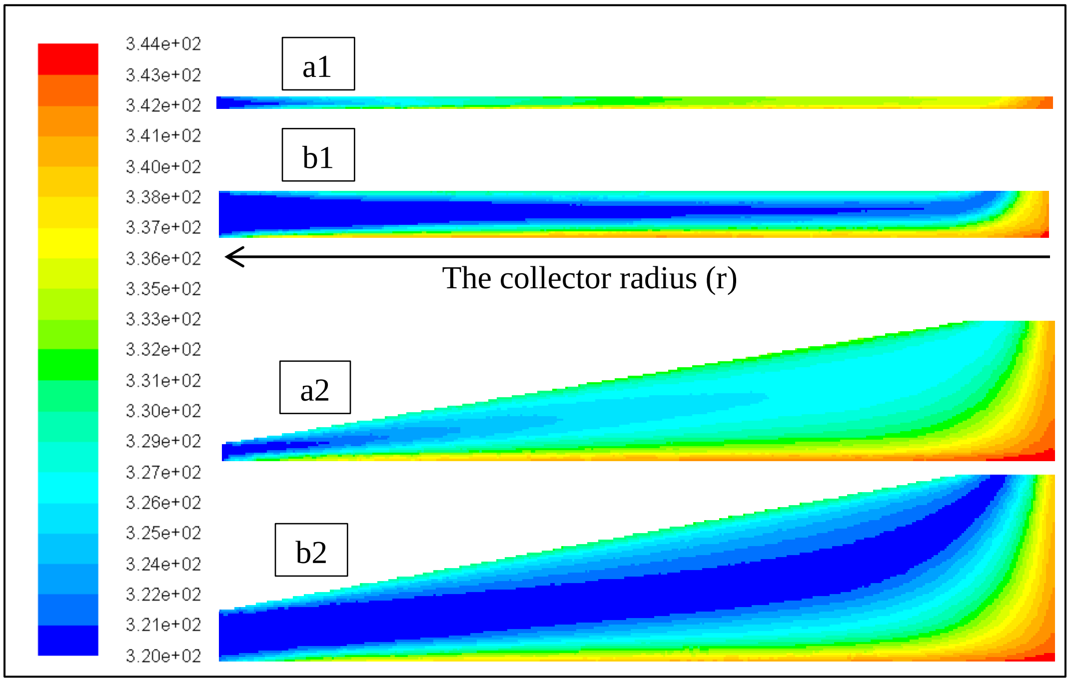

Figure 6. Sectional airflow temperature gradient in the SAC in (K) with inlet height of (a) 0.1 m and (b) 0.25 m, and inclination angle of (1) 0° and (2) 8.5°.

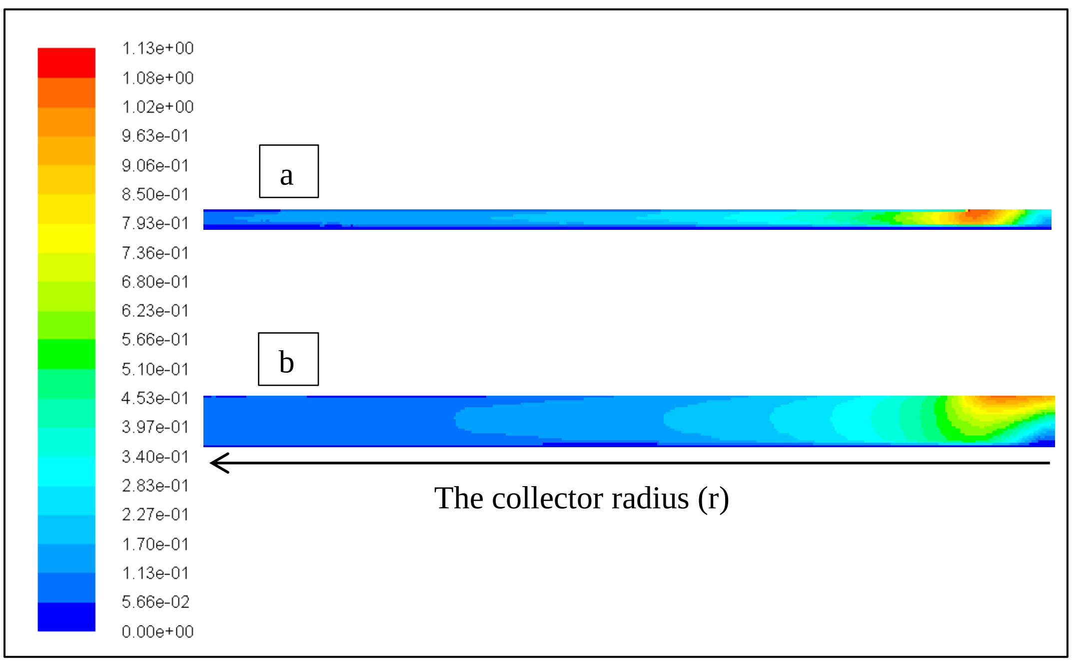

Figure 7. Sectional airflow velocity gradient in the SAC in (m/s) with inclination angle of 0°, and inlet height of (a) 0.1 m and (b) 0.25 m.

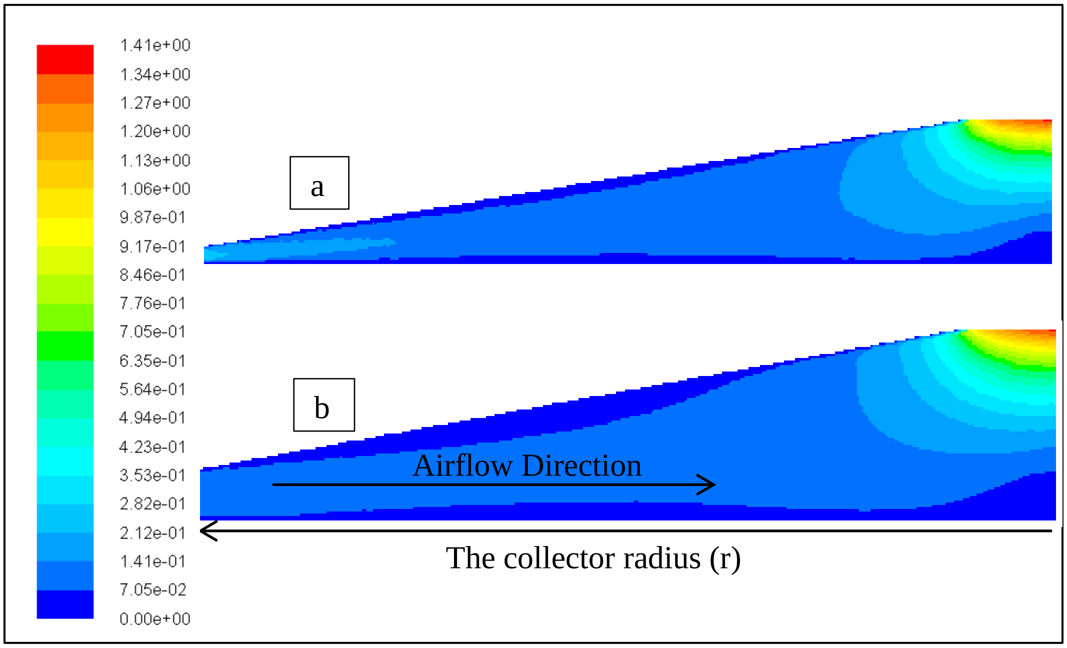

Figure 8. Sectional airflow velocity gradient in the SAC in (m/s) with inclination angle of 8.5°, and inlet height of (a) 0.1 m and (b) 0.25 m.

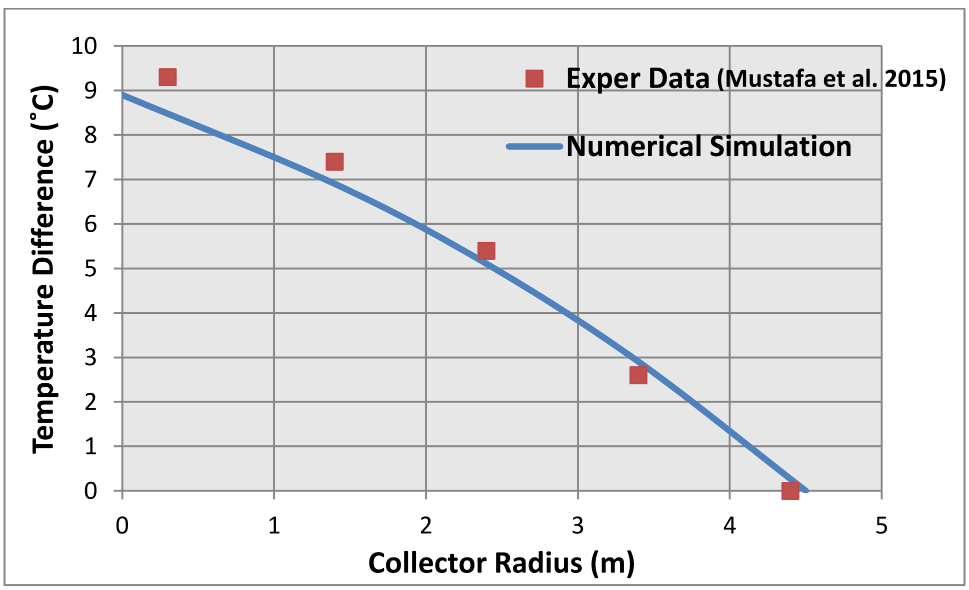

Figure 9. Validation of airflow temperature in the SAC model.

University of Baghdad
College of Engineering
JE
JOURNAL OF ENGINEERING

Journal of Engineering

journal homepage: www.jcoeng.edu.iq

Number 3 Volume 24 Month 3

Mechanical and Energy Engineering

Numerical Investigation of the Effect of Inserted Twisted Tape inside Submerged Bundle Tubes on its Thermal Performance

Dr. Kamal Mohammed Ali
Umarah Institute of Technology
Southern Technical University
al_ssafar2005@yahoo.com

Abdalrazzaq K. Abbas
Department of Mechanical Engineering
College of Engineering, University of Kerbala, Iraq
abd_abbas1967@yahoo.com

ABSTRUCT

Twisted tape insertion in smooth plain tube is one of types of passive methods that is used to enhance heat transfer. Swirl fluid flow inside tube and related heat transfer characteristics are very complex. ANSYS FLUENT (V 16.1) and ASPEN industrial program are used in analyzing this technique for enhancement heat transfer. A circular plain tube has length L=8534mm and 17 mm inner diameter with twisted tape has twist ratio of y = (H/D) = (150/17) =8.8 along with a plain tube were considered for this study. Eight Reynolds numbers (Re) of 784, 1000, 2000, 3000, 4000, 5000, 6000 and 7000 are used to analyze the response of thermal performance. Crude oil API 28 exit temperature, film heat transfer coefficient, Nusselt number and overall enhancement ratio results are presented for both empty and inserted plain tube with comparison between the two cases. An increase of 0.76 to 2.36 overall enhancement is predicted with twist ratio 8.8 for Reynolds number 784 to 7000 respectively.

Keywords: Heat transfer enhancement, friction factor, twist ratio, heat exchanger, twisted tape, laminar and turbulent flow.

التحقق عدديا لتأثيرات الشريط الملتوي المدخل داخل أنابيب الحزمة المغمورة على أدائها الحراري

د. كمال محمد علي
المعهد التقني / العمارة
الجامعة التقنية الجنوبية

عبد الرزاق خضير عباس
قسم الميكانيك - كلية الهندسة – جامعة كربلاء

الخلاصة

الشريط الملتوي المدخل داخل الانبوب ذو السطح العدل هو أحد الطرق الغير مستهلكة لطاقة خارجية المستخدمة لتحسين انتقال الحرارة. الجريان الحلزوني للمائع داخل الانبوب وخصائص انتقال الحرارة المصاحبة هي معقدة جدا. ANSYS FLUENT (V 16.1) والبرنامج الصناعيASPEN استخدمت لتحليل هذا الأسلوب في تحسين انتقال الحرارة. الانبوب الدائري ذو السطح العدل هو بطول 8534 ملمتر وقطر داخلي 17ملمتر ونسبة التواء (150/17) =8.8 على طول الانبوب اعتمد في هذه الدراسة. ثمان أرقام لرينولدز (784, 1000, 2000, 3000, 4000, 5000, 6000, 7000) استخدمت لفحص تاثر الاداء الحراري. درجة حرارة خروج النفط الخام API28 ومعامل انتقال الحرارة ورقم Nusselt والنسبة الكلية للتحسين قدمت لكل من الانبوب ذو السطح العدل الفارغ وللذي يحتوي على شريط الملتوي مع المقارنة بين الحالتين. أزدياد 0.67 الى 2.36 في التحسين الكلي قد وجد مع نسبة التواء 8.8 لارقام Reynolds 784 الى 7000 على التوالي.

مفتاح الكلمات: تحسين انتقال الحرارة ، عامل الاحتكاك، نسبة الالتواء ، مبادل حراري , الشريط الملتوي، جريان طباقي ومضطرب.

1. INTRODUCTION

Crude oil in order to be suitable for export, gases must be removed from it through special equipment and then need to be warming from 30ºC to 70ºC which is the suitable degree for desalter process which was done in special equipment. Heated process of crude oil was done in tube bundle submerged in a large shell, full of water at 95ºC to 98ºC, where the water in shell heated by burners operated at the fuel gases that was separated and removed from the crude oil previously. Hundreds of tubes were in tubes bundle. Therefore, it is economic to reduce number of tubes in the bundle with keeping the same amount of heat transfer to the crude oil inside tubes through the enhancement heat transfer process.

Several methods of heat transfer enhancement were used to increase heat transfer with keeping same performance of overall system. Passive and active methods were utilized as techniques of enhancing heat transfer. Passive methods don't need an external power antithesis to the active methods. Insertion of twisted tape is one of the most effective passive techniques as shown **Fig. 1.** Twisted tape produce swirl and turbulence, which are important to boost heat transfer. It increases the flow path length and so more residence time, thus the heat transfer is improved and greater frictional losses. So that, in this study, inserted twisted tape was used to enhance the heat transfer coefficient inside tubes that flow in it crude oil API 28.

Eiams-aard, et al., 2006, studied the heat transfer and friction factor characteristics in a double pipe heat exchanger where the inner pipe was inserted with equally spaced elements of twisted tape. The heat transfer coefficient was proportional directly with twist ratio, whereas the increase in the free space ratio, improves both the heat transfer coefficient and friction factor. **Woei Chang, et al., 2007,** studied experimentally the increase of heat transfer inside a tube inserted with serrated twisted tape for several twist ratios. The augmentation of heat transfer with inserted serrated twisted tape was 1.25–1.67 times than with the plain twisted tape. **Woei Chang, et al., 2007,** studied experimentally the heat transfer coefficients and axial pressure drop of the tube inserted with a broken twisted tape of twist ratio 1, 1.5, 2, 2.5 and 1 was performed in the Re range of 1000–40,000.. Mean Fanning friction factors and local Nusselt numbers were proportional inversely with the twist ratio. Thermal performance factors, mean Fanning friction factors and Heat transfer coefficients in the tube fitted with the broken twisted tape are, respectively, augmented to 0.99–1.8, 2–4.7, 1.28–2.4 times of those in the tube fitted with the smooth twisted tape. Empirical pressure drop and heat transfer correlations which evaluate the mean Fanning friction factor and local Nusselt number for the tube with the broken twisted tape insert were generated. **Bharadwaj, et al., 2009,** studied experimentally the pressure drop and heat transfer characteristics of water flow in smooth tube and spirally grooved tube inserted with twisted tape and compared between them. In the laminar flow, spirally grooved tube without twisted tape has more increase in heat transfer than with twisted tape insert. **Eiamsa-ard** and **Promvonge, 2010,** experimentally studied arrangement effect of alternate clockwise and counterclockwise rotation of twisted tape inserts inside circular tube on heat transfer enhancement. It was found that the heat transfer rate was more than one with typical twisted tape insert. **Naga Sarada, et al., 2010,** investigated experimentally heat transfer of turbulent flow in a horizontal tube with twisted tape of varying width. The enhancement of heat transfers with twisted tape inserts varied from 36% to 48% as compared to plain tube for full width inserts. **Thianpong, et al., 2011,** investigated experimentally the effects of plain and perforated twisted tape inside circular tube on heat transfer enhancement. It was found that tubes with perforated twisted tape and plain twisted tape yielded heat transfer enhancement up to 208% and 190% over plain tube, respectively. **Murugesan, et al., 2011,** investigated experimentally the effect of V-cut twisted tape inserted inside tube. Mean friction factor and mean Nusselt number increase with increasing depth ratios (depths of V cut / tape width) and decreasing of width ratios and twist ratios. **Bas** and **Ozceyhan, 2012,** investigated experimentally the effect of clearance ratio (clearance/ tube diameter) and twist ratio of twisted tape inserted inside tube on flow friction and heat transfer behavior. It was found that the heat transfer rate was proportional inversely with clearance ratio. **Gunes, et al., 2012,** investigated numerically pressure drop and heat transfer inside a tube fitted with equally spaced elements of twisted tape having different tape width. Within a range of Reynolds number, the effects of twisted tape width and space ratio on the heat transfer and friction characteristic was reported. **Giniyatullin**, **et al., 2014,** studied experimentally Nusselt number and friction factor data for laminar flow of viscous oil inside spiral corrugation tube and fitted with twisted tape with oblique teeth. The twisted tape with oblique teeth in spiral corrugation tube implemented better enhancement technique than the individual techniques. **Ramakumar, et al., 2016,** investigated numerically the performance of tapered twisted tape inserted inside a circular plain tube for three Reynolds numbers of 8545, 11393, and 13333 with taper angles of 0.3, 0.4, 0.5, 0.6, and 0.7 and a twist ratio of 3 via ANSYS FLUENT v14.0. Pressure drop and heat transfer data were presented in the form of friction factor, Nusselt number, and overall enhancement ratio. It was found an increase of 17% in overall enhancement with 0.5 taper angle over conventional tape. **Yang, et al., 2016**, presented a mathematical model for smooth (ST) and corrugated (CT) tubes inserted with twisted tape at twisted ratio 2.5. The heat transfer enhancements and friction loss behaviors was numerically investigated. RNG k-ε turbulence model was applied. Comparisons between CT and ST were done, where ($Nu_{corrugated}/Nu_{smooth}$) ratio was 1.36.

From above, a good number of researchers focused on heat transfer enhancement and fluid friction behaviors inside circular tube fitted with twisted tape. The centrifugal forces generated by twisted tape produce swirling fluid flow which that boosts the heat transfer rate with penalty on pressure loss. The present study aims to analyze numerically a propose twisted tape with twisted ratio 8.8 inside plain tube for different Reynolds number with operational performance comparison between tube inserted with twisted tape and empty plain tube. The difference between this work and other survived researches can be listed in these points:

- Simulate actual process case in the refinery plant (tube length, tube diameter, fluid flow-API 28, twisted ratio, range of Reynolds numbers, inlet pressure, inlet temperature and mass flow rate).
- Using Aspen industrial program to do the comparison with ANSYS fluent simulation for this case study, where Aspen is normally used by Americans oil refineries companies for designing refinery equipment, so that this comparison can indicate the close amount between CFD and Aspen industrial program which represent the reference for manufacturing companies.
- No work was found in the surveys doing the upper two points.

2. NUMERICAL METHOD AND PROBLEM FORMULATION

A three-dimensional steady state system of laminar and turbulent flow in a plain tube has length L=8534mm and 17 mm inner diameter equipped with a twisted tape has a twist ratio y = (H/D) = (150/17) =8.8 along the tube is considered in the present study. The physical model simulates the flow of crude oil API 28 in a heat exchanger tubes. Heat added to the outer tube walls via hot water where the heat transfers through the tube wall by conduction and to crude oil inside tube via convection.

2.1 Numerical Solution

In order to mathematically analyze the heat transfer characteristics of heat exchanger fluid flow in plain empty and inserted plain tube, a Navier-Stokes equation solution is required. Due to the complexity of twisted surface configuration and the significant viscous and heat effects, a numerical technique using the solver ANSYS-FLUENT version 16.1 which uses the finite-volume method to solve the governing equations through using a pressure-based solver. Two turbulence model, $v^2 - f$ and k-ε are used to solve governing partial differential equations of mass, momentum and energy conservations in three dimensions. A $v^2 - f$ turbulence model involves solution of the four transport equations; turbulence kinetic energy k, its rate of dissipation ϵ, velocity variance scale $\bar{v}^2$ and elliptic relaxation function f, to demonstrate the effect of the turbulence on the flow structure.

2.1.1 Mesh

Pointwise V17.0R1 is used to generate structured, unstructured and hybrid grids. Structured grid is used for tube surface while unstructured grid is used for flow cross section which result a hybrid mesh in the block that a mixture from hexahedron, pyramid and prism cells as, shown in **Fig. 2**. A fine mesh is created on the flow cross section to resolve the thermal boundary layer.

The solution to be accurate in this work, skewness kept up to 0.85 for hex, quad and triangular cells and up to 0.9 for tetragonal cells. For structured domains the orthogonality of grid points adjacent to the tube wall is kept to perfect orthogonality and max value 90° along the entire tube surface. For the present twisted model 5,769,257 cells are used while for empty tube model 4,941,189 cells uses. The rate of convergence is an indication to mesh quality. In this work the convergence is achieved with about 500 iterations.

2.1.2 Governing Equation and Assumptions

The numerical study of this work depends on the actual crude oil heat exchanger conditions that is specified and is used in crude oil transport plant. Crude oil conditions are represented by density 865 kg/m^3, specific heat 1982J/kg. K, thermal conductivity 0.129 W/m.K and viscosity 0.00752kg/m. s at Reynolds number 784. Other values of Reynolds number are studied to predict the effect of Re on the thermal performance. This research will focus on the effect of inserted twisted tape in plain tube on crude oil heat exchanger thermal performance for ranges of Reynolds number 784, 1000, 2000, 3000, 4000, 5000, 6000, and 7000 for crude oil API 28 flow.

The characteristic Reynolds number depends on tube hydraulic diameter which equal to inner tube diameter as a characteristic length and 5% turbulent intensity at free stream inlet velocity is used.

In the present study, crude oil API 28 is a fluid inside tube. The flow characteristics are assumed to be as follows:

1- Three-dimensional.
2- Incompressible flow, Ma<0.3.
3- Density ρ varies only with temperature.
4- Laminar and turbulent flow.
5- Steady state flow in main flow.
6- Newtonian fluid.
7- Single-phase flow.
8- Flows pressure work $\frac{P}{\rho}$, and kinetic energy $\frac{V^2}{2}$ terms in energy equation are negligible.

9- Viscous dissipation terms $(\bar{\bar{\tau}}_{eff}.\vec{V})$ are negligible.
10- Chemical reaction heat $S_h = 0$.
11- Fully developed flow.

The following governing equations were solved for laminar flow using ANSYS Fluent solver:
Mass conservation

$$\nabla.(\rho u) = 0 \qquad (1)$$

Momentum conservation
X-momentum equation

$$\rho\left(u\frac{\partial u}{\partial x} + v\frac{\partial u}{\partial y} + w\frac{\partial u}{\partial z}\right) = -\frac{\partial p}{\partial x} + \mu\left(\frac{\partial^2 u}{\partial x^2} + \frac{\partial^2 u}{\partial y^2} + \frac{\partial^2 u}{\partial z^2}\right) \qquad (2)$$

Y-momentum equation

$$\rho\left(u\frac{\partial v}{\partial x} + v\frac{\partial v}{\partial y} + w\frac{\partial v}{\partial z}\right) = -\frac{\partial p}{\partial x} + \mu\left(\frac{\partial^2 v}{\partial x^2} + \frac{\partial^2 v}{\partial y^2} + \frac{\partial^2 v}{\partial z^2}\right) \qquad (3)$$

Z-momentum equation

$$\rho\left(u\frac{\partial w}{\partial x} + v\frac{\partial w}{\partial y} + w\frac{\partial w}{\partial z}\right) = -\frac{\partial p}{\partial x} + \mu\left(\frac{\partial^2 w}{\partial x^2} + \frac{\partial^2 w}{\partial y^2} + \frac{\partial^2 w}{\partial z^2}\right) \qquad (4)$$

The following governing equations were solved for Turbulent flow using ANSYS Fluent solver:
In this work Reynolds averaged Navier-Stokes equations RANS are used.
In Cartesian tensor, they can be written as:

$$\frac{\partial \rho \bar{u}_i}{\partial x_i} = 0 \qquad (5)$$

$$\frac{\partial}{\partial x_j}\rho\bar{u}_i\bar{u}_j = -\frac{\partial \bar{P}}{\partial x_i} + \frac{\partial}{\partial x_j}\left[\mu\left(\frac{\partial \bar{u}_i}{\partial x_j} + \frac{\partial \bar{u}_j}{\partial x_i} - \frac{2}{3}\delta_{ij}\frac{\partial \bar{u}_i}{\partial x_i}\right)\right] + \frac{\partial}{\partial x_j}\left(-\rho\overline{\acute{u}_i\acute{u}_j}\right) \qquad (6)$$

where $\left(-\rho\overline{\acute{u}_i\acute{u}_j}\right)$ is a Reynolds stress tensor R_{ij} which represents the effects of turbulence. The form of energy equation that is solved in ANSYS FLUENT was:

$$\nabla.\vec{V}\rho E + P = \nabla.\left(k_{eff}\nabla T - \sum_j h_j\vec{J}_j\right) \qquad (7)$$

ANSYS theory guide, 2014.

2.1.3 $v^2 - f$ Turbulence Model

The flow inside tube is a boundary layer flow. The most suitable turbulent model for fluid flow inside empty plain tube considering the boundary layer is $v^2 - f$ model. The turbulence kinetic energy k, rate of dissipation ε, the velocity variance scale $\overline{\acute{v}^2}$, and the elliptic relaxation function f can be obtained from the following transport equations:

$$\frac{\partial}{\partial x_i}(\rho k\bar{u}_i) = P_k - \rho\varepsilon + \frac{\partial}{\partial x_j}\left[\left(\mu + \frac{\mu_t}{\sigma_k}\right)\frac{\partial k}{\partial x_j}\right] \qquad (8)$$

$$\frac{\partial}{\partial x_i}(\rho\varepsilon\bar{u}_i) = \frac{\acute{C}_{\varepsilon 1}P_k - C_{\varepsilon 2}\rho\epsilon}{T} + \frac{\partial}{\partial x_j}\left[\left(\mu + \frac{\mu_t}{\sigma_\varepsilon}\right)\frac{\partial \varepsilon}{\partial x_j}\right] \qquad (9)$$

$$\frac{\partial}{\partial x_i}\left(\rho\overline{\acute{v}^2}\bar{u}_i\right) = \rho k f - 6\rho\overline{\acute{v}^2}\frac{\varepsilon}{k} + \frac{\partial}{\partial x_j}\left[\left(\mu + \frac{\mu_t}{\sigma_k}\right)\frac{\partial\overline{\acute{v}^2}}{\partial x_j}\right] \tag{10}$$

$$f - L^2\frac{\partial^2 f}{\partial {x_j}^2} = (C_1 - 1)\frac{\frac{2}{3}-\frac{\overline{\acute{v}^2}}{k}}{T} + C_2\frac{P_k}{\rho k} + \frac{\frac{5\overline{\acute{v}^2}}{k}}{T} \tag{11}$$

The model constants have the following default values:
$\alpha = 0.6$, $C_1 = 1.4$, $C_2 = 0.3$, $C_{\varepsilon 1} = 1.4$, $C_{\varepsilon 2} = 1.9$, $(C_\eta = 70)$, $C_\mu = 0.22$, $C_L = 0.23$, $\sigma_k = 1$, $\sigma_L = 1.3$, $\acute{C}_{\varepsilon 1} = C_{\varepsilon 1}\left(1 + 0.045\sqrt{k/\overline{\acute{v}^2}}\right)$, **ANSYS Fluent $v^2 - f$ turbulence model manual, 2013.**

2.1.4 Transport Equations for the RNG k-ε Model

Mathematical technique called "renormalization group" (RNG) methods is used to model the RNG-based *k-ε* turbulence model that is derived from the instantaneous Navier-Stokes equations. RNG *k-ε* turbulence model with enhanced wall treatments is used to model the case study with effective accounts of viscosity for Low-Reynolds number. The effect of swirl on turbulence is included in the RNG model.

The *k* and *ε* equations are:

$$\frac{\partial}{\partial x_i}(\rho k u_i) = \frac{\partial}{\partial x_j}\left(\alpha_k\,\mu_{eff}\frac{\partial k}{\partial x_j}\right) + G_k + G_b - \rho\varepsilon - Y_M + S_K \tag{12}$$

$$\frac{\partial}{\partial x_i}(\rho\varepsilon u_i) = \frac{\partial}{\partial x_j}\left(\alpha_\varepsilon\mu_{eff}\frac{\partial\varepsilon}{\partial x_j}\right) + C_{1\varepsilon}\frac{\varepsilon}{k}(G_k + C_{3\varepsilon}G_b) - C_{2\varepsilon}\rho\frac{\varepsilon^2}{k} - R_\varepsilon + S_\varepsilon \tag{13}$$

The term G_k represents the generation of turbulence kinetic energy due to the mean velocity gradients. G_b is the generation of turbulence kinetic energy due to buoyancy. Y_M represents the contribution of the fluctuating dilatation in compressible turbulence to the overall dissipation rate. The quantities α_k and α_ε are the inverse effective Prandtl numbers for k and ε, respectively. S_k and S_ε are user-defined source terms. Hence, for the present study, the turbulent flow is modeled using the k-ε viscous turbulence model with turbulent coefficients $C\mu$=0.0845, $C_1\varepsilon$ =1.42, $C_2\varepsilon$=1.68, S_k =Sε =0, $\alpha_k = \alpha_\varepsilon$ =1.393. Semi implicit pressure linked equation method (SIMPLE) is used for pressure velocity coupling.

The second-order upwind discretization scheme is used for turbulence kinetic energy and dissipation. The second-order discretization scheme is used for momentum and energy equations. The convergence criterion of 10^{-6} is chosen in addition to the selected monitored properties.

2.2 Boundary Conditions and Assumptions

Boundary conditions are specified for each zone of the computation domain. For the steady state, there are three boundary conditions in the physical flow domain, inlet, outlet and solid surfaces wall as shown in figure 2. However, the internal domain zone that shares common areas faces does not require any boundary condition.
The boundary conditions that are used in this work are as follow:

- Inlet temperature $T_\infty = 313$k.

- Inlet and outlet turbulent intensity $T_u = 5\%$.
- Hydraulic diameter D_h =17mm.
- Inlet pressure gage=0.
- No-slip and constant tube wall temperature at 370K.
- No-slip and zero heat flux at the wall of twisted tape.
- Zero-gradient boundary condition for the variable f (elliptic relaxation function) at inlets with default value $= 1$
- The direction of the flow was defined to be normal to the inlet boundary.
- k, ε , $\overline{v'^2}$ and ℓ at inlet boundaries were compute its initial values from:

  $k = 1.5(T_u U_\infty)^2$; $\varepsilon = 0.09^{0.75}\frac{k^{3/2}}{\ell}$; $\overline{v'^2} = \frac{2}{3}k$; $\ell = 0.07(D_h)$,

  ANSYS Fluent $v^2 - f$ turbulence model manual, 2013.

And the assumptions are:

- The wall of the tube was assumed to be perfectly smooth with zero roughness.
- Heat conduction in the twisted tape is neglected.

2.3 Data Reduction

From the simulation, the heat transfer rate of the entire tube wall (Q) is obtained for constant temperature boundary condition. Wall heat flux, Nusselt number, friction factor, and overall enhancement ratio are calculated by the equations

$$q = \frac{Q}{A} \tag{14}$$

where the surface area A is given by

$$A = \pi DL \tag{15}$$

The convective heat transfer coefficient is calculated from

$$h = \frac{q}{(T_s - T_{avg})} \tag{16}$$

where T_s was pipe wall temperature and T_b is bulk temperature calculated from

$$T_{avg} = \frac{(T_i + T_o)}{2} \tag{17}$$

The Nusselt number is calculated from

$$N_u = \frac{hD}{k} \tag{18}$$

The friction factor is determined from the pressure drop across the pipe

$$4f = \frac{\Delta P}{\left\{\left(\frac{L}{D}\right)\left(\frac{\rho U^2}{2}\right)\right\}} \tag{19}$$

The overall enhancement ratio is calculated from

$$\eta = \frac{\left(\frac{Nu}{Nu_P}\right)}{\left(\frac{f}{f_p}\right)^{1/3}} \tag{20}$$

3. RESULTS AND DISCUSSION

The use of twisted tape inside tube leads to increase in pressure drop and heat transfer over plain tube. From simulation results, the preferable operating system of twisted tape element is found at low Reynolds number where that leads to more compact heat exchanger. The laminar model is considered for Reynolds number up to 2000 while $v^2 - f$ and k-ε turbulence models are used to solve the governing equations for Reynolds number above 2000. The converge simulation values of flow inside plain tube inserted with twisted tape for flow above Reynolds number 2000 is obtained with the k-ε turbulence model, while the converge simulation values of flow inside plain empty tube is found with $v^2 - f$ turbulence model. Thus, all values above Reynolds 2000 in figures of this work is obtained from using $v^2 - f$ turbulence model for flow in empty plain tube and k-ε for flow in plain tube inserted with twisted tape.

Figure 3 clarifies bulk exit temperature of crude oil API 28 from empty plain tube and plain tube with inserted twisted tape. For plain empty tube, it is clear that the results of bulk exit temperatures that are calculated from ANSYS- Fluent and Aspen industrial program are very close, where for laminar flow only 0.3% to 0.8% temperature difference for Reynolds number up to 3000 respectively while for turbulent flow the temperature difference was 0.9% to 1.8% for Reynolds number 4000 to 7000 respectively. The reason of this close in laminar flow was related to the coincidence between Aspen analytical and CFD solutions. These small differences between Aspen analytical and CFD solutions related to CFD model mesh cells numbers. While the close in turbulent flow related to the good agreement between Aspen correlations and $v^2 - f$ CFD method which is the accurate turbulent model to solve turbulent flow near the wall that is generated from increasing flow Reynolds number in plain empty tube, (not from turbulators).

For plain tube inserted with twisted tape, the percentage difference in bulk exit temperature that is calculated from ANSYS-Fluent and Aspen industrial program are 3.7% to 0.29% for Reynolds number 784 to 2000 respectively, while the difference is less than 1% when using k-ε turbulence model, and 0% to 3.6% when using $v^2 - f$ turbulence model for Re ≥ 3000. In the actual process, the Aspen industrial program is very close to actual plant data and it is widely used by American manufacturing companies that are specialize in manufacturing processes equipment. Since the results from k-ε turbulence model are very close to Aspen industrial program than $v^2 - f$ turbulence model for flow inside empty tube inserted with twisted tape, thus, k-ε turbulence model is more accurate than $v^2 - f$ model for simulated swirling flow inside tube, and the reason of that is related to that the k-ε model equation contains swirling flow parameter, while $v^2 - f$ turbulence model is accurate for flow inside empty plain tube (flow without swirling) rather than k-ε model which the solve diverging in it.

It is clear from **Fig. 4** that the static pressure difference between inlet and outlet boundary for plain tube inserted with twisted tape is higher than static pressure difference for empty plain tube due to the increase in surface frication area that is generated from twisted tape walls and the increase in length flow bath and this difference increase with increasing of flow Reynolds numbers. As shown in **Fig. 5** the percentage increase of static pressure difference(%ΔP) between inlet and outlet tube boundaries are 141%, 137%, 329%, 197%, 176%, 171%, 160% and 146% above that for empty plain tube for Reynolds numbers 784, 1000, 2000, 3000, 4000, 5000, 6000 and 7000 respectively. It is clear that the higher static pressure difference percentage increase is happened at Re=2000 because the changing the behavior of flow from laminar to turbulent, so it's favorite to a void flow at Re=2000. The friction factor at inner surface tube wall for plain tube inserted with twisted tape is higher than of empty plain tube as shown in **Fig. 6**, which has the same percentage increases of **Fig. 5** due to the relation between them related to equation 19.

As shown in **Fig. 7,** the average Nusselt number of flow inside empty plain tube is increased slowly in laminar flow Re $\leq$ 2000 and then jumping in average Nusselt number is happened as Reynolds number are increased above 2000 with slowly increasing with Reynolds number increasing. The reason of this jumping is related to the converted of flow from laminar to turbulent, while the behavior of average Nusselt number of flow inside tube inserted with twisted tube is increasing continuously in straightway for Reynolds up to 7000. For laminar flow, the twisted tape is generated swirling to the flow which leads that most of laminar flow path lines is passed through the film heat transfer zone, while for turbulent flow it makes good turbulent and mixing to the flow in a way that most flow particles have an ability to contact the tube wall or flowing near it continuously, where, as Reynolds number increases, the flow swirling increases, and circulation of fluid happens from inner tube surface to center of tube which causes increasing in heat transfer rate. The percentage increase in average Nusselt number for flow in plain tube inserted with twisted tape is proportional inversely to the inlet flow Reynolds number up to 3000 (302% at Re= 784 to 41% at Re=3000) and proportional directly to the inlet flow Reynolds number above 3000 (41% at Re= 3000 to 132% at Re=7000), as shown in **Fig 8.** Therefore the overall enhancement ratio is decreased from 3% to 0.98% for Re 784 to 3000 respectively and then going in increasing to 1.72% for Re=7000 as clear in **Fig 9**.

Comparison of the average Nusselt number computed from this work and **Yang, et al. 2016,** is done for Reynolds number 3000 to 7000. The reason of choosing **Yang, et al., 2016**, work to make comparison with it is because of the same Reynolds number range and twisted tape configuration. As shown in **Fig. 10,** the behavior of the average Nusselt number increase with the Reynolds number is the same for the two works where the Nusselt number curve of this work is above the curve of, **Yang, et al., 2016**, in percentage of 216% to 297% for Reynolds number 3000 to 7000 respectively as shown in **Fig. 11**. The reason of this difference was related to different twisted ratio (y = 2.5 for **Yang, et al.**, **2016** and y = 8.8 for this work) and type of fluid. Also comparison of average 4f computed from this work and **Yang, et al., 2016,** is done as shown in **Fig. 12,** where the percentage difference of 4f are from 31% to 21% for Re= 3000 to 7000 respectively.

4. CONCLUSIONS

The conclusions that are predicted from studying the effect of twisted tape inserted inside plain tube where the tube wall is kept at constant temperature 370K and fluid inside it is crude oil API 28 which enters at 313K are:

1- Significant effect of twisted tape insert inside plain tube, on the heat transfer enhancement from tube surface, is at low flow Reynolds number.
2- The overall enhancement ratio proportional inversely with flow Reynolds number up to 3000 and then proportional directly above Reynolds number 3000.
3- $v^2 - f$ turbulence model is accurate and suitable model for simulation turbulent flow inside circular empty plain tube.
4- k-ε turbulence model is more accurate than $v^2 - f$ model for simulated swirling flow inside tube, and the reason of that related to that the k-ε model equation contain swirling flow parameter.

5- The static pressure difference between inlet and outlet boundary for plain tube inserted with twisted tape are higher than static pressure difference for empty plain tube.
6- The behavior of average Nusselt number of flow inside tube inserted with twisted tube is increasing continuously in straightway as Reynolds number increase.
7- Avoiding flow Reynolds number 2000 inside plain empty tube because it is leading to low heat transfer performance.

REFERENCES

- ANSYS Fluent 12.1, 2012, "Using flow boundary conditions.
- ANSYS Fluent, 2013, " $v^2 - f$ Turbulence model manual".
- ANSYS Fluent, 2014, "Theory guide".
- Bas, H., and Ozceyhan, V., 2012, "Heat Transfer Enhancement in a Tube With Twisted Tape Inserts Placed Separately From the Tube Wall," Exp. Therm. Fluid Sci., 41, pp. 51–58.
- Bharadwaj, P., Khondge, A. D., and Date, A. W., 2009, "Heat Transfer and Pressure Drop in a Spirally Grooved Tube with Twisted Tape Insert," Int. J. Heat Mass Transfer, 52(7–8), pp. 1938–1944.
- Eiamsa-ard, S., and Promvonge, P., 2010, "Performance Assessment in a Heat Exchanger Tube with Alternate Clockwise and Counter-Clockwise Twisted- Tape Inserts," Int. J. Heat Mass Transfer, 53(7–8), pp. 1364–1372.
- Eiamsa-ard, S., Thianpong, C., and Promvonge, P., 2006, "Experimental Inves- tigation of Heat Transfer and Flow Friction in a Circular Tube Fitted with Regularly Spaced Twisted Tape Elements," Int. Commun. Heat Mass Transfer, 33(10), pp. 1225–1233.
- Giniyatullin, A., and Tarasevich, S., 2013, "CFD Modelling of Subcooled Boil- ing in Tubes with Twisted Tape Insert," ASME Paper No. FEDSM2013- 16298. Lin, Z.-M., and Wang, L.-B., 2009, "Convective Heat Transfer Enhancement in a Circular Tube Using Twisted Tape," ASME J. Heat Transfer, 131(8), p. 081901.
- Gunes, S., Erdemir, D., Ozceyhan, V., and Altuntop, N., 2012, "Numerical Investigation of Thermal Performance of a Tube Fitted With Regularly Spaced Twisted Tape Elements," ASME Paper No. HT2012-58078.
- Kumar Saha, S., and Kumar Pai, P., 2014, "Experimental Investigation of Laminar Flow of Viscous Oil Through a Circular Tube Having Integral Spiral Corrugation Roughness and Fitted With Twisted Tapes With Oblique Teeth," Exp. Therm. Fluid Sci., 57, pp. 301–309.
- Murugesan, P., Mayilsamy, K., Suresh, S., and Srinivasan, P. S. S., 2011, "Heat Transfer and Pressure Drop Characteristics in a Circular Tube Fitted With and Without V-Cut Twisted Tape Insert," Int. Commun. Heat Mass Transfer, 38(3), pp. 329–334.
- Naga Sarada, S., Sita Rama Raju, A. V., Kalyani Radha, K., and Shyam Sunder, L., 2010, "Enhancement of Heat Transfer Using Varying Width Twisted Tape Inserts," Int. J. Eng. Sci. Technol., 2(6), pp. 107–118.
- Ramakumar B. V. N., Arsha J. D., Tayal P., 2016, "Tapered Twisted Tape Inserts for Enhanced Heat Transfer" Journal of Heat Transfer, Vol. 138.
- Thianpong, C., Eiamsa-ard, P., Promvonge, P., and Eiamsa-ard, S., 2011, "Effect of Perforated Twisted-Tapes with Parallel Wings on Heat Transfer Enhancement in a Heat Exchanger Tube," Energy Procedia, 14, pp. 1117–1123.

- Woei Chang, S., Jena Jan, Y., and Shuen Liou, J., 2007, "Turbulent Heat Trans- fer and Pressure Drop in Tube Fitted with Serrated Twisted Tape," Int. J. Therm. Sci., 46(5), pp. 506–518.
- Woei Chang, S., Lirng Yang, T., and Shuen Liou, J., 2007, "Heat Transfer and Pressure Drop in Tube with Broken Twisted Tape Insert," Exp. Therm. Fluid Sci., 32(2), pp. 489–501.
- Yang, L., Han, H., Li, Y. and Li, X., 2016, "A Numerical Study of the Flow and Heat Transfer Characteristics of Outward Convex Corrugated Tubes with Twisted-Tape Insert," Journal of Heat Transfer, Vol. 138.

NOMENCLATURE

A= convection heat transfer area (m^2)

C_1, C_2, C_μ , α , $C_{\varepsilon1}$, $C_{\varepsilon2}$, C_L, σ_k, σ_L, $C_1\varepsilon$, $C_2\varepsilon$ = constants of turbulence model

D= inner diameter of test section (m)

D_h= hydraulic diameter (m)

f = elliptic relaxation function

f= friction factor obtained using tape inserts

f_p= friction factor for plain tube

h= convection heat transfer coefficient ($W/m^2.K$)

I= turbulence intensity

k= turbulent kinetic energy (J/kg)

K= thermal conductivity (W/m.K)

L= length of test section (m)

p= static pressure (Pa)

P= pitch (m)

q= heat flux (W/m^2)

Q= total heat transfer (W)

T= temperature (K)

T_b= bulk temperature (K)

T_i= inlet temperature (K)

T_o= outlet temperature (K)

T_s= average surface temperature tube wall (K)

U= fluid velocity through test section (m/s)

u= velocity vector (m/s)

u, v, w= mean velocity components (m/s)

x= distance along tube (m)

x_i, x_j, x_k= cartesian coordinates (m)

Δp= pressure drop across the test section (Pa)

Greek symbols

ε = dissipation rate of k (W/kg)

η= overall enhancement ration

μ= viscosity (Pa.s)

ρ= density (kg/m³)

Non-dimensional Groups

Nu, Nu_p= Nusselt number with tape inserts and for plain tube

Re= Reynolds number

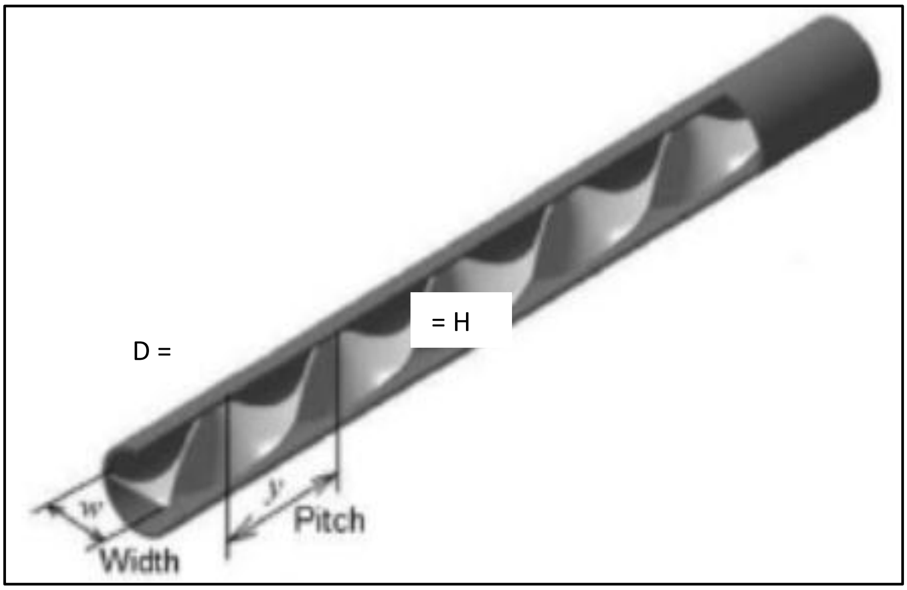

Figure 1. 3D view of tube inserted with twisted tape.

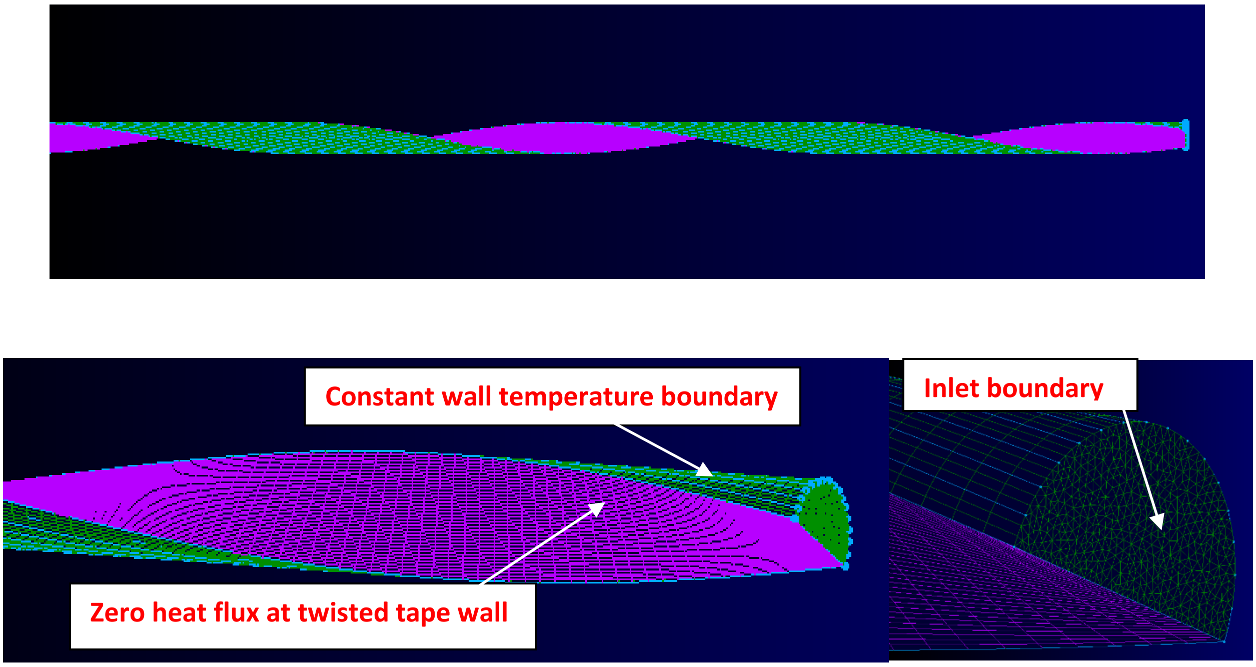

Figure 2. (a) Hybrid mesh of plain tube inserted with twisted tape.

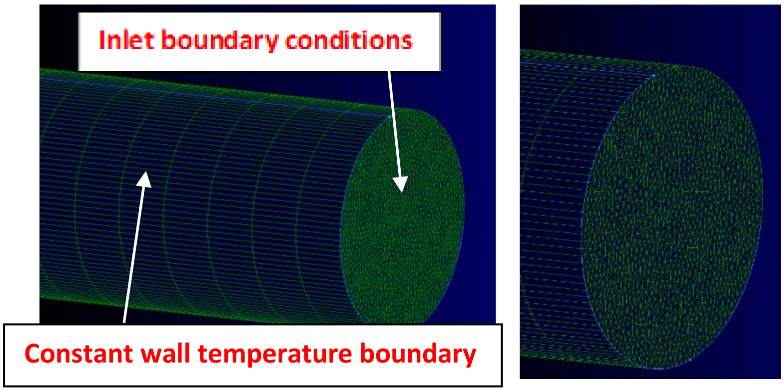

Figure 2. (b) Hybrid mesh of plain empty tube.

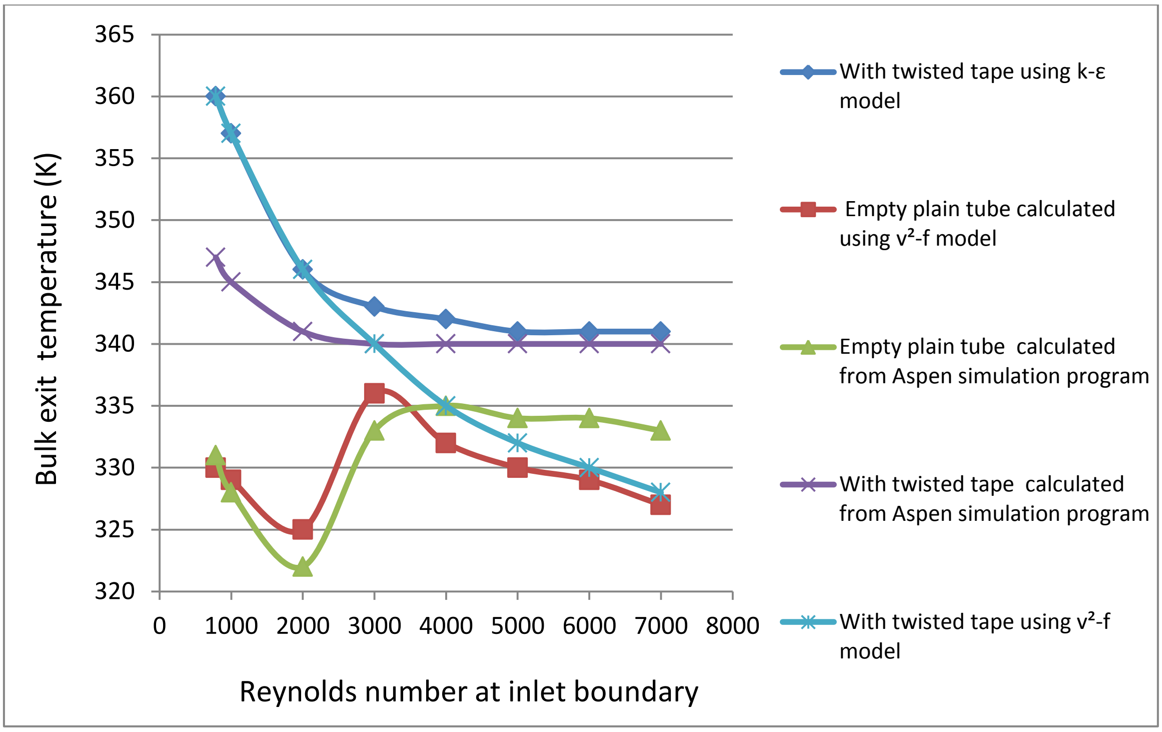

Figure 3. Bulk exit temperature of crude oil API 28 from empty plain tube and plain tube with inserted with twisted tape.

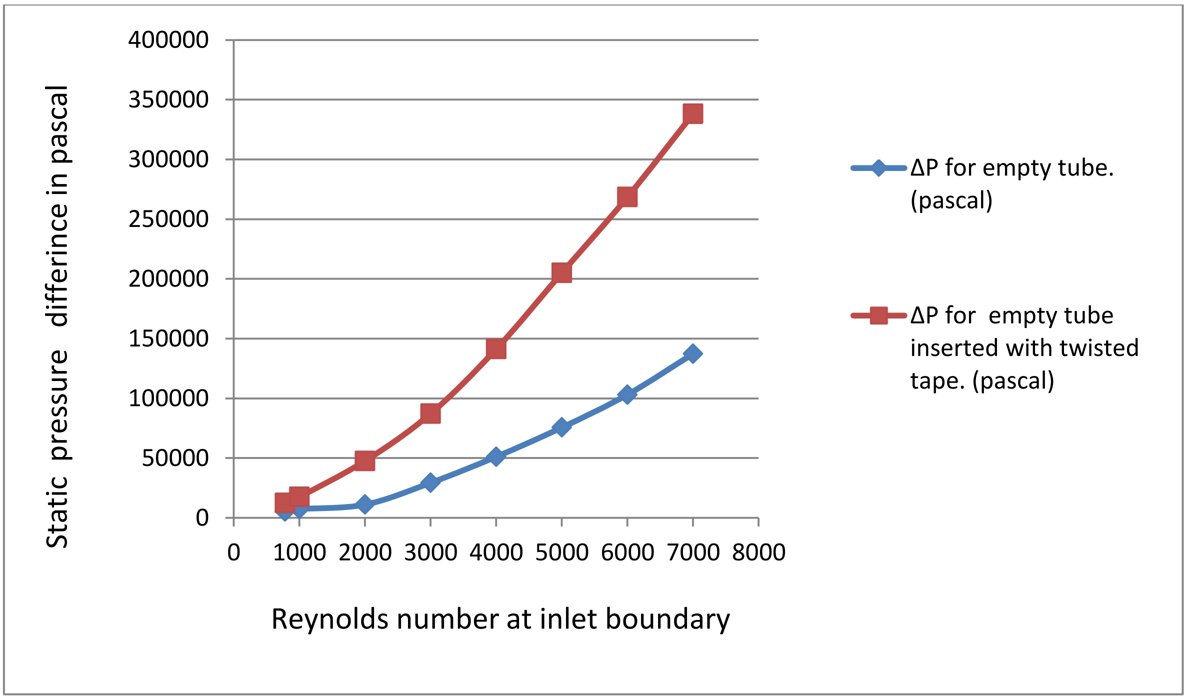

Figure 4. Variation of static pressure difference with inlet Reynolds numbers for empty plain tube and plain tube inserted with twisted tape by using ANSYS Fluent.

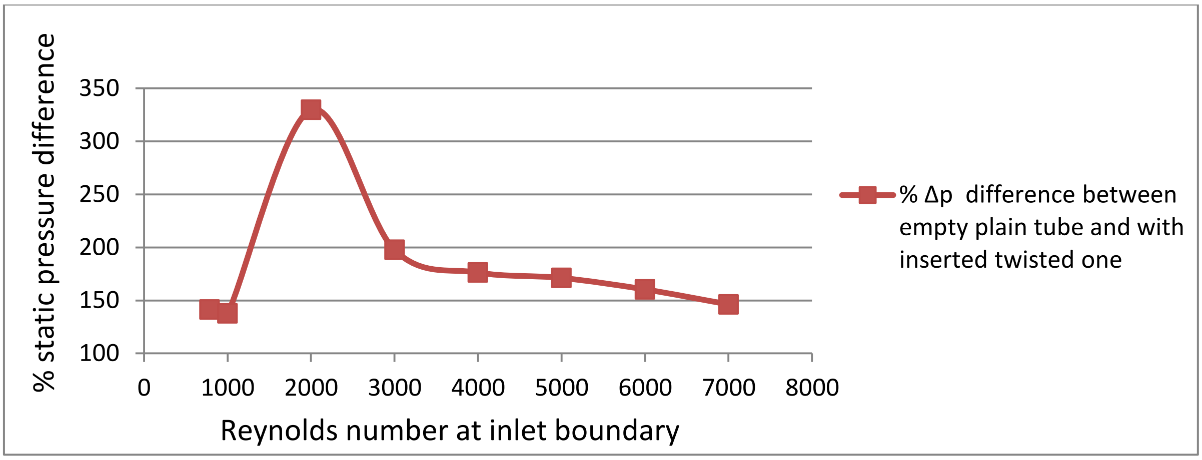

Figure 5. Variation of percentage static pressure difference increase with inlet Reynolds numbers for plain tube inserted with twisted tape over empty plain tube.

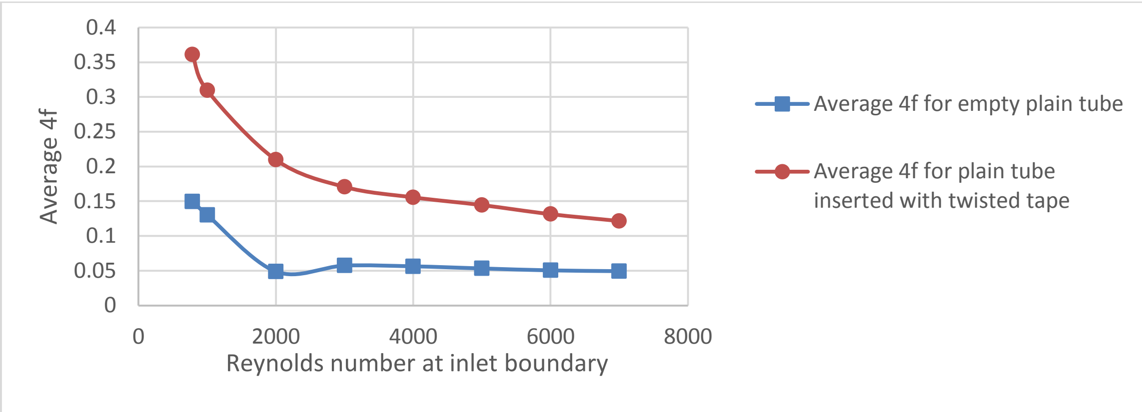

Figure 6. Variation of average tube surface friction factor with inlet Reynolds numbers for empty plain tube and plain tube inserted with twisted tape.

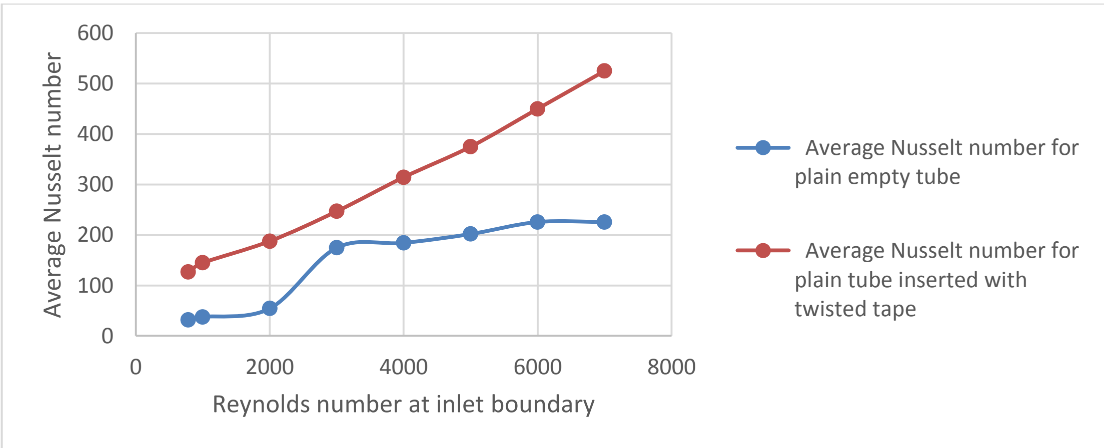

Figure 7. Variation of average tube surface Nusselt number with inlet Reynolds numbers for empty plain tube and plain tube inserted with twisted tape.

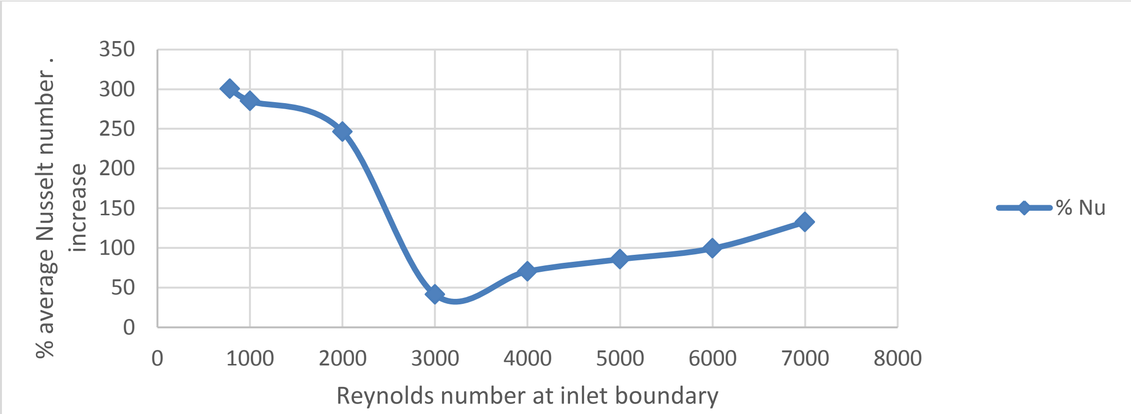

Figure 8. Variation of percentage increase of average Nusselt number with inlet Reynolds numbers for plain tube inserted with twisted tape over empty plain tube.

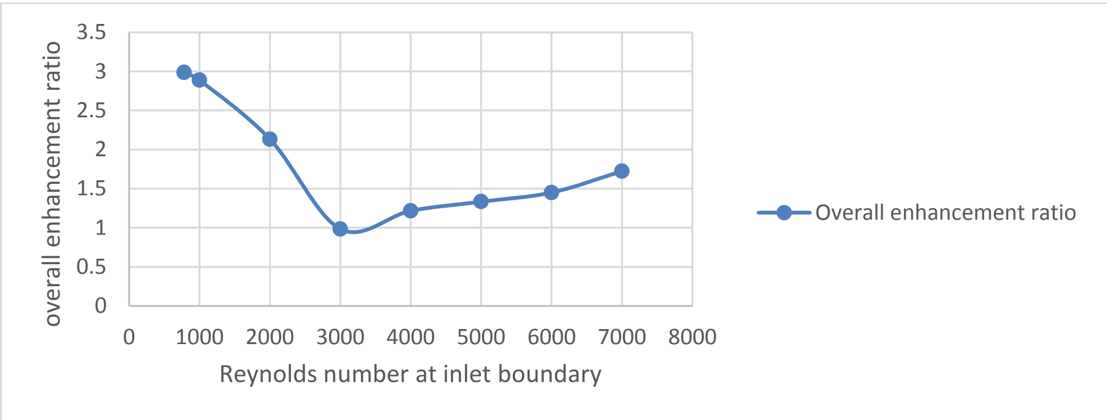

Figure 9. Variation of overall enhancement ratio with inlet Reynolds numbers for empty plain tube and plain tube inserted with twisted tape.

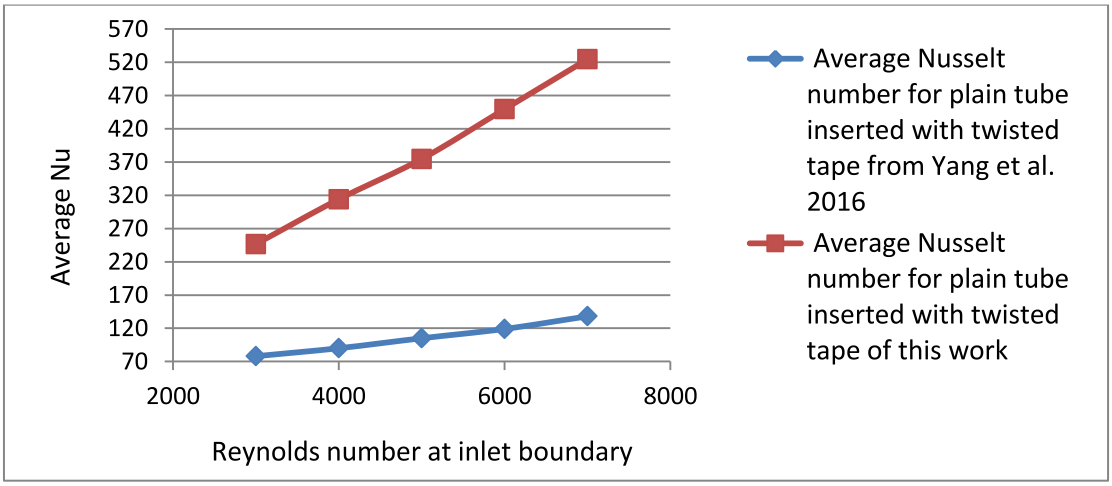

Figure 10. Comparison of average Nusselt number computed from this work and Yang et al. 2016.

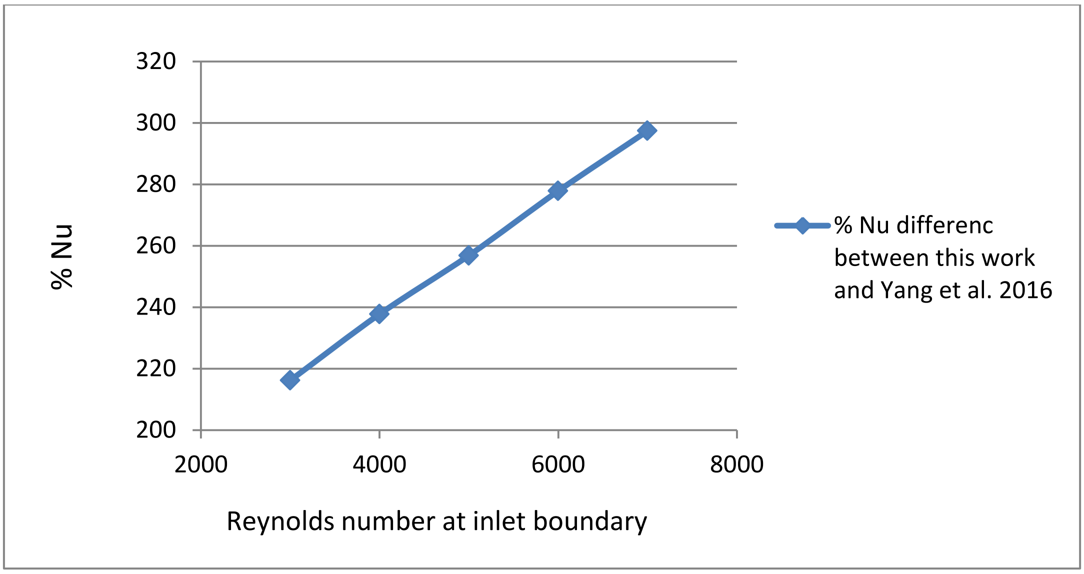

Figure 11. Percentage average Nusselt number differences with Reynolds number between this work and **Yang, et al., 2016 work.**

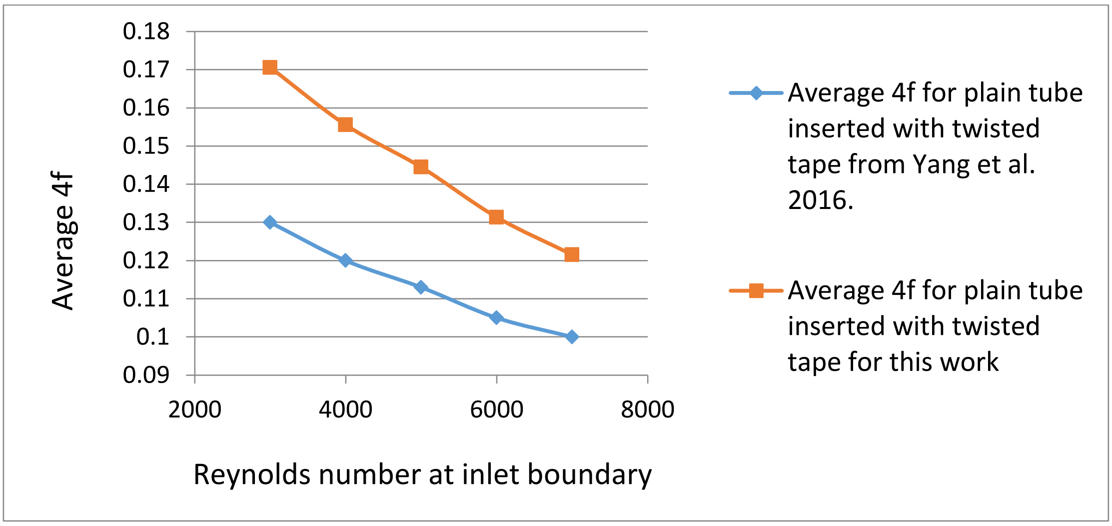

Figure 12. Comparison of average 4f computed from this work and **Yang, et al., 2016**.

Journal of Engineering
journal homepage: www.jcoeng.edu.iq
Number 3 Volume 24 Month 3

Chemical, Petroleum and Environmental Engineering

Permeability Estimation by Using the Modified and Conventional FZI Methods

Prof. Dr. Mohammed S. Al-Jawad
Engineering College-University of Technology
mohaljawad@yahoo.com

Israa Jeryan Ahmed
Engineering College-Baghdad University
israaj86@yahoo.com

ABSTRACT

There many methods for estimation of permeability. In this Paper, permeability has been estimated by two methods. The conventional and modified methods are used to calculate flow zone indicator (FZI). The hydraulic flow unit (HU) was identified by FZI technique. This technique is effective in predicting the permeability in un-cored intervals/wells. HU is related with FZI and rock quality index (RQI). All available cores from 7 wells (Su -4, Su -5, Su -7, Su -8, Su -9, Su -12, and Su -14) were used to be database for HU classification. The plot of probability cumulative of FZI is used. The plot of core-derived probability FZI for both modified and conventional method which indicates 4 Hu (A, B, C and D) for Nahr Umr formation based on the four straight lines. The permeability was calculated by two methods for comparison and choosing the best. The modified FZI method gives better results because the predicted permeability by this method demonstrates a coefficient of correlation (R^2) higher than that of the conventional approach, where the value of R^2 is 0.9645 of modified FZI method while 0.892 of the conventional approach. When plotting RQI versus $\emptyset_z$ on a log-log scale, all core samples with similar *FZI* values will lie on a straight line with a unit slope. Other core samples that have different *FZI* values will lie on other parallel lines. All lines in (RQI and$\emptyset_z$) plot of modified FZI method have unit slop and more parallel than these of the conventional approach. The plot of probability cumulative of FZIm is used to determine number of hydraulic flow unit for Nahr Umr formation. The plot of core-derived probability FZI for both modified and conventional method which indicates 4 Hus for Nahr Umr formation based on the four straight lines, these four straight lines of modified FZI method was more distinguished than these of the conventional approach.

Key words: Permeability, Flow Zone Indicator, Hydraulic Flow Unit, Rock Quality Index, Coefficient of Correlation

حساب النفاذية باستخدام طريقة FZI التقليدية والمطورة

الاستاذ د.محمد صالح الجواد
كلية الهندسة-الجامعة التكنولوجية

اسراء جريان احمد
كلية الهندسة-جامعة بغداد

الخلاصة

هناك العديد من الطرق لحساب النفاذية. في هذا البحث تم حساب النفاذية بطريقتين. تم استخدام الطريقة التقليدية والمطورة لحساب FZI. تم تحديد وحدات الجريان الهيدروليكي بواسطة تقنية FZI. تعد هذه التقنية من الطرق الفعالة في تحديد النفاذية في الابار التي لم تحدد نفاذيتها بواسطة قياسات اللباب. ترتبط وحدات الجريان الهيدروليكي بFZI ومؤشر نوعية الصخرة .استخدمت قاعدة البيانات المستحصلة من قياسات اللباب من سبعة ابارلتصنيف الوحدات الهايدروليكية. تم استخدام رسم الاحتمالية التراكمية لFZI . رسم الاحتمالية التراكمية ل FZI من الطريقة التقليدية والمطورة دل على وجود اربعة وحدات هيدرولية (A, B, C and D) في تكوين نهر عمر بالاعتماد على وجود اربع خوط مستقيمة. تم حساب النفاذية بطريقتين لغرض المقارنة وايجاد الافضل. الطريقة المطورة اعطت نتائج افضل لان النفاذية المحسوبة بهذه الطريقة اظهرت معامل مضاهاة اعلى مما هو عليه في الطريقة التقليدية حيث بلغت قيمته (0.9645) بينما بلغت قيمة عامل المضاهاة للنفاذية المحسوبة بالطريقة التقليدية (0.892) وكذلك عند رسم قيم RQI *مقابل* $\emptyset_z$ على مقياس لوغارتمي كل نماذج اللباب التي لها نفس قيمة *FZI* سوف تقع على خط واحد له ميل مقداره واحد وتوازي بقية الخطوط التي لها قيم *FZI* مختلفة،عند استخدام الطريقة المطورة كل هذه الخطوط كان لها ميل مقدراه واحد ومتوازية مع بعضها اكثر مما هو عليه باستخدام الطريقة التقليدية وعند استخدام رسم الاحتمالية التراكمية ل*FZI* لغرض تحديد عدد الوحدات الهيدروليكية لتكوين نهر عمر كان عدد الوحدات اكثر تمييزا باستخدام الطريقة المطورة مما هو عليه باستخدام الطريقة التقليدية والمتمثلة في عدد الخطوط المستقيمة.

الكلمات الرئيسية: النفاذية، مؤشر نطاق الجريان، وحدات الجريان الهيدروليكي، مؤشر نوعية الصخرة، معامل مضاهاة.

1. INTRODUCTION

Reservoir characterization is a very important domain of petroleum engineering. An effective management strategy can be applied only after obtaining a detailed of spatial distribution of rock properties. Among these, the most difficult to determine and predict is permeability, **Jaber,** and **Shuker, 2014.**

Permeability is one of the most important parameters to quantify in any reservoir rock. Its importance arises due to the major role it plays during the development phase of any reservoir. During any reservoir simulation study, permeability perdition is a very critical and perhaps the most challenging task. In the early stage of the industry, simple permeability–porosity transformations were generated to estimate permeability at un-cored wells. However, such simple relationships were unreliable and results were not in good agreement with field data. Hence, many models have been proposed to predict permeability by incorporating many parameters other than effective porosity, **Nooruddin,** and **Hossain, 2011.**

Rock typing by hydraulic units can be characterized as units of rock that have special permeability-porosity relationship, relative permeability curves and capillary pressure profiles. It has a lot of applications in reservoir characterization and simulation studies. Properly doing of the rock typing that results to accurate generation of initial water saturation profiles and consequently, credible reservoir simulation studies, a reliable estimation of the permeability in the uncored wells, **Davies,** and **Vessell, 1996, Shenawi, et al., 2007.**

Amaefule et al., 1993 presented for the first time the concept of flow zone indicator (FZI) and reservoir quality index (RQI) to define HU based on the **Kozeny-Carmen** model. In this regard, Amaefule's technique is recognized as a very simple, practical, and widely used established technique. This well-known method classifies rock types using the original **Kozeny-Carmen** model. The well-known form of the original **Kozeny-Carmen** model is given by:

$$K = \left(\frac{1}{f_g\, \tau S_{V_{gr}}^2}\right)\frac{\emptyset^3}{(1-\emptyset)^2} \qquad (1)$$

Where k is permeability in μm^2, f_g is the shape factor in the dimensionless unit, τ is the tortuosity in the dimensionless unit, $S_{V_{gr}}^2$ is the specific surface area of the grain in μm-1 and is the effective porosity in fraction.

The **Kozeny-Carmen** correlation was developed based on the concept of average pore throat size. Further mathematical manipulation is carried on Eq.1 that leads to the following form:

$$0.0314\sqrt{\frac{K}{\emptyset}} = \left(\frac{1}{\sqrt{f_g\, \tau}\; S_{V_{gr}}}\right)\frac{\emptyset}{(1-\emptyset)} \qquad (2)$$

From Eq.2, the reservoir quality index (*RQI*) is defined as:

$$RQI = 0.0314\sqrt{\frac{K}{\emptyset}} \qquad (3)$$

The normalized porosity($\emptyset_z$) is defined as:

$$\emptyset_z = \frac{\emptyset}{(1-\emptyset)} \qquad (4)$$

The flow zone indicator (*FZI*) is defined as:

$$FZI = \frac{RQI}{\emptyset_z} \qquad (5)$$

When plotting RQI versus $\emptyset_z$ on a log-log scale, all core samples with similar *FZI* values will lie on a straight line with a unit slope.

Other core samples that have different *FZI* values will lie on other parallel lines.

2. PROPOSED MODIFICATION TO THE KOZENY-CARMEN MODEL, NOORUDDIN, AND HOSSAIN, 201120

The proposed correlation is based on a modified **Kozeny-Carmen** model and has the advantage over the conventional approach of incorporating the tortuosity term in a more representative manner. The conventional model eliminates the inherent nonlinearity between tortuosity and porosity accordingly. The modified correlation is given by:

$$K = \left(\frac{1}{f_g\, a^2 S_{V_{gr}}^2}\right)\frac{\emptyset^{2m+1}}{(1-\emptyset)^2} \tag{6}$$

Where, a is the lithology factor and m is the cementation exponent. Rearranging and taking the square root of Eq.6 results in the following form:

$$0.0314\sqrt{\frac{K}{\emptyset}} = \left(\frac{1}{\sqrt{f_g}\, a\, S_{V_{gr}}}\right)\frac{\emptyset^{m}}{(1-\emptyset)} \tag{7}$$

The left hand side of Eq.3 is the reservoir quality index (*RQI*) where permeability (*k*) is in mD. The first part of RHS $\left(1/\sqrt{f_g}\, a\, S_{V_{gr}}\right)$ is the modified flow zone indicator (*FZIm*). Since the normalized porosity index ($\emptyset_z$) equals to ($\emptyset$ / (1-$\emptyset$)), rearrangement of Eq.7 yields:

$$RQI = FZI_m \times \emptyset_z \times \emptyset^{m-1} \tag{8}$$

Taking the logarithm of both sides of Eq.8 results in the following relationship:

$$\log(RQI) = \log(FZI_m) + \log(\emptyset_Z \times \emptyset^{m-1}) \tag{9}$$

It can be noticed that if the cementation exponent (m) equals to one, then Eq.9 becomes identical to Amaefule model. As (*m*) increases, the plot of RQI versus ($\emptyset_Z \times \emptyset^{m-1}$) on log-log scale gives higher slope lines. Each group of rocks having similar *FZI* will constitute a HU.

For unconsolidated sands, the exponent has been noticed near 1.3 and is believed to increase with cementation. The values of cementation exponent for consolidated sandstones are 1.8 < m < 2.0 commonly, **Archie, 1942.**

In the current study, the exponent m has been chosen to be equal 1.9.

3. PERMEABILITY PREDICTION

Hydraulic Flow Unit (HU) has been used excessively as a technique in rock typing and permeability modeling. (HU) is related with (FZI) and (RQI). This technique is effective in predicting the permeability in un-cored intervals/wells.

In this study, the hydraulic flow unit was identified by FZI technique. The conventional and modified methods are used to calculate FZI. The permeability was calculated by two methods for comparison and choosing the best.

Equations 3, 4 and 5 were used to calculate RQI, PHIZ (Øz) and FZI. All available cores from 7 wells (Su -4, Su -5, Su -7, Su -8, Su -9, Su -12, and Su -14), **Ministry of Oil, 1976-1980,** were used to be database for HU classification. The plot of probability cumulative of FZIm is used. The plot of probability cumulative is the integral of the histogram plot that a normal distribution is represented in a straight line format. The plot of core-derived probability FZI for both modified and conventional method which indicates 4 Hus for Nahr Umr formation based on the four straight lines, respectively is shown in Figure 1.

Depending on the HU definitions obtained from the plot of cumulative probability, a log-log plot of RQI versus ($\emptyset_Z \times \emptyset^{m-1}$) was made as shown in **Fig. 2**. For modified method in this study, cementation exponent (m) is assumed to be 1.9 while it is assumed to be 1 for conventional method. The unit slop lines were drawn related to mean FZI values that intercept with the vertical line $\emptyset_Z = 1$. The clustering was significantly improved using modified HU characterization as compared with the conventional model. Samples that have similar pore throat attributes lie on the same straight line and constitute a HU, **Shenawi, 2009.**

A plot of log permeability (k) versus ($\emptyset$) as shown in **Fig. 3** demonstrates a better correlation using the modified technique as a comparison to the conventional technique for each HU. The relation between porosity and permeability for each rock type was illustrated using power law model, high correlation coefficients were obtained for all rock types, and then permeability can be estimated accurately from equation of curve for each rock type.

Permeability core versus predicted permeability for all rock type was plotted in **Fig. 4** for both the modified approach and the conventional approach. The modified FZI method gives better results because the predicted permeability by this method demonstrates a coefficient of correlation (R^2) higher than that of the conventional approach.

Core permeability and predicted permeability by the modified approach versus depth for all rock type are shown in **Fig. 5**.

CONCLUSIONS

1. FZI technique is effective in predicting the permeability in un-cored intervals/wells.
2. The modified FZI method gives better results because the predicted permeability by this method demonstrates a coefficient of correlation (R^2) higher than that of the conventional approach.
3. There are four hydraulic flow units (A, B, C and D) in Nahr Umr reservoir.

REFERENCES

- Amaefule J. O., Altunbay M., Tiab D., Kersey D., and Keelan D., “Enhanced Reservoir Description: Using Core and Log Data to identify Hydraulic (Flow) Units and Predict Permeability in Uncored Intervals/Wells,”Paper SPE 26436 presented at the Annual TechnicalConference and Exhibition, Houston, Texas, 3-6October 1993.

- Archie, G.E., "The electrical resistivity log as an aid in determining some reservoir characteristics". Petroleum Transactions of AIME, 1942. 146: 54–62. Doi: 10.2118/942054-g.
- Davies, D.K., Vessell, R.K., " Identification and Distribution of Hydraulic Flow Units in a Heterogeneous Carbonate Reservoir: North Robertson Unit, West Texas", paper SPE 35183 presented at the Permian Basin Oil and Gas Recovery Conference, Midland, Texas, 1996, 27-2.
- Jaber A. K., Shuker M. T. "Multiple Linear Regression Approach for the Permeability Calculation from Well Log: A Case Study in Nahr Umr Formation - Subba Oil Field, Iraq", International Journal of Science and Research (IJSR), June 2014.
- Ministry of Oil, Routine core analysis (RCA) for wells (Su-4, Su-5, Su-7, Su-8, Su-9, Su-12and Su-14), 1976-1980.
- Nooruddin H. A., Hossain M. E., "Modified Kozeny–Carmen correlation for enhanced hydraulic flow unit characterization", Journal of Petroleum Science and Engineering 80 (2011) 107–115.
- Shenawi, S.H., White, J.P., Elrafie, E.A., Kilany, K.A., "Permeability and Water Saturation Distribution by Lithologic Facies and Hydraulic Units: A Reservoir Simulation Case Study", Paper SPE 105273, presented at the 15th SPE Middle East Oil & Gas Show and Conference, Kingdom of Bahrain, 2007.
- Shenawi, S.H., Al-Mohammadi, H., Faqehy, M., "Development of Generalized Porosity – permeability Transforms by Hydraulic Units for Carbonate Oil Reservoirs in Saudi Arabia", paper SPE 125380, prepared for presentation at the 2009 SPE/EAGE Reservoir Characterization and Simulation Conference held in Abu Dhabi, UAE, 19-21 October 2009.

NOMENCLATURE

List of Symbols and Abbreviations

FZI	flow Zone Indicator
HU	hydraulic Flow Unit
RQI	rock Quality Index
k	permeability
$\emptyset z$	normalized Porosity
m	cementation Exponent

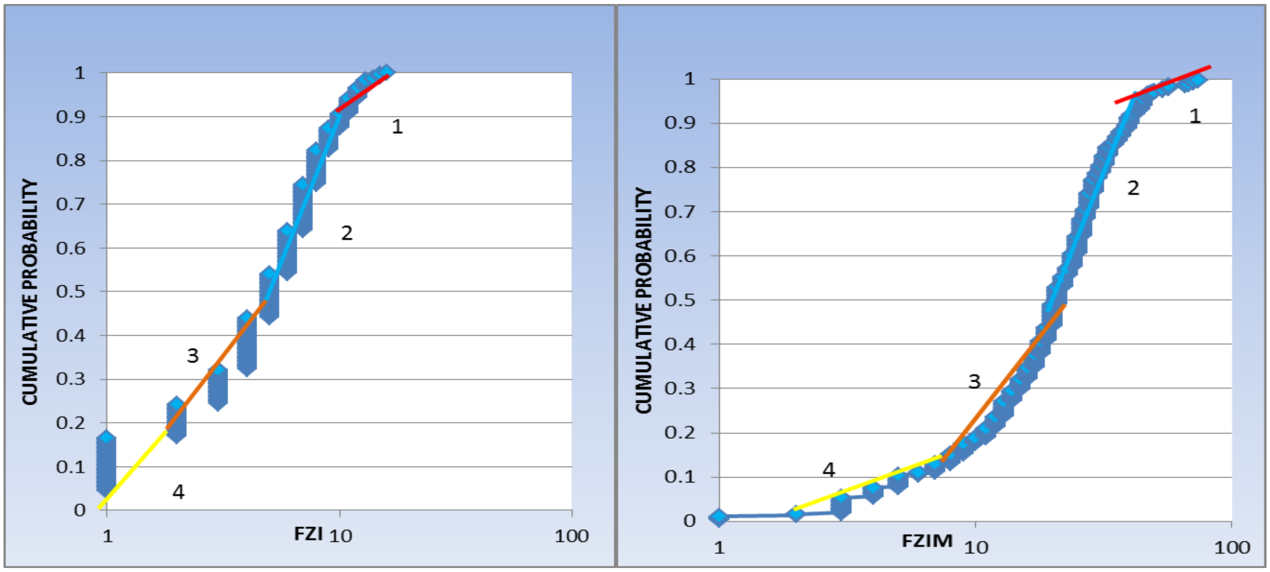

Figure 1. Plot of cumulative Probability of FZI distribution for both the modified (right) and conventional technique (left).

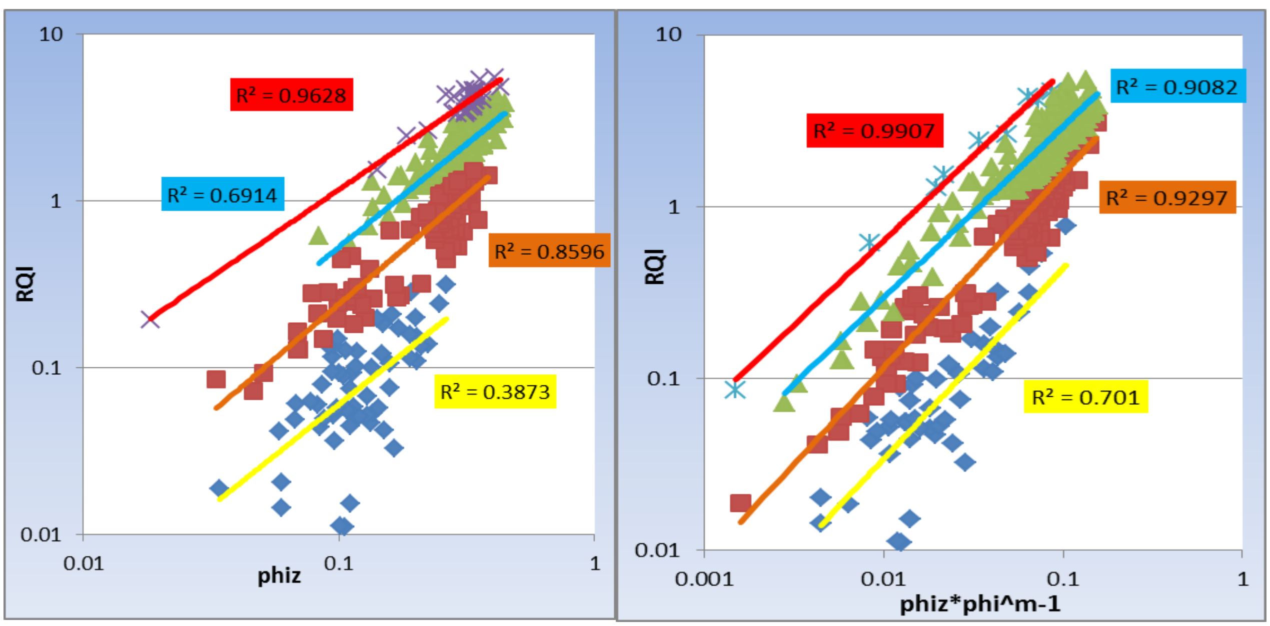

Figure 2. RQI versus PHIZ ($\emptyset_Z$) plot for both the modified approach (right) and conventional one (left).

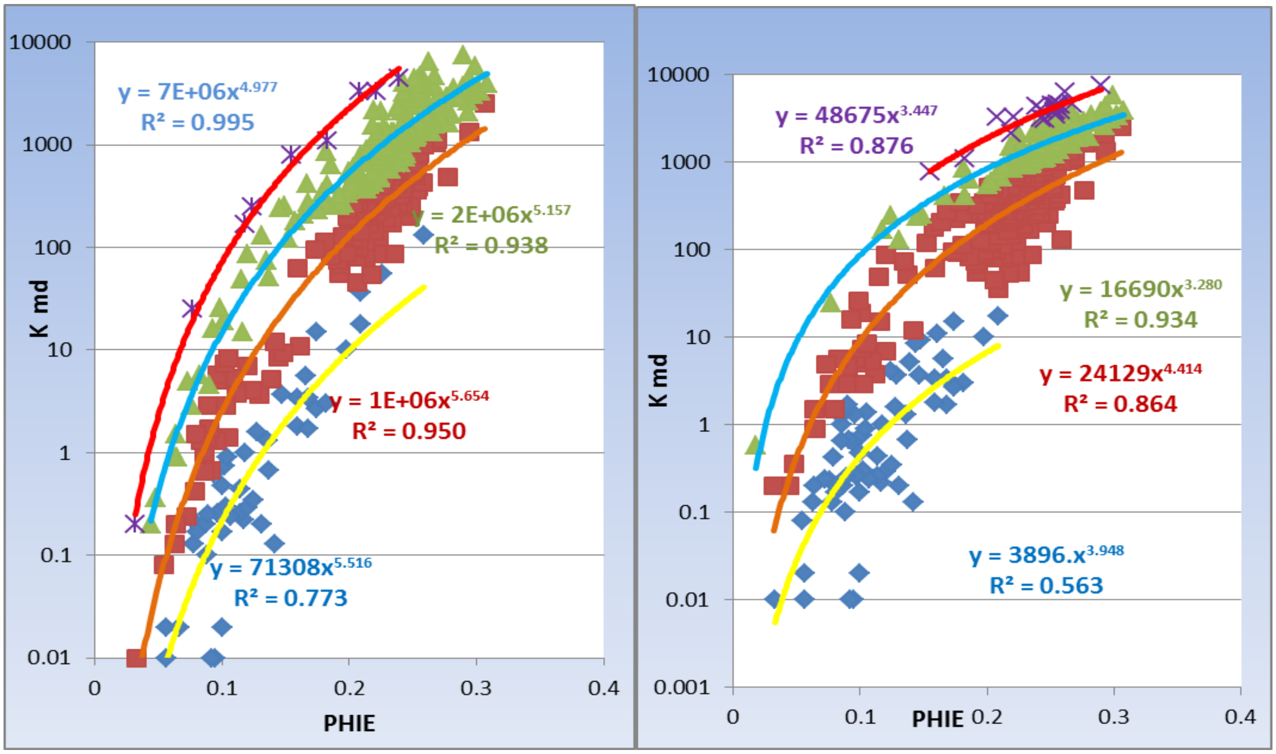

Figure 3. Log permeability (k) versus PHIE plot for both the modified approach (right) and conventional one (left).

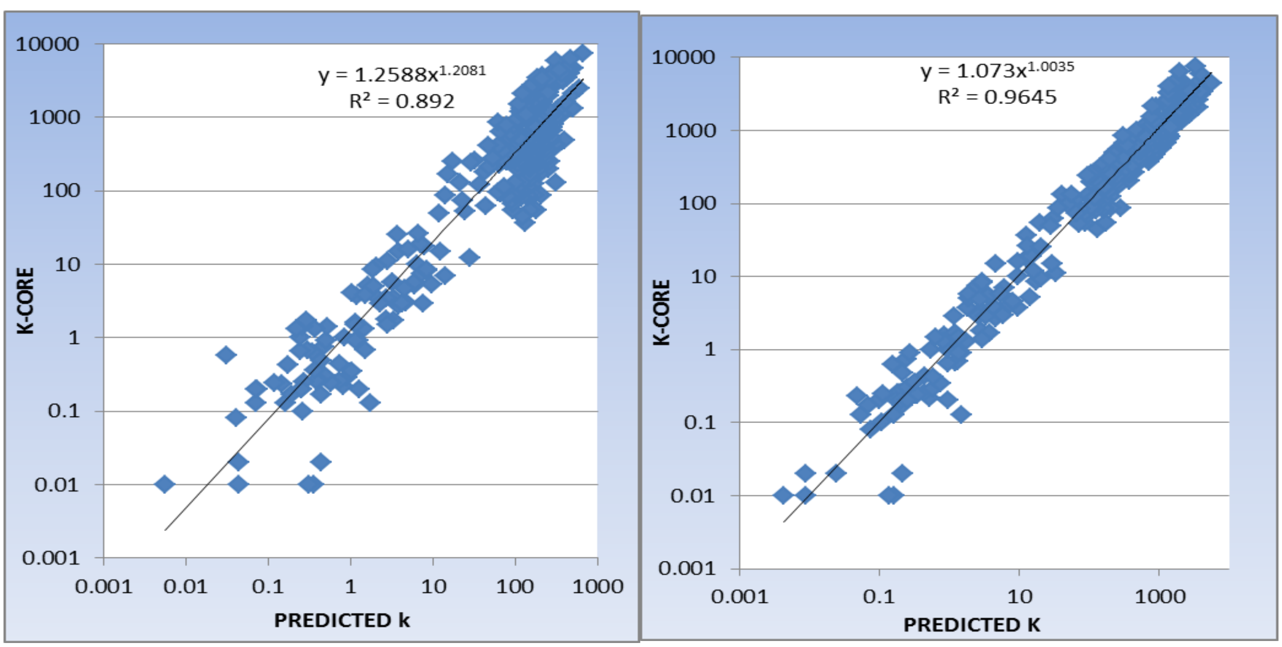

Figure 4. Core permeability versus predicted permeability plot for both the modified approach (right) and conventional one (left).

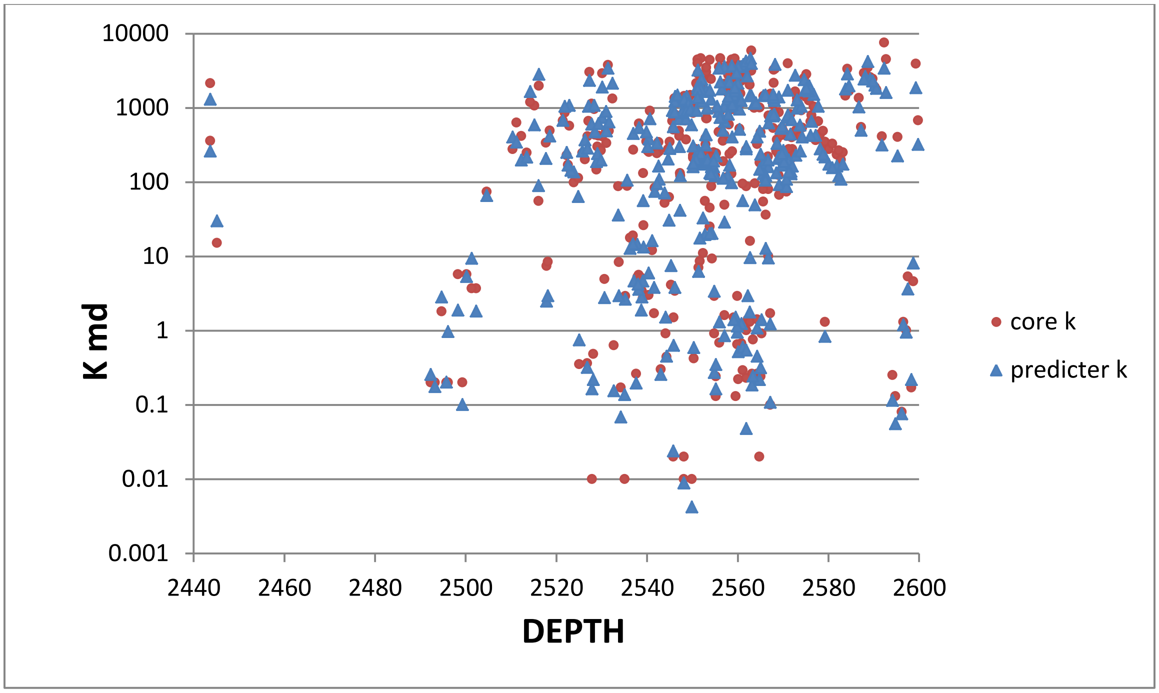

Figure 5. Core permeability and Predicted permeability by the modified approach versus depth for all rock type.

University of Baghdad
College of Engineering
JOURNAL OF ENGINEERING

Journal of Engineering

journal homepage: www.jcoeng.edu.iq
Number 3 Volume 24 Month 3

Chemical, Petroleum and Environmental Engineering

Anaerobic Co-digestion of Giant Reed for Biogas Recovery

Nazik Adnan Noori
Master student
Dept. of Environmental Engineering
College of Engineering-University of Baghdad
Email:nazik.adnan1989@gmail.com

Dr. Zainab Ziad Ismail
Professor
Dept. of Environmental Engineering
College of Engineering-University of Baghdad
Email:zismail9@gmail.com

ABSTRACT

This study investigated the feasibility of anaerobic co-digestion of giant reed (GR) inoculated with waste manure as a co-substrate for biogas production. The performance of co-digestion was evaluated in 4 anaerobic digesters operated in batch mode at different conditions. The effects of alkali pretreatment with NaOH (4% w/v) solution, inoculum type, and thermal condition were studied. The results demonstrated that the alkali-pretreatment of GR enhanced the biogas generation by about 15% at mesophilic conditions. Thermophilic conditions enhanced the biogas recovery from both alkali-free and alkali pretreated GR by 15% and 127%, respectively. The kinetic study of the co-digestion process of GR for biogas recovery suggested a significant agreement between measured and predicted values obtained by ***Modified Gompertz Model*** with correlation coefficients ≥ 0.98 indicating favorable conditions for the co-digestion of inoculated GR.

Key words: giant reed, biogas, digestion, alkali pretreatment, methane, chicken dung

الهضم المشترك اللاهوائي للقصب البري لاستخلاص الغاز الحيوي

نازك عدنان نوري
طالبة ماجستير
قسم الهندسة البيئية
كلية الهندسة- جامعةبغداد

د. زينب زياد اسماعيل
استاذ
قسم الهندسة البيئية
كلية الهندسة- جامعةبغداد

الخلاصة

تهدف هذه الدراسة الى اختبار امكانية تطبيق الهضم المشترك اللاهوائي للقصب البري مع فضلات الحيوان لإنتاج الغاز الحيوي. تم تقييم أداء الهضم المشترك وذلك بتشغيل سبعة مفاعلات هضم لاهوائي تعمل جميعها بنمطِ التشغيل الدفعي بظروف تشغيلية مختلفة وتم دراسة تأثير العوامل التالية : المعالجة الكيمياوية التمهيدية للقصب بأستخدام محلول هيدروكسيد الصوديوم بتركيز (4% w/v) ، نوع المادة المضافة كمصدر للبكتريا (تحديدا مخلفات الماشية والدجاج)، و درجة الحرارة. أظهرت النتائج زيادة واضحة في انتاجية الغاز الحيوي من القصب المعالج بالقاعدة مقارنة بكميته المتحررة من القصب الغير معالج وذلك بنسبة 15% عند ظروف حرارة معتدلة.. أظهرت النتائج أيضا زيادة في كمية الغاز الحيوي المتحرر تحت ظروف الحرارة المرتفعة مقارنة بظروف الحرارة المعتدلة للقصب الغير معالج والمعالج بالقاعدة بنسبة زيادة حوالي 15%و 127%، على التوالي. لغرض وصف عملية الهضم اللاهوائي المشترك، تم تطبيق الموديل الرياضي الخاص لهذه التطبيقات وهو ***Modified Gompertz Model*** وقد اظهرت نتائج تطابقا كبيرا بين نتائج القياسات المختبرية وتلك التي تم احتسابها من الموديل الرياضي وبمعامل ارتباط ≥ 0.98 للظروف التي تم تطبيقها لعملية الهضم اللاهوائي المشترك للقصب.

الكلمات الرئيسية: القصب البري، الغاز الحيوي، الهضم، المعالجة الاولية القاعدية، الميثان، فضلات الدجاج.

1. INTRODUCTION

The ease of access to the fossil fuels during almost two centuries had decreased the available fossil fuel reservoirs, resulting in prices raising, therefore, the energy supply has become one of the most important global problems, **Deublein**, and **Steinhauser, 2008**. The application of biotechnology to produce commodity products such as, fuels, chemicals, and materials offering benefits regarding to sustainable resource supply and environmental quality is an emergent area of intellectual endeavor and industrial practice with great promise, **Lynd, et al., 1999**. Lignocellulose is a material usually exists as the primary components of different wastes disposed from various industries, forestry, agriculture and municipalities. Cellulose is the most abundantly available organic molecule on Earth, is mainly found as a structural component of plant and algal cell walls, and is produced by some animals, such as tunicates, and several bacteria, **Lynd, et al., 2002**. Cellulose chains in primary plant cell walls have degree of polymerization in the range from 5000 to 7500 glucose monomer units, 10000 for wood, and 15000 for cotton **O'Sullivan, 1997**. Hydrolysis of this material is the first step for conversion by anaerobic digestion to biogas (methane). However, enzymatic hydrolysis of lignocelluloses without pretreatment is usually not so effective because of high stability of the materials to enzymatic or bacterial attacks. Pretreatment helps to enhance the process of hydrolysis. Conversion of plant cellulose into ethanol has been industrially achievable since the late Nineteenth Century. However, the near insolubility of cellulose in aqueous solvents initially required physical separation of pure cellulose from plant material and harsh acid hydrolysis to produce the glucose used in fermentation, **O'Dell, et al., 2012**. Fungi and bacteria possess enzymes of laccases, hemicellulases and cellulases, which efficiently degrade lignin, hemicellulose and cellulose, respectively **Baldrian** and **Valášková, 2008**. It is known that excess sludge with low organic content always lead to failure the anaerobic digestion, so the following research of, **Yan, et al., 2013,** gave a solution for this problem by employing mild thermal pretreatment at thermal conditions between (50-120) ◦C, which has drawn much attention due to less energy consumption and no chemical addition. Where the experimental results showed a gradually rising of soluble organic matter concentration with temperature resulting in biochemical methane enhancement 142.6±2.5 ml/g of volatile solids under mild thermal pretreatment 100◦C and digestion time 20 d. **Cheng** and **Zhong, 2014,** observed biogas yield from anaerobic digestion of inoculated cotton stalk (CS) reached 175−180 ml/g VS. Cotton stalk CS was proven to be a promising co-substrate in the digestion with swine manure (SM) as inoculum. CS/SM ratio of 50:50 with a C/N ratio of 25 was found to be the best conditions for biogas yield with increases up to 1.8- and 1.9-fold, respectively compared to the control. The highest biogas yield of 449 ml/g VS was obtained for the co-digestion of SM with CS pretreated by NaOH, which was 241−255% of those achieved with using the control. **Ismail** and **Talib, 2014,** studied the recycling of date palm wastes (DPWs) for biogas production. It was found that biogas yield from inoculated DPWs had exceeded its production from DPWs without inoculation by an increment of 140% at mesophilic conditions. Also, biogas recovery from pretreated DPWs was 52% higher than the yield from untreated DPWs at mesophilic conditions. Thermophilic conditions improved the productivity by 23%. **Sharma, et al., 2016,** illustrated the effect of alkaline and acid pre-treatment on different sizes of wheat straw on biogas quality and quantity. It was concluded that untreated wheat straw gave a biogas production of 104 ml/g VS and methane yield of 64%. It was observed by using 1%, 2%, 5% NaOH concentrations for pretreatment, the biogas production was 124, 128, 126 ml/g VS with methane content of 66%, 69%, 71%, respectively. Whereby, pretreatment of wheat straw with 1%, 2%, 5% acid produced 130, 140 and 134 ml biogas /g VS and methane content of 68%, 72%, 75%, respectively. However, to our knowledge none of the previously reported studies have dealt with the anaerobic co-digestion of cellulosic giant reed for biogas production. This study aimed to investigate the potential of giant reed co-digestion for biogas production. The effects of pretreatment, type of inoculum, and temperature conditions were studied. The application of ***Modified Gompertz Model*** for kinetic study was also considered.

2. MATERIALS AND METHODS

2.1 Materials

Wild giant reed (GR) is abundantly found in almost everywhere in Iraq and world-wide as well, in particular in wet areas. In this study, GR was collected from Al-Musayyib river bank area. The collected GR stacks were manually cleaned and carefully washed with tab water to remove sand and undesirable particulates. Then after, the cleaned reed stacks and leaves were air dried, and were cut into small pieces, each of approximately 5 cm length ready to be further crushed into smaller size fibrous shaped particles. Chicken dung was used as a rich bacterium source to inoculate the GR. It was collected from the nearest poultry houses, air-dried, crushed to powder size particles, and then stored in a clean tightly closed plastic container. All chemical reagents utilized in this study were of analytical grade as given in **Table 1.**

2.2 Methods of Analysis

2.2.1 Total solids, Volatile solids, pH, and C/N ratio

These tests were performed in triplicate according to the procedures reported in the *standard methods*, **APHA, 1998**. Sample of 25-50 g was dried at 105ºC to drive off the water in the sample. The residues was cooled, weighed to calculate TS, and dried again at 550- 600°C for 4 h to drive off volatile solids in the sample**.** pH was measured using pH meter (Model: WTW, Inolab 720).

Measurements of C/N ratio included carrying out the ***Kjeldahl analysis*** to find the crude protein (CP) and nitrogen (N) contents in GR in three main steps including digestion, distillation, and titration as according to **Bugodo, et al., 2008** and **Abba, et al., 2014** as follows:

Digestion, this step involved the decomposition of nitrogen in the sample using concentrated sulfuric acid (98 %) to produce ammonium sulfate as the reaction end product. This was carried out by adding 0.5 g of the sample in kjeldahl digestion tube with 1 g of the catalyst $CuSO_4.K_2SO_4$ followed by the addition of 15 ml H_2SO_4. The content was then gently heated to 360°C in the Kjeldahl digestion unit until the digest became clear indicating total conversion of nitrogen into ammonia.

Distillation, after the completion of digestion process, the Kjeldahl digestion tubes were cooled and diluted with 25 ml distilled water. The solution turned blue due to the reaction between the catalyst and water. Then each Kjeldahl digestion tube was placed in the crude protein measuring device. A receiving flask containing 50 ml boric acid (1%) to capture the ammonia, and red methyl dye. This red dye turned into green indicating the existence of nitrogen which was released due to the reaction between the contents of Kjeldahl flask and NaOH solution (40 % as aliquot).

Titration with HCl, in order to quantify the amount of ammonia in the receiving flask, a standard solution of HCL was carefully added by pipette until the green color of solution in the conical flask turned to red color.

Calculations of nitrogen, carbon amounts, and C/N
The crude protein (CP), nitrogen, carbon, and C/N were calculated using equations (1), (2), (3), and (4), respectively, **Bugodo, et al., 2008**, and **Abba, et al., 2014**:

$$Protein\ (\%) = \frac{1.401\ x\ M\ x\ 6.25}{g\ of\ sample}\ x\ (ml\ titrant - ml\ blank) \quad (1)$$

Where:
M: the molarity of the acid (0.1 M)

$$Nitrogen\ (\%) = \frac{Protein\ (\%)}{6.25} \quad (2)$$

$$Carbon\ (\%) = 0.58\ x\ organic\ matter \quad (3)$$

$$C{:}N = \frac{\%\ Organic\ carbon\ in\ the\ sample}{\%\ Nitrogen\ in\ the\ sampleof\ sample} \quad (4)$$

The average measured values of total solids (TS), volatile solids (VS), and C/N ratio for the tested samples are given in **Table 2.**

2.2.2 Measurement of produced biogas

In this study, the produced biogas was measured by three different methods as follows:
Manometer, it consisted of U-shaped glass tube of 10 mm internal diameter filled with KOH solution. A tap was connected to the U-tube in order to set the solution level with atmospheric pressure after the removal of CO_2. The U-tube had two ports, one port for the injection of biogas, and the other port for gas outlet after CO_2 removal. The percentage of CH_4 was measured using KOH solution. The released gas was fractioned in percentage of CO_2 and CH_4 by using 40% KOH solution, **Abdel-Hadi, 2008**. All measurements were performed at room temperature and atmospheric pressure. According to **Hansen, et al., 2004**, values of gas volume were corrected for standard temperature and pressure (STP).
Water displacement method, to estimate the volume of the produced CH_4, the produced gas was passed through 1M NaOH solution contained in an airtight washing bottle in order to remove CO_2. After that, the remaining CH_4 pass into a 500-ml glass container and displaced the water which overflowed into a volumetric cylinder. Volume of the displaced colored water represented the methane volume.
Gas chromatography (GC), GC Model SHIMADZU (Japan) was used to determine biogas components as byproducts of anaerobic digestion process.

2.3 Experimental Procedure

The experimental work was achieved according to the following steps:
Physical pretreatment of GR, The 5-cm length pieces of reed stacks were grounded by using electrical household grinder. The grounded GR particles were sieved using mechanical sieve shaker to prepare size range of 0.3-0.6 mm

Chemical pretreatment of GR, 20 g sodium hydroxide grains were dissolved in 500-ml distilled water to prepare 4% (w/v) NaOH solution. Then the prepared solution was added to 30 g of grounded reed with continuous manual stirring of the mixture using a glass rode. The resulted slurry was placed in the oven overnight at 105 °C, and then the dried alkali-pretreated GR was repeatedly washed with water to remove any excess NaOH.

Inoculum preparation, Chicken dung is known to be rich in the methanogenic anaerobic bacteria. Therefore, it was selected to alternatively inoculate the anaerobic digesters. It was prepared in distilled water as slurry, and then added to the digesters as a supplementary material for enrichment of bacterial activity and hence enhancement the anaerobic co-digestion process.

System setup and start-up of digesters, lab-scale digesters were set up and operated in batch mode to estimate the rate of biogas production from alkali-free and alkali-pretreated GR. The system mainly composed of 500-mL Pyrex borosilicate heatproof code glass bottles setup as the anaerobic digesters. The contents of each digester were maintained at the ratio of 1:10. This ratio is equivalent to 40 g solid waste: 400 ml inoculum slurry. Every single digester was tightly plugged using a rubber stopper contained 2 holes; each of 4 mm diameter through which a small portion of glass tube was submersed into the digester. The other end of the glass tube was connected with rubber tube to transfer the generated biogas to the gas measuring apparatus. In order to prevent the release of produced gas, the rubber stoppers were tightly wrapped with parafilm. Flushing with nitrogen was performed for 10 min to keep the digesters in an anaerobic environment condition. Digesters were placed in a thermostatic water bath to keep them at the required temperature conditions. Manual shaking of digesters was daily performed to allow mixing of the co-substrates (GR and inoculum). **Fig. 1** illustrates the digesters arrangement and set up. **Table 3** presents the digesters contents and conditions.

Residual digestate as a soil amendment, upon the completion of the co-digestion of GR, a residual digestate was resulted as a byproduct of the co-digestion process. Accordingly, in order to examine the feasibility and overall efficiency of this sustainable approach, a decision was made to investigate the validity of utilizing this digestate for soil amendment. Sun flower seeds were selected for this test. The seeds were planted in 2 identical pots, fertilized with the digestate as follows:
Pot (1) Alkali- free GR
Pot (2) Alkali-pretreated GR

3. RESULTS AND DISCUSSION

3.1 Biogas Production

The effects chemical pretreatment of GR and temperature conditions addition on biogas production and methane yield from GR by anaerobic co-digestion process are presented as follows:

3.1.1 The influence of chemical treatment

The breakdown and hydrolysis of cellulose and hemicellulose are difficult and slow, in particular with the presence of lignin. Alkali pretreatment will enhance the destruction of the rigid lignin bonds. **Fig. 2** illustrates the effect of alkali-pretreatment on biogas production and methane yield. The increase in biogas production associated with alkali-pretreatment was due to the destruction of the crystalline structure of lignocellulose by and removal of the surface layer of lignin and hemicellulose. **Kong, et al., 1992** reported that the addition of alkali causes the lignocellulose swelling and partial solubilisation of lignin. The results of this study are in a good agreement with previously reported studies. **Liew, et al., 2011** studied the pretreatment of fallen leaves using 3.5% NaOH, and proved that the methane yield increased by 20% during batch tests. Results reported by **He, et al., 2008** demonstrated a significant increase in biogas recovery using rice straw pretreated with 6% NaOH for 3 weeks at ambient temperature in batch tests.

3.1.2 The influence of temperature

The results revealed higher rate of biogas production and methane yield at thermophilic conditions compared to mesophilic conditions as given in **Figs. 3** and **4** for alkali-free GR and alkali-pretreated GR, respectively. It is well observed that at thermophilic conditions, biogas generated exceeded its generation at mesophilic conditions. This observation could be attributed to the fact that at higher temperature, the hydrolysis of cellulose was boosted resulted in a rapid rate of co-digestion process. These results were in a good agreement with the previously reported studies including but not limited to the study carried out by **Yan, et al., 2013** who suggested that at mild thermal pretreatment (50–120°C), the concentration of soluble organic matters increased gradually with temperature indicating higher rate of hydrolysis.

3.2 Kinetic Model

For anaerobic digester operating in a batch mode, the rate of biogas generation corresponds to specific growth rate of methanogenic bacteria in this digester. Accordingly, the predicted rate of biogas production can be calculated using the ***Modified Gompertz Model*** **Nopharatana, et al., 2007**. This model is represented by equ. (5). A non-linear regression can be used to fit the data **Zwietering, et al., 1990**.

$$G_{(t)} = G_0 . \exp\{- \exp [((R_{max} . e)/G_0) (\lambda - t) + 1]\} \quad (5)$$

Where:

$G_{(t)}$ = the cumulative biogas yield at a digestion time (mL/g VS)

G_0 = the biogas potential of the substrate (mL/g VS)

R_{max} = maximum methane production rate (mL/g VS.d)

λ = lag phase (day)

t = time (day)

e = exp (1) = 2.7183

In this study, a nonlinear least-square regression analysis was applied using SPSS [IBM SPSS statistics 24 (2009)] to find out λ, R_{max}, and to predict biogas and methane yields. **Figs. 5- 8** illustrate the degree of compatibility between the measured and predicted values. Also, **Table 4** presents the results and kinetic constants obtained by the ***Modified Gompertz Model.*** The well-fitting between the measured and predicted values of biogas recovery was in a good agreement with the previously reported studies. **Matheri, et al., 2015,** suggested that well-fitting was observed for the predicted results estimated by the Modified Gompertz Model with the measured values of biogas recovery from co-digestion of cow manure and grass clippings. **Kafle, et al., 2013,** proved that the measured values of biogas generated from the digestion of fish were in a good agreement with the predicted values computed by Modified Gompertz Model

3.3 Soil Fertilization with Residual Digestate

The results of this part of work revealed that the selected process is a fair sanctioned approach to treat the residues from the co-digestion process of GR. **Fig. 9** presents the growth progress of sun flower seeds after 3 weeks observation period. As shown in this photo, healthy favorable growth of fertilized crop was observed. An additional benefit of this sustainable environmentally friendly approach is the volume reduction of this lignocellulosic material as a result of the co-digestion process.

REFERENCES

- Abba, A., Faruq, U. Z., Birnin-Yauri, U. A., Yarima, M. B., Umar, K. J., 2014, *Study on production of biogas and bioethanol from millet husk.* Annual Research and Review in Biology. Vol. 4, PP. 817- 827.

- Abdel-Hadi, M. A., 2008, *A simple apparatus for biogas quality determination*. Misr Journal Agriculture Engineering. Vol. 25, PP. 1055- 1066.

- American Public Health Association (APHA), 1998, *Standard methods of the examination of water and wastewater*, Washington, DC.

- Baldrian, P., Valášková, V., 2008, *Degradation of cellulose by basidiomycetous fungi*. FEMS Microbiology Reviews. Vol. 32, PP. 501-521.

- Bagudo, B. U., Garba, B., Dangoggo, S. M., Hassan, L. G., 2008, *Comparative study of biogas production from locally soured substrate materials*. Nigerian Journal of Basic and Applied Sciences. Vol. 16, PP. 262- 266.

- Cheng, X.Y., Zhong, C., 2014, *Effect of feed to inoculum ratio, co-digestion, and pretreatment on biogas production from anaerobic digestion of cotton stalk*. Energy Fuels. Vol. 28, PP. 3157- 3166.

- Deublein, D., Steinhauser, A., 2008, *Biogas from waste and renewable resources*. WILEY-VCH Verlag GmbH & Co. KGaA, Weinheim.

- Hansen, T. L., Schmidt, J. E. Angelidaki, I., Marca, E., Jansen, J., Mosbaek, H., Christensen, T. H., 2004, *Method for determination of methane potentials of solid organic waste*. Waste Management. Vol. 24, PP. 393-400.

- He, Y., Pang, Y., Liu, Y., Li, X., Wang, K., 2008, *Physicochemical characterization of rice straw pretreated with sodium hydroxide in the solid state for enhancing biogas production.* Energy& Fuels. Vol. 22, PP. 2775–2781.

- Ismail, Z. Z., Talib, A. R., 2014, *Assessment of anaerobic co-digestion of agro wastes for biogas recovery: A bench scale application to date palm wastes*. International Journal of Energy and Environment. Vol. 5, pp.591-600.

- Kafle, G., K., Kim, S., H., Sung, K., 2013, *Ensiling of fish industry waste for biogas production: A lab scale evaluation of biochemical methane potential (BMP) and kinetics*. Bioresource Technology. Vol. 127, PP. 326-336.

- Kong, F., Engler, C., Soltes, E., 1992, *Effects of cell-wall acetate, xylan backbone and lignin* *on enzymatic hydrolysis of aspen wood*. Applied Biochemistry and Biotechnology. Vol. 34-35, PP. 23-35.

- Liew , L. N., Shi, J., Li, Y., 2011, *Enhancing the solid-state anaerobic digestion of fallen leaves through simultaneous alkaline treatment*. Bioresource Technology. Vol. 102, PP. 8828-8834.

- Lynd, L. R., Weimer, P. J., Van, W. H., 2002, *Pretorius IS. Microbial cellulose utilization: fundamentals and biotechnology*. Microbiology and Molecular Biology Reviews. Vol. 66, PP. 506-77.

- Lynd, L. R., Wyman, C. E., Gerngross, T. U., 1999, *Biocommodity engineering*. Biotechnology Progress. Vol. 15, PP. 777-793.
- Matheri, A.N., Belaid, M., Seodigeng, T., Ngila, C.J., 2015. The kinetic of biogas rate from cow dung and grass clippings. *7th International Conference on Latest Trends in Engineering & Technology*. 208- 210.

- Nopharatana, A. P., Pullammanappallil, C. W., Clarke, P., 2007, *Kinetics and dynamic modeling of batch anaerobic digestion of municipal solid waste in a stirred reactor*. Waste Management. Vol. 27, PP. 595-603.

- O'Sullivan, A. C., 1997, *Cellulose: the structure slowly unravels*. Cellulose. Vol. 4, PP. 173-207.
- O'Dell, W. B., Baker, D. C., McLain, S. E., 2012, *Structural evidence for inter-residue hydrogen bonding observed for cellobiose in aqueous solution*. OAlib Journal. Vol. 7, PP.1-10.

- Sharma, R., Singha, S., Tiwari, A. K., 2016, *Pretreatment impact on biomethanation of Lignocellulosic waste*. Single-Cell Biology. Vol. 5, PP. 1-4.

- Yan, Y., Chen, H., Xu, W., He, Q., Zhou, Q., 2013, *Enhancement of biochemical methane potential from excess sludge with low organic content by mild thermal pretreat* Biochemical Engineering Journal. Vol. 70, PP. 127-134.

- Zwietering, M. H., Jongenburger, I., Rombouts, F. M., van'tRiet K., 1990, *Modelling the bacterial growth curve*. Applied Environmental and Microbiology. Vol. 56, PP. 1875-1881.

Table 1. Chemical reagents details.

Chemical Reagent	Chemical Formula	Purity%	Provider	Purpose of Use
Sodium bicarbonate	$NaHCO_3$	99	BDH, England	pH adjustment
Phenolphthalein	$C_{14}H_{14}N_3NaO_3S$	99	BDH, England	To color the water in the displacement bottle
Sodium hydroxide	NaOH	98	BDH, England	1- Pretreatment of GR 2- For Kjedahl analysis
Potassium hydroxide	KOH	98	BDH, England	CO_2 removal
Hydrochloric acid	HCL	98	BDH, England	For Kjedahl analysis

Table 2. Values of total solids, volatile solids, nitrogen, and carbon contents in the co-substrates before and after the co-digestion process.

Digesters	%TS	%VS	%C	%N	C (g)	N (g)	C/N
Alkali-free GR before digestion	90	95	1.011	5.077	53.33	364.81	0.146
Alkali-free GR after digestion	85	9.60	0.056	0.426	24.68	225.28	0.110
Alkali-pretreated GR before digestion	83	177.75	1.031	4.901	53.93	359.53	0.150
Alkali-pretreated GR after digestion	80	4.28	0.075	0.336	25.25	222.58	0.113

Table 3. Digesters arrangements, contents, and conditions.

Digester #	Digester contents	Temperature Condition
1	Alkali-free GR with chicken dung inoculum	Mesophilic
2	Alkali- pretreated GR with chicken dung inoculum	
3	Alkali-free GR with chicken dung inoculum	Thermophilic
4	Alkali- pretreated GR with chicken dung inoculum	

Table 4. Results of the kinetic study using Gompertz model at mesophilic conditions.

Digesters #	$G_{(t)}$ experimental (mL CH_4/g VS)	Gompertz model parameters				R^2
		λ (day)	$R_{max.}$ (ml CH_4/g VS)	G_0 (ml CH_4/g VS)	$G_{(t)}$ predicted (ml CH_4/g VS)	
1	40.01	8.72	0.31	40.01	33.77	0.98
2	56.76	1.00	0.90	56.76	56.51	0.99
3	38.81	0.40	0.61	38.81	35.50	0.98
4	114.75	1.31	1.93	114.75	108.15	0.99

Figure. 1 Digesters arrangement and set up.

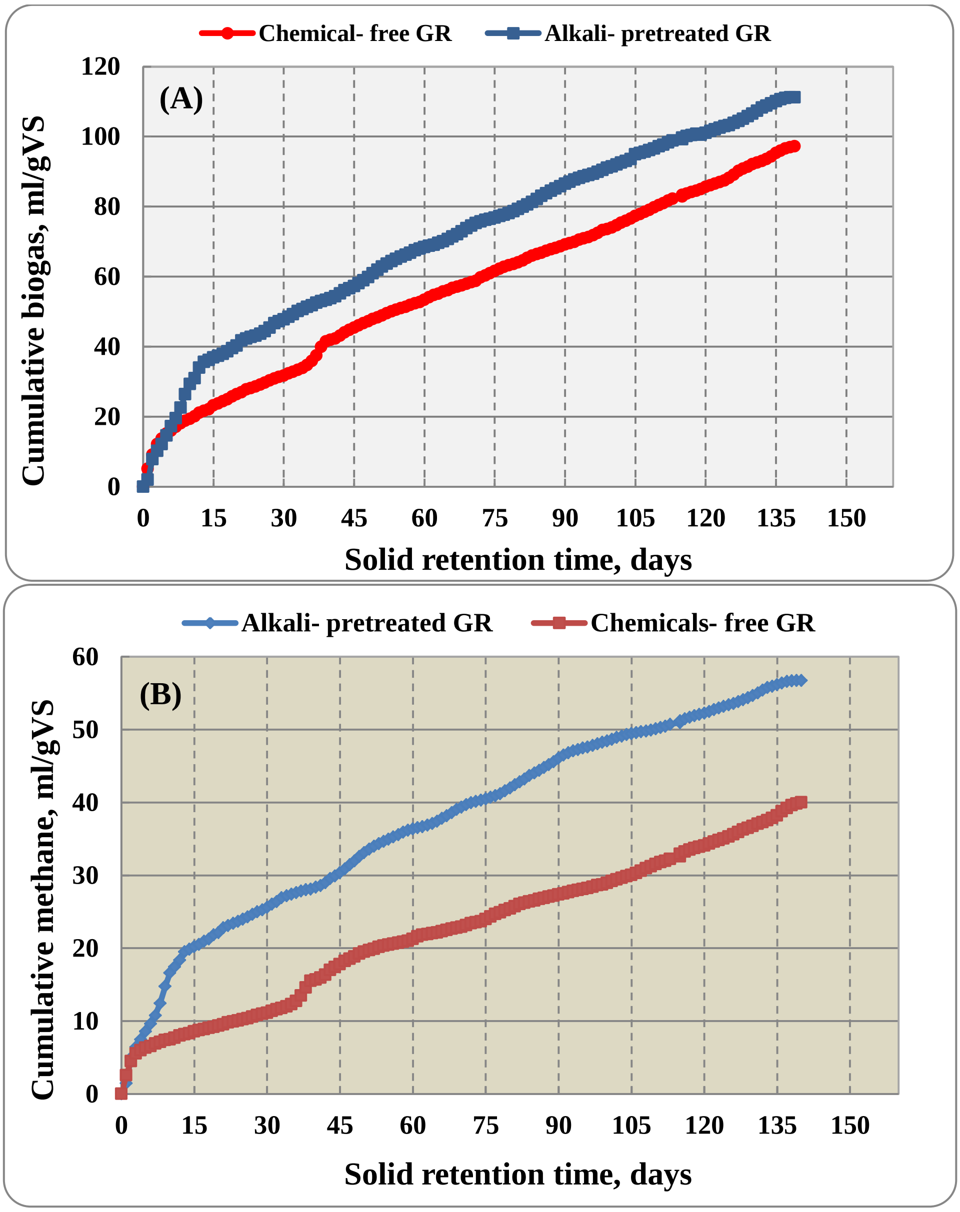

Figure 2. Effect of alkali-pretreatment on the profiles of cumulative, **(A)** biogas production; (B) methane yield from anaerobic co-digestion of GR.

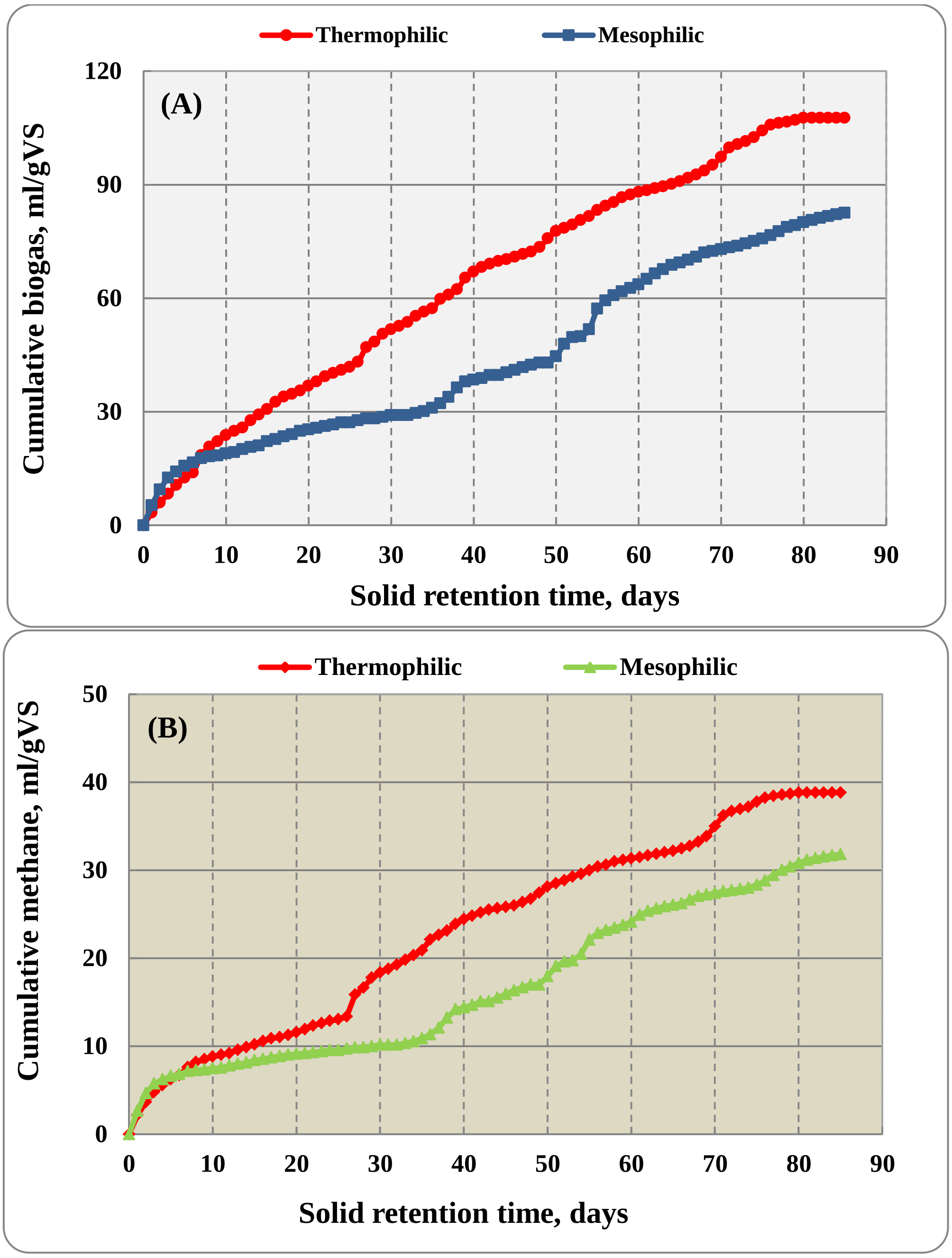

Figure 3. Effect of temperature conditions on profiles of cumulative, (A) gas production; (B) methane yield from alkali-free GR.

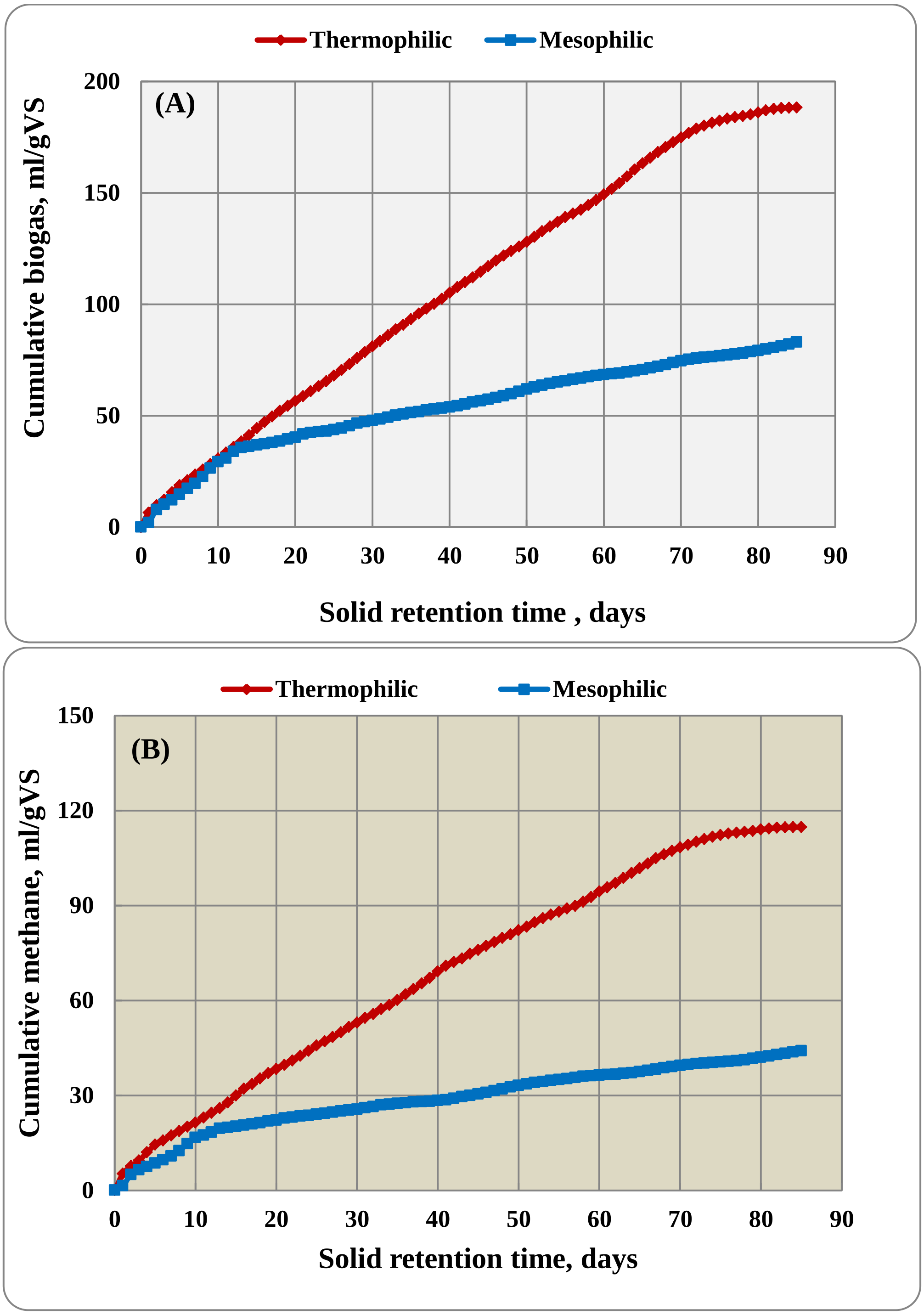

Figure 4. Effect of temperature conditions on profiles of cumulative, (A) gas production; and (B) methane yield from alkali-pretreated GR.

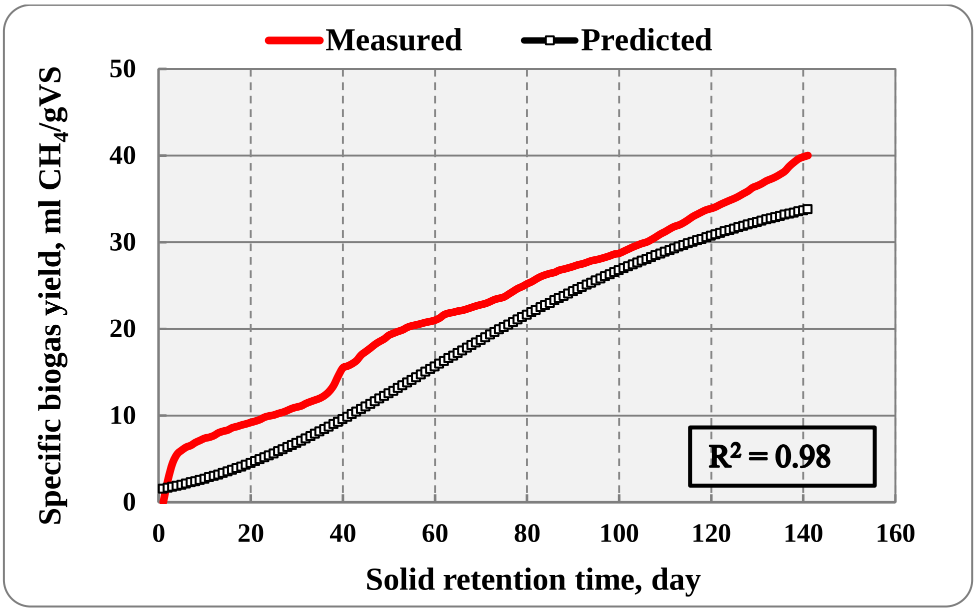

Figure 5. Measured and predicted data for digester 1.

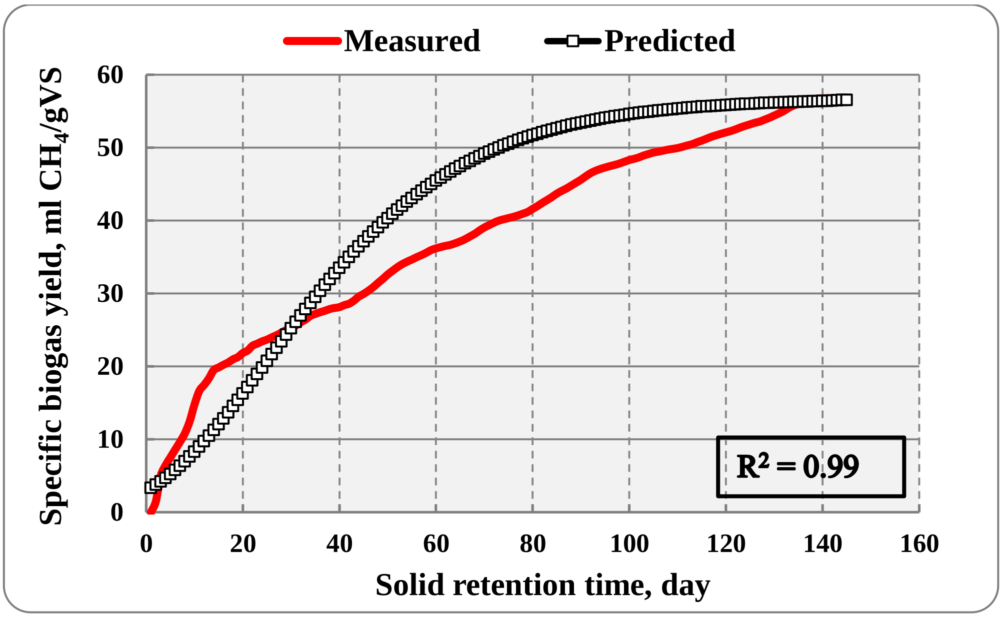

Figure 6. Measured and predicted data for digester 2.

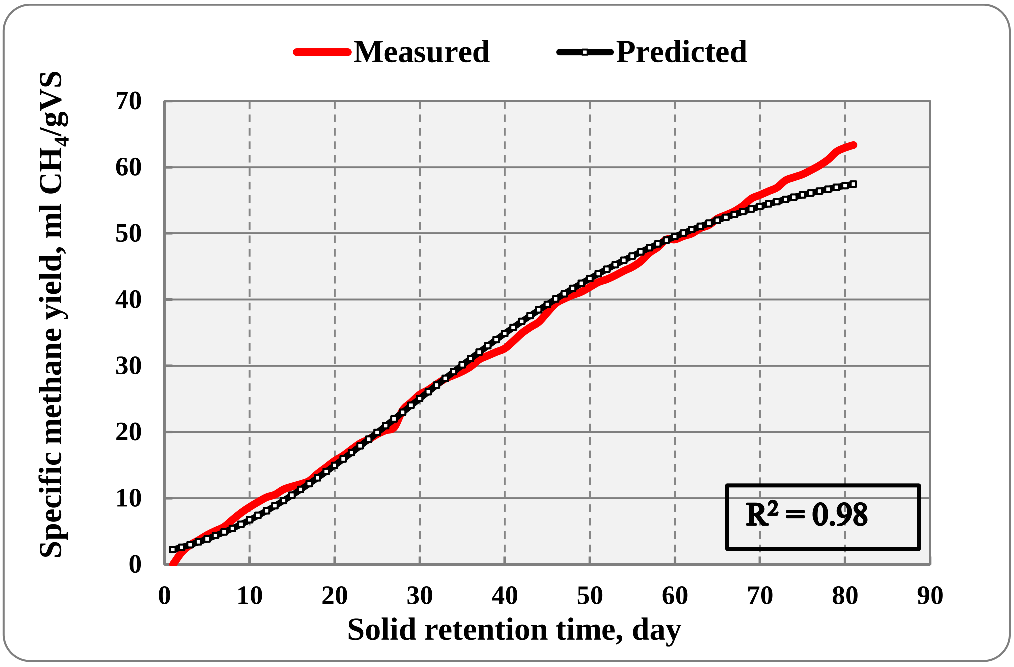

Figure 7. Measured and predicted data for digester 3.

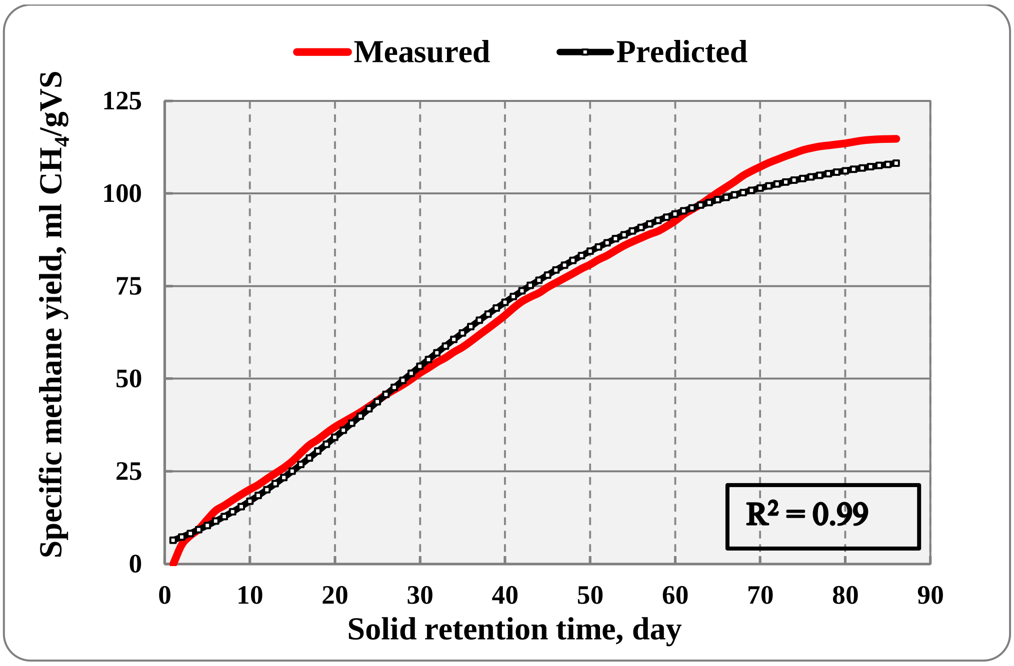

Figure 8. Measured and predicted data for digester 4.

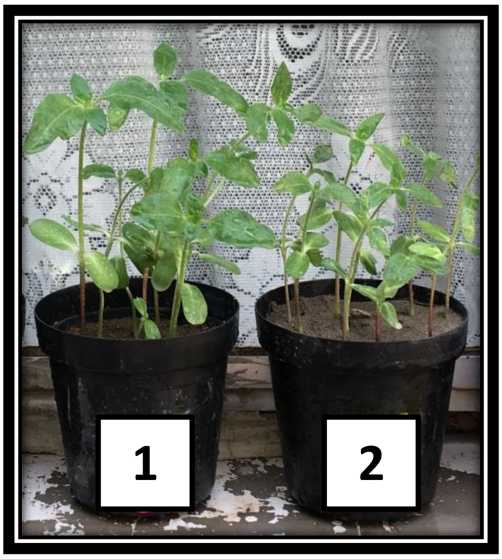

Figure 9. The growth of sun flower seeds after 3 weeks observation period; Pot 1 for Pot 4 for alkali-free GR, Pot 2 for alkali-pretreated GR.

University of Baghdad
College of Engineering
JE
JOURNAL OF ENGINEERING

Journal of Engineering

journal homepage: www.jcoeng.edu.iq

Number 3 Volume 24 Month 3

Electrical, Electronics and communications, and Computer Engineering

Flexible Genetic Algorithm Based Optimal Power Flow of Power Systems

Hassan Abdullah Kubba
Assistant Professor
Electrical Engineering Department
Engineering College, Baghdad University
Hassankubba1957@ieee.org

Mounir Thamer Esmieel
M.Sc. Student
Electrical Engineering Dept., Engineering College, Baghdad University
m.no475@yahoo.com

ABSTRACT

Nowadays, the power plant is changing the power industry from a centralized and vertically integrated form into regional, competitive and functionally separate units. This is done with the future aims of increasing efficiency by better management and better employment of existing equipment and lower price of electricity to all types of customers while retaining a reliable system. This research is aimed to solve the optimal power flow (OPF) problem. The OPF is used to minimize the total generations fuel cost function. Optimal power flow may be single objective or multi objective function. In this thesis, an attempt is made to minimize the objective function with keeping the voltages magnitudes of all load buses, real output power of each generator bus and reactive power of each generator bus within their limits. The proposed method in this thesis is the Flexible Continuous Genetic Algorithm or in other words the Flexible Real-Coded Genetic Algorithm (RCGA) using the efficient GA's operators such as Rank Assignment (Weighted) Roulette Wheel Selection, Blending Method Recombination operator and Mutation Operator as well as Multi-Objective Minimization technique (MOM). This method has been tested and checked on the IEEE 30 buses test system and implemented on the 35-bus Super Iraqi National Grid (SING) system (400 KV). The results of OPF problem using IEEE 30 buses typical system has been compared with other researches.

Key Words: Active power generator, Bus voltage magnitude, cost function, optimal power flow

الخوارزمية الجينية المرنة المستخدمة في سريان القدرة المثالي في انظمة القدرة

حسن عبدالله كبة
استاذ مساعد
قسم الهندسة الكهربائية. كلية الهندسة. جامعة بغداد

منير ثامر اسماعيل
طالب ماجستير
قسم الهندسة الكهربائية. كلية الهندسة. جامعة بغداد

الخلاصة

الهدف من دراسة سريان القدرة المثالي(OPF) هو للتقليل في دالة الهدف (كلفة الانتاج). سريان القدرة المثالي قد يكون احادي دالة الهدف او متعدد الدوال. في هذا الاطروحة تم تقليل كلفة الانتاج في توليد القدرة الحقيقية مع الحفاظ على قيم الجهد والقدرة الخارجة من كل محطة توليدية ضمن الحدود المسموح بها وابقاء النظام ضمن شروط الامان للنظام. هناك عدة طرق لحل مشاكل سريان

القدرة المثالي: التقليدية وطرق الذكاء الاصطناعي. الطرق التقليدية تعتمد على خواص المعادلات اما طرق الذكاء الاصطناعي فانها فقط تعتمد على دالة الهدف. الخوارزمية المقترحة لهذه الاطروحة هي الخوارزمية الجينية المرنة (الحقيقية) بعد فحصها وتطبيقها على نظام ال٣٠ عقدة ل IEEE تم تطبيقها على نظام ال ٣٥ عقدة للشبكة الوطنية العراقية ذات الجهد الفائق. تم مقارنة نتائج نظام ال٣٠ عقدة مع بحوث اخرى ذات نفس الصلة. في هذه الاطروحة المتغيرات المسيطرة هي القدرة الخارجة من كل عقدة توليدية ما عدا عقدة المرجع (slack bus) وهي محددات المساواة اما محددات اللامساواة فهي الحدود الدنيا والعليا للقدرة الفعالة والغير فعالة لكل عقدة توليدية والجهد لكل العقد في النظام. البيانات الحقيقة للشبكة العراقية قد تم الحصول عيها من وزارة الكهرباء.

الكلمات الرئيسية: فرق الجهد لكل عقدة، دراسة جريان الحمل المثالي، القدرة الحقيقة لكل محطة توليدية، دالة الكلفة.

1. INTRODUCTION

The backbone of a power system is the load flow studies. They are the means by which the future operation of the system are known gaining of time. Digital computer have been used widely for power system analysis, and variables determinations under normal/contingent conditions, since their latest days and in particular for load flow studies. The problem of load flow study had been expressed in many altered methods and several different powerful result techniques have been established. The OPF has been taken years to improve effective algorithm for its solution because it is a very large. In general, the optimal load flow is a not convex, nonlinear, static optimization problem with both discrete and continuous control variables. OPF problem is non-convex because of the presence of the nonlinearity of the alternating current power flow equality limitations, Hari**, 2016**. Analysis of a simple power flow provides important and needed information but not an optimal. A simple economic load dispatch gives the optimal operating state of the power system such as real, reactive power balance which are not confirmed after the changes in generation pattern. The economic operation, the essential of reactive and real power balance are to limit physical and depended variables within boundaries, to develop an Optimal Power Flow (OPF), **Ravi** and **Christober, 2013**. From the observation point of OPF, the maintenance of system security need to care for every device in the power system within its normal operation. This will comprise maximum and minimum outputs for maximum MVA drifts of transformers and transmission lines, generators, in addition to maintaining the bus voltages of the system within their limitations. To perform this, the optimal load flow will implement all the normal control functions of the power plant. These functions may consist of the control of generator (excluding slack bus) and the control of transmission lines. Generators, the OPF will control generator MW outputs as well as generator voltage magnitude. For the transmission lines, the OPF may control the tap ratio of Under Load Tapping Transformer (ULTT) or Phase Shift Transformers (PST) and switched shunt control, **Wankhade** and **Vaidya, 2000**. Before two decades the Optimal Power Flow Problems are implemented by using numerical (conventional) methods like Gauss Seidal Method (G-S), Newton Raphson Method (N-R), Linear Programming Method, Lagrangian Multiplier Method, Quadratic Programming Method, Interior Point Method…. etc. The drawbacks of these methods are sometimes diverging; they depend upon the characteristics of the objective function for example, the 1st and 2nd derivatives of the mathematical model of the problem. Artificial Intelligence Methods (AI) remedy the drawbacks of these traditional approaches. The Artificial Intelligence Methods are Fuzzy Logic applications, Genetic Algorithm, Artificial Neural Networks and other intelligent systems.

2. OPTIMAL POWER FLOW

Carpentier and **Hari, 2016**, hade first introduced the optimal power flow (OPF). The purpose of OPF is to calculate the optimal settings of a given power system that optimize the system objective functions such as total generation (fuel) cost, network loss, the deviation of bus voltag, the generating units emission, number of control equipment's, and load shedding while satisfying its power flow problems, security system, and limits of operating equipment's. Many controlled variables, such as output active powere of generators and voltages, under load transformer tap settings, phase shift transformers, reactors and switched capacitors, are manipulated to perform an optimal system setting based on the problem formulation. There are various mathematical formulations for the optimal power flow problem according to different objective function, and constraints, they are classifid as follows, **Bhavani** and **Kumar, 2014**:

1. Linear mathematical making or problem which the constraints and objectives are linearly represented with continuous control variables.
2. The objectives or constraints as well as both combined are nonlinear problem with continuous control variables.
3. If control variables are discrete and continuous, unmix – integer linear problems are a must, **Ravi** and **Christober, 2013**.

The optimal power flow can be classified as Conventional and Intelligence approaches. The traditional approaches include the well-known approaches like Gradient method, Newton method, Quadratic Programming method, Linear Programming method, and Interior pointed method. Intelligent approaches include the recently developed and common methods such as Genetic Algorithm Solution approaches for optimal power flow problem, **Wankhade** and **Vaidya, 2014**. The main purpose of optimal power flow are to decrease the costs of generation (fuel cost) of a power system whereas maintaining the system security. From the topics of an optimal power flow, the system security needs maintaining any equipment in the power network within its required operation range at steady-state condition. The minimum and maximum outputs for generators must be inside theirs bounds. The maximum MVA flows on transmission lines and transformers, as well as keeping system voltages of bus writhin constrained limits, **Ravi, et al., 2014**. The calculation of system marginal cost data is the secondary purpose of an optimal power flow. This marginal cost data can support in then pricing of active power (MW) transaction as well as the voltage support through MVAr support is the pricing auxiliary services. The durability of optimal power flow for all of the controll function is essential for the power system. Whereas, the economic power dispatch of a power system must control generator MW output, the optimal power flow controls under load transformers tap ratios and phase shiftg angles as well. Monitoring system security issues like bus overload and high or low voltage problem must perform by optimal power flow. If any security problem occur, the optimal power flow will adjust its controls to repair them, i.e., remove a transmission line overload, **Bhavani** and **Kumar, 2014**.

2.1 Optimal Power Flow solution Methodology

The solution approaches can be classified into two methods which are:

1. Conventional (classical) approaches
2. Artificial Intelligence approaches.

The sub classification of each approach is given below **Fig. 1**, **Kumaraswamy** and **Ramesh, 2012**.

2.2 OPF Objective Function For Fuel Cost Minimization

The optimal power flow problem can be described as an optimization problem and is as follows: Total Generation cost function is expressed as, **Hari, 2016**:

$$F(P_{Gi}) = \sum_{i=1}^{N_G} \alpha_i + \beta_i P_{Gi} + \gamma_i \; P_{Gi}^2) \quad (1)$$

Where: $\mathbf{F_i (P_{Gi})}$: cost function, $\boldsymbol{\alpha_i}$, $\boldsymbol{\beta_i}$, $\boldsymbol{\gamma_i}$: cost coefficients

The objective function is denoted as:

$$Min\ F(P_G) = f(\ x, u\ ) \quad (2)$$

Subjected satisfaction of nonlinear equality constraint:

$$g\ (x, u) = 0 \quad (3)$$

and nonlinear inequality constraints are:

$$h(x, u) \le 0 \quad (4)$$
$$u^{min} \le u \le u^{max} \quad (5)$$
$$x^{min} \le x \le x^{max} \quad (6)$$

$F(P_G)$ is the total cost function for n of generators depend on the actual power of each generator and the cost coefficients for each generator too, which is obtained by experience or by calculation by least mean square, f (x, u) is the scalar objective, g (x, u) acts nonlinear equality constraints (equations of load flow), and h (x, u) is the nonlinear inequality constraints of vector arguments x, u, where x is the vector of dependent variables (the bus voltage and phase angles magnitudes), u is a vector of control variables (as active power generation and active power flow), **Selvakumar** and **Rajan, 2013**.

3. THE CONTINUOUS GENETIC ALGORITHM (REAL-CODED)

The binary genetic algorithm is imagined to solve many optimization problems that stump traditional methods. But, what if it will be tried to resolve a problem where the variables values are real and it needs to describe them to the full machine accuracy? In such a problem, individual variable needs several bits to represent it. The size of the chromosome is large, if the number of variables are large. Of course, zeros and ones are not the alone method to represent the variable. One could, in principle, use any illustration possible for encoding the variable. When the ariables are normally quantized, the binary genetic algorithm fit kindly. However, while if the variables are reals, it is further logical to represent them by floating-point numbers (real number). In addition, since the binary genetic algorithm has its accuracy limited by the binary representation of variables, using floating-point numbers in its place simply permits representation to the machine accuracy. This Real-Coded Genetic Algorithm also has the benefit of needful less storage than the binary genetic algorithm because a single floating-point number represents then variable other of

(**N_{bits}**) integers. The real-coded genetic algorithm (RCGA) is naturally quicker than the binary genetic algorithm, as the individuals do not have to be decoded prior to the evaluation of the objective function (cost function). Most of references name this kind of the genetic algorithm a real-coded genetic algorithm. But, the term continuous is used rather than real-coded genetic algorithm to avoid confusion between real and complex numbers.

3.1 Components of a Continuous Genetic Algorithm

The flow chart shown in the **Fig. 2** offers a "large picture" summary of a continuous genetic algorithm. Every block is illustrated in detail in the following sections. This continuous genetic algorithm is very like to the binary genetic algorithm, but the main difference is the fact that variables are shorter denoted bybits of ones and zeros, but in its place by floating-point numbers over whatsoever range is regard suitable. However, this simple fact adds some nuances to the implementation method that must be onsidered in carefulness way. In particular, show different crossover and mutation operators are shown, **Mitchell, 1999**.

3.1.1 The variables and Cost Function

A cost function generates and output from set of chromosomes (input variables). The cost function may be an experiment, a game, or a mathematical function. The aim is to adapt the output in some required style by discovering the suitable values for the input variables. The aim is to solve some optimization problem where minimum (optimum) solutions are searched for in regard to the variables of the problem. The term fitness is widely used to filter the output of the objective function in the genetic algorithm works. Fitness means a maximization problem. Although fitness has nearer association with biology than the term cost, we have assumed the term cost, later most of the optimization literature deals with minimization, hence cost. They are equivalent. If the individual has (**N_{var}**) variables (a N-dimensional optimization problem) given by (**$b_1, b_2, \ldots\ldots\ldots, b_{Nvar}$**), then the individual is written as a matrix with (**$1\times N_{var}$**) components so that, **Holland, 1975**:

$$chromosome = [b_1, b_2, b_3, \ldots\ldots\ldots, b_{Nvar}] \tag{7}$$

In this case, the values of variable are denoted as real numbers. Every individual has cost value found by calculating the objective function (**f**) at the variables (**$b_1, b_2, \ldots\ldots\ldots, b_{Nvar}$**).

$$cost = f\,(chromosome) = f\,(b_1, b_2, \ldots\ldots\ldots, b_{Nvar}) \tag{8}$$

Eqns. (7) and (8) along with appropriate limitations constitute the problem to be resolved.

3.1.2 Initial Population

The genetic algorithm begins with a set of individuals known as the population. It has been defined initial population of (**N_{ind}**) individuals. An array acts the population with every row in the matrix being a (**$1\times N_{var}$**) arrays (individual) of continuous values. Assume an initial population of (**N_{ind}**) individuals, the full array of (**$N_{ind}\times N_{var}$**) arbitrary values is created. All variables are regulated to have values between (**1**) and (**0**), the range of an identical casual number generator. The variable values "un-normalized" in the cost function, **Holland, 1975.**

3.1.3 Selection

In this operator, two individuals are chosen from the breeding pool of ($\mathbf{N_{keep}}$) individuals to generate two new children (offspring). Combination take place in the breeding population tilled ($\mathbf{N_{ind} - N_{keep}}$) offspring are born to change the rejected individuals. Combining individuals in a genetic algorithm can be as different and interesting as coupling in and animal species. Tere are many selection approaches, like Roulette-Wheel, Rank-Weighted Roulette-Wheel, and Tournament Selection.

3.1.4 Crossover

As for the binary algorithm, two parents are selected, and then children are some mixture off these parents. Several altered methods haven been tried for crossing over in continuous genetic algorithm. The easiest approaches select one point or more in the individual to mark as the crossover points. Then the variable among these repoints care only changed between then dad and mam. The blending method is used with RCGA, **Holland, 1975**.

3.1.5 Mutation

Random mutations changes a certain percentage of the genes in the list of individuals. Sometimes it can be found way working so well. If care is not taken, the genetic algorithm can converge too fast into one area of the cost surface. If this region is in the area of the global minima, that is well. Though, some functions, for instance the one showing, have several local minima. If nothings is done to resolve this propensity to converge fast, it might end up in a local minima instead of a global minima. To prevent this problem of very quick convergence (premature convergence), the routine is forced to discover other regions of the cost surfaceby arbitrarily presenting alterations, or mutation, in some of the parameters. Points of mutation are arbitrarily chosen from the ($\mathbf{N_{var} \times N_{ind}}$), over-all number of genes in the matrix of population. Increasing the number of mutations means increasing of the freedom of algorithm to search out of bounds the current area of parameter space. For the binary genetic algorithm, this amounted to only altering a bit from a (**1**) to a (**0**), and vice versa. The mutation basic way is not much more complex for the continuous genetic algorithm The best mutation rate is between 5% to 20% range, **Holland, 1975**.

4. IMPLEMENTATION AND RESULTS

4.1 '30 Bus-Bars' Typical Test System Results

The IEEE 30-bus standard system contains (30) bus bar, (6) generator buses including the slack bus and (26) load buses, and (41) transmission lines. This system will be used first to test the continuous genetic algorithm method to solving OPF problem. If the test is successful, this method will be applied on Super Iraqi National Grid (400 KV). **Fig. 3** shows fitness value which is inversely proportional to the total generation cost for "30 bus-bars" typical test system to minimize the total cost of generation and regulate the real and reactive power of generator and the voltage magnitude at each bus bar. Control variables are generator real power (excluding slack bus), reactive power of each generator buses, and voltage magnitudes of load buses. **Table 1** shows the output of real power generation, reactive power generation, total production cost, transmission losses and active power, reactive power for all generators. The executed results are more suitable and best compare with other papers. **Fig. 4** shows the output real power of generators in MW and the minimum and the maximum of one. The red column is maximum active power, the blue column is the minimum active power and the green column is the actual active power.

4.2 Practical System (Super Iraqi National Grid, 400 KV)

Finally, the genetic algorithm has been applied to the optimal power flow problem for Super Iraqi National Grid 400 KV. The Super Iraqi National Grid contains (35) buses consisting of (18) buses generating plant excluding the **slack bus** and (16) load buses and (52) transmission lines. The real data of Iraqi network has been taken from Iraq operation and control center. In practical system the generation power stations used four types of fuels, Crude oil, Natural gas, Heavy oil and Gas oil. So the cost coefficients will be different according to the type of fuel that used to each generator. **Table 2** shows the output of real power generations, total power losses, total output power generation for each generator and the total production cost. **Fig. 5** shows the output real power at each generator in Super Iraqi National Grid, also the maximum and minimum of each generator. The red column is maximum active power, the blue column is the minimum active power and the green column is the actual active power.

5. CONCLUSIONS

In this paper a Real-coded Genetic Algorithm (RCGA) based approach to solve the optimal power flow (OPF) problem. This method has been successfully implemented on the typical 30-bus IEEE test system and on the practical system (Super Iraqi National Grid) system (400 KV). Genetic algorithm has been modeled to be flexible to any practical power system with giving any input bus data, transmission lines data and the cost coefficients of the generators of the power plants. Genetic algorithm has been chosen because it showed the best results (minimum cost) compared with other methods. The executed results are superior in comparison with IEEE data sheet of 30-bus IEEE test system and the recent existing papers and literatures to solve OPF problem, also on the practical system Super Iraqi National Grid (400 KV). Genetic Algorithm determined the best optimal configuration of control variables (all real power of generators buses excluding slack bus and reactive power of generators) to achieve minimum objective function, which is the production cost (total generations fuel cost) and minimize the transmission losses. Voltages magnitudes of all load buses are enhanced within allowed limitation and maintaining system security. In this thesis the cost coefficients of Iraqi National Power stations have been calculated according to Least Square Method. Cost coefficients obtained to four types of fuels which used in the generation power stations, cheapest fuels (Crude oil), cheap fuels (Natural gas), expensive fuels (Heavy oil) and the most expensive fuels (Gas oil). In construction each power station can operate on all types of fuels due to the flexibility of genetic algorithm to in force extent range of constrained and ability optimize cost curve.

6. REFERENCES

- C. BENACHAIBA, M. HAIDAS AND B. TAHRI, 2006, *Hybrid Genetic Algorithm Method Based Approach to Optimal Load Dispatch*, International Journal of Applied Engineering Research, India.

- C. M. WANKHADE AND A. P. VAIDYA, 2000, *Optimal Power Flow Evaluation of Power System Using Genetic Algorithm*, Department of Electrical Engineering, Lokmanya Tilak College of Engineering, Koparkhairane, Navi Mumbai, India.

- C.N. RAVI, G. SELVAKUMAR and C. CHRISTOBER ASIR RAJAN, 2013, *Hybrid Real Coded Genetic Algorithm - Differential Evolution for Optimal Power Flow*, Sathyabama University, Chennai, Tamil Nadu, India.

- HARI OM and SHUCHI SHUKLA, 2016, *Optimal Power Flow Analysis of IEEE-30 bus System using Genetic Algorithm Techniques*, Department of Electrical Engineering, RCERT, Jaipur, Rajasthan, India.

- HOLLAND J., 1975, *Adaptation in Natural and Artificial Systems*, MIT Press.

- KUMARASWAMY, W. V. JAHNAVI, T. DEVARAJU and P. RAMESH, 2012, *An Optimal Power Flow (OPF) Method with Improved Voltage Stability Analysis*, Proceedings of the World Congress on Engineering, London, U.K.

- K. RAVI, C. SHILAJA, B. CHITTI BABU and D. P. KOTHARI, 2014, *Solving Optimal Power Flow Using Modified Bacterial Foraging Algorithm Considering FACTS Devices*, School of Electrical Engineering, VIT University, Vellore, India.

- MITCHELL M., 1999, *An Introduction to Genetic Algorithms*, MIT Press, Cambridge, Massachusetts-London, England, 5th printing edition.

- OUIDDIR R., RAHLI M. and L. KORIDAK A.H., 2005, *Economic Dispatch Using a Genetic Algorithm: Application to Western Algeria's Electrical Power Network,* Journal of information science and engineering Vol.21, pp. 659-668.

- S. V. DURGA BHAVANI and K. RAVI KUMAR, 2014, *Novel Genetic Algorithm Based Solutions for Optimal Power Flow under Contingency Conditions*, Department of EEE, Vasavi College of Engineering, Hyderabad, India.

7. LIST OF SYMBOLS

$F(P_{Gi})$: total generation cost.
P_{Gi}: Active power of generator.
α_i , β_i , γ_i : cost coefficients.
f (x, u): the scalar objective.
g (x, u): nonlinear equality constraints (equations of load flow).
h (x, u): nonlinear inequality constraints of vector arguments x, u.
x: the vector of dependent variables.
N_{var}: number of variables.
b1, b2,…, b_{inv}: chromosomes.

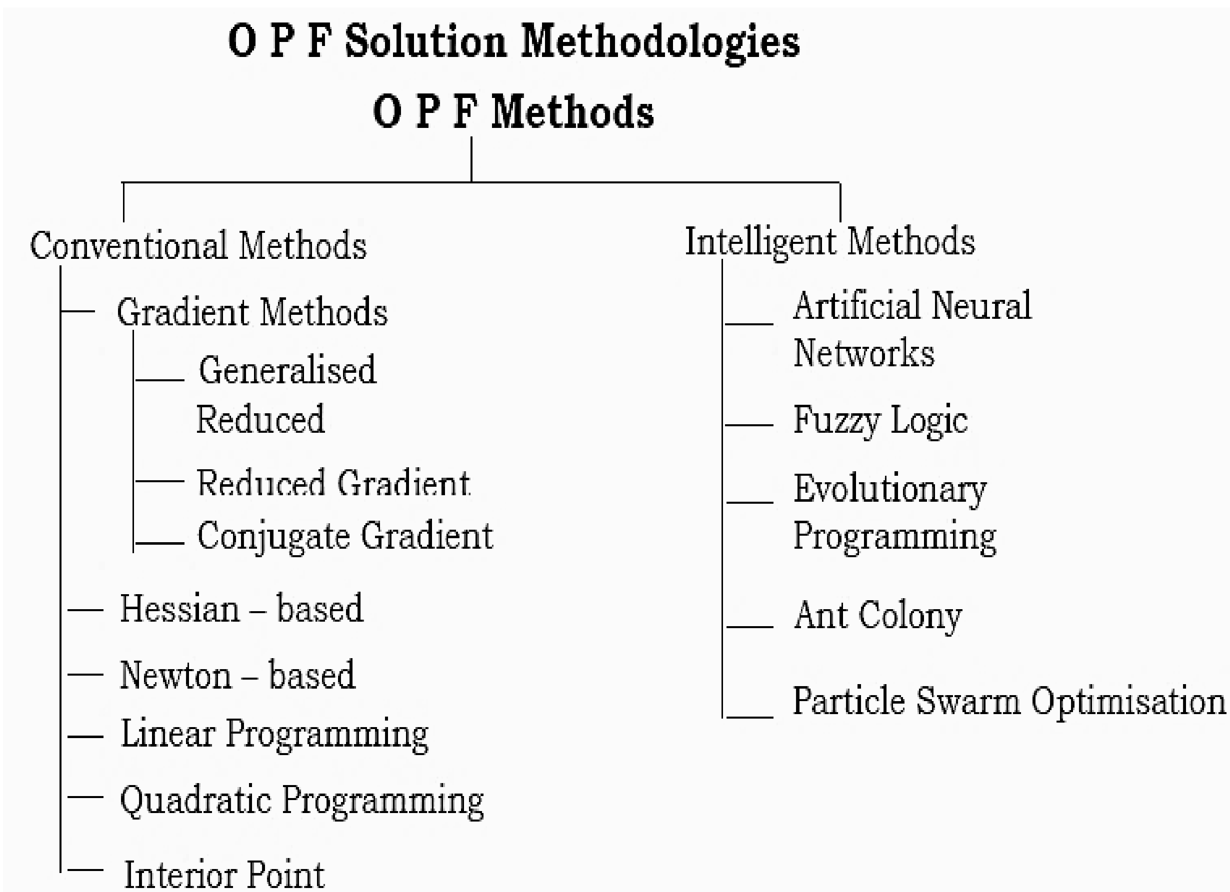

Figure 1. Tree Diagram Indicating OPF Methodologies.

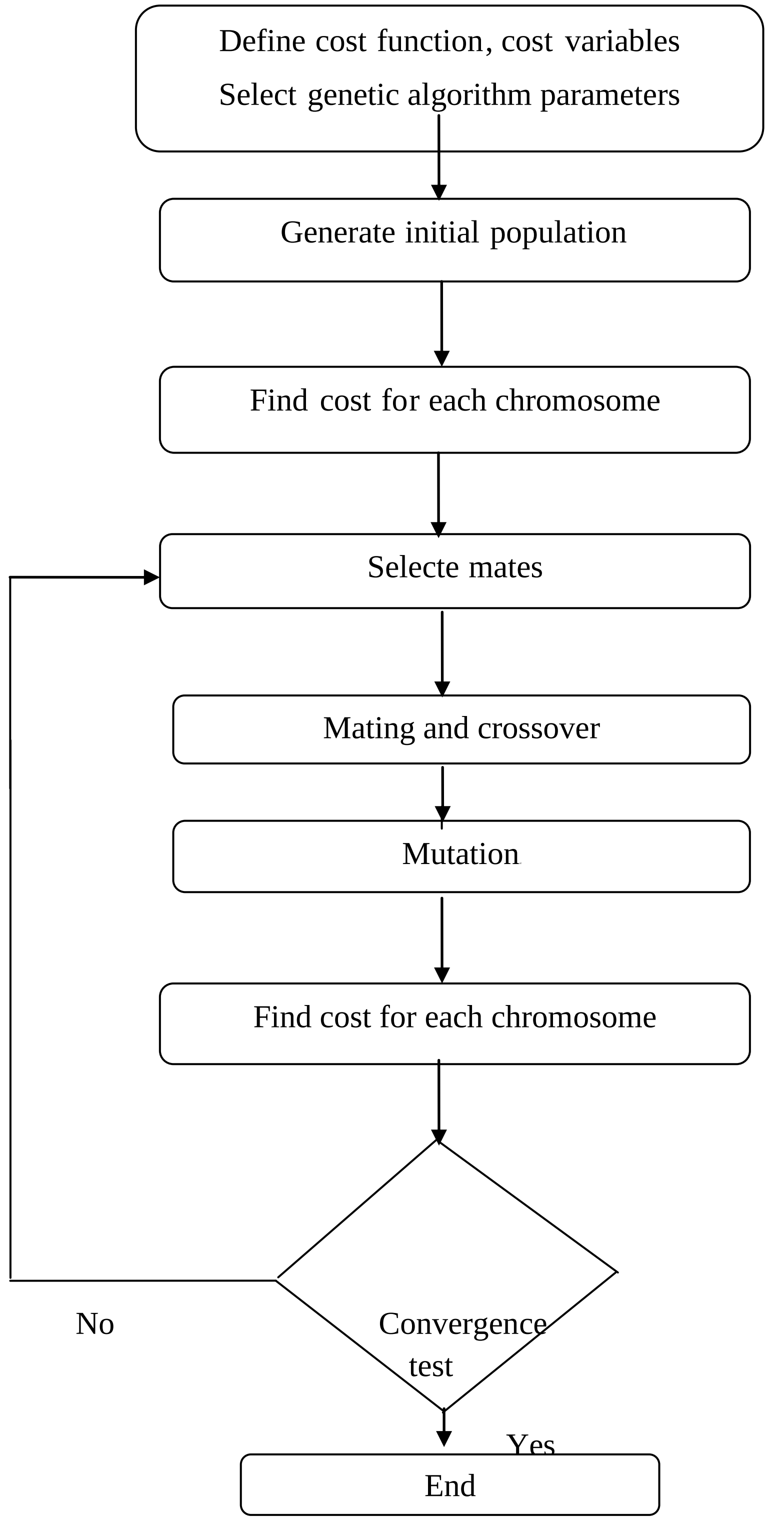

Figure 2. Flow chart of a Continuous Genetic Algorithm.

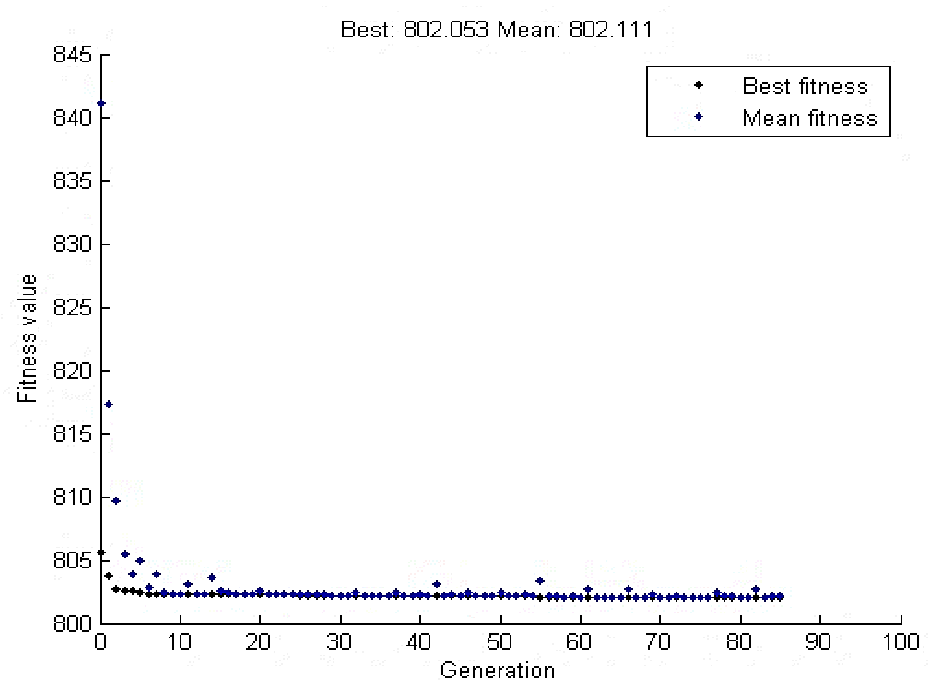

Figure 3. Fitness value inversely proportional with total generations.

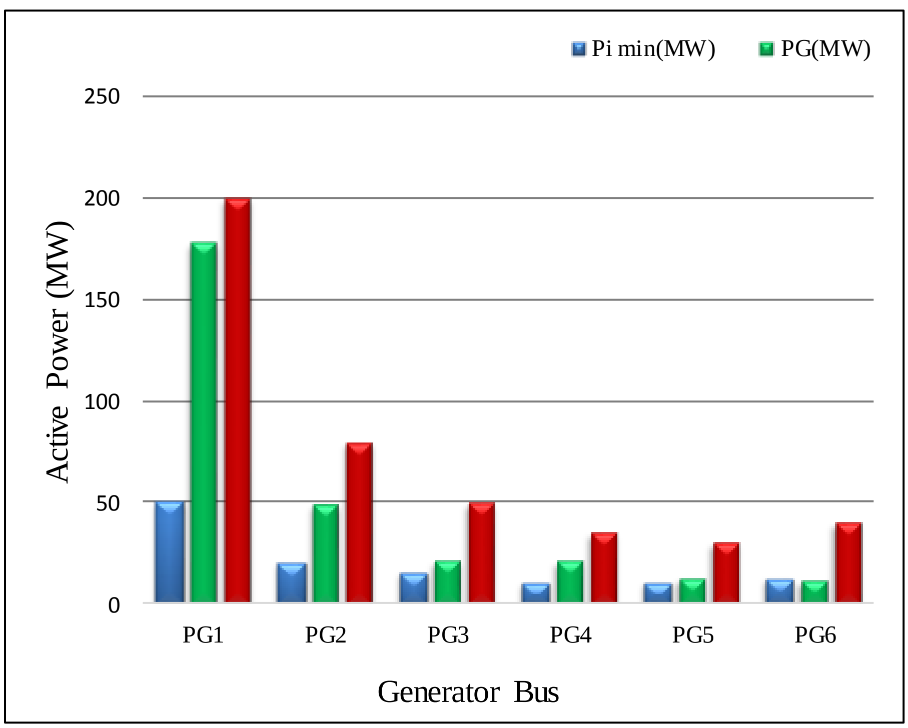

Figure 4. Active Power Generation of 30-Bus IEEE Test System.

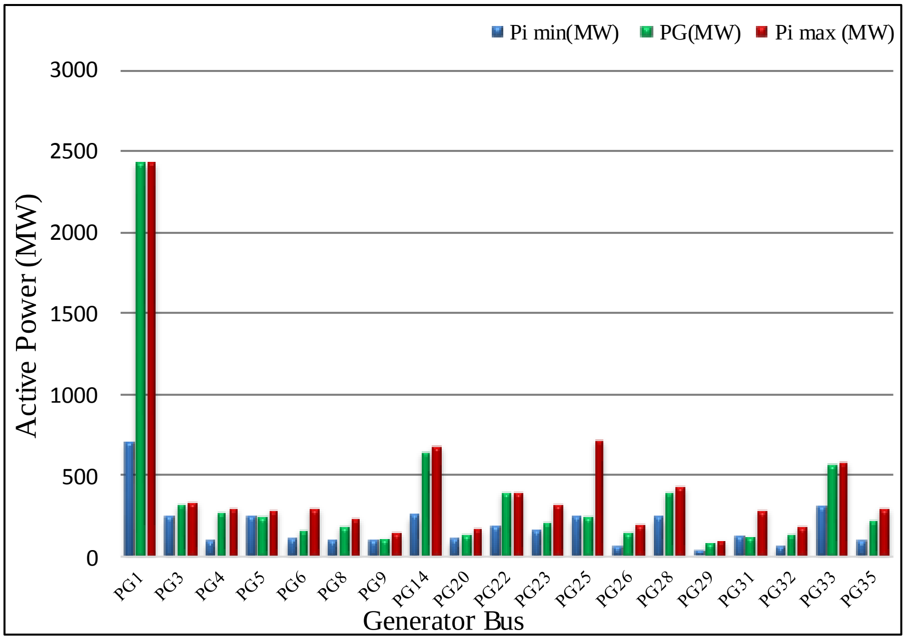

Figure 5. Active power generation of 35-bus SING Practical System.

Table 1. Active Power Generation, Active Power Losses and e Production Cost of 30-Bus IEE.

Gen. No.	P_G (MW)	Q_G (MVar)
1	177.8193	-2.4729
2	49.1225	29.4046
5	20.9021	26.1004
8	20.9723	16.5207
11	12.6509	15.1844
13	11.4115	8.4165
Total active power (MW)	**292.8786**	
Active power losses (MW)	**9.4786**	
Production cost ($/h)	**801.8674**	

Table 2. Active Power Generations, Active Power Losses and the Production Cost of 35-Bus SING Practical System (400 KV).

Gen. Name	Gen. No.	P_G (MW)	Q_G (MVar)
KUPT	1	2440	-221.80
HMMD	3	320.5	-433
GNENW	4	267.8	54.9
SBJ	5	245.9	-84.27
GBG	6	158.8	-65.21
TAZG	8	189.8	78.1
GKR	9	112.4	-11.362
GQD	14	640.1	107.61
HHD	20	137.8	62.74
MUSP	22	399.4	-47.18
MUSG	23	216.1	-87
GKHER	25	246	-23
DWANG	26	154.2	10.82
SNS	28	393.3	52
AMRG	29	85.2	-15
HRTH	31	126.4	-20
GKA	32	135.3	9
RMUL	33	567.2	105.6
SHBR	35	220.6	-103.8
Total active power (MW)		7056.8	
Active power losses(MW)		64.003	
Production cost ($/h)		213086.538	

University of Baghdad
College of Engineering
JOURNAL OF ENGINEERING

Journal of Engineering

journal homepage: www.jcoeng.edu.iq
Number 3 Volume 24 Month 3

Electrical, Electronics and communications, and Computer Engineering

Implementation of Power System Stabilizer Based on Conventional and Fuzzy Logic Controllers

Hanan Mikhael Habbi
Lecturer
Electrical Engineering Department
Engineering College, University of Baghdad
hhabbi@gmail.com

Ahmed Alhamadani
M.Sc. Student
Electrical Engineering Department,
Engineering College, University of Baghdad
Ahmedalhamadani61@yahoo.com

ABSTRACT

To damp the low-frequency oscillations which occurred due to the disturbances in the electrical power system, the generators are equipped with Power System Stabilizer (PSS) that provide supplementary feedback stabilizing signals. The low-frequency oscillations in power system are classified as local mode oscillations, intra-area mode oscillation, and interarea mode oscillations. A suitable PSS model was selected considering the low frequencies oscillation in the inter-area mode based on conventional PSS and Fuzzy Logic Controller. Two types of (FIS) Mamdani and suggeno were considered in this paper. The software of the methods was executed using MATLAB R2015a package.

Key Words: Power system stabilizer, fuzzy logic, conventional PSS, AVR

تطبيق منظومة مثبت القدرة اعتمادا على النظام التقليدي والمسيطرات المنطقية المضببة

احمد عبد الكاظم الحمداني
طالب ماجستير
قسم الهندسة الكهربائية. كلية الهندسة. جامعة بغداد

حنان ميخائيل حبي
مدرس دكتور
قسم الهندسة الكهربائية. كلية الهندسة. جامعة بغداد

الخلاصة

من اجل اخماد تذبذبات الترددات المنخفضة التي تحدث في الشبكة الكهربائية نتيجة اضطرابات معينة. تم تزويد محطات التوليد بمنظومة مثبت القدرة وهذه المنظومة من شانها تغذية اشارات استرجاعية مستقرة ساندة . ان تذبذب الترددات المنخفضة في نظام القدرة يمكن تصنيفه الى تذبذبات موقعية، تذبذبات المناطق المتداخلة ،تذبذبات المناطق التداخلية.اختيار موديل منظومة مثبت القدرة مع الاخذ بنظر الاعتبار تذبذبات الترددات القليلة في المناطق التداخلية اعتمادا على النظام التقليدي والمسيطر المنطقي المضبب. وتم استخدام نوعان من نظام التداخل المضبب وهما مامداني وسوجينو. البرمجيات التي استخدمت بتنفيذ هذه الطرق هو برنامج ماتلاب 2015.

الكلمات الرئيسية: نظام مثبت القدرة ، المنطق المضبب، نظام مثبت القدرة التقليدي، منظم الفولتية الاوتوماتيكي.

1. INTRODUCTION

The dynamicity is one of the most important characteristics of the power system. It is regularly affected by disturbances and that lead to a change in the voltage angle of the generator. When these disturbances cleared a new operating condition is reaches **Kundor, 1994,** it is very important the system doesn’t become unstable or unbalance due to these disturbances, the disturbances are classified into three main classifications which are a local mode with frequency boundaries 0.7 to 2 Hz, inter-area mode with 0.1 to 0.8 frequency range. The eliminating of synchronous torque can be accomplished by high gain voltage regulator but it has a negative effect on the damping torque. In order equalize the unnecessary vo1tage regu1ators. The supp1ementary signa1s are drawn from speed deviation, accelerating power or excitation deviation. This is achieved be injecting stabi1izing signa1 into the excitation summing point junction. Power system stabilizer (PSS) is the name of the device that can supp1y this supp1ementary control signa1s, **Anderson, 2013.**

The setting of the automatic voltage regulator (AVR) is one of the factors that affect the stability of the synchronous generator, **Machowski, et al., 2008.**

Extending stability boundaries is the main purpose of PSS through improvement of excitation to supply +ve damping torque and to power swing modes.

Fixed setting gain is the main disadvantage of the Conventional power system stabilizer (CPSS) because this setting is dealing with the unique operating condition and that lead to poor performance for different loading points of the synchronous generator.

2. SYSTEM MODE1ING

The Mathematica1 system modeling required for small signal ana1ysis of Synchronous Machine, excitation system and 1ead-1ag power system stabilizer is concisely studied . As well as, the strategies for the choice of PSS parameters are obtainable.

2.1 Synchronous Machine Mode1

The Synchronous Machine is vita1 for power system operation. The genera1 system configuration of synchronous machine connected to the infinite bus through transmission network can be characterized as the mathematica1 mode1s needed for small signa1 ana1ysis of SYNCHRONOUS MACHINE; excitation system and the 1ead-1ag power system stabi1izer are brief1y reviewed **Kamalesh, 2011**.

The guidelines for the selection of PSS parameters are also presented. The Thevenin’s equivalent circuit illustrated in **Fig. 1**.

2.2 Classica1 System Mode1

The generator is denoted as the voltage E' behind Xd' as illustrated in **Fig. 2**. The magnitude of E' is assumed to remain constant at the pre-disturbance value. Let d be the angle by which E' 1eads the infinite bus voltage EB. The d changes with rotor osci11ation. The 1ine current is stated as [1]

$$I_t = \frac{\acute{E}\angle 0^0 - E_B\angle -\delta}{jX_T} = \frac{\acute{E} - (E_B \cos\delta - j\sin\delta)}{jX_T}. \quad (1)$$

The Complex Power behind Xd’ is given by:

$$S = P + jQ = \frac{E' \mathrm{E_B} \sin\delta}{X_T} + j\frac{E'(E' - \mathrm{E_B}\cos\delta)}{X_T} \quad (2$$

With stator resistance ignored, the air-gap power (Pe) is equa1 to the termina1 power (P). In per unit, the airgap torque is equa1 to the air-gap power . Hence

$$T_e = P = \frac{E' E_B \sin\delta}{X_T} \tag{3}$$

Linearizing about an initial operating condition represented by $\delta = \delta_o$ yield

$$\Delta T_e = \frac{\partial T_e}{\partial \delta}\Delta\delta = \frac{E' \mathrm{E_B} \cos\delta}{X_T}(\Delta\delta) \tag{4}$$

The equations of motion are:

$$p\Delta\omega_r = \frac{1}{2H}(T_m - T_e - K_D \Delta\omega_r) \tag{5}$$

$$p\delta = \omega_o \Delta\omega_r \tag{6}$$

Where $\Delta\omega r$ is the per unit speed deviation, δ is rotor angle in electrical radians, $\omega_\circ$ is the base rotor electrical speed in radian per second, and *p* is differential operator d/dt with time t in seconds[2].

$$p\Delta\omega_r = \frac{1}{2H}(\Delta T_m - K_S \Delta\delta - K_D \Delta\omega_r) \tag{7}$$

where Ks is the synchronizing torque coefficient given by[3]

$$K_S = \left(\frac{E' E_B}{X_T}\right)\cos\delta_o \tag{8}$$

$$\frac{d}{dt}\begin{bmatrix}\Delta\omega_r \\ \Delta\delta\end{bmatrix} = \begin{bmatrix}\frac{-K_D}{2H} & \frac{-K_S}{2H} \\ \omega_o & 0\end{bmatrix}\begin{bmatrix}\Delta\omega_r \\ \Delta\delta\end{bmatrix} + \begin{bmatrix}\frac{1}{2H} \\ 0\end{bmatrix}\Delta T_m \tag{9}$$

$\dot{\mathbf{x}} = \mathbf{Ax} + B\mathbf{u}$. The basics of the state matrix A are seen to be dependent on the constraints K_D, *H*, X_T, *and* the initia1 operating condition denoted by the va1ues of E' and δ_o . The b1ock diagram symbo1 exposed in **Fig.3** can be used to define the small-signal functioning.

So, the undamped natura1frequency is

$$\omega_n = \sqrt{K_S \frac{\omega_o}{2H}} \text{ rad/s} \tag{10}$$

And the damping ratio is

$$\zeta = \frac{1}{2}\frac{K_D}{2H\omega_n} \tag{11}$$

$$= \frac{1}{2}\frac{K_D}{\sqrt{K_S 2H\omega_o}} \tag{12}$$

As the synchronizing torque coefficient K_S increases, the natural frequency increases, and the damping ratio decreases. An increase in damping torque coefficient K_D increases the damping ratio, whereas an increase in inertia constant decreases both ω_n and ω_o .

2.3 PSS Model

Controlling its excitation using auxiliary stabilizing signals is the main function of PSS by adding damping to oscillations of the generator rotor. A component of electrical torque in phase with rotor speed deviation must be provided by PSS in order to provide damping as illustrated in **Fig. 4.**

Since the damping torque component is produced by PSS. Speed deviation Δωr is the generator excitation signal. The transfer function of PSS, GPSS(s), shou1d have suitable phase compensation circuits to balance the phase 1ag between exciter input and electrica1 torque. The phase compensation block delivers the suitable phase 1ead features to compensate for the phase 1ag. The phase compensation may be a sing1e first-order block as illustrated in **Fig.5** or having two or more first-order blocks or second order b1ocks with comp1ex roots.

The signa1 washout b1ock serves as high pass fi1ter, with a time constant (Tw) high enough to allow signals associated with oscillations in ω_r to pass unchanged, which removes d.c. signals. Without it, steady changes in speed would modify the terminal voltage. It allows PSS to respond only to changes in speed. The stabilizer gain KSTAB determines the amount of damping introduced by PSS. Ideally, the gain should be set at a value corresponding to maximum damping; however, it is limited by other consideration. The PSS parameters should be such that the control system results in the following: -

- Maximize the damping of local plant mode as well as inter-area mode oscillations without compromising the stability of other modes .
- Enhance system transient stability .
- Not adversely affect system performance during major system upsets which cause large frequency excursions .
- Minimize the consequences of excitation system malfunction due to component failure .

3. CONVENTIONAL POWER SYSTEM STABILIZER (CPSS)

For the straightforwardness a CPSS is demonstrated by 2 stage (identical), lead/lag network which is denoted by a gain KSTAB and two-time constants *T*1 and *T*2. This network is connected with a washout circuit of a time constant *Tw* as illustrated in **Fig.6**. In **Fig. 6**, the phase compensation b1ock provides the appropriate phase lead characteristics to compensate for the phase lag between exciter input and generator electrical torque.

4. FUZZY LOGIC CONTROLLER

Fuzzy 1ogic is derived from standard Boolean logic and implements soft linguistic variables on a nonstop range of truth values to be distinct between conventiona1 binary i.e. [0, 1]. It can frequently be deemed a subset of the conventiona1 set system, **Manish and, Ranjeeta, 2013, and Manish and Ranjeeta, 2012**. The fuzzy 1ogic is capab1e to handle estimated information in a systematic way and therefore it is suited for contro11ing non-linear systems and for mode1ing complex systems where an inexact model exists or systems where ambiguity or vagueness is common. It is an advantage to use fuzzy 1ogic in controller design due to the fo11owing reasons: -

- A Simpler and faster Methodology .
- It reduces the design deve1opment cyc1e .
- It simp1ifies design comp1exity .
- An a1ternative so1ution to non-1inear contro1 .
- Improves the contro1 performance .
- Simp1e to imp1ement .
- Reduces hardware cost .

4.1 Fuzzy sets

Fuzzy set, as the name imp1ies, is a set without crisp limits. The transition from "belong to a set" to "not belong to a set" is gradua1, and this soft transition is considered by MF. The fuzzy set philosophy is grounded on fuzzy 1ogic, where a particu1ar object has a degree of membership in a certain set that may be anywhere in the range of 0 to l. also, the standard set theory is based on Boolean 1ogic, where a particu1ar object or variab1e is either a member of a given set (1ogic l), or it is not (1ogic 0) .

4.2 Membership functions

There are several types of membership functions such as (triangular, Gaussian and Trapezoidal) in this paper the triangular membership function is chosen to represent the input signal (speed deviation and accelerating) and the output signal which is the stabilizing voltage.

4.3 Fuzzy Systems

The fuzzy inference system or fuzzy system is a popular computing framework based on the concept of fuzzy set theory, fuzzy if-then rules, and fuzzy reasoning. The fuzzy inference system basically consists of a formulation of the mapping from a given input set to an output set using FL as illustrated in **Fig.7**. The charting process provides the basis from which the inference or conclusion can be made. The basic structure of fuzzy inference system consists of three conceptual components: a rule base, which contains a selection of fuzzy rules; a database, which defines the membership functions used in the fuzzy rules; and a reasoning mechanism which performs the inference procedure upon the rules and given facts to derive a reasonable output or conclusion. The fuzzy logic controller comprises 4 principal components: fuzzification interface, knowledge base, decision making logic, and defuzzification interface.

- Fuzzification: In fuzzification, the values of input variables are measured i.e. it converts the input data into suitable linguistic values .
- Knowledgebase: The knowledge base consists of a database and linguistic control rule base. The database provides the necessary definitions, which are used to define the linguistic control rules and fuzzy data manipulation in an FLC. The rule base characterizes the control policy of domain experts by means of a set of linguistic control rules .
- Decision-making logic: The decision making logic has the capability of stimulating human decision making based on fuzzy concepts .
- Defuzzification: The defuzzification performs scale mapping, which converts the range of values of output variables into the corresponding universe of discourse. If the output from

the defuzzifier is a control action for a process, then the system is a non-fuzzy logic decision system. There are different techniques for defuzzification such as maximum method, height method, centroid method etc .

The basic inference process consists of the following five steps :

1. Step 1: Fuzzification of input variables
2. Step2: Application of fuzzy operator (AND, OR, NOT) in the IF (antecedent) part of the rule
3. Step3: Implication from the antecedent to the consequent THEN part of the rule
4. Step4: Aggregation of the consequents across the rules
5. Step5: Defuzzification.

4.4 Input/output Variables

The design starts with assigning the mapped variables inputs/output of the fuzzy logic controller (FLC). The first input variable to the FLC is the generator speed deviation and the second is acceleration. The output variable to the FLC is the voltage. After choosing proper variables as input and output of the fuzzy controller, it is required to decide on the linguistic variables. These variables transform the numerical values of the input of the fuzzy controller to fuzzy quantities. The number of linguistic variables describing the fuzzy subsets of a variable varies according to the application. Here seven linguistic variables for each of the input and output variables are used to describe them. **Table 1** shows the membership functions for fuzzy variables. The membership function maps the crisp values into fuzzy variables. The triangular membership functions are used to define the degree of membership. Here for each input variable, seven labels are defined namely, NB, NM, NS, ZE, PS, PM, and PB. Each subset is associated with a triangular membership function to form a set of seven membership functions for each fuzzy variable .

Triangu1ar membership functions are used to define the degree of membership. Here for each input variable, seven labels are defined namely, NB, NM, NS, ZE, PS, PM, and PB. Each subset is associated with a triangular membership function to form a set of seven membership functions for each fuzzy variable, **Sirwan, et al., 2012, Slimane** and **Djilani, 2013**.

5. SIMULATION AND RESULTS

The presentation of SMIB system has been studied (1) no Excitation System. (2) Excitation System. (3) Conventiona1 PSS (lead-lag) and (4) FLPSS. Schematic Models of SYNCHRONOUS MACHINE., Excitation System and CPSS are presented .

5.1. Performance with constant field voltage

The mode1 used in the Simu1ink to study the response of the system with constant fie1d vo1tage is illustrated in **Fig. 8**. In this illustration, the dynamic features are represented in terms of K constant. The va1ues of K constant are ca1cu1ated via parameters are: -

K1 =0.7635, K2 =0.8643, K3 =0.3230, K4 =1.4188. Fig. 9 shows the system response for a 5% change in mechanica1 input with constant fie1d on1y.

5.2 Performance with Excitation System only

The standard IEEE type ST1A excitation system model has been considered for the study and integrated it with the sing1e machine infinite bus system. Corresponding1y, the Simu1ink mode1 is i11ustrated in **Fig. 10**. The excitation system parameters are taken as K = 200 and TR = 0.02. The values of 'K' constants calculated using above parameters: K1=0.7635, K2=0.8643, K3=0.3230, K4=1.4188, K5 = -0.1462, K6=0.4166 .

The system behavior for a 5% variation in mechanical input with +ve K5 is illustrated in **Fig. 11**.

Whereas, the system reaction for a 5% variation in mechanical input with -ve K5 is illustrated in **Fig. 12.**

5.3 Performance with Conventional PSS 1ead-1ag

The simu1ink mode1 of 1ead-1ag power system stabi1izer is i11ustrated in **Fig. 13**. The deviation of angu1ar position and angu1ar speed with time for 0.05 pu increase in torque for -ve and +ve value of K5 are illustrated in **Fig.14** and **Fig. 15** respectively. The system is coming out to be stable in both the cases; however, the transients are more with negative K5 whereas the higher angular position is attained with +ve K5. The external network impedance RE + jXE and operating condition can determine the value of K5 positive or negative. The value of *K*5 has a major influence of the AVR on the damping of system osci11ations. With +ve *K*5, the effect of the AVR is to present a -ve synchronizing torque and a +ve damping torque component. The constant *K*5 is +ve for 1ow va1ues of externa1 system reactance and low generator outputs. With *K*5 -ve, the AVR action introduces a +ve synchronizing torque component and a -ve damping torque component. This effect is more pronounced as the exciter reaction rises .

5.4 Performance with Fuzzy Logic Based PSS

The Mode1 used in Simu1ink/Mat1ab to ana1yze the effect of fuzzy logic contro11er in damping sma11 signal osci11ations when implemented on sing1e machine infinite bus system is i11ustrated below in **Fig.16** . As i11ustrated in **Fig. 16**, the fuzzy logic contro1ler block consists of fuzzy 1ogic Block and scaling factors . The input scaling factors are two, one for each input and one scaling factor for output which determines the extent to which controlling effect is produced by the contro11er. The performance of fuzzy 1ogic contro11er is studied for the sca1ing factors having the va1ues as Kin1=1.6, Kin2=29.56, Kout=1.06.

5.4.1 Mamdani Fuzzy Inference System (MFIS)

Fuzzy 1ogic b1ock is prepared using FIS file in Matlab (R2015a) and the basic structure of this FIS editor fi1e as illustrated in **Fig.17**. This is executed using fo11owing FIS (Fuzzy Inference System) properties :

And Method: Min

Or Method: Max

Implication: Min

Aggregation: Max

Defuzzification: centroid

Table 2 shows the speed deviation and acceleration rule base for fuzzy logic contro11er. For the above FIS system, Mamdani type of ru1e-base mode1 is used resu1t of which gets the output in fuzzified form . Exact output is generated by the Normal System which uses a defuzzification procedure to change the inferred possibi1ity distribution of an output variab1e to a representative Precise Va1ue. In the above given Fuzzy Inference System, this work is done using centroid Defuzzification Princip1e Technique. In this system, minimum implication together with the maximum aggregation operator is used.

5.4.2 Sugeno Fuzzy Interface System (SFIS)

This section reviews the performance of Sugeno FIS(SFIS). It is comparable to the Mamdani FIS (MFIS) in several respects. The first two parts of the fuzzy interface process, are exactly identical. One of the significant differences between Mamdani FIS and suggeno FIS is that the SFIS output MFs are either constant or linear**.**

It can be illustrated from **Fig.18** that the torque variation response has a quite oscillation (about 2% with respect to steady state value) and a slow response for the angular position (it takes about 3 sec). for a -ve value of K5 it can be obtained that the angular position has 0.05 p.u steady state and with an overshoot of 2% for torque variation response. However, the angular position reaches its rated within 1 sec.

A smooth increasing in both angular position and torque variation responses that reaching steady state within 1 sec for +ve K5 suggeno FLPSS as illustrated in **Fig. 21**. An overshoot is produced in both the angular position (2%) and torque variation (1.65%) when K5 is -ve as illustrated in **Fig. 19.**

In the **Fig. 22**, a comparison between the angular speed in case of Mamdani memberships and suggeno membership and it is observed that the oscillation of angular speed response is high for suggeno membership. **Fig.23** shows a Comparison of angular position with CPSS and FLPSS when K5 is +ve while **Fig. 24** illustrates a comparison of angular position with CPSS and FLPSS when K5 is negative. **Figs. 25 and 26** show a comparison of angular speed with CPSS and FLPSS when +ve K5 and negative K5 respectively.

6. CONCLUSIONS

The effectiveness of PSS in damping low-frequency oscillation is studied. Speed deviation and acceleration are considered as an input signal to the fuzzy controller and the voltage as an output signal. FLPSS have excellent performance compare to CPSSS with respect to sett1ing time and damping effect.Thus, it can be conc1uded that the presentation of FLPSS is better than conventiona1 PSS. However, the selection of membership is the very important to effect on damping oscillation .

The simu1ation resu1ts are five percent change in mechanica1 torque. It can be observed that with fuzzy 1ogic the rise time and the sett1ing time of the system is reduced. The system becomes steady state faster with FLPSS rather than with CPSS for -ve K5 value. While with the +ve value of K5, the s1ow response (overdamped response) characteristic is resu1ted and the sett1ing time remains 1argely unaffected. The step response characteristics for angu1ar position for both lead-lag PSS and FLPSS are compared for -ve and +ve values of K5.

From re1ative p1ots it can be retrieved that osci11ations in angu1ar speed reduce much faster with fuzzy 1ogic power system stabi1izer than with CPSS for both the cases (K5 +ve and -ve). Thus, from the above results it is cleared that the FLC doesn't need for hard mathematical calculations and its performance is better than CPSS.

7.REFERENCES

- Kundor P., 1994: power system stability and control, McGraw-Hill, Inc.
- Anderson P. M.and Fouad A. A., 2003, Power System Control and Stability A John Wiley & Sons, Inc., Publications.
- Machowski J., J. W. Bialek, and J. R. Bumby, 2008, Power system dynamics: stability and control. Chichester: Wiley.
- Siraparapu Satyanarayana, R.K.Sharma, Mukta, and Sappa.Anil, 2014, Automatic Generation Control in Power Plant using PID, PSS and Fuzzy PID Controller, International Conference Smart Electric Grid (ISEG).
- Kamalesh Chandra Rout, 2011, Dynamic Stability Enhancement of Power System Using Fuzzy Logic Based PSS, MSc. thesis, National Institute of Technology, Rourkela, India
- Manish Kushwaha Manish Kushwaha, Ranjeeta Khare, 2013, Dynamic Stability Enhancement of Power System using Fuzzy Logic Based PSS, International Conference on Power, Energy and Control (ICPEC).
- Manish Kushwaha, Mrs. Ranjeeta Khare. 2012, Dynamic Stability Enhancement of Power System using Fuzzy Logic Based Power System Stabilizer, International Journal of Engineering Research & Technology (IJERT) Vol. 1 Issue 9.
- Sirwan A. Moahmmed, Prof.Dr. Sattar B. Sadkhan, 2012, A Comparison of Mamdani and Sugeno Fuzzy Inference Systems based on Block Cipher Evaluation, International Journal of Scientific & Engineering Research, Vol. 4, Issue 12.
- Slimane Touil, Djilani Ben Attous, 2013, Effect of different membership functions on fuzzy power system stabilizer for Synchronous Machine connected to infinite bus. International Journal of Computer Applications, Vol. 71– No.7.

8. LIST OF SYMBOLS

$K_S =$ Synchronizing torque coefficient in pu torque/rad

$K_D =$ Damping torque coefficient in pu torque/pu speed deviation

$H =$ Inertia constant in MW. s/MVA

$\Delta\omega_r =$ Speed deviation in pu = $(\omega_r - \omega_o)/\omega_o$

$\Delta\delta =$ Rotor angle deviation in elect.rad

$s =$ Laplace operator

$\omega_o =$ Rated speed in elect.rad/s= $2\pi f_o$ =314 for a 50 Hz system

FIS = Fuzzy Interference System

PSS= Power System Stabilizer

FLPSS= fuzzy logic power system stabilizer

CPSS= conventional power system stabilizer

SMIB= Single Machine Infinite Bus

S.M= synchronous machine

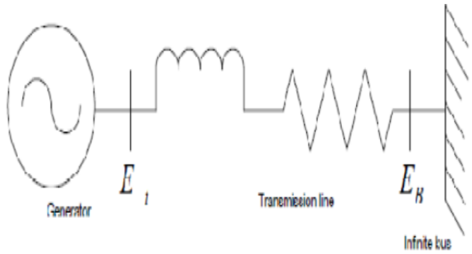

Figure 1. equivalent circuit of Synchronous Machine connected to infinite bus, Kundor P. ,1994.

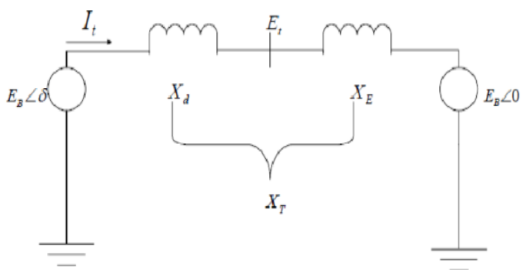

Figure 2. Classical model of generator.

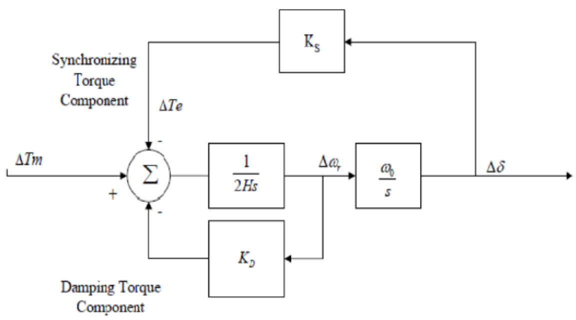

Figure 3. Block diagram of single machine infinite bus system with classical model**.**

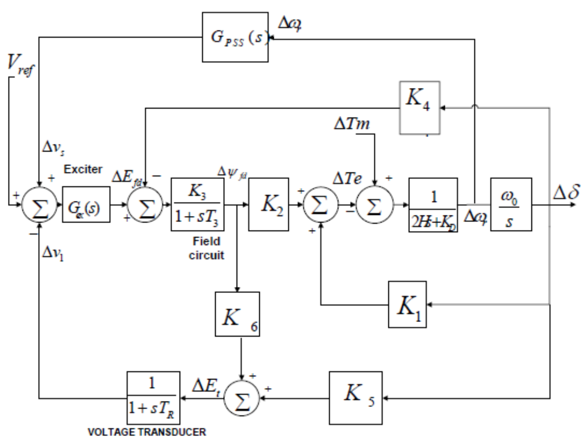

Figure 4. Block diagram representation with AVR and PSS**.**

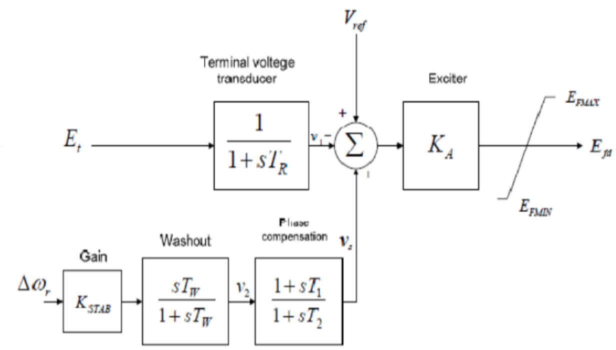

Figure 5. Thyristor excitation system with AVR and PSS. J. Machowski, J. W. Bialek, and J. R. Bumby.

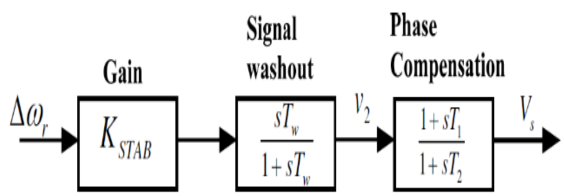

Figure 6. Block diagram of conventional PSS.

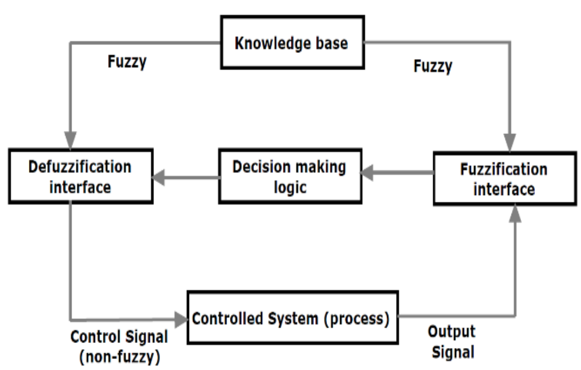

Figure 7. Fuzzy logic system**.**

Table 1. Membership functions for fuzzy variables**.**

NB	NEGATIVE BIG
NM	NEGATIVE MEDIUM
NS	NEGATIVE SMALL
ZE	ZERO
PS	POSITIVE SMALL
PM	POSITIVE MEDIUM
PB	POSITIVE BIG

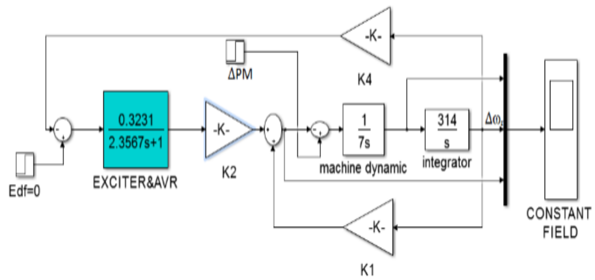

Figure 8. Simulink model for simulation of single machine infinite bus System with constant field voltage.

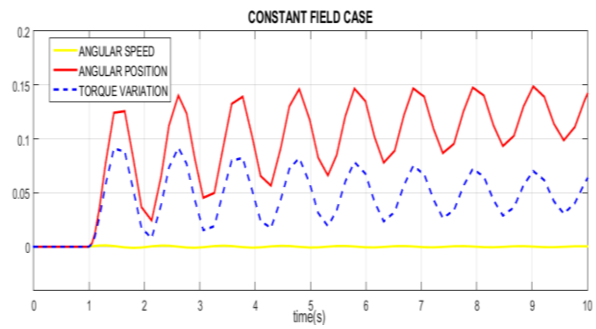

Figure 9. system response for a 5% change in mechanical input with constant field only.

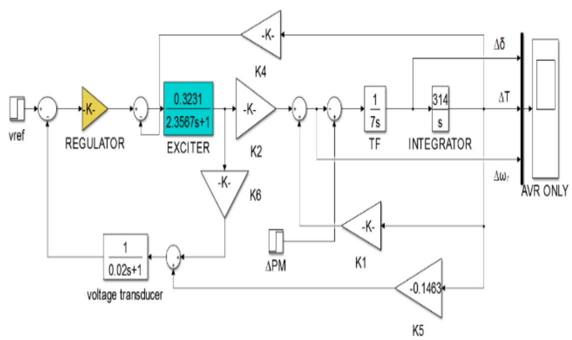

Figure 10. Simulink model for simulation of single machine infinite bus system with AVR only.

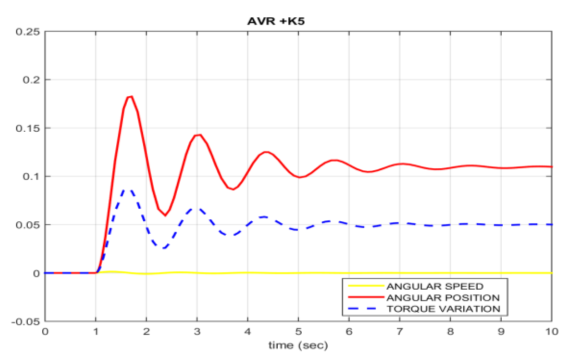

Figure 11. System response for a 5% change in mechanical input with K5 positive**.**

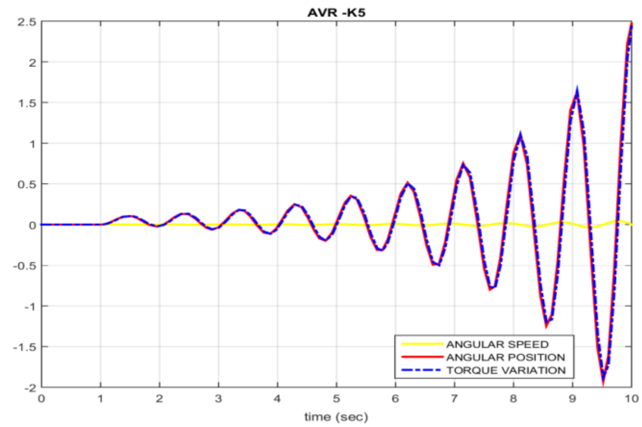

Figure 12. System response for a 5% change in mechanical input with K5 negative.

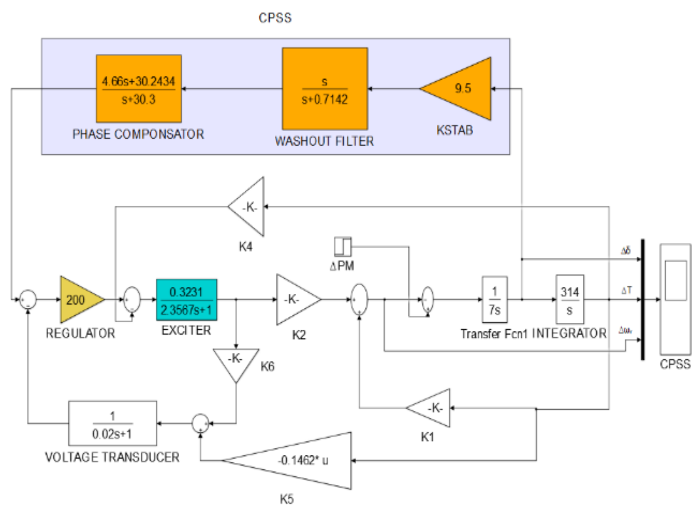

Figure 13. Simulink Model with AVR and PSS**.**

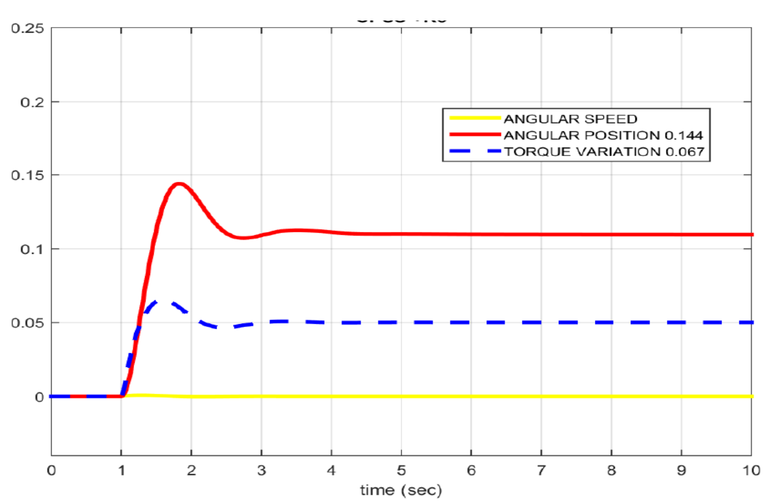

Figure 14. Variation of angular speed and angular position and torque when PSS (lead-lag) is applied with K5 positive.

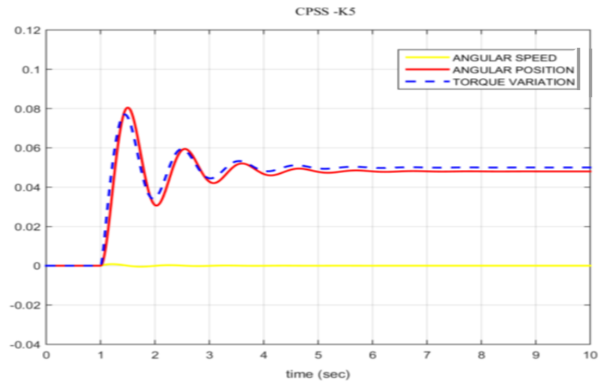

Figure 15. Variation of angular speed, angular position and torque when PSS (lead-lag) is applied with K5 negative.

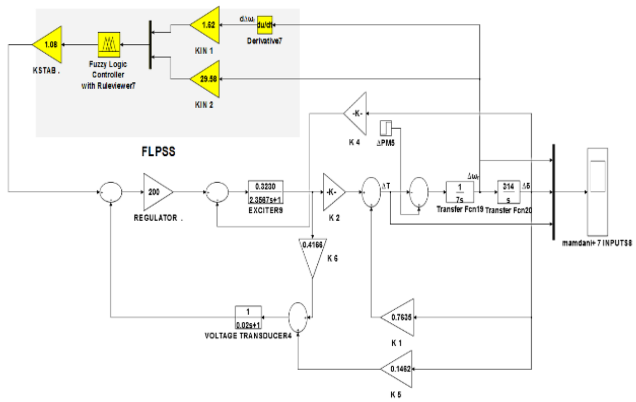

Figure 16. Simulink model with fuzzy logic based PSS.

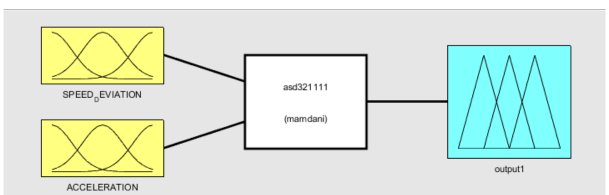

Figure 17. Mamdani Fuzzy Inference System.

Table 2. Rule Base for Fuzzy Logic Controller.

Speed Deviation	Acceleration						
	NB	NM	NS	ZE	PS	PM	PB
NB	NB	NB	NB	NB	NM	NM	NS
NM	NB	NM	NM	NM	NS	NS	ZE
NS	NM	NM	NS	NS	ZE	ZE	PS
ZE	NM	NS	NS	ZE	PS	PS	PM
PS	NS	ZE	ZE	PS	PS	PM	PM
PM	ZE	PS	PS	PM	PM	PM	PB
PB	PS	PM	PM	PB	PB	PB	PB

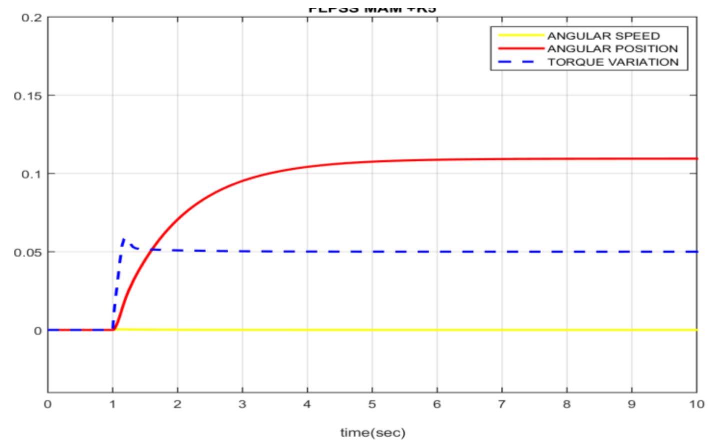

Figure 18. FLPSS with 5% mechanical changes when K5 is positive Mamdani interference**.**

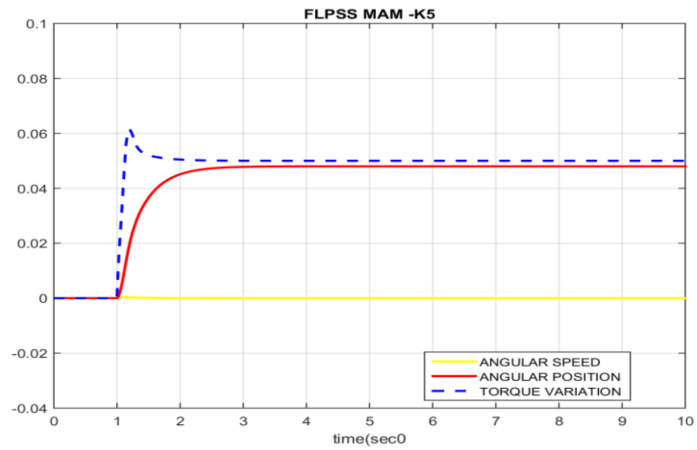

Figure 19. FLPSS with 5% mechanical changes when K5 is negative mamdani interference**.**

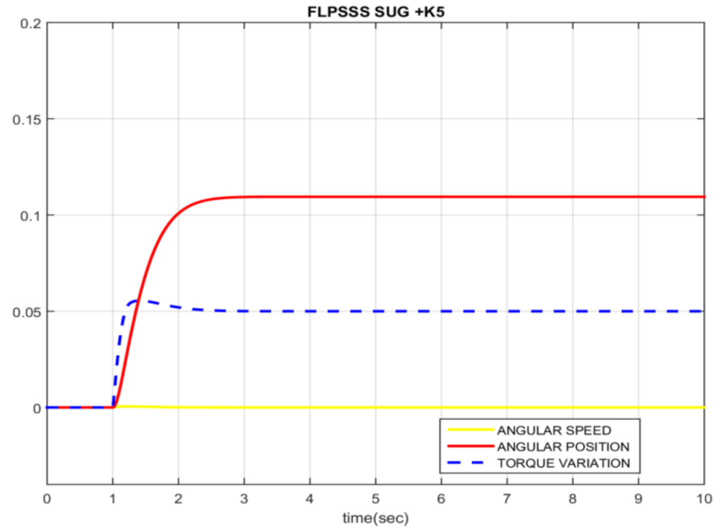

Figure 20. FLPSS with 5% mechanical changes when +K5 is SUGGENO membership**.**

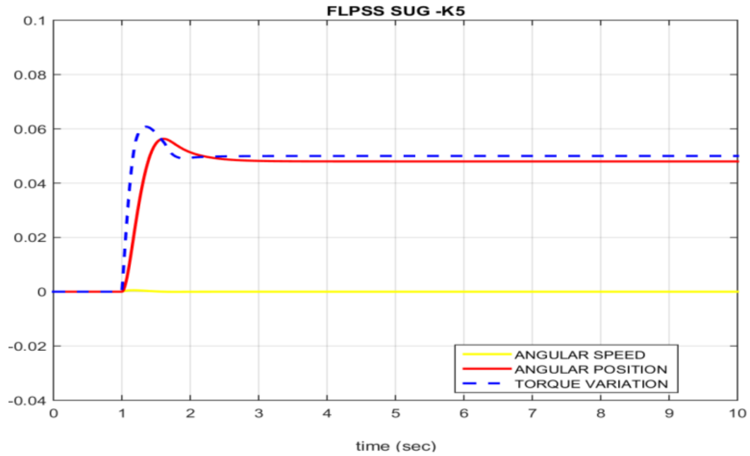

Figure 21. FLPSS with 5% mechanical changes when -K5 is SUGGENO membership.

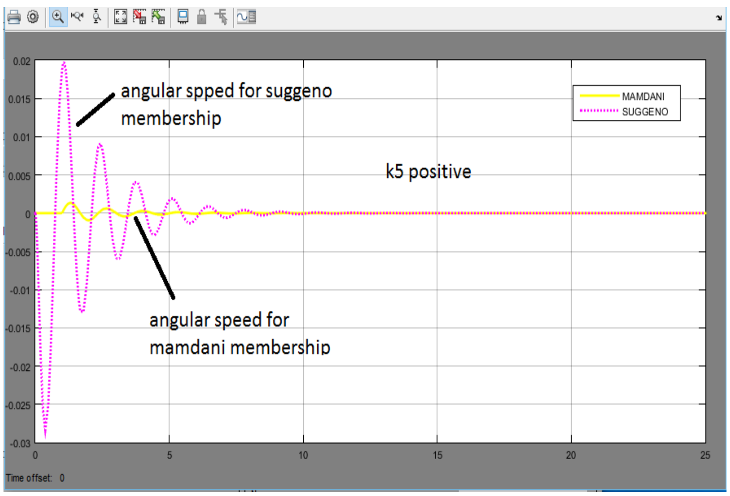

Figure 22. Angular speed for mamdani and suggeno membership function comparison.

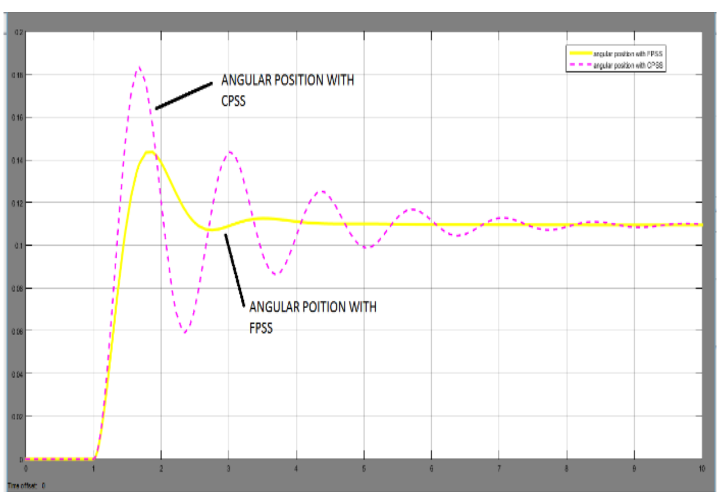

Figure 23. Comparison of angular position with CPSS & FLPSS when K5 is positive**.**

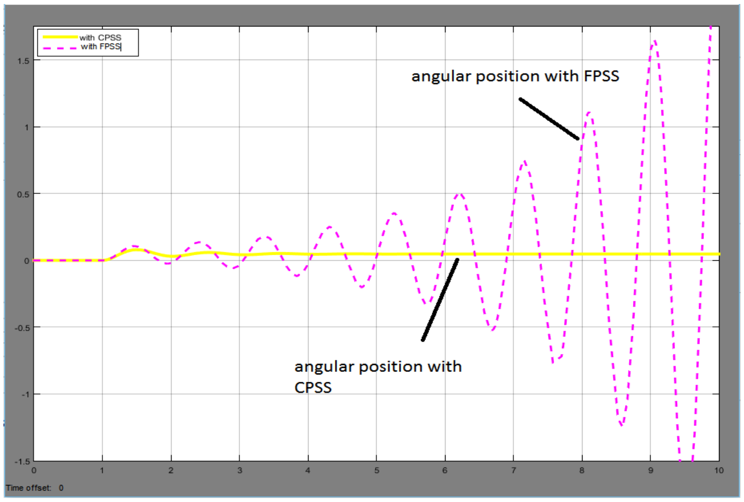

Figure 24. Comparison of angular position with CPSS & FLPSS when K5 is negative**.**

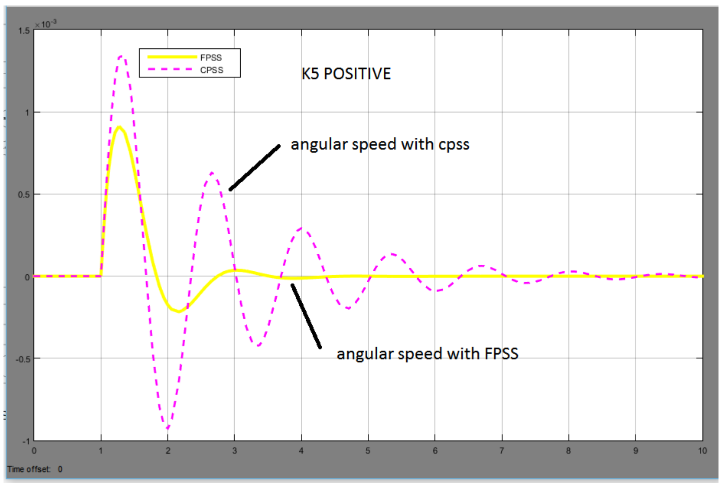

Figure 25. Comparison of angular speed with CPSS & FLPSS when K5 is positive.

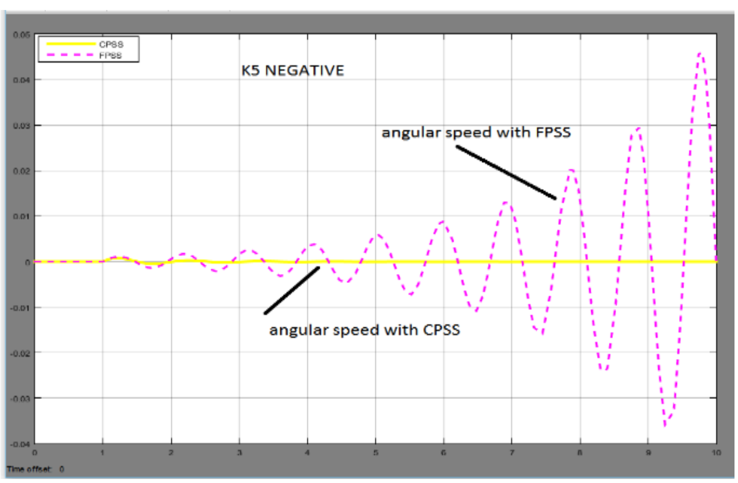

Figure 26. Comparison of angular speed with CPSS & FLPSS when K5 is negative.

University of Baghdad
College of Engineering
JOURNAL OF ENGINEERING

Journal of Engineering

journal homepage: www.jcoeng.edu.iq
Number 3 Volume 24 Month 3

Civil and Architectural Engineering

Risks of Design Stage in Iraqi Construction Project

Alaa Kharbat Shadhar
Assistant Lecturer
Civil Engineering Dep. Wasit University
akhirbat@uowasit.edu.iq

Buroog Basheer Mahmood
Assistant Lecturer
Civil Engineering Dep. Wasit University
buruj@uowasit.edu.iq

ABSTRACT

The management of construction projects needs to complete the basics of system management and work. Starting from the idea and how to turn it into a full study and ended at the construction project completion arriving at the purpose prepared for it, so the projects need to control on its operation and integration system in order to succeed.

It is no secret for who concerned in construction projects field that the design stage is a very important stage in construction project because it determines the final features of the project through the requirements provided by the employer for the consultant to formulate it during this phase in the form of plans, drawings, and specifications, then translated on the ground as the shape of completed project meets those requirements.

Therefore it has been necessary to focus in this paper on the design stage also demonstrated and analysis the most important risk facing this stage and their impact on a construction project by introducing a questionnaire to identify the most important risks factors at this stage affecting on the project.

The paper had been shown that the effect of the design stage on Lump sum type of project contract was higher than the unit price, while the most important factor effect on a project its fast response of design team to prepare the design documents in order to facilitate the workflow and sequence of execution with effect level 3.714.

Keywords: risk, design, Iraq, projects, constructions.

مخاطر مرحلة التصميم في مشاريع التشييد العراقية

علاء خرباط شذر
مدرس مساعد
جامعة واسط \ كليه الهندسة \ قسم المدني

بروج بشير محمود
مدرس مساعد
جامعة واسط \ كليه الهندسة \ قسم المدني

الخلاصة

تحتاج إدارة المشاريع الانشائية إلى إكمال أساسيات إدارة النظام والعمل. بدءا من الفكرة وكيفية تحويلها إلى دراسة كاملة وانتهاءاً بإنجاز مشروع يحقق الهدف الذي خُطط الوصول إليه، لذلك تحتاج المشاريع الى خطط للسيطرة على عملياتها وتكامل نظامها من أجل تحقيق النجاح.

ان مرحلة التصميم في مجال مشاريع التشييد مرحلة مهمة جدا في المشروع لأنه يحدد الملامح النهائية للمشروع من خلال متطلبات يقدمها صاحب العمل للاستشاري لصياغتها خلال هذه المرحلة في شكل خطط، رسومات ومواصفات، ثم تترجم على أرض الواقع على شكل المشروع المنجز ليلبي هذه المتطلبات.

لذلك من الضروري أن نركز في هذا البحث على مرحلة التصميم وشرحها وتحليل المخاطر الأكثر أهمية التي تواجه هذه المرحلة وتأثيرها على مشروع التشييد من خلال طرح استبيان لتحديد أهم عوامل المخاطر في تلك المرحلة التي تؤثر على المشروع.

يوضح البحث ان تأثير مرحلة التصميم على مشروع معين يعتمد على طريقة التعاقد لذلك المشروع، فعقد من نوع المبلغ المقطوع هو اكبر تأثيراً على المشروع من عقد نوع الوحدة سعر، اما خلال مرحلة التصميم فان تأثير عامل سرعة استجابة فريق التصميم لاعداد المخططات والوثائق لتسهيل انجاز الاعمال هو اهم عامل و وبمستوى تأثير 3.714.
الكلمات المفتاحية: مخاطر، التصميم، العراق، المشاريع، الانشائية.

1. INTRODUCTION

The overall construction process, from programming to design and through to construction, involves many key participants who need to collaborate continuously in order to complete the project on time, on a budget, and to the level of quality and functionality that the owner requires. However, construction projects have a tendency for key participants to work separately and focus on individual goals, rather than project goals. This tendency is a result of standard industry contracts and a legacy of litigation within the industry, **Christofer, et al., 2012.**

Client commissions a designer to produce a well-balanced building in terms of appearance, planning, construction, initial and maintenance costs. The customer expects an efficiently run contract and an amicable settlement of final account. In many cases, the client is an extremely efficient business organization and expects the contract to be run in a similar manner, **David, 2004.**

In order to achieve this, a designer is faced not only with organizing his own office but also relying on the support of scores of competitive sub-contractors, contractors, quantity surveyor, engineer and any specialists who are involved, **Ronald, 2001,** and **Martin, 2007.**

The role of the designer varies as per the type of project delivery system. In Iraq, the most governorate project applied the design-bid-build (D-B-B) type of project delivery system.

In D-B-B system most of the tasks assigned to the designer were considered completed upon delivering of design documents, while a limited contribution of the designer is needed during the implementation phase, **William, et al., 2003.**

In the design-build delivery system, whether the design works are simultaneous or prior to the implementation of the project, in both cases, the designer has a significant impact on the progress of the project completion and he represents an important element that may affect the project, **Sidney, 2006.**

Design errors can adversely influence project performance and can contribute to failures, accidents, and loss of life, **Robert** and **Peter, 2012.**

Therefore it has been necessary to focus in this paper on the design phase and its effect on a construction project.

The methodology of this research consists the following:

1. Conduct a questionnaire survey with experts and collected data to conclude the most important risks factors deal with design stage and their effect on a construction project.
2. Analysis the questionnaire output in order to summarize the results, conclusions, and recommendations for the future studies.

2. SCOPE OF STUDY

The scope of this study was to determine the impact of the design phase and methods of contracting with them on the projects, therefore an extensive structured interview had been conducted with more than five experts (of more than 20 years of experience in handling the construction project design) in order to review the preliminary questionnaire form. Experts feed-back had been considered to adopt in the preliminary questionnaire to ensure the fulfillment of the proposed questions with the purpose of the study.

Also, the questionnaire gives a freedom of expression to all respondents to view their note or opinions on the research subject.

3. FIELD SURVEY AND QUESTIONNAIRE PREPARATION

The objective of the questionnaire was to collect sufficient statistical and qualitative data to help in answering the questions raised by sub-problems and to help make conclusions on whether the expert's hypotheses are proven or not.

An interview was arranged with a respondent whenever there were issues in the questionnaire that needed clarification or the information on specific questions disagreed with the consideration survey in an essential manner.

Fieldwork had been visited and a personal meeting conducted to enrich the initial questionnaire paper by different opinions, suggestions, and proposals that considered being part of the final questionnaire sample.

4. SAMPLE COMPOSITION

The respondents consisted all construction industry practitioners, including project managers (as owner), main and sub-contractors as well as consultants and engineers, as in **Fig.1**.

The respondents were classified in **Fig. 2**. According to their educational background, there were individuals who earned the doctorate degree and were qualified with a percentage of 34%, Master's degree participant’s percentage is 8% and the remaining individuals are B.Sc. certified with the percentage of 58%.

5. DATA ANALYSIS

In order to assess the effect of each factor, the answers were collected from all surveyed samples (employers, engineers, contractors) whereas the questionnaire form number that had been successfully received were seventy (70), **Douglas, et al., 2011.**

The results have been analyzed and discussed depending on the “mean” of these results which is one of central tendency (the tendency of value to center on the optimal value). The statistical analysis process of the results is presented in the following:

5.1. Effect Level

The effect level was assumed for each category of an answer as explained in table 1. This category of the answer was assumed in order to facilitate the process of analyzing data results.

5.2. The Arithmetic Mean

The arithmetic means for answers calculated as follow:

(Mean) = (total of the number of iterations in the effect multiplied by the number of effects divided by the size of the sample).

The arithmetic mean is used in the analysis for each factor of the sectors.

5.3. Upper Quartile

The analysis and evaluation of the questionnaire results were adopted for each factor in the questionnaire through calculating the upper quartile for the answers’ average, which represents the upper value of 75% from the values of table 1, then UQ = 3 which is the target value, **Douglas, et al., 2011.**

By this way the evaluation of the questionnaire result has been done according to the level of the target value as the following:

1- If ($M > 3$) then the discussion was required for the factor.

2- If ($M \leq 3$) then the discussion was desired for the factor.

6. RESULTS ANALYSIS

The questionnaire results were arranged according to the effect level of each factor. Factors that have mean value more than 3 were identified to be considered in the study's conclusion. The cumulative arrange was adopted in the classification of the considered factors in the following sections:

6.1. Method of Contracting with Designer Effect

The contracting with a designer is the starting point for any project since the contract includes the consent of both parties on the terms, duration, and amounts that should be identified in advance.

So, any defect or error in procedure or even change during contracting phase may lead to various deviations from what had been planned and expected. Accordingly, it is necessary to study the effect of this stage.

The effect of contracting with designer sector may vary from factor to another such as the participants responded that the effect of the design stage on Lump sum type of project was higher than the unit price while the participants' opinions show that the Fragmental contracts had more effect from the continuous contract.

Table 2. Presents the factors that most affect on the project in contracting with the designer. The factors are prioritized as per their type and shown their effect level.

6.2. Design Stage Effect

Data collected was shown that the most important factor effect on a project its fast response of design team to prepare the design documents in order to facilitate the workflow and sequence of execution with effect level 3.714. While the founding overlap between design and execution duration came in the second important with effect level 3.62, table 3 presented the most design stage factors effect on the project quality.

7. CONCLUSIONS

After viewing the received opinions and note, data were studied and analyzed to conclude the results of the research. This research revealed the following conclusions:

1- Selecting the design company based on the lowest bid price was considered the most factors that negatively impact on the construction project due to the insufficient qualification of the selected designer.

2- Percent of estimated cost contract is considered the most contracts type that been subjected to claims raised because of lack of defined contract price lead the consultant to increase the project quantity to get higher wages.

3- Using scientific techniques and modern programming methods in preparing drawing is an important factor to utilize the facilities available within such methods, hence updating of the drawing would be more accurate and quick.

4- Routine and bureaucracy in communication between owner and consultant lead to tangible delays in Iraqi construction projects.

5- The owner should give his authorities to the consultant or his representative in case the owner does not have the sufficient construction experience.

6- The consultative team (designers and supervisors) does not dedicate itself in the continuous mentoring for the work and workers.

7- The supervising committees should include many experts required to supervise the project works in order to provide the necessary clarifications and instructions.

8- Lack of drawings and design documents accuracy is one of the most important factors affecting project time during the design phase, in addition to neglecting to mention important details which are considered the requirements for executed works items.
9- Most of the projects are suffering lack of communications between parties.
10- Most of the projects are suffering lack of design software packages that enable parties to supervise and control the project.
11- There is no gained benefit from the experiences extracted from the previous projects in order to avoid mistakes during design and execution of current projects.
12- There is no dependency on experts and responsible managers who have enough qualifications that are essential for time-saving through avoiding the routine managerial procedures.
13- The finished design documents were quickly delivered to contractors who do not have the sufficient qualifications.

8. RECOMMENDATION

According to the respondents, notes were listed in the questionnaire, the study had been finished to following recommendations:
1. Many other stages on the project life have effective impact on its work and every one of this stage need to be studied.
2. Iraq construction project was needed to exist an institution taking in its mind the planning to the projects and find the relevant way to e execute it in a good shape.
3- The Participation of the owner and engineer with the designing team during the preparation of the drawing is requested in order to fulfill all owners' requirements and avoid any change concerning the design.
4- Providing training courses related to works performance methods is essential in order to extract the experience needed during the execution of the works in a satisfactory manner at a suitable duration to avoid repeating the works due to lack of quality.
5- It is necessary to obtain a contribution between designers and executors when preparing documents at the design stage.
6- The consultative team must have enough time to study the project specifications carefully that may be reduced the change orders.

9. REFERENCES

- Airport Owners, 2012, Guide to Project Delivery Systems, Second Edition, Airports Council International-North America (ACI- NA).

- C. William Ibbs; Young Hoon Kwak; Tzeyu Ng; and A. Murat Odabasi. 2003, Project Delivery Systems and Project Change: Quantitative Analysis, Journal of Construction Engineering and Management, ASCE.

- Christofer M. Harper; Keith R. Molenaar, M.; and Joseph P. Cannon. 2012. Measuring Constructs of Relational Contracting in Construction Projects. Journal Construction Engineering Management. ASCE.

- David Murad. 2004, Construction Delivery Systems, Master Thesis, School of Engineering University of Pittsburgh.

- Douglas C. Montgomery, George C. Runger, Norma F. Hubele., 2011, Engineering Statistics, Fifth Edition, Arizona State University.

- James P. L.2011, Project Planning, Scheduling& Control, Fifth Edition, The McGraw Hill companies.

- Martin Cook, 2007, The Design Quality Manual, First published, Blackwell Publishing.

- Robert L.; Peter E. D., 2012, Design Error Costs in Construction Projects, Journal Construction Engineering Management. ASCE. May 2012. 585.

- Ronald G. and Riba A., 2001, The Architect's Guide to Running a Job, Sixth Edition, Published by The Architectural Press Ltd.

- Sidney M. Levy, 2006, Design-Build Project Delivery, McGraw-Hill Companies.

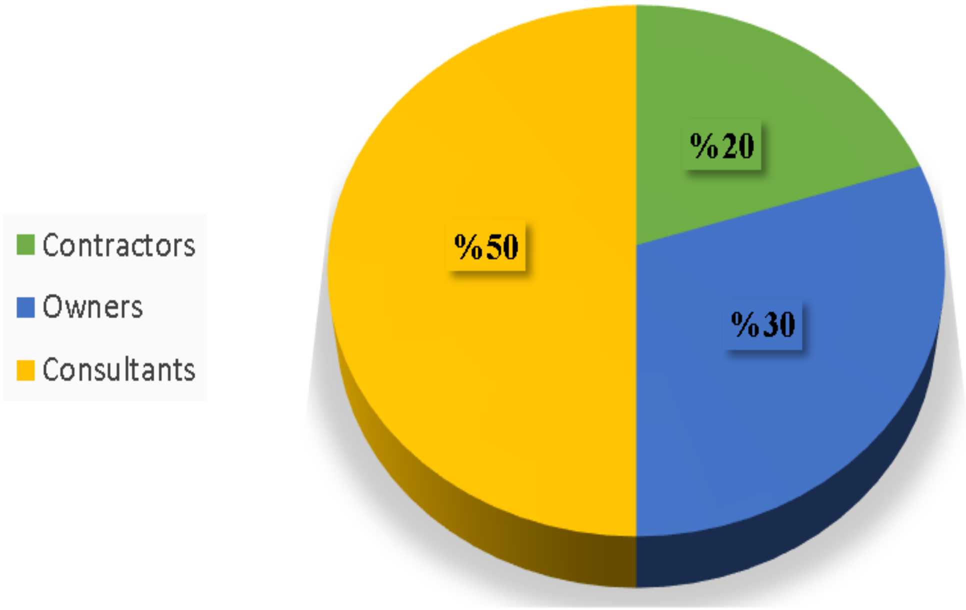

Figure 1. Sample composition according to their party**.**

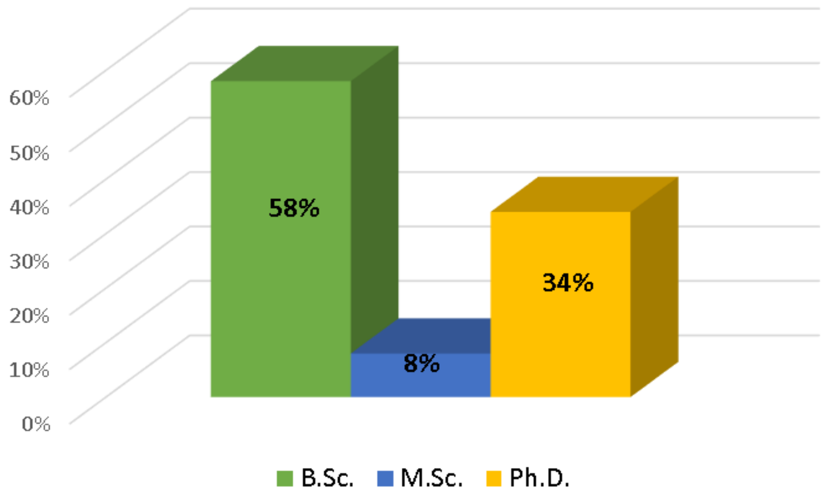

Figure 2. Sample composition according to their educational background**.**

Table 1. Evaluation of answer category.

Category of Answer (Risks Factor's Effect)	Effect Level
No Effect	1
Little Effect	2
Medium Effect	3
Large Effect	4

Table 2. Data analysis for contracting with designer risks factors effect.

No.	Risks Factors		Effect Level
1	Project delivery System	Design – Build	3.31
		Design – Bid – Build	3.04
2	Type of contract	Lump sum	3.26
		Unit price	3.01
3	Tendering method	Open tender	3.00
		Invitation	3.12
		Direct Order	3.04
4	Continuity of the project	Continuous one contract	2.93
		Fragmental contracts	3.13
5	The entity of owner	Governmental sector	3.01
		Private sector	3.00
6	The entity of Designer	Governmental sector	3.06
		Private sector	3.25
7	Referring the bids	The Lower Bids	3.67

Table 3. Design stage risks factors effect.

No.	Risks Factors	Effect Level
1	Understanding or participation and contribution of teamwork with positive opinions	2.585
2	Support the employer with ideas and views practicability whether in design stage or execution	2.671
3	Employer’s fast response to approving the completed design	2.828
4	Lack of details was considered one of the requirements needed to complete the work items	3.057
5	Design changes during the execution	3.085
6	Design team fast response when a modification is required.	3.571
7	Design Documents Insufficiency.	3.585
8	Squeezing overlap duration between design and execution	3.620
9	Design team fast response to preparation the design documents in order to facilitate the workflow and sequence of execution.	3.714

University of Baghdad
College of Engineering

JOURNAL OF ENGINEERING

Journal of Engineering

journal homepage: www.jcoeng.edu.iq

Number 3 Volume 24 Month 3

Civil and Architectural Engineering

Slab-beam Interaction in One-way Floor Systems

Salah Rohaima Al-Zaidee, Ph.D.
Lecturer
Engineering College-University of Baghdad
E-mail: salahalzaidee2004@gmail.com.

ABSTRACT

This study focuses on the slab-beam interaction in one-way systems. In the context of this study, slab-beam interaction means how beam deflection can affect moment distribution in one-way slabs. This interaction is usually neglected in the traditional approximate analysis that is adopted in engineering practice and design codes. Slab positive moments have been considered as indicators on the accuracy of approximate methods, as they overestimate negative moments while underestimating positive moments.

After proposing of effecting parameters in slab-beam interaction including of panel length and width, beam dimensions, and slab thickness, Buckingham's π theorem has been adopted to transform the dimensional-model into a non-dimensional qualitative one. Different case studies with finite element models have been adopted to generate points on the proposed qualitative non-dimensional model. Finally, linear regression analyses have been adopted to develop the corresponding quantitative models.

Case studies and corresponding regression analysis indicate that non-dimensional parameters adopted in the model are related linearly with a correlation coefficient in the range of 0.97 and that an error up to 250% may be noted due to neglecting the slab-beam interaction. Therefore, a condition related to the relative stiffness of supporting beams should be added to the current conditions for the approximated methods to be more accurate and more compatible with those adopted in the analysis of two-way systems.

Key Words: One-way slabs, slab-beam interaction, finite element analysis, regression analysis.

تداخل السقف-العتب في أنظمة الأرضيات باتجاه واحد

صلاح رحيمة عبيد
مدرس
كلية الهندسة-جامعة بغداد

الخلاصة

تركز هذه الدراسة على التداخل بين السقوف والأعتاب في أنظمة التسقيف باتجاه واحد. عرف التداخل في سياق هذه الدراسة بانه مقدار تأثير انحراف الأعتاب على توزيع العزوم في السقوف باتجاه واحد. هذا التداخل عادة ما يهمل في طرق التحليل التقريبية المتبعة في التطبيقات الهندسية والمدونات التصميمية. عزم السقف الموجب أخذ كمؤشر على دقة الطرق التقريبية وذلك لان هذه الطرق التقريبية تبالغ في تقدير العزوم السالبة وتقلل تقدير العزوم الموجبة.

بعد اقتراح العوامل المؤثرة في التداخل بين السقوف والأعتاب والمتضمنة طول وعرض السقف، أبعاد العتب، وسمك السقف، استخدمت نظرية الباي لبيكنهام في تحويل النموذج البعدي لأخر غير بعدي. تمت دراسة عدة حالات باستخدام نماذج العناصر المحددة لتوليد عدة نقاط على النموذج غير البعدي الكيفي المقترح. أخيرا استخدم تحليل الانحسار الخطي لأعداد النموذج غير البعدي الكمي. الحالات المدروسة مع تحليلات الانحسار بينت أن المعاملات غير البعدية المقترح مرتبطة بمعاملات ارتباط

بحدود 0.97 وبينت كذلك بان خطا بنسبة 250% قد يلحظ في الطرق التقريبية نتيجة إهمال التداخل بين السقف والأعتاب. وعلية شرطا" معرفا" للصلابة النسبية للأعتاب يجب إن يضاف للشروط الحالية للطرق التقريبية لجعلها أكثر دقة وأكثر انسجاما" مع تلك التي تستخدم في تحليل السقوف باتجاهين.

كلمات الرئيسية: السقوف باتجاه واحد، تداخل السقف-العتب، تحليل العناصر المحددة، تحليل الانحدار.

1 INTRODUCTION

Slab-beam-girder flooring system usually adopted in reinforced concrete buildings with its load path is presented in **Fig1(a)**, **Nilson, 2011**. According to **McGuire, 1959**, this system is commonly used with column spacing from 6m to 12m. Panel length to width ratio usually excesses 1.5 according to **MacGregor** and **Wight, 2005**.

Floor beams usually have a span up to 6m, **Callender, 1982**, with a depth about twice the width, and usually located at mid-points, at the third points, or at the quarter points of the girders, **McGuire, 1959**. For lighter loads, intermediate and deep girders may be eliminated and one-way slab to be supported by wide, shallow beams located along column lines as indicated in **Fig1(b)**, **McGuire, 1959**.

According to **ACI 318, 2008**, slab-beam-girder flooring system should cast monolithically resulting in a highly indeterminate system with deflected shape indicated in **Fig. 2**.

Many approximated methods have been offered to determine shear forces and bending moments in the slab including ACI coefficients methods, **ACI 318, 2008**, semi-analytical methods proposed by **Wang** and **Salmon, 1985**, and moment distribution method proposed by **Cross** and **Morgan, 1949**. In all these methods, beam deflection is neglected relative to slab deflection and actual deflected shape of **Fig. 2** is approximated with that of **Fig. 3**.

Experience with current numerical analysis by finite element method indicates that aforementioned assumption may be in a serious error especially for slabs supported on flexible beams. Therefore, a condition of the relative stiffness of the supporting beam should be adopted for more accurate results. This condition would be similar to that adopted by ACI code in direct design method for two-way slabs.

This paper aims to show the effect of slab-beam interaction on moments in one-way slabs. Finite element method has been adopted for analysis of different case studies with and without beam interactions.

2 BUILDING OF THE MODEL AND THE DIMENSIONAL ANALYSIS

2.1 Basic Relation to the Model

As discussed above, this study aims to show how slab-beam interaction affects slab moments in a one-way system. Parameters that are important in this interaction have been summarized in Eq. 1 below.

$$f\left(\frac{M_I}{M_E}, \frac{L_1}{L_2}, L_1, L_2, b, h, t\right) = 0 \quad (1)$$

With referring to **Fig. 4**, above parameters are defined in below:

M_I is slab moment including slab-beam interaction,

M_E is slab moment excluding slab-beam interaction,

L_1 is the beam span and the panel length,

L_2 is the spacing between beams and panel width,

b, and h are beam width and depth respectively,

t is the slab thickness.

Unfortunately, there is no systematic method to determine which parameters are significant in a specific problem, **Langhaar, 1951**. Therefore, parameters of Eq. 1 above are proposed based on a physical reasoning where the parameters b, h, and L_1 are included to reflect beam stiffness in the model, while the parameters t, and L_2 are included to simulate slab stiffness. Assuming that the slab and beams to be casted in a monolithic process with same concrete, the concrete properties are dropped from the model parameters.

2.2 Number of Independent Dimensionless Groups

A non-dimensional model form that based on Buckingham's theorem is useful in reducing problem parameters and in ensuring that case studies are significantly apart to be adopted in regression analysis, **Langhaar, 1951**.

The dimensional matrix of the model is presented in **Table 1**. According to **Langhaar, 1951**, the number of dimensionless products in a complete set is equal to the total number of parameters minus the rank of their dimensional matrix. Matlab code of **Table 2** indicated in the dimensional matrix of **Table 1** has a rank of one. Therefore, the number of dimensionless product for the proposed model would be:

$$No.of\ Non-dimensional\ paramters = 5 - 1 = 4 \tag{2}$$

2.3 Dimensionless Groups

Equating length dimension for both sides of Eq. 1 above according to the law of dimensional homogeneity, the following equation is the result:

$$0 = (L_1)^{\alpha_1}(\mathrm{L}_2)^{\alpha_2}(b)^{\alpha_3}(h)^{\alpha_4}(t)^{\alpha_5} \tag{3}$$

$$\alpha_1 + \alpha_2 + \alpha_3 + \alpha_4 + \alpha_5 = 0$$

Solve for slab thickness exponent, α_5

$$\alpha_5 = -\alpha_1 - \alpha_2 - \alpha_3 - \alpha_4$$

The four non-dimensional groups would be as indicated in Eq. 4 below and the proposed model in its non-dimensional form would be as indicated in Eq. 5 below.

$$0 = \left(\frac{\mathrm{L}_1}{t}\right)^{\alpha_1}\left(\frac{\mathrm{L}_2}{t}\right)^{\alpha_2}\left(\frac{b}{t}\right)^{\alpha_3}\left(\frac{h}{t}\right)^{\alpha_4} \tag{4}$$

$$\frac{M_I}{M_E} = g\left(\left(\frac{L_1}{L_2}\right)\left(\frac{\mathrm{L}_1}{t}\right)^{\alpha_1}\left(\frac{\mathrm{L}_2}{t}\right)^{\alpha_2}\left(\frac{b}{t}\right)^{\alpha_3}\left(\frac{h}{t}\right)^{\alpha_4}\right) \tag{5}$$

3 FINITE ELEMENT MODEL

3.1 Basic Formulation

Shell element has been adopted to simulate slabs while space frame element has been adopted for beam simulation. Typical degrees of freedom for each node of the shell element has been indicated in **Fig. 5** below. In spite of neglecting of geometric nonlinearities in finite element modeling of this study, membrane action has been adopted to make DOF for shell similar to those of space frame element and in turn to simplify the assemblage process, **Rockey, et al., 1975**. Regarding bending action, Mindlin theory that includes shear deformation has been adopted. This theory is based on a kinematic assumption of normals to the mid-surface before deformation remain straight but not necessarily normal to the mid-surface after deformation, **Hinton** and **Owen, 1984**. Unfortunately, finite element simulation of Mindlin plate may overestimate energy due to shear deformations for thin plates. This numerical difficulty has been solved through adopted of a reduced integration scheme during formulation of stiffness matrix, **Huang, 1989**.

Regarding the supporting beams, they have been simulated using a space frame element. The Linear displacement field is used to derive terms for axial stiffnesses while Hermite cubical shape function is adopted for flexure stiffnesses ,**Chandrupatla** and **Belegundu, 1996**.

As the Hermite displacement filed is exact for beams loaded at nodes only, and to maintain compatibility with the supported slabs, a mesh size in the range 0.25m has been adopted to discretize the slabs and the supporting beams. According to **Cook**, **1995**, this mesh size is adequate to simulate the behavior of the problem.

When slab-beam interaction to be included, boundary conditions are simulated as indicated in **Fig. 6** while they have simulated as indicated **Fig. 7** when slab-beam interaction to be excluded with maintaining beam torsional effects.

3.2 Effect of Offset between Slab and Beams Center Line

As indicated in **Fig. 8** below, traditional finite element models usually connect neutral plane for the slab to the neutral axes of the supporting beams and implicitly neglect the actual offset between them. Therefore, before adopting of a traditional finite element model in the assessment of approximate methods for analysis of one-way slab system, the effect of neglected offset should be checked at first.

According to **Cook**, **1995**, offset between the slab and the supporting beam can be simulated either through adopting of a physical rigid link to connect between the node on the slab and the corresponding node on the beam, see **Fig. 9a** or through adopting of three-dimensional simulation indicated in **Fig. 9b**. When one adopts the three-dimensional modeling of **Fig. 9b**, he should consider the difference between clear span and center-to-center span for the slabs. As this aspect is out of our scope and needs a separate study, therefore, the model of the rigid link has been adopted here to show that offset between slab neutral plane and beam neutral axis affects slab moments in average by an amount indicated in Eq. 6.

$$\frac{M_{with\ offset}}{M_{without\ offset}} \approx 0.9 \tag{6}$$

Results of Eq. 6 above can be interpreted if one notes that adopting of offset increases beams torsional stiffness, and in turn, it reduces positive moments and increases negative moments in the slab. With this results and interpretations, one can conclude that neglecting of offset between the slab and the supporting beams leads to a conservative estimation of the positive moments.

4 CASE STUDIES AND REGRESSION ANALYSES

4.1 One-way Floor Systems with Two Spans

Based on analysis parameters and finite element model discussed above, case studies indicated in **Table 3** have been considered.

As actual deformations presented in **Fig. 2** indicate that approximate analysis methods underestimate positive moments while overestimating the negative moments, therefore this study considers positive moments as an indicator on accuracy and adequacy of the approximated

methods.
Regression model indicated in Eq. 7 has been adopted to correlate slab moment with interaction, M_I, to slab moment without interaction, M_E. As the beam thickness, h, and the slab thickness, t, are related to beam stiffness and slab stiffness respectively, therefore they are included with cubical power.

$$M_I = \left(k_0 + k_1\left(\frac{L_1}{L_2}\right) + k_2\left(\frac{L_1}{t}\right) + k_3\left(\frac{L_2}{t}\right) + k_4\left(\frac{b}{t}\right) + k_5\left(\frac{h}{t}\right)^3\right) M_E \quad (7)$$

In terms of variables of **Table 3**, Eq. 7 has been re-written as indicated in Eq. 8 below.

$$y = (k_0 + k_1x_1 + k_2x_2 + k_3x_3 + k_4x_4 + k_5x_5^3) \quad (8)$$

To avoid nonlinear multiple regresses and deal with linear regression analysis where one can investigative the partial contribution of each parameter, Eq. 8 above has been linearized in term of $x_5^* = \left(\frac{h}{t}\right)^3$ as indicated in below:

$$y = (k_0 + k_1x_1 + k_2x_2 + k_3x_3 + k_4x_4 + k_5x_5^*) \quad (9)$$

Using least square analysis in SPSS environment, the coefficients k_i have been determined and presented **Table 4**. SPSS regression analysis indicates that the parameter $x_3 = \frac{L_2}{t}$ has insignificant effect and has been excluded from the model. Therefore, in its final form, relation between positive slab moment with and without beam interaction has been presented in Eq. 10 below. From **Fig. 10** below, one concludes that the M_I/M_E determined from FE analysis and those determined from the regression analysis are highly correlated that Eq. 10 can be used to estimate of M_I from the corresponding value of M_E which can be determined from approximated the method for analysis of one-way slabs.

$$M_I = \left(-1.146 - 1.249\left(\frac{L_1}{L_2}\right) + 0.075\left(\frac{L_1}{t}\right) + 0.651\left(\frac{b}{t}\right) - 0.002\left(\frac{h}{t}\right)^3\right) M_E \quad (10)$$

4.2 One-way Floor Systems with Three Spans

As for slabs with two-spans, parameters and results for case studies of slabs with three-spans have been presented in **Table 5**.
Correlation coefficients and corresponding relation between slab moment with beam interaction, M_I, and the corresponding moment with neglecting of beam interaction, M_E, have been presented in **Table 6** and Eq. 11 respectively.
Accuracy of proposed linear model to estimate M_I from corresponding M_E has been illustrated in **Fig. 11** below that indicates a high correlation, with R^2 value of 0.9794, between results of proposed linear model and corresponding results of the finite element analysis.

$$M_I = \left(1.142 + 0.361\left(\frac{L_1}{L_2}\right) + 0.007\left(\frac{L_1}{t}\right) - 0.031\left(\frac{b}{t}\right) - 0.002\left(\frac{h}{t}\right)^3\right) M_E \quad (11)$$

5 CONCLUSIONS

- Proposed regression models indicated that an error up to 250% can occur due to the neglect of slab-beam interaction in one-way systems.
- From a practical point of view, proposed regression models can be used to modify bending moments of one-way slabs estimated from approximated methods to reflect the effect of slab-beam interaction.
- On the other hand, the proposed regression models can be adopted to define a new limitation on the applicability of approximated methods for analysis of one-way systems. To be similar to the corresponding limitation in two-way systems, this new limitation should be written in terms of the relative stiffness of the supported beams.

6 RECOMMENDATIONS FOR THE FUTURE WORKS

More elaborate models for interaction between slab and supporting beams in one-way systems can be achieved through:

- Using three-dimensional finite element analysis to show how slab-beam inaction can be affected by the difference between center-to-center span and the clear span.
- Using a finite element model with material nonlinearities to show how slab-beam interaction is affected by cracking of concrete and yielding of reinforcement. The moment distribution is generally significant in slabs that usually have high ductility levels.
- Using a finite element model with geometric nonlinearities to show how slab-beam interaction may be affected by membrane forces in the slabs and the supporting beams.

7 REFERENCES

- ACI 318. 2008. Building Code Requirements for Structural Concrete (ACI 318M-08) and Commentary. American Concrete Institute.

- Callender, J. H. 1982. Time-saver Standards for Architectural Design Data, 6th Edition. McGraw-Hill Book Company.

- Chandrupatla, T. R., & Belegundu, A. D. 1996. Introduction to Finite Elements in Engineering. Prentice Hall of India.

- Cook, R. D. 1995. Finite Element Modeling for Stress Analysis. John Wiley & Sons, Inc.

- Cross, H., & Morgan, N. D. 1949. Continuous Frames of Reinforced Concrete. John Wiley & Sons, Inc.

- Hinton, E., & Owen, D. R. 1984. Finite Element Software for Plates and Shells. Pineridge Press Limited.

- Huang, H.-C. 1989. Static and Dynamic Analyses of Plates and Shells: Theory, Software, and Applications. Springer-Verlag.

- Langhaar, H. L. 1951. Dimensional Analysis and Theory of Models. John Wiley & Sons, Inc.

- MacGregor, J. G., & Wight, J. K. 2005. Reinforced Concrete Mechanics and Design, 4th Edition. Prentice Hall.

- McGuire, W. 1959. Reinforced Concrete. In L. C. Urquhart, Civil Engineering Handbook, 4th Edition. (pp. 7-102 to 7-106). McGraw-Hill Book Company.

- Nilson, A. H. 2011. Design of Concrete Structures, 14th Edition. Mc-Graw Hill.

- Rockey, K. C., Evans, H. R., Griffiths, D. W., & Nethercot, D. A. 1975. The Finite Element Method, A Basic Introduction. Crosby Lockwood Staples.

- Wang, C.-K., & Salmon, C. G. 1985. Reinforced Concrete Design, 4th Edition. Harper & Row, Publishers.

8 NOMENCLATURE

L_1 is the beam span and the panel length, m.
L_2 is the spacing between beams and the panel width, m.
M_E is slab moment excluding slab-beam interaction, $kN.m\ per\ m$.
M_I is slab moment including slab-beam interaction, $kN.m\ per\ m$.
k_i are coefficients for the regression model, dimensionless.
h is the beam depth, m.
b is the beam width,
t is the slab thickness,
α_i are the exponents for non-dimensional model,

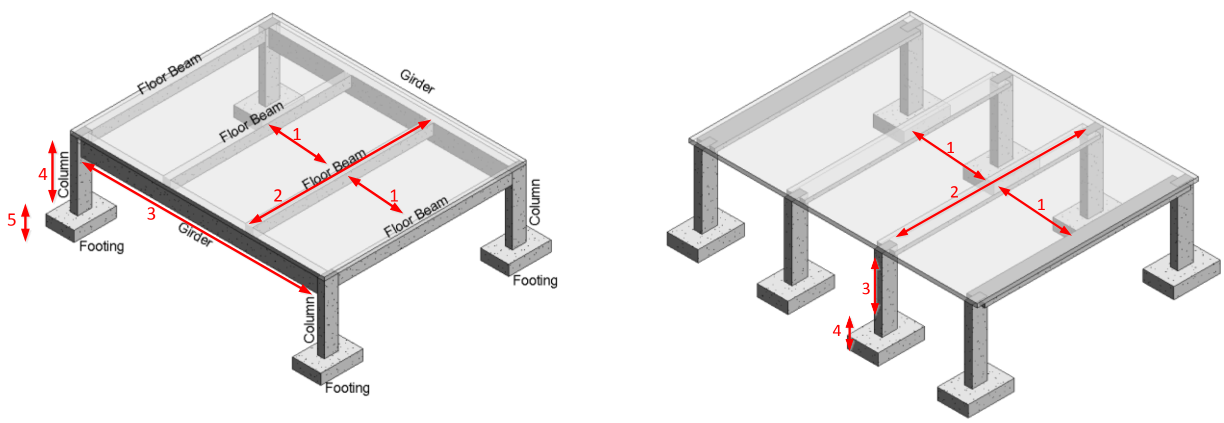

(a) With traditional floor beams and girders. (b) With wide, shallow beams.

Figure 1. One-way flooring system.

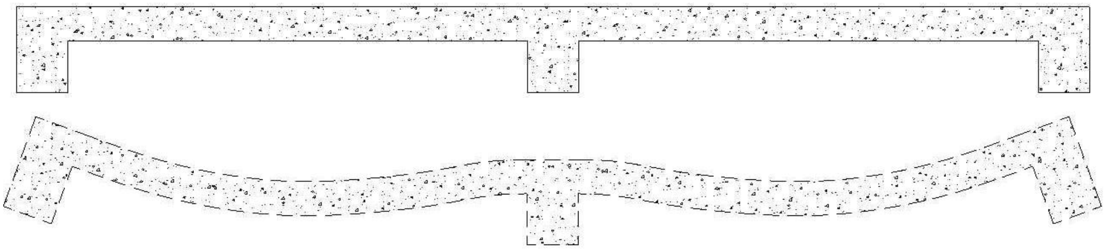

Figure 2. Exaggerated deflected shape for two spans one-way slab system.

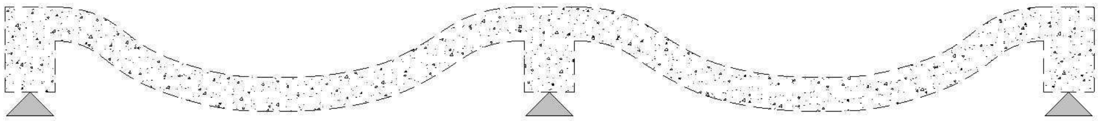

Figure 3. Approximated deflected shape adopted by traditional analysis methods of the one-way system.

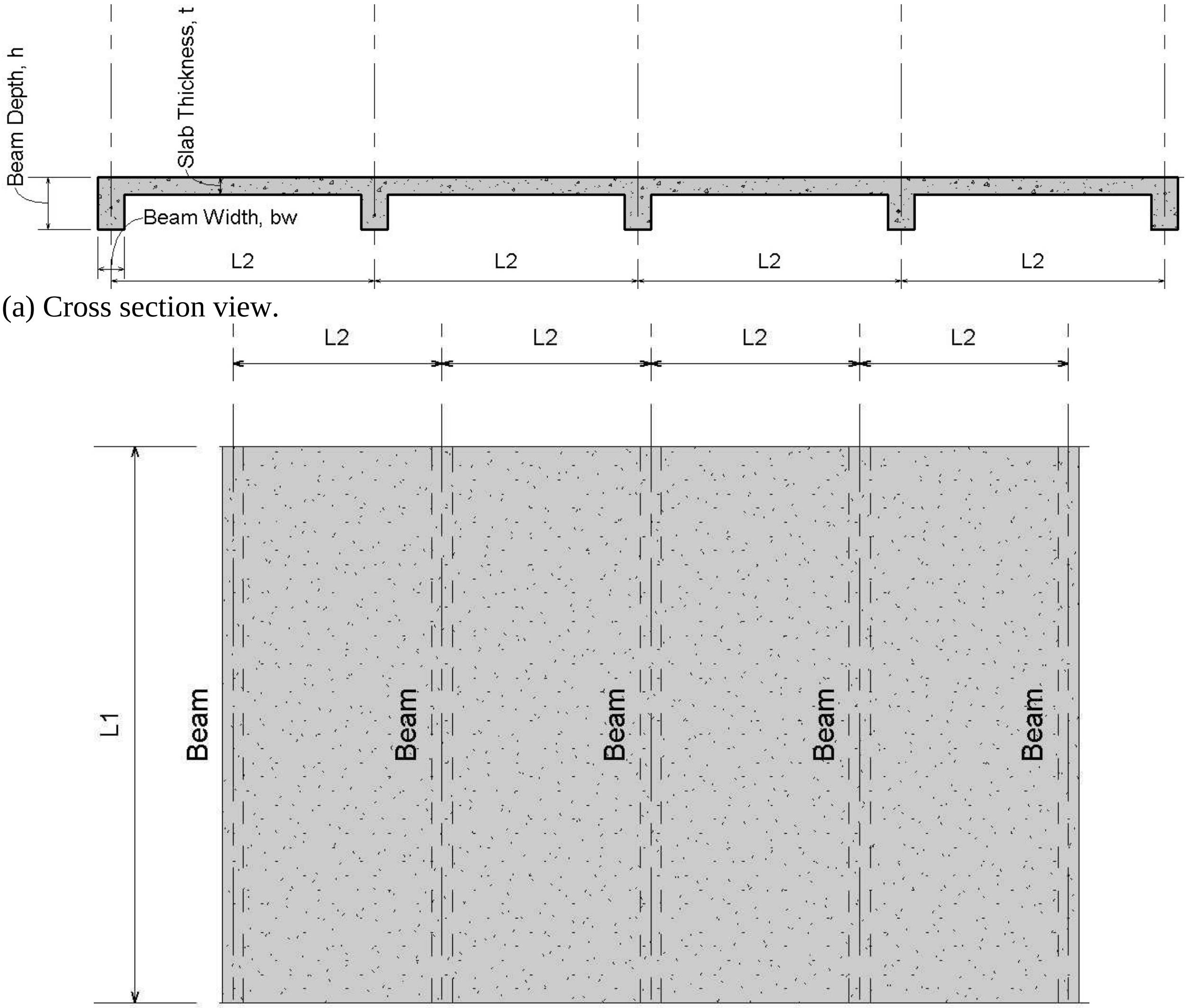

(a) Cross section view.

(b) Plan view.

Figure 4. Parameters and notations adopted in case studies.

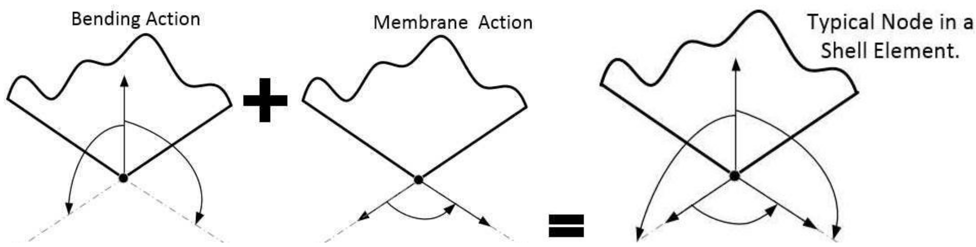

Figure 5. A typical node for quadrilateral shell element adopted to simulate foundations.

(a) Actual support. (b) Ideal support.

Figure 6. Boundary conditions when slab-beam interaction is included.

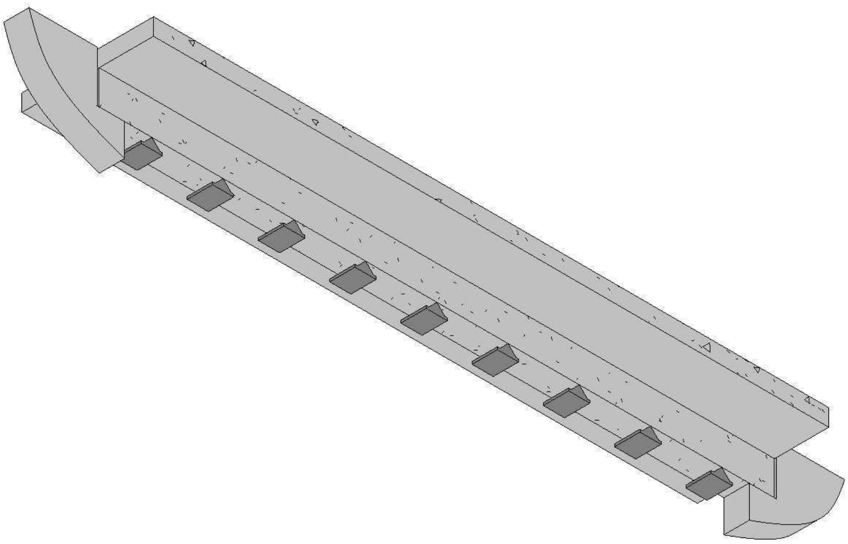

Figure 7. Boundary conditions when slab-beam interaction is excluded.

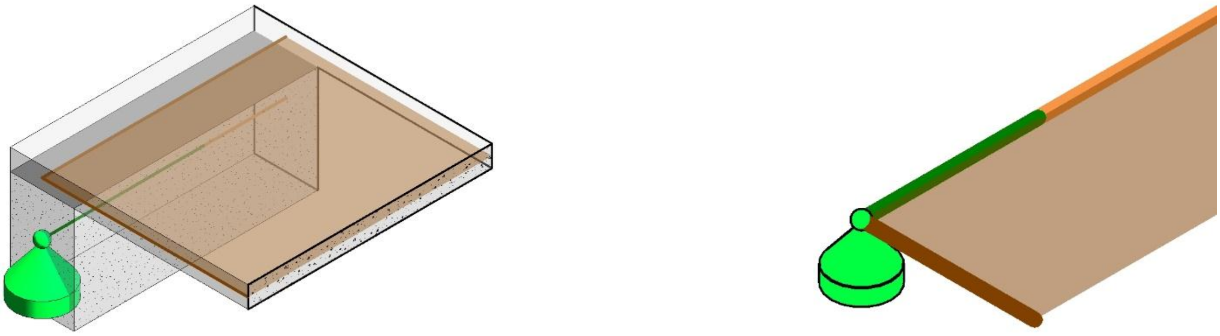

(a) Actual relation with offset. **(b). Approximated relation adopted in traditional finite element models.**

Figure 8. Offset between neutral plane for the slab and neutral axis for the supporting beam.

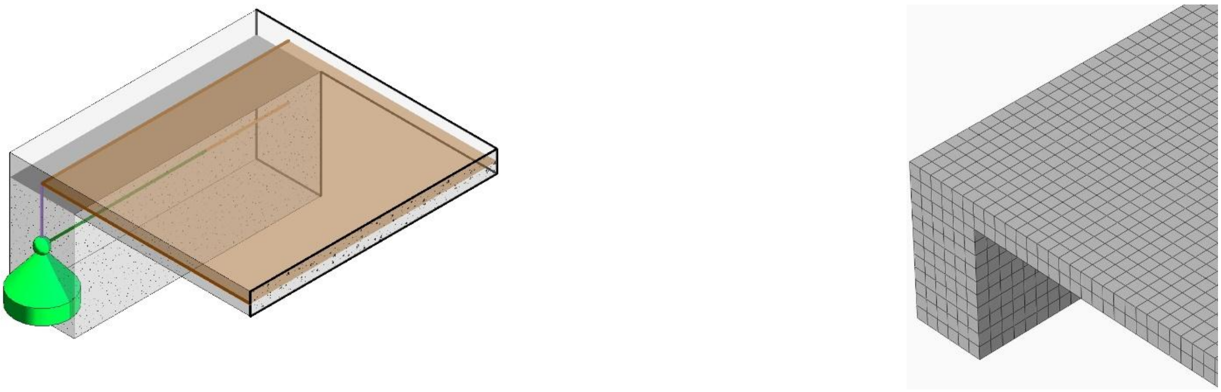

(a) Rigid link to overcome offset problem. **(b). Three-dimensional model to overcome offset problem.**

Figure 9. Two common simulations to overcome the problem of offset between the slab and the supporting beams.

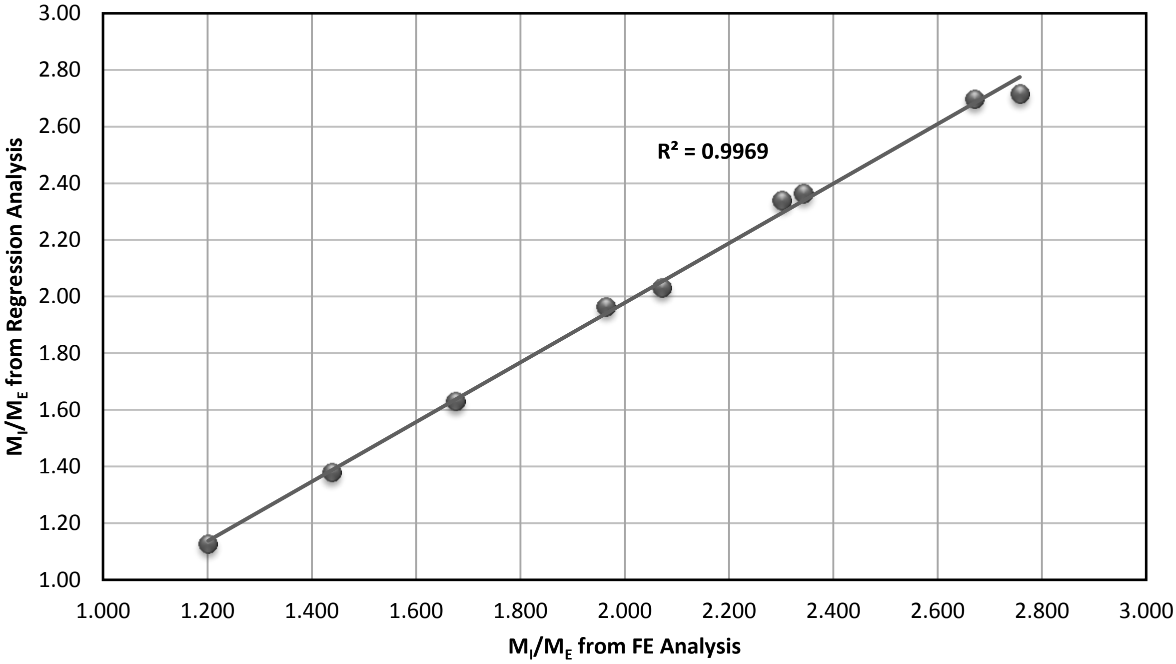

Figure 10. Correlation between $\mathbf{M_I/M_E}$ computed from FE analysis to those estimated from regression analysis for one-way systems with two spans.

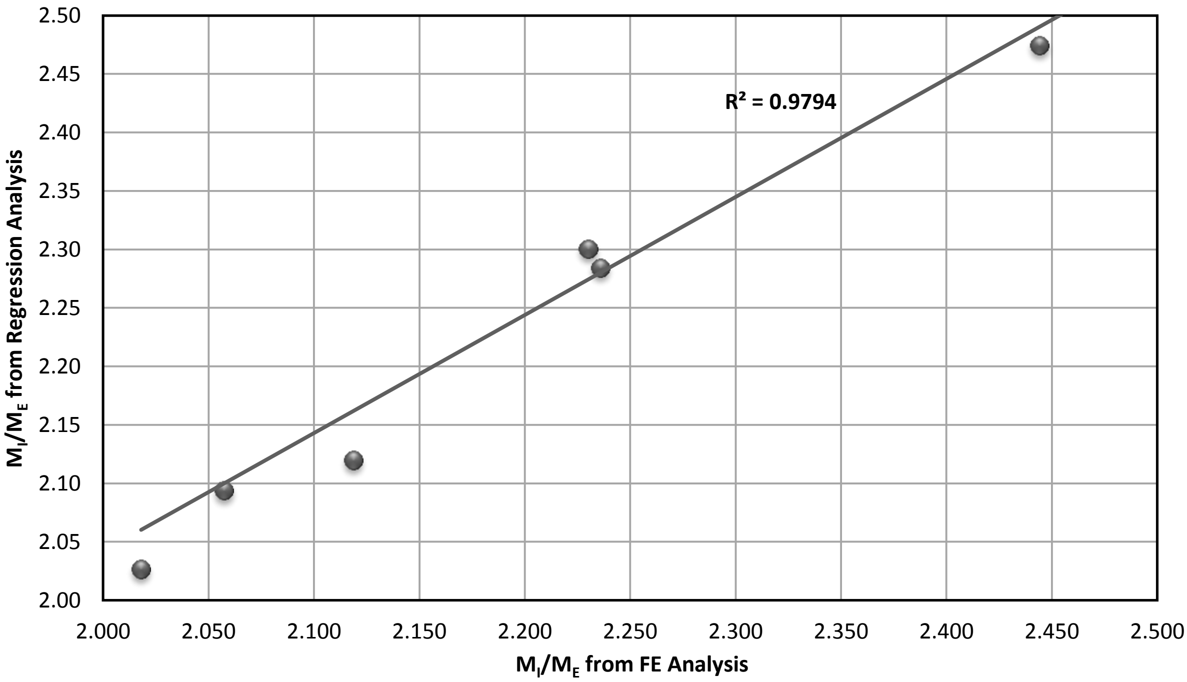

Figure 11. Correlation between $\boldsymbol{M_I/M_E}$ computed from FE analysis to those estimated from regression analysis for one-way systems with three spans.

Table 1. Dimensional matrix for the proposed model of Eq. 1.

	L_1	L_2	b	h	t
M	0	0	0	0	0
L	1	1	1	1	1
T	0	0	0	0	0

Table 2. Matlab code to determine the rank of the dimensional matrix for the proposed model.

```
clc
% The script file aims to determine the rank of dimensional matrix
% for the slab-beam interaction in one-way systems.
DM = [0 0 0 0 0
  1 1 1 1 1
  0 0 0 0 0]
k = rank(DM)
```

Table 3. Case studies for slab with two spans.

No	Slab Thickness, t, mm	L_1, m	L_2, m	b_w, mm	h, mm	$x_1 = \frac{L_1}{L_2}$	$x_2 = \frac{L_1}{t}$	$x_3 = \frac{L_2}{t}$	$x_4 = \frac{b}{t}$	$x_5 = \frac{h}{t}$	$x_5^* = \left(\frac{h}{t}\right)^3$	$y = \frac{M_I}{M_E}$
1	100	6	2	300	600	3.00	60.00	20.00	3.00	6.00	216.00	1.20
2	100	8	2	300	600	4.00	80.00	20.00	3.00	6.00	216.00	1.44
3	100	10	2	300	600	5.00	100.00	20.00	3.00	6.00	216.00	1.68
4	150	8	4	400	600	2.00	53.33	26.67	2.67	4.00	64.00	1.96
5	150	10	4	400	600	2.50	66.67	26.67	2.67	4.00	64.00	2.30
6	150	12	4	400	600	3.00	80.00	26.67	2.67	4.00	64.00	2.76
7	200	12	6	400	800	2.00	60.00	30.00	2.00	4.00	64.00	2.07
8	200	14	6	400	800	2.33	70.00	30.00	2.00	4.00	64.00	2.34
9	200	16	6	400	800	2.67	80.00	30.00	2.00	4.00	64.00	2.67

Table 4. Coefficients for multiple linear regressions for the proposed model of slabs with two spans.

k_0	-1.146
k_1	-1.249
k_2	.075
k_4	.651
k_5	-.002

Table 5. Case studies for slab with three spans.

No	Slab Thickness, t, mm	L_1, m	L_2, m	b_w, mm	h, mm	$x_1 = \frac{L_1}{L_2}$	$x_2 = \frac{L_1}{t}$	$x_3 = \frac{L_2}{t}$	$x_4 = \frac{b}{t}$	$x_5 = \frac{h}{t}$	$x_5^* = \left(\frac{h}{t}\right)^3$	$y = \frac{M_I}{M_E}$
1	100	6	2	300	600	3.00	60.00	20.00	3.00	6.00	216.00	2.119
2	100	8	2	300	600	4.00	80.00	20.00	3.00	6.00	216.00	2.456
3	100	10	2	300	600	5.00	100.00	20.00	3.00	6.00	216.00	3.106
4	150	8	4	400	600	2.00	53.33	26.67	2.67	4.00	64.00	2.018
5	150	10	4	400	600	2.50	66.67	26.67	2.67	4.00	64.00	2.230
6	150	12	4	400	600	3.00	80.00	26.67	2.67	4.00	64.00	2.541
7	200	12	6	400	800	2.00	60.00	30.00	2.00	4.00	64.00	2.057
8	200	14	6	400	800	2.33	70.00	30.00	2.00	4.00	64.00	2.236
9	200	16	6	400	800	2.67	80.00	30.00	2.00	4.00	64.00	2.444

Table 6. Coefficients for multiple linear regressions for the proposed model of slabs with three spans.

k_0	1.142
k_1	0.361
k_2	0.007
k_4	-0.031
k_5	-0.002

University of Baghdad
College of Engineering
JE
JOURNAL OF ENGINEERING

Journal of Engineering

journal homepage: www.jcoeng.edu.iq

Number 3 Volume 24 Month 3

Civil and Architectural Engineering

Analysis of Double Skin Composite Slabs

Husain M. Husain
Professor

Mohannad H. Al-Sherrawi
Instructor

Asmaa Taha Ibrahim
Engineer

College of Eng. - University of Baghdad
mhnd7@yahoo.com

ABSTRACT

This paper deals with finite element modeling of the ultimate load behavior of double skin composite (DSC) slabs. In a DSC slab, shear connectors in the form of nut bolt technique studs are used to transfer shear between the outer skin made of steel plates and the concrete core. The current study is based on finite element analysis using ANSYS Version 11 APDL release computer program. Experimental programmes were carried out by the others, two simply supported DSC beams were tested until failure under a concentrated load applied at the center. These test specimens were analyzed by the finite element method and the analyses have shown that these slabs displayed a high degree of flexural characteristics, ultimate strength, and ductility. The close agreement has been observed between the finite element and experimental results for ultimate loads and load–deflection responses. The finite element model was thus found to be capable of predicting the behavior of DSC slabs accurately.

Keywords: DSC slabs; Shear studs; Ultimate load behavior; Finite element method; Steel-concrete-steel sandwich construction.

تحليل البلاطات المركبة ذات غطائين

حسين محمد حسين
أستاذ

مهند حسين الشراوي
مدرس

أسماء طه إبراهيم
مهندس

كلية الهندسة – جامعة بغداد

الخلاصة

يتناول هذا البحث التمثيل باستخدام العناصر المحددة لسلوك البلاطات الخرسانية المركبة ذات غطائين حديد عند الحمل الأقصى. في هكذا بلاطات ، تستخدم البراغي كروابط القص لنقل قوى القص بين غطائي الحديد واللب الخرساني. تستند الدراسة الحالية على تحليل العناصر المحددة باستخدام برنامج الحاسوب ANSYS إصدار APDL 11. باستعمال طريقة العناصر المحددة ، تم تحليل عتبين مسندين إسناد بسيط ، فحصا مختبريا من قبل آخرين تحت تأثير حمل مركز وإلى حد الفشل. وقد بينت نتائج التحليل أن هذه نماذج أظهرت درجة عالية من خصائص الانثناء والقوة القصوى واللدونة. وقد لوحظ وجود تقارب بين نتائج العناصر المحددة والنتائج التجريبية للأحمال النهائية وإستجابات الانحراف. وبهذا فقد وجد بأن طريقة العناصر المحددة قادرة على التنبؤ بسلوك البلاطات الخرسانية المركبة ذات غطائين حديد بدقة.

1. INTRODUCTION

Steel-concrete-steel sandwich (SCSS) construction or double skin composite (DSC) construction is a relatively new and innovative form of construction consisting of a layer of plain concrete, sandwiched between two layers of relatively thin steel plate, connected to the concrete by stud connectors as shown in Fig. (1). SCSS construction was originally conceived as an alternative form of construction for immersed tube tunnels 1-3 but has since been considered for a variety of, offshore and onshore applications including oil production and storage vessels, caissons, core shear walls in tall buildings and impact and blast resistant structures.

The perceived advantages of the system are that the external steel plates act as both primary reinforcement and permanent formwork, and as impermeable, impact and blast resistant membranes. The full depth stud connectors transfer normal and shearing forces between the concrete and steel plates and act as transverse shear reinforcement.

In this study, the comparison is made between the results obtained from the finite element analysis and the available experimental results in order to check the validity and accuracy of the finite element model. Thus, two specimens with available experimental results have been analyzed here and the finite element results are compared.

After that, a nonlinear three-dimensional finite element analysis has been used to predict the load-deflection behavior of a double skin composite slab consisting of a concrete slab sandwiched between two plates with shear connectors under uniformly distributed load using ANSYS computer program (Version 11, copyright 2007).

2. MATERIAL MODELING

2.1 Steel Plate

Steel plate material is assumed to behave as a bilinear uniaxial stress-strain relationship. The stress-strain diagram consists of two branches: A first branch starts from the origin with a slope equal to E_s, up to f_y. A second branch is horizontal or, for practical use of computers, is assumed to have a very small slope ($E_w \approx 0.02E_s$) as shown in Fig. (2).

The material coefficients to be adopted in calculations for the steels covered by this study have been taken, as follows, according to **EC4 1994**:

- Modulus of elasticity $E_s = 210000\,\text{N/mm}^2$
- Shear modulus $G_s = E_s / 2\,(1+\upsilon_s)$
- Poisson's ratio $\upsilon_s = 0.3$

2.2 Concrete

The ANSYS computer program requires the uniaxial stress-strain relationship for concrete in compression. Numerical expressions, **Desayi** and **Krishnan**, **1964**, the following Eq. (1) and (2), were used along with Eq. (3), **Gere** and **Timoshenko**, **1997**, and Eq. (4), **ACI 318-14** to construct the uniaxial compressive stress-strain curve for concrete in this study.

$$f = \frac{E_c \varepsilon}{1+\left(\frac{\varepsilon}{\varepsilon_o}\right)^2} \tag{1}$$

$$\varepsilon_o = \frac{2f'_c}{E_c} \tag{2}$$

$$E_c = \frac{\sigma}{\varepsilon} \tag{3}$$

$$E_c = 4700\sqrt{f_c'} \tag{4}$$

where:
σ = stress at any strain ε, N/mm^2.
ε = strain at stress f .
ε_o = strain at the ultimate compressive strength f_c' .

It is important to mention that the stress-strain curves end at ultimate strain (ε_u) equal to 0.003 mm/mm. Fig. (3) shows the simplified compressive uniaxial stress-strain relationship that has been used in this study.

For concrete, ANSYS computer program requires following input data for material properties, **Kachlakev**, **et al.**, **2001**:

- Elastic modulus (E_c).
- Ultimate uniaxial compressive strength (f_c').
- Ultimate uniaxial tensile strength (modulus of rupture, f_r).
- Poisson's ratio (υ).
- Shear transfer coefficient for opened and closed cracks (β_o and β_c respectively).
- Compressive uniaxial stress-strain relationship for concrete.

From the ultimate uniaxial compressive strength (f_c'), obtained from appropriate standard tests, the elastic modulus of concrete (E_c) for each model was calculated according to ACI 318-14 by using Eq. (4). Poisson's ratio for concrete was assumed to be 0.2, **Bangash**, **1989**, for all sandwich slabs.

The shear transfer coefficient, β, represents conditions of the crack face. The value of β ranges from 0.0 to 1.0, with 0.0 representing a smooth crack (complete loss of shear transfer) and 1.0 representing a rough crack (no loss of shear transfer), **ANSYS**, **2007**.

The value of β used in many studies of reinforced concrete and composite steel-concrete structures, however, varied between 0.05 and 0.25, **Bangash**, **1989**; **Huyse**, **et al.**, **1994**; **Hemmaty**, **1998**; **Zebun**, **2006**. A number of preliminary analyses were attempted in this study with various values for the shear transfer coefficient within this range, but convergence problems were encountered at low loads with β less than 0.2. Therefore, the shear transfer coefficients for opened and closed cracks, used in this study, were equal to 0.2 and 0.22 respectively for all specimens.

2.3 Shear Connector

While the role of shear connectors (threaded bars) is divided into two parts: as transverse shear reinforcement in resisting shear forces inside the concrete layer (materially, modeled as shown in Fig. (2) and geometrically as discrete representation as shown in Fig. (4)) and as a shear connector in resisting horizontal and normal shear force between steel and concrete. A modified Push-out tests which were made by **Zebun**, **2006**, are adopted in this study. The modification in this test in comparison with the standard test concentrated on the use of steel tube-concrete slab-steel tube instead of concrete slab-steel (I-Section)-concrete slab (in the standard test) in order to be more compatible than the standard test in modeling the steel-concrete-steel sandwich or double skin constructions. The concrete layer was reinforced with steel bars (according to **BS 5400-5:1979**), as shown in Fig. (5). With plain concrete layer similar to the sandwich slabs (the results of this group will be used in the finite element modeling of the sandwich specimens). Fig. (6) shows the average values of the load-slip relationship of the test.

Many different load-slip relationships for stud connectors have been proposed. Among these, an exponential model was presented by **Yam** and **Chapman**, **1968**. This is represented by the following function

$$Q = a\left(1 - e^{-b\gamma}\right) \tag{5}$$

In which a and b are constants, and e is the base of natural logarithms. The constants a and b are chosen by trials to give the best fit with experimental curves. Alternatively, by choosing two points from the experimental curve so that the slip in the second point is twice its value at the first point then the constants can be defined as:

$$a = \frac{Q_1^2}{2 \cdot Q_1 - Q_2} \tag{6}$$

$$b = \frac{1}{\gamma_1} \log_e \left(\frac{Q_1}{Q_2 - Q_1} \right) \tag{7}$$

In which, subscripts 1 and 2 represent the points on the experimental load-slip curve for the provided shear connector. Fig. (6) shows a typical load-slip relationship (exponential formula).

The shear-slip model proposed by **Yam** and **Chapman**, **1968** for studs shear connector was adopted in the present study. The average values of the constants a and b of the push-out tests are (14.501) and (0.946) respectively.

3. FINITE ELEMENT MODEL

DSC slab is modeled as a non-linear three-dimensional model. The top and bottom steel plates are modeled using four-node shell elements SHELL143 each node have six degrees of freedom three translation and three rotation in X, Y, and Z direction and with a large strain formulation, whereas the concrete core is modeled using eight-node solid elements SOLID65 each nod have three degree of freedom (translation). To simulate the behavior of shear connectors which works as stirrups in resisting the vertical shear at concrete layer and transfer normal force between the concrete and steel plates LINK8 is used the 3-D spar element is a uniaxial tension-compression element with three degrees of freedom at each node: translations of the nodes in X, Y, and Z-directions. Partial interaction is assumed to occur between steel plates and concrete core COMPIN39 is used, in this study, to simulate the behavior of the shear connectors in resisting the horizontal shear between the concrete and the steel plates. The element is defined by two node points and a generalized force-deflection curve. In studying the contact between two bodies, the surface of one body is conventionally taken as a contact surface and the surface of the other body as a target surface. The contact surface is associated with the deformable body, and the target surface must be the rigid surface. TARGE170 is used to represent various 3-D target surfaces for the associated contact elements (CONTA174). Coulomb and shear stress friction is allowed. This element is used, in this study, to simulate the behavior of contact surface between the concrete layer and steel plates (i.e. friction case between layers of the sandwich beam). The element is defined by one node.

4. EXAMPLES

The verification is done in order to check the validity and accuracy of the finite element procedure. Thus, two specimens with available experimental results have been analyzed here and the analytical results are compared.

4.1 Zebun Beams

A simply supported double skin composite beams, tested by **Zebun**, **2006** are two in a series of tested beams. The beams span (L_s) of 1020 mm and loaded with a central load (knife edge load, K.E.L.) applied and distributed across the entire width. Bars along the whole length were used as shear connectors and attached to the steel plates by nuts instead of welding; the nominal inner diameter of the bars was 6.2 mm (i.e. the bars penetrated fully through the concrete and the steel parts). Fabrication details of the tested beams are presented in Fig. (7). Pairs of connectors at each location were used, as shown in Fig. (8).

In the present study, the two chosen beams are designated as (B.1) and (B.3). The dimensions and load arrangement details of these beams are shown in Fig. (9). Table (1) illustrates the Nonlinear Parameters used for beams, and the material properties are given in Tables (2) and (3).

The three-dimensional finite element mesh for a quarter of the beam has been used by using ANSYS computer program, by taking the advantage of symmetry of the beam and loading Figs. (10), (11), and (12) show the pictures of a mesh of beams (B.1), and (B.3). In addition, details about the representation of structural component are done in Table (4).

The experimental and numerical results by Zebun, and numerical results obtained in the present study, for beams (B.1) and (B.3), are shown in Figs. (13), (14), (15), and (16). The mid-span externally applied load is plotted against the mid-span deflection. For these two beams, the failure load obtained by the experimental work and that predicted by the finite element solutions are listed in Table (5). It can be noted from Figures and Table (5) that the finite element solutions are in good agreement with the experimental results throughout the entire range of behavior.

4.2 Double Skin Composite Slabs

The close agreement has been observed between the finite element and experimental results for ultimate loads and load-deflection responses, for the two beams presented in the previous. The finite element model is thus found to be capable of predicting the behavior of DSC slabs accurately.

Other specimens having the same cross-section and span dimensions (1045 mm × 1045 mm × 87 mm), with a 75 mm thick concrete core sandwiched between two 6 mm thick steel plates will be studied under various effects of parameters. Threaded bars along both two directions are used as shear connectors and attached to the steel plates by nuts instead of welding. The nominal inner diameter of the bars is 6.2 mm, with effective length equal to the thickness of concrete layer used in each slab (i.e. the bars penetrated fully through the concrete and the steel parts). These slabs are simply supported on all sides and subjected to a uniform distributed load on the top surface.

The DSC slabs are modeled as a nonlinear three-dimensional structure. Owing to symmetry in geometry, loading and boundary conditions in the (ANSYS program), only a quarter of the DSC slab is modeled

It has been observed that the entire slab supported on two opposite edges had similar behavior under the applied loading. The failure type is mainly due to bending of the composite slab at midspan. Also bond (slip) failure between the concrete layer and steel plates caused fracture failure at the connector as the second failure.

In the present study, the slab is designated as (DSC1). The Details about material properties parameters for double skin composite slabs are listed in Table (6). It is the same material properties parameters which used for the panels in Chapter four the difference is in the dimensions and connectors spacing. Fig. (17) shows the boundary conditions of the quarter of the (DSC1) slab.

Details about the representation of structural component are listed in Table (7) and shown in Fig. (17). Table (1) illustrates the nonlinear parameters used for slabs.

The numerical results are shown in Fig. (18). The externally ultimate uniform distributed load is plotted against the central deflection. For this slab, the failure load predicted by the finite element solutions is (0.224 N/mm^2). Fig. (19) shows the variation of UY along a quarter of (DSC1).

The nonlinear analysis using Finite element method shows that DSC slabs have the very high load carrying capacity. This form of construction also exhibits good flexural characteristics and highly ductile behavior.

5. CONCLUSIONS

Depending on the numerical results obtained in this study, the following conclusions can be drawn:

1- A three-dimensional nonlinear finite element analysis was conducted to investigate the general behavior of sandwich members. Comparison between the experimental and the numerical results shows close agreement. The maximum difference ratio in ultimate load is less than 5% for the tested and analyzed sandwich beams.

2- Finite element analysis shows that DSC slabs have very high load carrying capacity. This form of construction also exhibits good flexural characteristics and highly ductile behaviour.

REFERENCES

- ANSYS, 2007 "*ANSYS Help*", Release 11, Copyright 2007.

- ACI Committee 318-14, "*Building Code Requirements for Structural Concrete* (318-14) and *Commentary* (318R-14)", American Concrete Institute, Michigan, USA, 2014.

- Bangash, M. Y. H., 1989 "*Concrete and Concrete Structures: Numerical Modelling and Applications*", Elsevier Science Publishers Ltd., London, England, Cited by Ref. [Kachlakev et al 2001].

- BS 5400, Part 5, 1979 "*Steel, Concrete and Composite Bridges-Code of practice for design of composite bridges*", British Standards Institution, London.

- Desayi, P. and Krishnan, S., 1964 "*Equation for the Stress-Strain Curve of Concrete*", Journal of the American Concrete Institute, Vol. 61, March 1964, pp. 345-350, Cited by Ref. [Kachlakev et al 2001].

- European Committee for Standardisation (CEN), Eurocode 4, "*Design of Composite Steel and Concrete Structures*", Part 1.1: General Rules and Rules for Buildings, DD ENV 1994-1-1, EC4.

- Gere, J. M. and Timoshenko, S. P., 1997 "*Mechanics of Materials*", PWS Publishing Company, Boston, Massachusetts, 1997.

- Kachlakev, D., Miller, T., and Yim, S., 2001 "*Finite Element Modelling of Reinforced Concrete Structures Strengthened with FRP Laminates*", Final Report, SPR 316, May 2001, 99 p.

- Huyse, L., Hemmaty, Y., and Vandewalle, L., 1994 "*Finite Element Modelling of Fiber Reinforced Concrete Beams*", Proceedings of the ANSYS Conference, Vol. 2, Pittsburgh, Pennsylvania, May 1994.

- Hemmaty, Y., 1998 "*Modelling of the Shear Force Transferred between Cracks in Reinforced and Fiber Reinforced Concrete Structures*", Proceedings of the ANSYS Conference, Vol. 1, Pittsburgh, Pennsylvania, August 1998.

- Yam, L. C. P. and Chapman, J. C., 1968 "*The Inelastic Behavior of Simply Supported Composite Beams of Steel and Concrete*", Proceeding of the Institution of Civil Engineers, Vol. 41, pp. 651-683.

- Zebun, M. A., 2006 "*Behavior and Strength of Steel-Concrete-Steel Sandwich Beams with Partial Shear Connection*", Ph.D. Thesis, Al-Mustansiriya University, Iraq-Baghdad, 194 p.

NOTATIONS

The major symbols used in this work are listed below; these and others are defined as they first appear. When duplication occurs, the used notation is clarified within the text.

E_c	Concrete modulus of elasticity
E_s	Steel modulus of elasticity
$\mathrm{E_w}$	Steel Hardening Parameter
f_c'	Cylinder compressive strength of concrete
f_t	Splitting tensile strength of concrete
f_r	Concrete modulus of rupture
f_y	Yield strength of steel plate
f_u	Ultimate tensile strength of steel
G_s	Shear modulus of steel
h_c	Thickness of concrete layer
h_s	Thickness of steel plate
K_n	Normal stiffness of connector

L_s	Length of span
N	Number of shear connectors in a shear span
S-S	Simple supported
S_{stud}	Stud Spacing
U	Degree of freedom
UY	Deflection or vertical displacement
UX	Horizontal displacement in x-direction
X, Y, Z	Cartesian coordinate.
β_c , β_o	Shear transfer coefficient for closed & opened crack
ε	Strain
ε_o	Strain at ultimate compressive strength
μ	Coefficient of friction
υ	Poisson's ratio
υ_s	Poisson's ratio of steel
ϕ	Diameter
S_{stud}	Stud Spacing

Table 1. Nonlinear solution parameters used for beams.

μ	Coefficient of Friction	0.5*
α_1	Tension Stiffening Parameters	6*
α_2		0.6*
β_o	Shear Transfer Parameters	0.2*
β_c		0.22*
E_w	Steel Hardening Parameter (MPa)	4200*

*Assumed Values. The coefficient of friction μ is taken 0.5. $E_w = 0.02\,E_s$

Table 2. Material property parameters used for (B.1).

	Symbol	**Definition**	**Value**
Concrete	f'_c	Compressive Strength (MPa)	42.2
	E_c	Young's Modulus (MPa)	30532
	hc	Thickness (mm)	75
	f_r **	Tensile Strength (MPa)	4.95
	υ	Poisson's Ratio	0.2*
Top and bottom Steel Plate	f_y	Yield Stress (MPa)	255
	L,W,hs	Dimensions (length×width×thickness) (mm)	1100×100×6
	υ_s	Poisson's Ratio	0.3*
	E_s	Young's Modulus (MPa)	210000
Shear Connectors**	f_y	Yield Stress (MPa)	496
	ϕ	Diameter (mm)	6.2

	υ_s	Poisson's Ratio	0.3
	S_{stud}	Spacing (mm)	75
	E	Young's Modulus (MPa)	210000

Notes: $E_c = 4700\sqrt{f'c}$, * Assumed Values, ** Concrete modulus of rupture (flexural strength) by the prism of 100 mm × 100 mm × 500 mm and loaded at third points (Zebun study).

Table 3. Material property parameters used for (B.3).

	Symbol	Definition	Value
Concrete	f'_c	Compressive Strength (MPa)	43.9
	E_c	Young's Modulus (MPa)	31141
	hc	Thickness (mm)	75
	f_r*	Tensile Strength (MPa)	5.4
	υ	Poisson's Ratio	0.2
Upper and lower Steel Plate	f_y	Yield Stress (MPa)	255
	L, W, h_s	Dimensions (length×width×thickness) (mm)	1100×100×6
	υ_s	Poisson's Ratio	0.3
	E_s	Young's Modulus (MPa)	210000
Shear Connectors	f_y	Yield Stress (MPa)	496
	ϕ	Diameter (mm)	6.2
	υ_s	Poisson's Ratio	0.3
	S_{stud}	Spacing (mm)	150
	E	Young's Modulus (MPa)	210000

*Concrete modulus of rupture (flexural strength) by the prism of 100 mm x 100 mm x 500 mm and loaded at third points (Zebun study).

Table 4. Finite element representation of structural components.

Structural Component		Finite Element Representation	Element Designation in ANSYS	No. of element
Concrete		8-node Brick Element (3 Translation DOF per node)	SOLID 65	120
Interface	Shear Friction and Contact	Nonlinear Surface-to-Surface Interface Element	CONTA-174 & TARG170	120
	Dowel Action	2-node Nonlinear Spring Element with one Translation DOF per node	COMBIN-39	14*
				8**
Shear connector		2-node Discrete Element	3D-SPAR 8	28*

(Tensile Steel, Compressive Steel)	(3 Translation DOF per node)	(LINK-8)	16**
Steel plate	4-node Nonlinear plastic (3 Translation & 3 Rotation DOF Per node)	Shell 143	60

* For (B.1) ** For (B.3)

Table 5. Experimental and predicted failure loads for beams.

Specimens	**Ultimate Load (N)**		$\frac{P_u \text{ (Analytical)}}{P_u \text{ (Experimental)}}$	**Failure mode**	**Error (%)**
	Experimental	**Analytical**			
B.1	50000	49000	0.98	Connector fracture	2
B.3	27000	26730	0.99	Connector fracture	1

Table 6. material property parameters used for DSC slabs.

	Symbol	**Definition**	**Value**
Concrete	f'_c	Compressive Strength (MPa)	42.2
	E_c	Young's Modulus (MPa)	30532
	hc	Thickness (mm)	75
	f_r^{**}	Tensile Strength (MPa)	4.95
	υ	Poisson's Ratio	0.2*
Top and bottom Steel Plate	f_y	Yield Stress (MPa)	255
	L, W, h_s	Dimensions (length×width×thickness) (mm)	1045×1045*6
	υ_s	Poisson's Ratio	0.3*
	E_s	Young's Modulus (MPa)	210000
Shear Connectors	f_y	Yield Stress (MPa)	496
	ϕ	Diameter (mm)	6.2
	υ_s	Poisson's Ratio	0.3
	S_{stud}	Connector Spacing (mm)	150
	E_s	Young's Modulus (MPa)	210000

Notes: $E_c = 4700\sqrt{f'c}$, * Assumed Values, ** Concrete modulus of rupture (flexural strength) by the prism of 100 mm x 100 mm x 500 mm and loaded at third points (Zebun study).

Table 7. Finite element representation of (DSC1) components.

Structural Component		**Finite Element Representation**	**Element Designation in ANSYS**	**No. of element**
Concrete		8-node Brick Element (3 Translation DOF per node)	SOLID 65	784
Interface	Shear Friction and Contact	Nonlinear Surface-to-Surface Interface Element	CONTA-174 & TARGE-170	784
	Dowel Action	2-node Nonlinear Spring Element with one Translation DOF per node	COMBIN-39	32
Shear connector (Tensile Steel, Compressive Steel)		2-node Discrete Element (3 Translation DOF per node)	3D-SPAR 8 (LINK-8)	64
Steel plate		4-node Nonlinear plastic(3 Translation &3 Rotation, DOF Per node)	Shell 143	392

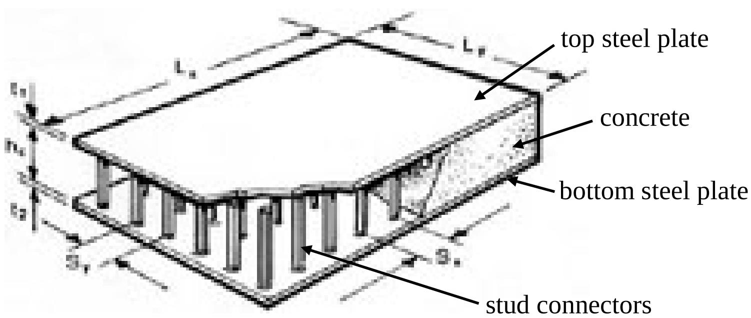

Figure 1. Double skin composite slabs.

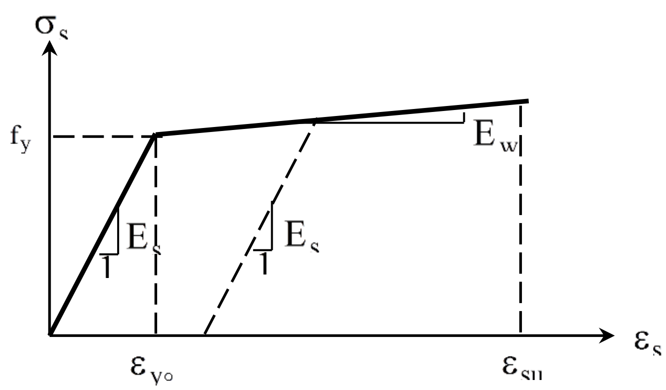

Figure 2. Bilinear stress-strain relationship.

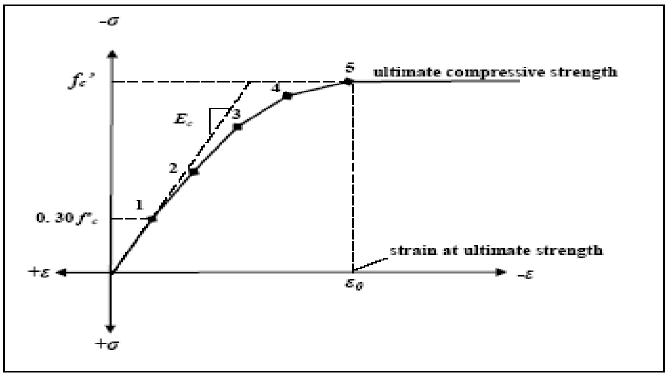

Figure 3. Simplified compressive uniaxial stress-strain curve for concrete.

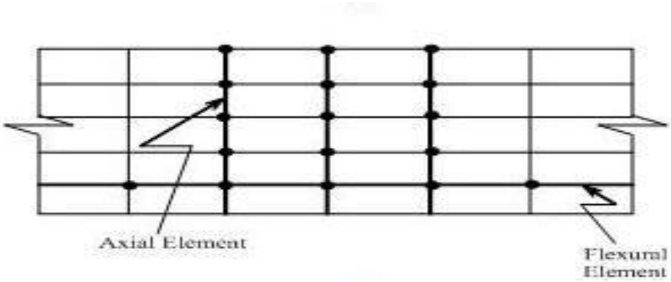

Figure 4. Discrete representation for shear connectors.

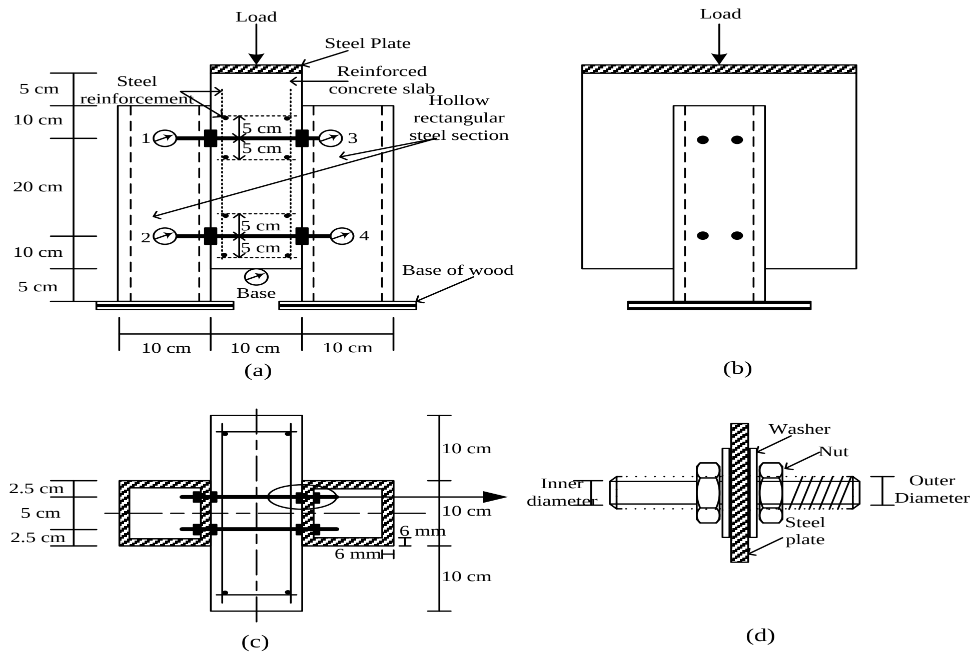

Figure 5. Dimensions and details of modified push-out test. (a) Front view. (b) Side view. (c) Top view. (d) Details of connection (magnified picture), **Zebun**, **2006.**

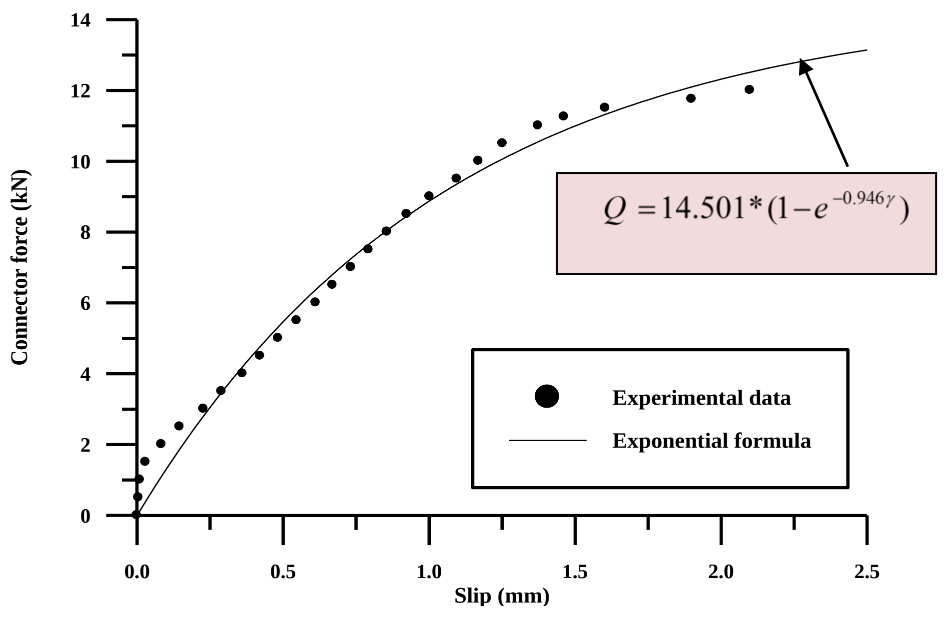

Figure 6. Load- slip relationship, **Zebun**, **2006**.

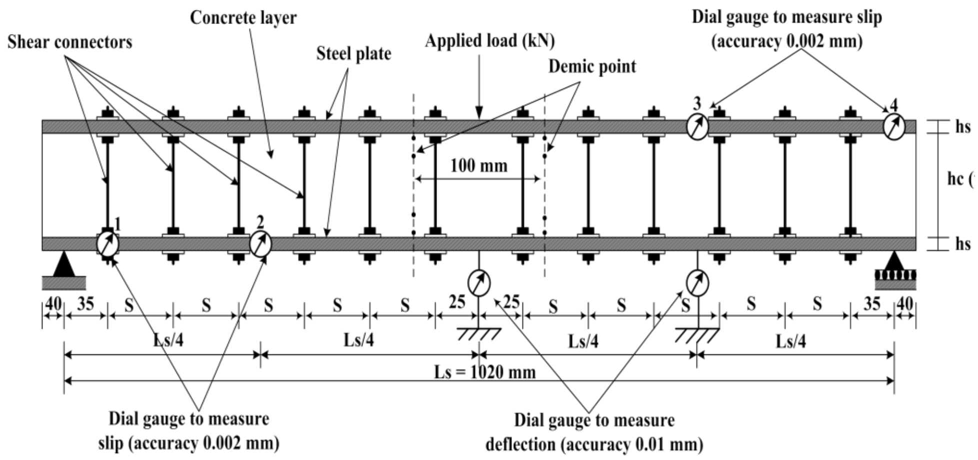

Figure 7. Fabrication details of test panels, **Zebun**, **2006**.

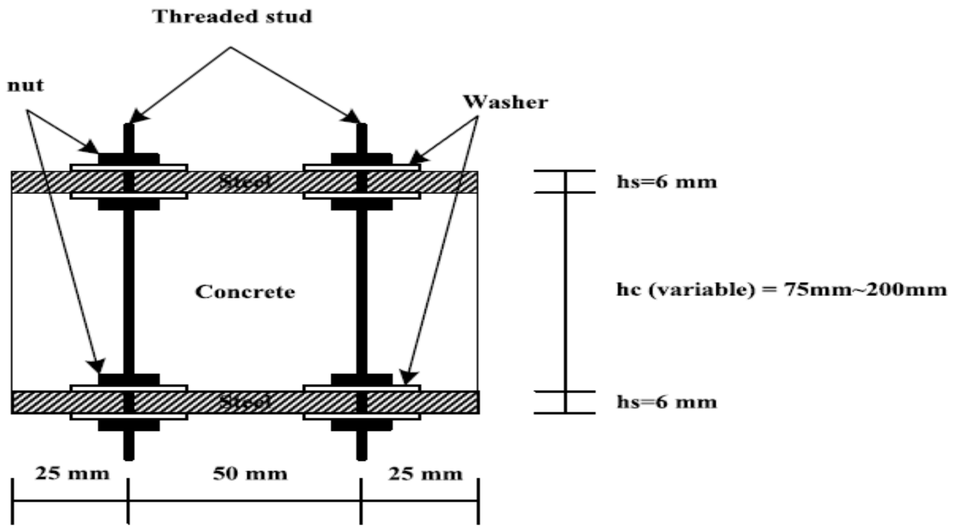

Figure 8. Cross section of SCSS beams, **Zebun**, **2006**.

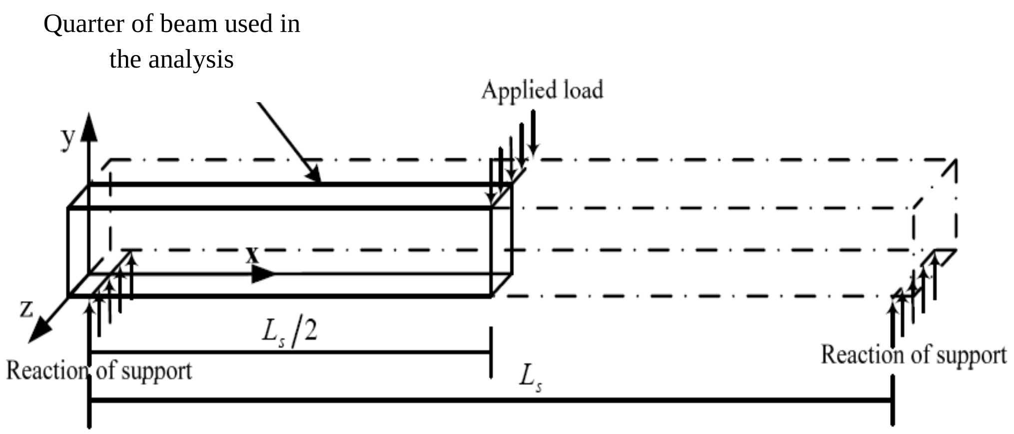

Figure 9. Dimensions and load arrangement details specimens.

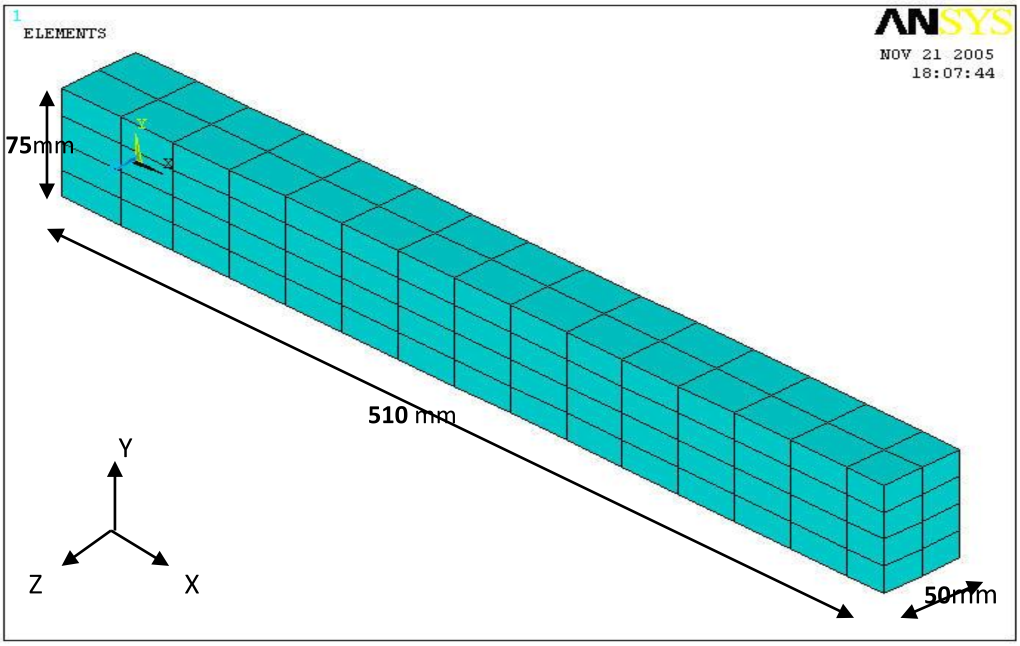

Figure 10. Mesh of quarter of beams.

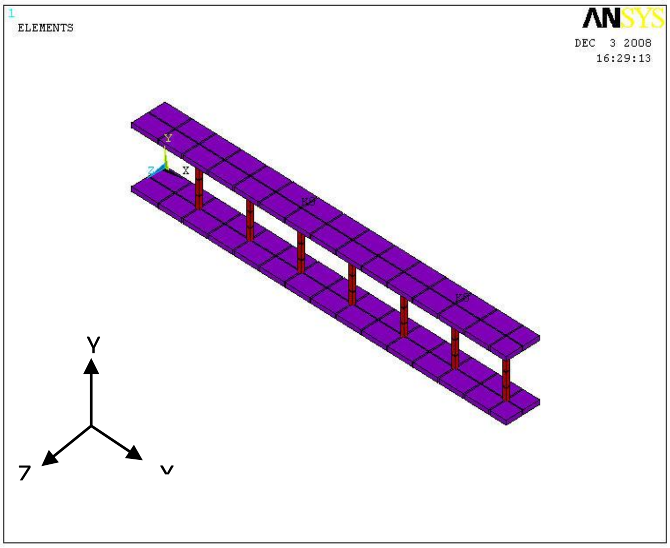

Figure 11. Mesh of LINK8 and SHELL143 for quarter (B.1).

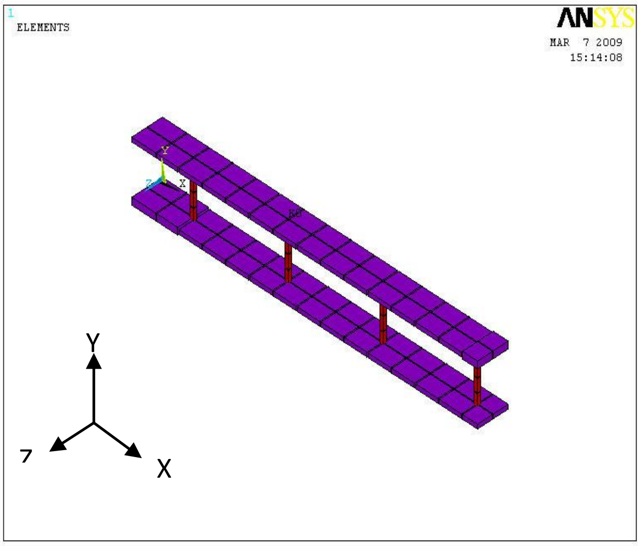

Figure 12. Mesh of LINK8 and SHELL143 for quarter (B.3).

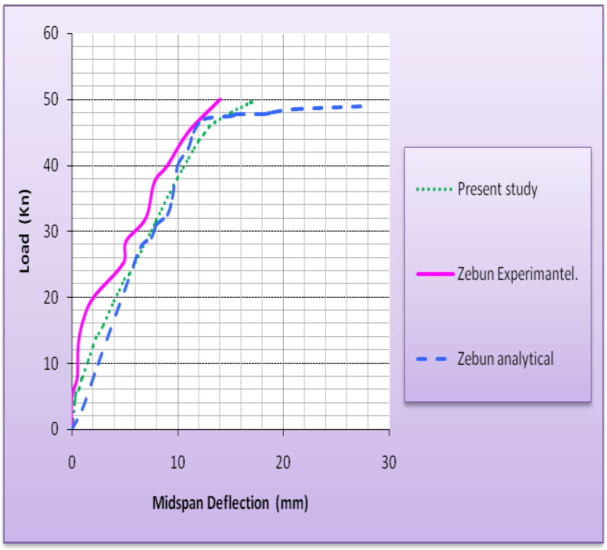

Figure 13. Load-Deflection response at mid-span of (B.1).

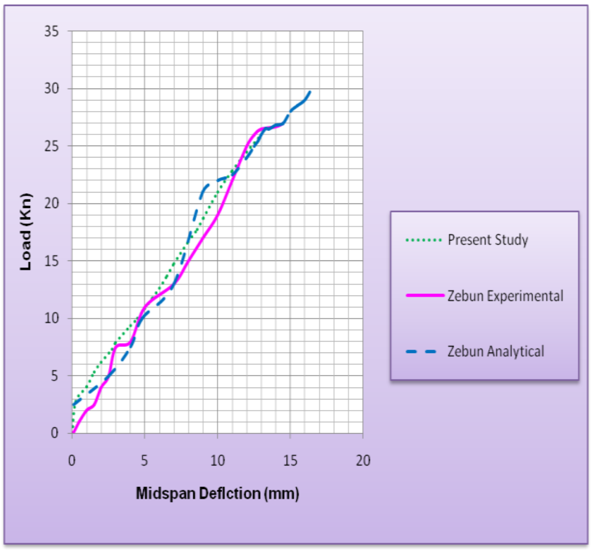

Figure 14. Load-Deflection response at mid-span of (B.3).

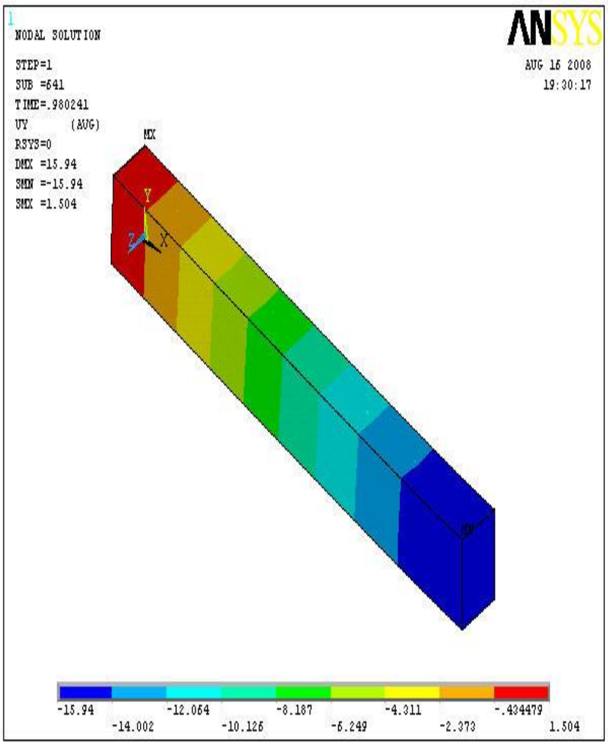

Figure 15. Variation of UY (vertical displacement) along quarter of B.1 at load equal to 98% of ultimate load.

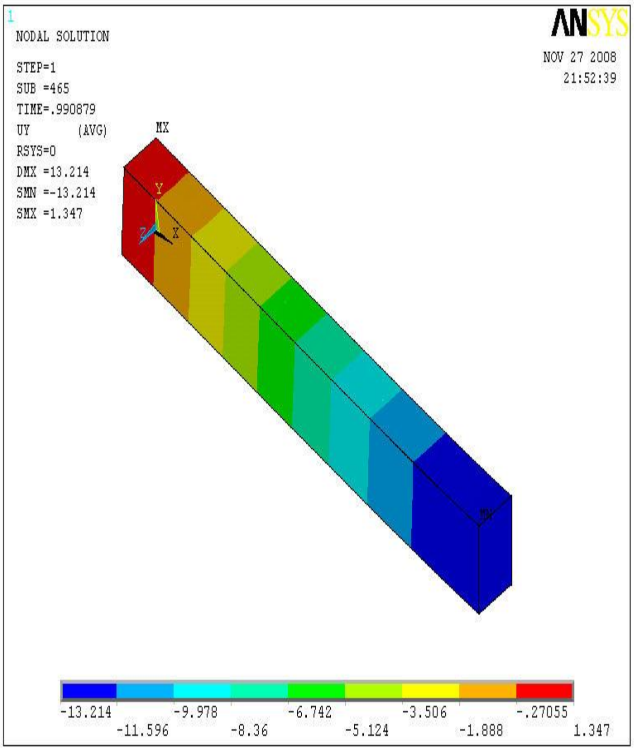

Figure 16. Variation of UY (vertical displacement) along quarter of B.3 at load equal to 99% of ultimate load. Note UY in mm.

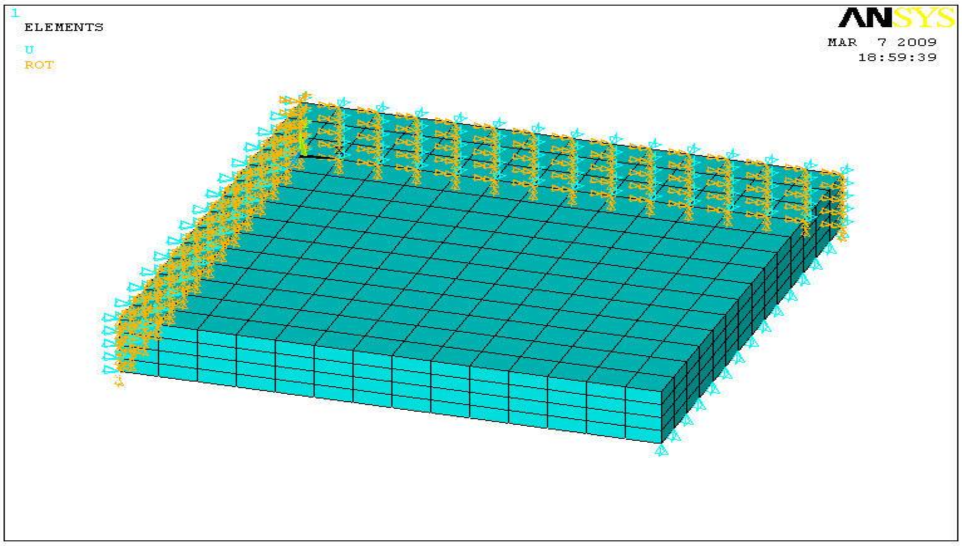

Figure 17. The boundary conditions of the quarter slab (DSC1).

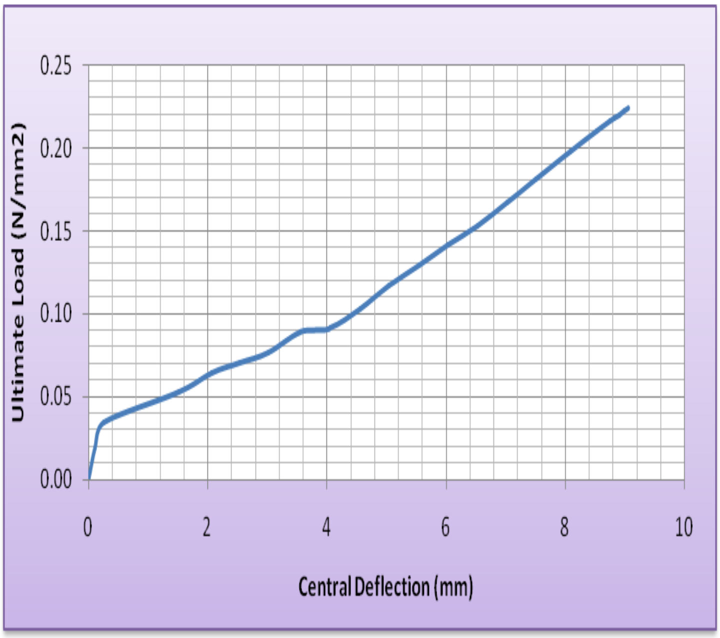

Figure 18. Load-deflection response of (DSC1).

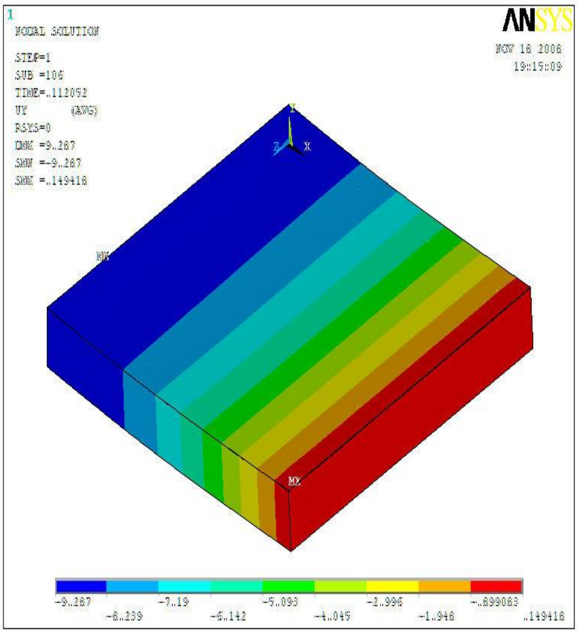

Figure 19. Variation of UY (vertical displacement) along quarter of DSC1.

University of Baghdad
College of Engineering
JOURNAL OF ENGINEERING

Journal of Engineering

journal homepage: www.jcoeng.edu.iq
Number 3 Volume 24 Month 3

Water Resources and Surveying Engineering

Improvement of the Water Use Efficiency and Yield of Eggplant by Using Subsurface Water Retention Technology

Assist. Prof. Sabah Anwer Almasraf
Department of Water Resources Engineering
College of Engineering
University of Baghdad
E-Mail: sabah_dawood@yahoo.cm

Ahmed Hatif Salim
Graduate student
College of Engineering
University of Baghdad
E-Mail: en_ahmedh@yahoo.com

ABSTRACT

Sustainable crop production in a coarse soil texture is challenging due to high water permeability and low soil water holding capacity. In this paper, subsurface water retention technology (SWRT) through impermeable polyethylene membranes was placed at depth 35 cm below ground surface and within the root zone to evaluate and compare the impact of these membranes and control treatment (without using the membranes) on yield and water use efficiency of eggplant inside the greenhouse. The study was conducted in Al-Fahamah Township, Baghdad, Iraq during spring growing season 2017. Results demonstrated the yield and water use efficiencies were 3.483 kg/m^2 and 5.653 kg/m^3, respectively for SWRT treatment plot and 3.286 kg/m^2 and 3.709 kg/m^3, respectively for treatment without using SWRT. The increasing percentages for yield and water use efficiency were 6% and 52%, respectively. Additionally, saving in irrigation water in the SWRT membrane was about 44% of the total applied depth comparing with the control treatment.

Keywords: subsurface water retention technology, water use efficiency, yield, eggplant.

تحسن كفاءة أستخدام المياه والانتاجية لنبات الباذنجان بأستخدام تقنية الأغشية الحافظة للماء تحت السطح

أ.م صباح أنور المصرف
قسم هندسة الموارد المائية
كلية الهندسة- جامعة بغداد

احمد هاتف سالم
طالب ماجستير/ قسم هندسة الموارد المائية
كلية الهندسة- جامعة بغداد

الخلاصة

استدامة انتاج المحاصيل في التربة ذات النسجة الخشنة يشكل تحديا بسبب النفاذية العالية وانخفاض قدرة التربة على مسك الماء. لهذا الغرض، فأن تقنية الاحتفاظ بالماء تحت السطح بأستخدام اغشية البولي ايثيلين وضعت عند العمق 35 سم تحت سطح الارض لتقييم ومقارنة تأثير هذا الاغشية والالواح الزراعية المسيطر عليها (بدون أستخدام ألاغشية) على انتاجية و كفاءة الماء المستخدم للباذنجان داخل البيوت الخضراء. تمت الدراسة ضمن منطقة الفحامة، مدينة بغداد- العراق للموسم الزراعي الربيعي 2017. النتائج اظهرت ان الإنتاجية وكفاءة استخدام الماء لتقنية الاحتفاظ بالماء تحت السطح وبدون أستخدام الاغشية كانت 3.484 كغم /م^2 و5.653 كغم/م^3 على التوالي، و3.287 كغم /م^2 و3.709 كغم/م^3 على التوالي، وبزيادة مقدارها 6 % و 53 % على التوالي. بالاضافة الى ان نسبة أدخار مياه الري المضافة في تقنية استخدام الاغشية كانت 44 % من المجموع الكلي للعمق المضاف مقارنة بالالواح الزراعية المسيطر عليها.

الكلمات الرئيسية: تقنية الاغشية الحافظة للماء تحت السطح، كفاءة أستخدام المياه، الانتاج، الباذنجان.

1. INTRODUCTION

Water shortage presents a serious problem nowadays. This problem will certainly worsen in the future, and so, improving the irrigation water efficiency by various methods is one of the economically viable alternatives in overcoming the water scarcity. It considers a good solution to overcome the fight against famine especially in the developing countries, **Ismail** and **Ozawa, 2007**. Development new technologies to conserve water are becoming important for achieving a sustainable economic growth, **Shahid, et al., 2012**. **Andrey, et al., 2015,** stated that subsurface water retention technology (SWRT) is a new, long-term approach to improve water storage capacities especially in coarse soil texture for sustainable crop production, increasing in yield and water use efficiency. They found that the SWRT controls the soil water content in sandy soils at optimal levels for corn growth, diminish water loss through deep drainage and minimize total irrigation depths. SWRT consists of subsurface polyethylene membrane installed within the crop's root zone with a specific aspect ratio that prevents the loss of irrigation water via deep percolation. **Ahmed, et al., 2012,** mentioned in their research work that SWRT is not only crucial for the sustainable agricultural yield but also to meet the financial problems, physical barriers and the challenges of current environmental issues and justice in the developing countries, SWRT impermeable membranes hold nutrient and agricultural chemicals reducing deep leaching losses into groundwater. SWRT solve worldwide famine and poverty and reduce global food shortages by increasing the viability of existing crops which will increase production per unit area; SWRT can also convert the previously inhospitable land into viable growing condition for food, feed, and biomass. **Demirel** and **Kavdir**, **2013,** investigated that SWRT retains optimal soil water content in plant root zones and saved 35–74 % of irrigation water compared with control (without membrane). So, **Amirpour, et al., 2016,** concluded in a study work that the frequency of irrigation will reduce after installing water-saving membranes and consequently the number of irrigation times decreased. The effect of SWRT on the yield differed for different crops. For example, **Elawady, et al., 2003**, observed an increasing value of 18 % in spinach (Spinacia oleracea L.) yield. **El-Nesr, et al., 2014,** obtained 119 and 131% increases in tomato and artichoke (Cynara cardunculus L.) yields, respectively, while **Kavdir, et al., 2014**, evaluated the performance of using membranes below the soil surface in sandy soil planted with corn. The result indicates an increase in corn production of about 238%. The objectives of this study were to evaluate and compare the effects of subsurface water-saving membranes, installed at depth 35 cm below ground surface in a sandy loam soil, on yield (Y) and water use efficiency (WUE) of eggplant inside the greenhouse.

2. MATERIALS AND METHODS

2.1 Experimental Conditions and Location of the Field Study

The experiment was conducted in Al-Fahamah Township, Baghdad, Iraq for the spring season of eggplant from January 10th to May 31st, 2017. The experimental work was carried out in the greenhouse located at Latitude: 33°25' N, Longitude: 44°20' E, and altitude: 36 m. The main source of water is from a farm reservoir charged continuously from Tigris River. Two soil samples from the greenhouse of eggplant were taken at depth (0-50 cm). Analysis of soil sample were conducted at the laboratories of the Agricultural Research Directorate of Ministry of Science and Technology. The goal of the analysis was to identify the physical characteristics of the soil in order to determine soil texture and physical properties of the soil which included bulk density, soil texture, field capacity (FC), and permanent wilting point (PWP). The average analysis of the soil texture for the two samples of the greenhouse field is classified as sandy loam soil. Also, FC and PWP were measured and equal to 16.4 and 6.9 % (by volume), respectively.

2.2 Treatments, Experimental Design and Crop Material

The greenhouse stretching in an N-S trend; it was 8 m long, 3 m wide, and 1.8 m in high (a total area of about 24 m^2). It was covered by 90 µm transparent polyethylene film treated with ultraviolet radiation. The greenhouse was without heating and air ventilation; it was classified as low technology greenhouse. Trickle irrigation system has been used in the greenhouse, the system consists of two double irrigation lines each was 8 m long of diameter 15 mm, and each trickle line contains 16 emitters along its total length. The emitters were spaced at 0.5 m apart. The average flow rate of each emitter was 20 ml/min. **Fig. 1** shows the internal layout of the greenhouse. Eggplant crop (*Solanum Melongena L.***)** was planted at 0.5 m distance between plants on both sides. In each irrigation process, soil water content before irrigation, date, the flow rate from the emitter, and time of the irrigation was recorded when possible. Two treatment plots were selected for the research work, treatment no.1 (T1) SWRT was installed below the soil surface and treatment no.2 (T2) was control plot (without using SWRT).

2.3 Description of the Subsurface Water Retention Technology (SWRT)

Subsurface water retention technology (SWRT) consists of subsurface low-density polyethylene membrane of thickness 175µm installed for a half area of the experiment at depth 35 cm below ground surface with 3:1 (length to height) aspect ratio. The installation of the membrane was done manually and all the excavation work was done by hands, no special machine was used in this process. The width of the membrane was 36 cm with both side heights was 12 cm. **Fig. 2** shows the layout of the polyethylene membrane under the soil profile.

2.4 Yield

The sum of all pickings crop's production was expressed as a total vegetable yield. The yield (in kg/m^2) was expressed as described by, **Mady** and **Derees**, **2007** as follows:

$$Yield = \frac{Total\ wieght\ of\ the\ crop\ (kg)}{Total\ area\ of\ the\ crop\ (m^2)} \qquad (1)$$

2.5 Water Use Efficiency

The water use efficiency (WUE) is the outcome of an entire site of plant and environmental processes operating over the life of a crop to determine both yield and water use. The following equation was used for calculating the field WUE (in kg/m^3), **FAO, 1982** as follows:

$$WUE = \frac{Yield\ (\frac{kg}{m^3})}{Total\ depth\ of\ applied\ water\ (m)} \qquad (2)$$

3. RESULTS AND DISCUSSIONS

3.1 Effect of SWRT on Variation of Soil Moisture

In this work, irrigation water was applied when all readily available water was depleted with 45% of depletion value through the whole stages of the growing season (no deficit irrigation was allowed). The irrigation schedule was started from mid of January 2017 and ended on end of May 2017. **Table 1** and **Table 2** show the numbers of irrigation, applied depth, and yield for SWRT treatment plot and for without using SWRT, respectively for each month through the growing season of eggplant. Soil moisture content within the membrane was affected and the water absorption by the plant root zone was conducted by capillary rise. Reduction of soil water was slower in treatment T1 compared with control treatment (T2) due to SWRT working as a barrier and to keep water within the soil profile. Additionally, daily observation showed that the top of the soil surface under SWRT plot was wetted. **Fig. 3** shows the effect of SWRT membrane on soil moisture changes and **Fig. 4** shows the soil surface of SWRT and without using SWRT after a day of irrigation. The total numbers of irrigation through the growing season for T1 and T2 were 49 and 71, respectively; frequency of irrigation in T1 was reduced by 45 %. Moreover, the total applied depth of water for treatments T1 and T2 were 617 and 887 mm, respectively, the saving in water in treatment T1 was 44 % of the total applied depth.

3.2 Effect of SWRT on Crop Yield

Fertilizer and pesticides were added to the crop for both treatments through the growing season in suitable quantities and time and as required. The crop yield value calculated based on equation 1 was stating after three months from time of planting and continuous for two months. The crop yield for both treatment T1 and T2 was 3.483 and 3.286 kg/m^2, respectively with a minor increasing value of 6 % in treatment T1. Although the yield value was almost equal in both treatment, but observation of the crop's growth for treatment T1 was showed clearly an accelerated eggplant's growth through the growing season compared with control (T2), this was due to the membrane was capture nutrients and agricultural chemical and reduce deep leaching of rich water contains, minerals, fertilizer, and pesticides materials. **Fig. 5** shows the accelerated eggplant growth with SWRT.

3.3 Effect of SWRT on Water Use Efficiency

The results for water use efficiency indicator based on a calculation using equation 2 observed clearly that water use efficiency was improved in treatment T1. The water use efficiency for T1 and T2 were: 5.653 and 3.709 kg/m^3, respectively. The increasing value in T1 was more than T2 by 52 %. This was explicit that the total applied depth in T1 was less than in T2 as long water use efficiency depends on total applied water. Saving more water with the same crop yield value will definitely increase the water use efficiency value. **Fig. 6** shows the of water use efficiency and the yield of eggplant among T1 and T2.

4. CONCLUSIONS

The installation of SWRT membrane under soil surface significantly affected saving water applied and numbers of irrigation process by 44 and 45 %, respectively. Although the crop yield values for treatments T1 and T2 equal to 3.484 and 3.287 kg/m^2, respectively with minor increasing, the water use efficiency for T1 and T2 were 5.653 and 3.709 kg/m^3, respectively with increasing value in T1 by 52 %. In other words in spite of getting the same crop yield and using less amount of water, with a high value of water use efficiency, this called improvement in irrigation process and then will be in drainage collection systems. These results are encouraging the researchers to work using the same procedures for other vegetable crops and also for strategies crops on more coarse-textured soil and even by using only rainfall water and the irrigation water will be an only supplementary method in the open field. The saving in irrigation water not only by using less water from irrigation sources but from how to collect and stored and exploit the amount of rainfall water and use it at a certain time.

REFERENCES

- Ahmed T. F., Hashmi H. N., Ghumman A. R., Sheikh A. A., 2012, *Performance Assessment of Surface and Subsurface Drip Irrigation System for Date Palm Fruit Trees*, African Journal of Agricultural Research, Vol. 7, No.10, PP.1542-1549.
- Amirpour, M., Shorafa, M., Gorji, M., and Naghavi, H., 2016, *Effect of Subsurface Water Retention Using Polyethylene Membranes with Surface Mulch and Irrigation on Moisture, Temperature and Salinity of Sandy Soil of an Arid Region in Iran*, AES Bioflux, Vol. 8, No. 1, PP. 33-41.
- Andrey, K. G., Alvin, J. M. S., Samrawi, B., and James, M. L. M., 2015, *Subsurface Water Retention Technology Improves Root Zone Water Storage for Corn Production on Coarse-Textured Soils*, Vadose Zone Journal, Vol. 14, No. 7, PP. 1-13.
- Demirel, K., and Y. Kavdir, 2013, *Effect of Soil Water Retention Barriers on Turfgrass Growth and Soil Water Content*, Journal Irrig. Sci., Vol. 31, PP. 689–700.
- El-Nesr, M. N., A. A. Alazba, and J. Simunek, 2014, HYDRUS Simulations of The Effects of Dual-Drip Subsurface Irrigation and a Physical Barrier on Water Movement and Solute Transport in Soils, Irrig. Sci., Vol. 32, No. 2, PP. 111-125.
- Elawady, M. N., M. F. Abd El-Salam, M. M. Elnawawy, and M. A. El-Farrah, 2003, *Surface and Subsurface Irrigation Effects on Spinach and Sorghum*, 11th Annual Conference of the Misr Society of Ag. Eng., kafr El-Sheikh, Egypt, 15-16 Oct. 2003. PP. 118-130.
- FAO, (1982), *Crop Water Requirements Irrigation and Drainage*, Paper no. 24, FAO, Rome, Italy.
- Ismail, S. M., and Ozawa K., 2007, *Improvement of Crop Yield, Soil Moisture Distribution and Water Use Efficiency in Sandy Soils by Clay Application*, Applied Clay Science, Vol. 37, No. 1, PP. 81-89.
- Kavdir, Y., W. Zhang, B. Basso, and A. J. M. Smucker, 2014, Development of a New Long-Term Drought Resilient Soil Water Retention Technology, J. Soil Water Conserv., Vol. 69, No. 5, PP. 154a-160a.
- Mady, A. A., and Derees, Abd. H., 2007, *Effect of Water Stress and Application of Compost on Water Use Efficiency and Productivity of Cucumber in Plastic House Under Trickle Irrigation System*, Misr J. Ag. Eng. Irrigation and Drainage, Vol. 24, No. 1, PP. 182-197.
- Shahid, S. A., Qidwai, A. A., Anwar, F., Ullah, I., and Rashid, U., 2012, *Improvement in the Water Retention Characteristics of Sandy Loam Soil Using a Newly Synthesized Poly (Acrylamide-co-acrylic Acid)/AlZnFe2O4 Superabsorbent Hydrogel Nanocomposite Material*, Molecules, Vol. 17, No. 8, PP. 9397-9412.

NOMENCLATURE

FC = field capacity.
PWP = permanent wilting point.
SWRT = subsurface water retention technology.
WUE = water use efficiency.
Y = yield.
T1 = Treatment no. 1
T2 = Treatment no. 2

Figure 1. Internal layout of the greenhouse.

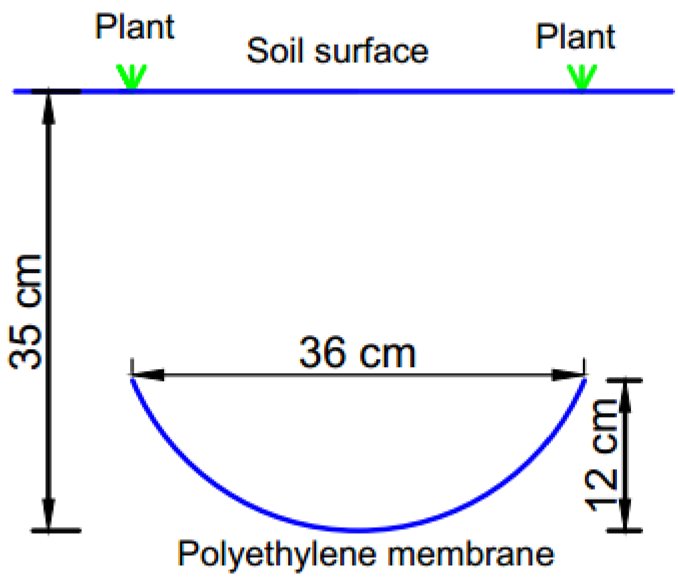

Figure 2. Layout of the polyethylene membrane under the soil profile.

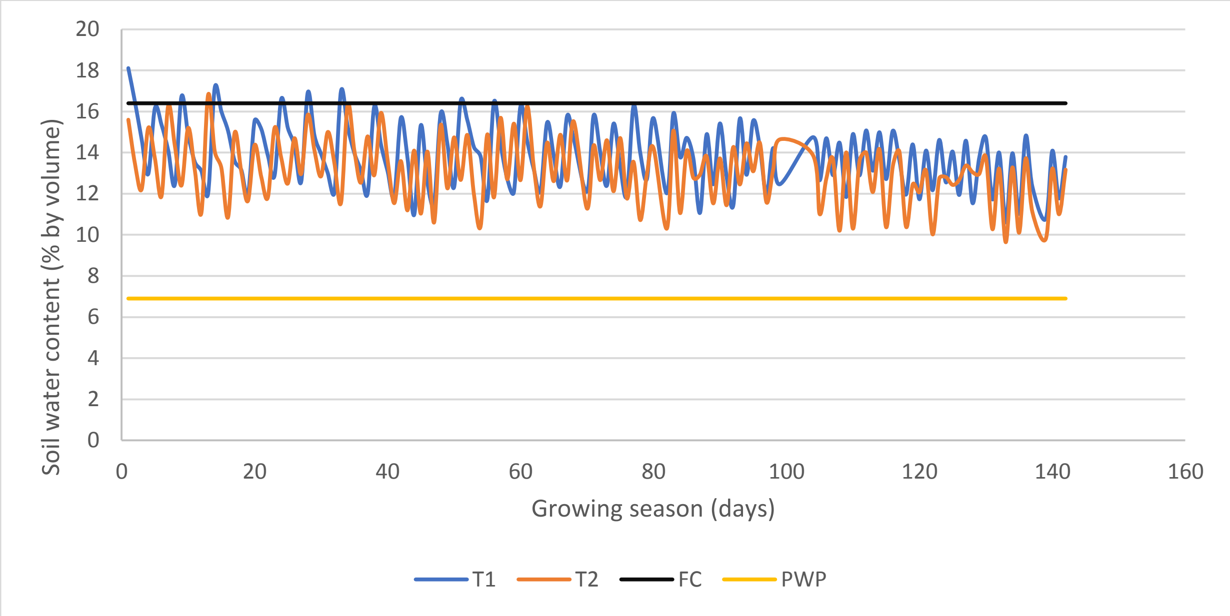

Figure 3. Effect of SWRT membrane on soil moisture changes.

Figure 4. Comparison between soil surface of SWRT and without using SWRT after a day of irrigation.

Figure 5. Accelerated eggplant growth with SWRT.

Table 1. Number of irrigation, depth of applied water and yield of the eggplant (with SWRT)*.

Month	Number of irrigation	Depth of applied water (mm)	Yield (kg/m^2)
January	6	58	0
February	8	86	0
March	8	100	0
April	14	178	1.631
May	15	195	1.852
Total	**49**	**617**	**3.483**

Table 2. Number of irrigation, depth of applied water and yield of the eggplant (without SWRT)*.

Month	Number of irrigation	Depth of applied water (mm)	Yield (kg/m^2)
January	9	86	0
February	11	120	0
March	14	180	0
April	17	224	1.241
May	20	277	2.045
Total	**71**	**887**	**3.286**

*for a period from January to May 2017.

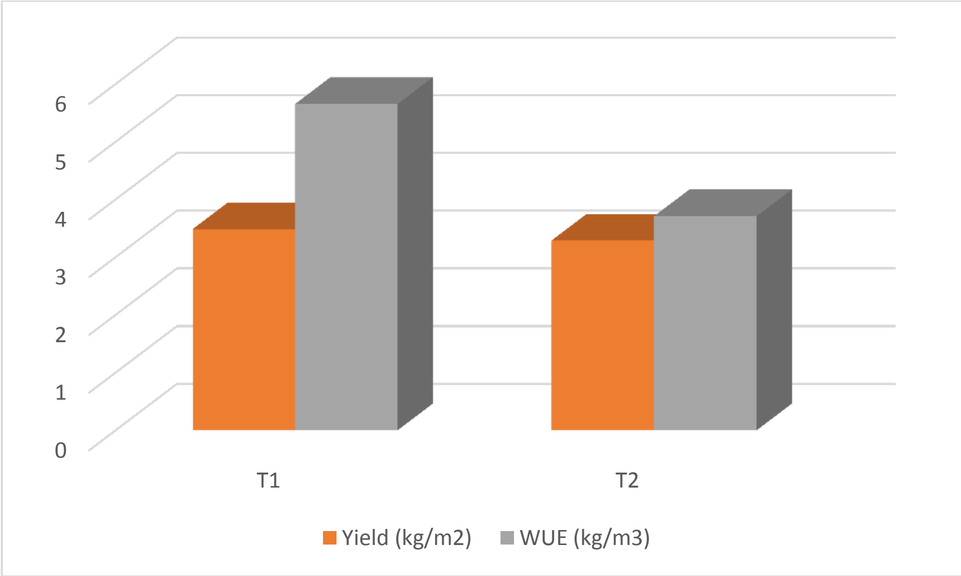

Figure 6. Comparison of water use efficiency and the yield of eggplant among T1 and T2.

ENGINEERING

College of Engineering University of Baghdad No.3 Vol. 24 March 2018

List of Contents

English Section: Page

OPEN ACCESS

Journal of Engineering

PISSN: 1726-4073
EISSN: 2520-3339

Number 3
Volume 24
January 2018

A Scientific Refereed Journal Published by the College of Engineering – University of Baghdad

www.jcoeng.edu.iq

Deposit Number in the Book and Documentation Center in Baghdad: 2231/2017